On the Diffuse Non-thermal Emission from Galaxy Clusters

Julius Donnert

München 2011

On the Diffuse Non-thermal Emission from Galaxy Clusters

Julius Donnert

Dissertation
an der Fakulät für Physik
der Ludwig–Maximilians–Universität
München

vorgelegt von
Julius Donnert
aus Braunschweig

München, den 8. Juni 2011

Erstgutachter: Prof. Dr. H. Lesch
Zweitgutachter: Prof. Dr. H. Zohm
Tag der mündlichen Prüfung: 21. Juli 2011

"Shine on you crazy diamond."
- (Pink Floyd, 1975)

Contents

List of Figures

List of Tables

Summary

A number of galaxy clusters show complex radio emission not associable with optical counterparts. These objects are commonly classified as radio relics, radio mini halos and *giant radio halos*. The latter are diffuse Mpc-sized objects centred on the intra-cluster medium (ICM) and are commonly observed in merging clusters. In this work we investigate the formation of radio halos by means of astrophysical numerical simulations.

Radio halos (RH) are observed in the GHz regime and show a complex broken power-law emission spectrum. This points to a population of relativistic electrons (CRe) interacting with the magnetic field present in the intra-cluster medium and emitting radio synchrotron radiation. Furthermore RH are transient phenomena, as inferred from the bimodal distribution of radio bright and radio quiet clusters found early on. Their scaling relations with thermal cluster observables breaks the self-similar model established from X-ray observations.

In general, relativistic particles are injected strongly localised by shocks and galactic outflows into the ICM with a power-law spectrum. They are then subject to energy losses via inverse Compton, synchrotron, bremsstrahlung and Coulomb processes. This results in a limited lifetime of cosmic-ray electrons at synchrotron bright energies in the intra-cluster medium of $\approx 10^8$ yrs. However, due to their interaction with the complex magnetic field of the ICM, it can be shown that cosmic-ray electrons have their effective diffusion speed limited to the Alvén velocity in the thermal plasma. This poses a problem on the formation of radio halos, because it is unclear how the cluster-wide synchrotron bright population of CRe, necessary to make a radio halo, can be maintained under these conditions.

Currently two competing models are heavily discussed to solve this problem. *Hadronic (secondary) models* consider the hadronic interaction of relativistic protons (CRp) with the thermal gas of the ICM. In contrast to CR electrons CRp have a sufficiently long lifetime to diffuse throughout the whole cluster. CRp - proton scattering produces charged pions, which decay into muons and subsequently into electrons. This process may lead to cluster-wide injection of synchrotron bright CR electrons with a power-law spectrum.

In contrast *reacceleration models* focus on the energisation of long-lived trans-relativistic electrons due to turbulence injected during violent cluster mergers. In these models the resonant coupling of supra-thermal electrons and MHD waves leads to stochastic phase-space diffusion of these particles to synchrotron-bright relativistic momenta.

Hadronic models received a lot of attention in the previous years. However the predictions of this model were never compared in detail to observations. We attempt to fill that

gap in the first part of this work. Also reacceleration models have never been coupled to astrophysical simulations. The second part of this thesis does this for the first time.

As a first step we use a cluster model from a cosmological MHD-simulation and three different hadronic models to compare the resulting radio halo to state-of-the-art observations of A1656. We show that the magnetic field in our simulation is in-line with the most detailed studies available for the observed cluster. In our first model we use a spatially constant scaling of CRp energy density with the thermal density. In the second one we use a radially increasing scaling motivated from direct cosmological simulations of CRp in clusters. In a third model we keep the latter CR proton scaling and upscale the magnetic field in the outer cluster regions to follow the thermal density.

We compare the expected synchrotron emission from these models with the observed halo and find a number of problems. All models predict too steep radio emission profiles and a fit to the observed profile yields unphysical CRp densities in the cluster outskirts. We for the first time use a self-consistent multi-frequency approach to investigate the modification of the predicted non-thermal radio synchrotron spectrum from secondaries by the Sunyaev-Zeldovich decrement. This way we demonstrate that hadronic models are not able to explain the spectral shape observed in RH, contrary to previous claims.

In a second step we extend our approach to a sample of 16 clusters from the simulation. Again invoking our three models we show that the predicted radio emission profiles are consistently too steep when compared with an observed sample. We demonstrate that the observed break in the self-similar model and the bimodal distribution of RH is not predicted by hadronic models. We show the gamma-ray emission from our sample and conclude that hadronic models are disfavoured by observations.

Eventually we for the first time investigate a model of CRe reacceleration by compressible magnetosonic turbulence coupled to simulations. We introduce a new implementation of a Fokker-Planck solver based on the Chang & Cooper algorithm to simulate reacceleration. This code accurately and efficiently solves the transport equation for millions of SPH particles.

To investigate the predictions of this model in detail we apply the new formalism to a simulation of a direct cluster merger, which gives us full control over the thermal model. We present a lightcurve and a spectrum of the synchrotron emission of the merger. This way we show for the first time that reacceleration models in simulations indeed predict the transient bimodal radio synchrotron emission with a broken non-thermal spectrum. We establish that turbulence driven by the DM core passages is the cause of this emission and the violation of the self-similar thermal model. We demonstrate the effect of stochastic momentum diffusion on a number of CRe spectra. The synchrotron spectrum of the simulated merger fits the spectrum observed in A1656 remarkably well. A direct comparison with a purely hadronic model as investigated before shows large differences in distribution, evolution, spectral shape and brightness. This way it is shown that reacceleration models can solve the problems in spatial distribution, radio spectrum and time evolution encountered with hadronic models before.

Zusammenfassung

In einer Reihe von Galaxienhaufen finden sich komplexe Radiostrukturen, die im Optischen nicht mit Galaxien übereinstimmen. Diese Objekte werden in der Regel als "Radiogischt", "radio Minihalos" und "riesen Radiohalos" klassifiziert. Von Interesse ist dabei vor allem die letzte Klasse von Objekten. Diese werden mit dem heissen Gas (ICM) im Zentrum von kollidierenden Galaxienhaufen identifiziert, sind Millionen von Parsec gross und diffuser Natur. In dieser Arbeit untersuchen wir die Vorhersagen zweier Modelle für die Entstehung und Entwicklung dieser Objekte mit Hilfe von Simulationen.

Riesen Radiohalos zeigen im Radiobereich bei ca. 1 Ghz ein nicht-thermales Emissionsspektrum in Form eines Potenzgesetzes. Es wird daher angenommen, dass es sich dabei um Synchrotronstrahlung von relativistischen Elektronen handelt, die sich im μG Magnetfeld des heissen, thermischen Gases im Zentrum des Haufens bewegen. Quellen relativistischer Teilchen sind grundätzlich stark lokalisierte Schocks im ICM oder galaktische Winde. Die Interaktion von kosmischer Strahlung (CR) mit the ICM führt dann zu starken radiativen Energieverlusten der Teilchenpopulation, sodass die Lebensdauer von relativistischen Elektronen (CRe) in Galaxienhaufen nur 10^8 Jahre beträgt. Dazu kommt, dass CRe durch Streuung am stark turbulenten Magnetfeld des ICM nur eine effektive Diffusiongeschwindigkeit nahe der Alvéngeschwindigkeit haben. Damit ist unklar wie es zu einer haufenweiten Population von relativistischen Elektronen kommen kann, da ihre Lebensdauer und Geschwindigkeit nicht ausreichen, um durch den gesamten Haufen zu diffundieren.

Zur Zeit werden zwei Modelle zur Lösung dieses Problems favorisiert: In *hadronischen oder sekundären Modellen* werden CRe global durch inelastische CR Proton-Proton Streuung injeziert. Denn im Gegensatz zu relativistischen Elektronen haben relativistische Protonen im ICM ausreichend lange Lebensdauern um durch den gesamten Haufen zu diffundieren. Kosmische Protonen werden dabei überall dort erzeugt, wo auch schnelle Elektronen entstehen.

Im Gegensatz dazu stehen *Wiederbeschleunigungsmodelle*. Hier werden transrelativistische Elektronen, die ähnlich wie CR Protonen eine längere Lebensdauer aufweisen, durch Turbulenz zu höheren Energien wiederbeschleunigt. Dabei injeziert die Kollision zweier schwerer Galaxienhaufen magnetohydrodynamische Turbulenz in das ICM. Die entstehenden Plasmawellen koppeln dann an die Elektronpopulation und führen durch stochastische Impulsdiffusion im Phasenraum zu einer Verschiebung der Verteilungsfunktion in Bereiche mit hoher Synchrotronemissivität.

In dieser Arbeit untersuchen wir die Vorhersagen beider Modelle mit Hilfe astrophysikalischer MHD Simulationen. Im ersten Teil verwenden wir dazu einen Galaxienhaufen aus einer kosmologischen MHD Simulation der ein grosse Ähnlichkeit mit dem Coma Haufen A1656 in den thermischen Eigenschaften und im Magnetfeld aufweist. Darauf aufbauend verwenden wir drei verschiedene hadronische Modelle um die nicht thermischen Observablen abzuleiten. Dabei skalieren wir die Dichte der relativistischen Protonen mit der thermischen Gasdichte: Im ersten Model in einem räumlich konstanten Verhältnis, im zweiten Model mit einem radial ansteigenden Verhältnis, das in direkten Simulationen von CR Protonen in Galaxienhaufen gefunden wurde. In unserem dritten Model verwenden wir die ansteigende Protonennormalisierung und skalieren das Magnetfeld unseres Haufens mit der thermischen Dichte. Dabei bleibt das Magnetfeld im hohen Konfidenzbereich der besten verfügbaren Beobachtungen.

Wir vergleichen die Radioemission der drei Modelle mit dem beobachteten Radiohalo von A1656. Dabei stossen wir auf eine Reihe von Problemen. Alle Modelle zeigen einen deutlich steileren Abfall der Emission mit dem radiale Abstand als die Beobachtungen. Dies führt bei Anpassung der Synchrotronemissivität an die Beobachtungen zu einer CR Protonendichte am Rand des Haufens, der nicht mit Beobachtungen des nichtthermischen Drucks vereinbar ist. Zudem führt ein detailierter Vergleich des Radioemissionsspektrums und des Compton-Y Parameters der Simulation und der Beobachtungen zu dem Schluss, dass, im Gegensatz zu früheren Behauptungen, der beobachtete Knick im Spektrum nicht mit dem SZ-Dekrement des Haufens erklärt werden kann.

In einer weiterführenden Studie erweitern wir unsere Betrachungen auf ein Ensemble von 16 simulierten Haufen, die wir mit einem Sample von beobachteten Haufen vergleichen. Dabei analysieren wir eine Reihe von beobachteten Skalierungsrelationen von Radiohalos und können so zeigen, dass sich die Verletzung des Prinzips der Selbstähnlichkeit von Galaxienhaufen durch Radiohalos nicht mit einem rein hadronischen Modell erklären lässt. Wir zeigen auch Vorhersagen für die Leuchtkraft der simulierten Haufen im Gammastrahlenbereich.

Schlussendlich untersuchen wir ein Wiederbeschleunigungsmodel, das auf kompressibler magnetosonische Turbulenz beruht. Dazu führen wir eine neue Methode zur Abschätzung von Turbulenz in SPH Simulationen ein. Wir stellen einen neuen numerischen Code zur Lösung der CR Transportgleichungen vor, der auf dem Chang & Cooper Algorithmus basiert. Mit Hilfe analytische Lösungen dieser Fokker-Planck Gleichung sind wir in der Lage Effizienz und Genauigkeit dieses Programms zu demonstrieren. Wir wenden unseren neuen Formalismus auf eine hochaufgelöste Simulation einer Kollision zweier schwerer Haufen an. Spektrum und Lichtkurve dieser Emission verdeutlichen eindrucksvoll, dass Wiederbeschleunigung die beobachtete bimodale Verteilung der Radiohalos reproduziert. Die Leuchtkraft des Objektes ist mit der, durch die Dynamik der dunklen Materie getriebenen, Turbulenz des thermische Gases korreliert. Dies belegen auch gezeigt Elektronenspektren. Das Radiospektrum der Kollision stimmt sehr gut mit dem beobachteten Spektrum von A1656 überein. Wir zeigen auf diese Weise glaubhaft, dass Wiederbeschleunigungprozesse eine wichtige Rolle bei der Entstehung von Radiohalos spielen.

Chapter 1

Introduction

It is believed today that matter in our universe is distributed by means of a cosmic web (figure 1.1). At the knots of this web the largest gravitationally bound objects are found, *galaxy clusters*.

Clusters are complex systems, where the gravitational potential is dominated by a dark matter halo. In its potential thousands of galaxies are moving. They account for about 2% of the clusters mass. 15% of the mass is in the *intra-cluster medium*, a blob of very hot (10^8 K), very thin (10^{-3} particles/cm^3) ionised gas (plasma) bound to the dark matter potential. This gas emits thermal radiation, which we observe with X-ray telescopes.

When a radio telescope of high sensitivity is pointed towards a cluster, complex emission patterns can be seen. A number of compact sources can be identified with galaxies seen in the optical regime. However some clusters show long elongated structures in the periphery with no optical counterpart, *radio relics*. Additionally some of them host diffuse low-surface brightness emission centred on the X-ray emission from the intra-cluster medium, *radio halos*. Both objects show a *non-thermal emission spectrum*, the former one emits strongly polarised-, the latter unpolarised light. In this work we conduct a detailed investigation of the latter objects.

The cause for the non-thermal emission from radio halos is a *population of relativistic electrons* emitting *synchrotron radiation*. These electrons (CRe) are *injected very localised* in shocks from radio galaxies or radio relics. An estimate of their *lifetime* at energies sufficient to emit the observed radiation and an estimate of their *diffusion speed* through the ICM yields a surprise: These electrons can not diffuse through the whole cluster and produce a radio halo. A number of models have been proposed in the past to solve this problem. This work attempts to critically investigate the two most promising models by means of astrophysical simulations.

In this chapter we introduce the reader to the history of giant radio halos over the last 50 years. We then motivate this work in the context of that perspective and the upcoming developments in the field.

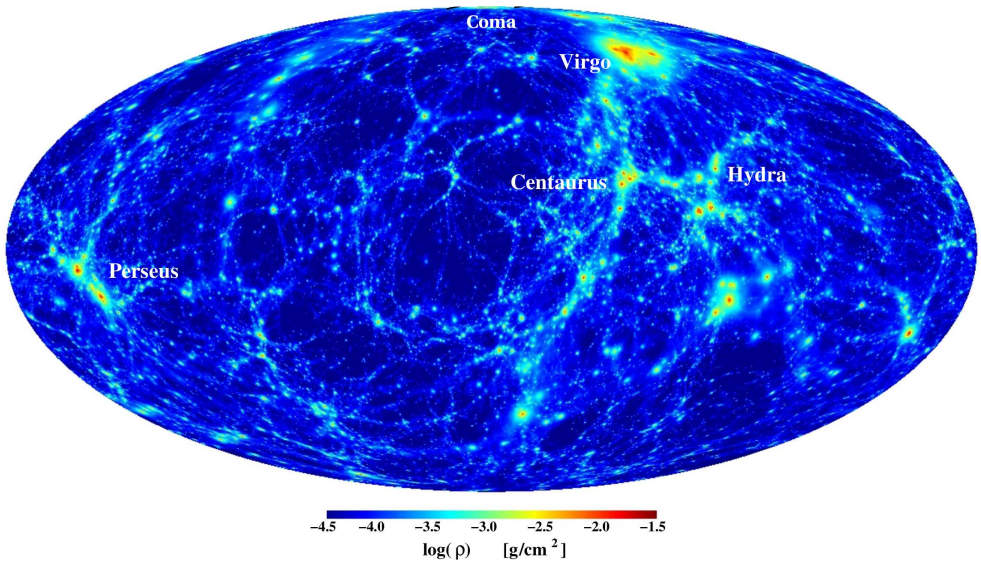

Figure 1.1: Cosmic web - a full-sky projection of the hydrogen density of a constrained cosmological simulation (Mathis et al., 2002; Donnert et al., 2009). Due to the constrained DM power spectrum the largest structures can be identified with real counterparts in the simulation.

1.1 Historical Perspective: 1957 - 2000

In his PhD thesis G. Abell prepared an optical catalog of galaxy clusters (Abell, 1957). These clusters were named after him, among them A1656 in Coma Berenices - the Coma cluster. In the same year the first radio signal at 75 cm was detected from A1656 (Seeger et al., 1957). Two years later in a letter to Nature Large et al. (1959) reported the first dedicated radio observations of the cluster. They found three strong sources (Coma A, B and C), but their observations were not accurate enough to identify optical counterparts. That made it impossible to separate contributions from compact sources like galaxies and diffuse sources.

This was of special interest because Baldwin & Elsmore (1954) observed that 20% of the radio mission from the Perseus cluster was not coming from the visible galaxy NGC 1275 in the cluster, but from a larger diffuse component. Subsequently Burbidge (1958) suggested that a similar component might be present in Coma, even though observations of the Virgo cluster did not show any diffuse emission (Baldwin & Smith, 1956) and Cygnus had only diffuse emission around its central galaxy (Jennison & Das Gupta, 1953). He proposed: "[...] considerable quantities of uncondensed intergalactic material [...]" (Burbidge, 1958) to be present in these clusters.

From work on the Crab nebula and galactic halos (Oort & Walraven, 1956; Burbidge & Burbidge, 1957) it was known that cosmic-rays with a power-law energy spectrum could be the cause of diffuse emission (Burbidge, 1956). Using the minimum energy criterion Burbidge derived magnetic field strengths of 10^{-7} G for a radio bright volume of 1 Mpc^3

size and used the original argument by Fermi (1949) to speculate: "If the intergalactic clouds [...] still containing some magnetic flux have random velocities [...], then particles will be accelerated by a variant of the original Fermi mechanism." (Burbidge, 1958).

A number of studies on the Coma cluster in the optical were done in the next decade, confirming distance and size of the Coma cluster to $\approx 70/h$ Mpc with an radius of ≈ 2 Mpc (close to todays values). Observations in the radio regime stayed inconclusive (Heidmann, 1965; Scheer & Kraus, 1967; Bozyan, 1968; Bridle, 1969).

Eventually Willson (1970) made use of the improvements in instrumentation and discovered diffuse emission from intra-cluster gas in Coma C. This observation was done at 0.4 and 1.4 GHz. The authors derive a radio spectrum as well, obtaining a power-law with spectral index 1.2. This was the first time discovery of the ICM and a radio halo and allowed to constrain temperature and size of the gas and was evidence for the presence of magnetic fields on the largest scales.

Not much later first results from X-ray rocket experiments confirmed the presence of the ICM in clusters (Meekins et al., 1971; Cavaliere et al., 1971). This marked the start of cluster astrophysics as we know it (Cavaliere & Fusco-Femiano, 1978).

At the same time theoretical progress was made in the description of cosmic-rays and astrophysical plasmas. "Radio tails" (AGN and SN driven jets and outflows) from active galaxies were discovered alongside with radio halos in a number of clusters (Ryle & Windram, 1968; Hill & Longair, 1971). The study of their interaction with the cluster atmosphere lead to the development of a more sophisticated picture of the plasma physics involved (e.g. Pacholczyk, 1970; Wentzel, 1974; Pacholczyk & Scott, 1976; Melrose, 1980). This included magnetic fields, reconnection and their measurement via Faraday rotation (Strom, 1972; Parker, 1973; Mitton, 1972).

By the end of the 1970s (Jaffe & Rudnick, 1979) a few more clusters showed diffuse emission: Harris et al. (1980) found A2255 and A401, Bridle & Fomalont (1976) discovered A2256 and diffuse emission was also seen in A2319 (Grindlay et al., 1977). Coma had been studied extensively (Grindlay et al., 1977; Wielebinski et al., 1977; Viner & Erickson, 1975; Jaffe et al., 1976). A special case was Perseus, where the situation was more complicated, because of the active galaxies involved. It became later the prototype of radio mini halos (Noordam & de Bruyn, 1982).

In a seminal paper Jaffe (1977) applied the new picture of galactic sources of cosmic-rays on the conditions in the ICM: Microgauss magnetic fields, CR electron streaming only at Alvén speed and the locality of injection by radio galaxies lead to the formulation of the cooling problem. The author proposed a number of models to solve the problem, among them in-situ acceleration by Fermi I and II processes, but found none of them to be satisfactory. Subsequent articles confirmed his work (Lea & Holman, 1978; Rephaeli, 1977).

More work was done on primary models which invoke Fermi I acceleration for cluster wide injection of CR electrons (Blandford & Ostriker, 1978; Rephaeli, 1979). Then Dennison (1980) proposed the hadronic model, after realising that protons have longer life-times in the ICM and make up most of the CR content of our own galaxy.

Throughout the 1980s X-ray observations made a leap forward with the Einstein satel-

lite and the understanding of the thermal properties of clusters hardened (Sarazin, 1988). The problem of cooling flow clusters emerged (Lea et al., 1973; Fabian et al., 1985). The situation was different in the radio regime. Only a few more clusters hosting radio halos were discovered (Cane et al., 1981; Hanisch, 1982). Most theoreticians still primarily worked on the Coma cluster. This culminated in an impressive work by Schlickeiser et al. (1987), who used preliminary new data on the Coma cluster: The authors developed a purely analytical formalism to predict the synchrotron luminosity from a number of primary, secondary and reacceleration models proposed. A comparison with the spectrum of the Coma cluster yielded a good match only for the reacceleration model[1]. With this work the predictive power of fully analytical approaches was effectively exhausted.

The following decade was mostly affected by advances in observations: first good observations of magnetic fields were available for many clusters (Kim et al., 1990, 1991). These established the presence of μG magnetic field in every cluster investigated. The problem of their origin and amplification (Kronberg, 1994) was discussed. The radio halo - merger connection was established (Tribble, 1993) and discussed in connection with the cooling flow phenomenon (Boehringer & Morfill, 1988).

The increase in resolution of radio telescopes (VLA) lead to the discovery of fainter halos (Venturi et al., 1997; Rottgering et al., 1997) and the classification of non-thermal emission from galaxy clusters we still use today (Feretti & Giovannini, 1996): giant radio halos, radio mini-halos and radio relics. Coma was investigated in even more detail (Deiss et al., 1997). This triggered the need for theoreticians to explain the new phenomena in the second half of the decade (Ensslin et al., 1997, 1998) and a renaissance of hadronic models.

At the same time numerical simulations of galaxy cluster formation started to become feasible (Roettiger et al., 1993, 1999). CR transport in our own Galaxy was modelled numerically (Moskalenko & Strong, 1998).

1.2 Recent Developments: 2000 - 2011

In the last ten years radio halo research has been pushed forward by advances in computer simulations and instrumentation.

This starts around 2000 when first numerical studies in this field arose. These studies focused on primary and hadronic models because the formalism of radio halo formation and subsequent synchrotron emission can be simplified considerably under this assumption.

Dolag & Ensslin (2000) investigated hadronic models using MHD simulations of galaxy clusters. Miniati et al. (2000, 2001) and (Miniati, 2000, 2003) used the MHD grid code of Ryu et al. (1998) to research the dynamics of shocks in the ICM. They investigated the subsequent formation of radio halos by modelling the production of primary and secondary cosmic-ray electrons.

Ensslin et al. (2007) reformulated CR proton transport by means of adiabatic invariants. This allowed an easy implementation of CR proton physics in the SPH code GADGET

[1]Compare their predicted spectrum figure 9 with figure 7.19.

(Springel, 2005; Jubelgas et al., 2008). The combination with an on-the-fly shock finder (Pfrommer et al., 2006) lead to an investigation of primary-secondary hybrid models for radio halos (Pfrommer et al., 2007, 2008; Pfrommer, 2008; Pinzke & Pfrommer, 2010). A solution for the break in the synchrotron spectrum of Coma was proposed early on (Ensslin, 2002)[2]. Some analytical work has been done recently on aspects of hadronic models in clusters (Keshet & Loeb, 2010; Kushnir et al., 2009; Enßlin et al., 2011).

In contrast to this branch of studies another group started to investigate reacceleration models in a semi-analytical approach (Brunetti et al., 2001; Gitti et al., 2002). Here the CR dynamics of a whole cluster was simulated in one spectrum, while the cluster physics was modelled analytically. These papers studied Alvénic (Brunetti et al., 2004; Brunetti & Blasi, 2005; Cassano & Brunetti, 2005) as well as magnetosonic reacceleration models (Brunetti & Lazarian, 2007; Brunetti et al., 2009; Brunetti & Lazarian, 2011b,b).

Throughout the decade the validity of hadronic/hybrid models and the necessity of reacceleration in radio halos was heavily discussed.

Turbulence in galaxy clusters and its connection to magnetic fields and radio halos was investigated analytically (Subramanian et al., 2006). An observational study on turbulence in Coma was done by Schuecker et al. (2004). Only upper limits are available for other clusters from Sanders et al. (2011). A number of methods have been proposed to observe turbulence in the ICM (Zhuravleva et al., 2010, 2011). They are based on a work by (Gilfanov et al., 1987), but will become feasible only with the next generation of X-ray satellites.

Numerical simulations were used throughout the decade to study turbulence and the cooling flow phenomenon in the ICM. This included studies with ENZO (Sunyaev et al., 2003; Inogamov & Sunyaev, 2003) and GADGET (Dolag et al., 2005). Later studies with the focus on radio halos and cosmic-rays were done by Vazza et al. (2009, 2010, 2011). Recently a Large Eddy approach to the problem was done (Iapichino et al., 2010, 2011), by implementing a sub-grid-scale model of turbulence.

Meanwhile, observations of non-thermal emission in galaxy clusters made a leap forward. We know about 50 radio halos today. More systematic observational studies yielded the first complete sample of radio halos (Kempner & Sarazin, 2001; Venturi et al., 2007, 2008) and the bimodality was established. Brunetti et al. (2008); Macario et al. (2010a) discovered steep spectrum halos. A number of scaling relations and the break of the self-similar thermal model in radio halos was established (Cassano et al., 2006, 2007, 2008). Coma's radio halo (Thierbach et al., 2003; Brown & Rudnick, 2011) and magnetic field (Bonafede et al., 2010) were studied in unprecedented detail. Murgia et al. (2004) proposed a technique based on Monte Carlo estimates to infer magnetic field power spectra from observations. It has been applied to many clusters (Govoni et al., 2006; Guidetti et al., 2008; Murgia et al., 2009; Vacca et al., 2010). A different approach based on Bayesian analysis was taken by Vogt & Ensslin (2005); Kuchar & Enßlin (2011) for Hydra A.

[2]We challenge this result in section 5.4.2.

1.3 Motivation and Placement

When this work was started in 2008 the scientific community researching radio halos was essentially split: On one side were theoreticians and two groups of numerical modellers pushing the hadronic/hybrid approach to halos. On the other side were most observers and a small group of theoreticians, pushing reacceleration models. There was heavy discussion between the two groups about which model was appropriate for halos. Hybrid approaches were very successful in explaining radio relics and were convenient to implement. Reacceleration models were claimed to be the proper approach to the halo problem, but were difficult to do. It should be noted here that the distinction between the two models (and the conflict) rooted in the two papers of Jaffe (1977) and Dennison (1980) more than 20 years ago, essentially about an approximation to the CR transport equation. It is of limited value to view these two models as distinct, as a reacceleration approach certainly can (and should) contain a hadronic approach as well. The author prefers to see reacceleration models as an extension of hadronic models. However, we adopt this distinction in our work for clarity.

The strong discussion was caused from the fact that it was (and is) difficult to conclusively test both models on observations. No article by the hadronic community offered a detailed comparison with observations, which were available in great detail since a few years. Everyone was waiting for FERMI's results on gamma-ray emission from clusters, which directly constrains these models (and is still inconclusive today). The reacceleration community had a model that offered testable predictions as well, but it was complicated (non-analytic synchrotron integral, Fokker-Planck equation) and a comparison with observations was so difficult in the details, that the supporters were unable to convincingly pin-point the superiority to the other approach.

In 2008 there was growing evidence from the first systematic observations and theoretical modelling that reacceleration (a second order process) was indeed important in clusters. Despite the number of studies on hadronic models of halos it remained unclear how these could match the observations. Specifically the bimodal distribution, the curved spectrum, and the flat spatial distribution of the emission and the break of the self-similar model in radio halos were hard to explain.

The arrival of new instruments like LOFAR (Brunetti, 2004a; Cassano et al., 2010) makes an investigation of the situation increasingly timely. Due to the spectral distribution of the radio-synchrotron emission, these low frequency instruments are expected to find many radio halos (Brunetti, 2009). This will allow a detailed study of the phenomenon. In addition radio halos will present a significant foreground source to studies involving reionisation of the universe and 21cm-tomography. A good understanding of these objects is essential for foreground removal.

Especially reacceleration models allow to test in great detail the micro-physics of plasmas acting in the cluster atmosphere. This regime is not testable in any laboratory, on or close to earth. An investigation may lead to a better understanding of collective effects in very hot, very low density plasmas.

> "In computer simulations we do not attempt to produce a perfect representation of reality in the computer, but to gain insight into the models describing it." (unknown origin) - with this in mind the present work attempts to investigate the situation of two competing models for the description of giant radio halos in galaxy clusters.

This work is structured as follows: Chapters 1 to 4 are an introduction to the field in detail. We attempt to explain all aspects of the research on radio halos, relevant to this work. After this introduction we start with the current observational status on non-thermal emission, magnetic fields and turbulence in clusters. Chapter **??** then explains the theory of CR emission, CR transport, the two competing models and the intra-cluster medium. We briefly comment on important articles in chapter 4. The following three parts are written as individual papers and present the actual core of the work:

In chapters 5 and 6 we start with a detailed comparison of pure hadronic models from MHD simulations of galaxy clusters. The simulations are available from the Diploma thesis of the author and are the first ones involving physically motivated magnetic fields (Donnert et al., 2009). We find a number of problems regarding hadronic models in a detailed comparison with the Coma cluster (chapter 5) and the cluster sample (chapter 6) from Cassano et al. (2007). With these two papers we attempt to fill the gap left by the hadronic community. They were published as Donnert et al. (2010a) and Donnert et al. (2010b) in MNRAS[3].

Chapter 7 then for the first time ever couples a reacceleration model with MHD simulations of galaxy clusters. To do so we had to develop a number of numerical tools to follow CR electron transport for millions of particles and extract the synthetic observations from the simulations. We chose to start with a merger of two galaxy clusters that would lead to a Coma-like object, because it gives us control over all relevant parameters of the simulation.

The numerical approach is especially useful here because the detailed predictions of this model regarding morphology, time evolution and spectral shape of the emission are impossible to obtain (semi-)analytically. The results give exciting new insights into predictions of reaccelerations models. We strongly recommend to view the animations of the merger, available online. The corresponding links can be found in the paper (section 7.6.2 and 7.6.2). Chapter 7 will be published as a paper and a letter in the next months. We hope this will significantly contribute to a change of opinion in the community towards a more detailed view on CR physics in the ICM.

[3]The Monthly Notices of the Royal Astronomical Society

Chapter 2

Phenomenology

This chapter is devoted to the observed non-thermal properties of galaxy clusters. We start with an introduction to the thermal observations of clusters, the ICM and its turbulence. We discuss the observational status of magnetic fields in section 2.2. Then we focus on radio halos and their observations. Finally we discuss the γ-ray non-detections recently obtained by FERMI and comment on radio relics and mini-halos.

2.1 Thermal Properties of Galaxy Clusters

Galaxy clusters are formed by the clumping of dark matter (DM) during structure formation. In the bottom-up scenario the infall of DM halos "grows" the largest structures as the universe evolves. DM dominates the gravitational potential and diffuse gas and galaxies follow its infall. At present redshifts the largest clusters host thousands of galaxies moving in the potential formed by the DM halo. The diffuse gas settles in the gravitational trough as well, forming the intra-cluster medium (ICM). The gas behaves as a collisional magnetised fluid and gets heated during the formation of the cluster to hundreds of millions of Kelvin. When a cluster is undisturbed by a recent major merging event the gas is ionised and in hydrostatic equilibrium. It accounts for roughly 15 % of the mass in a cluster, while 2% is in stars and galaxies and the rest in the dark matter halo.

The intra-cluster medium is observed in the X-ray regime. This is usually done with satellites, as the Earths atmosphere is optically thick in this regime. A typical energy range for the observations are 0.1 to 2.8 keV.

Temperature, mass and size of clusters can be derived from these observations, describing the ICM as a fluid in an external potential. In particular one finds *scaling relations* supporting the *self-similarity* of clusters (see also section 3.7). The relations include $L_{\rm X} - T$ and $M - T$. We show some findings from Arnaud & Evrard (1999); Markevitch (1998); Arnaud et al. (2005) in table 2.1 and the $L_{\rm X} - T$ relation from Markevitch (1998) in figure 2.1. The agreement of the $M - T$ relation with predictions from the theory of structure formation is very good for large clusters.

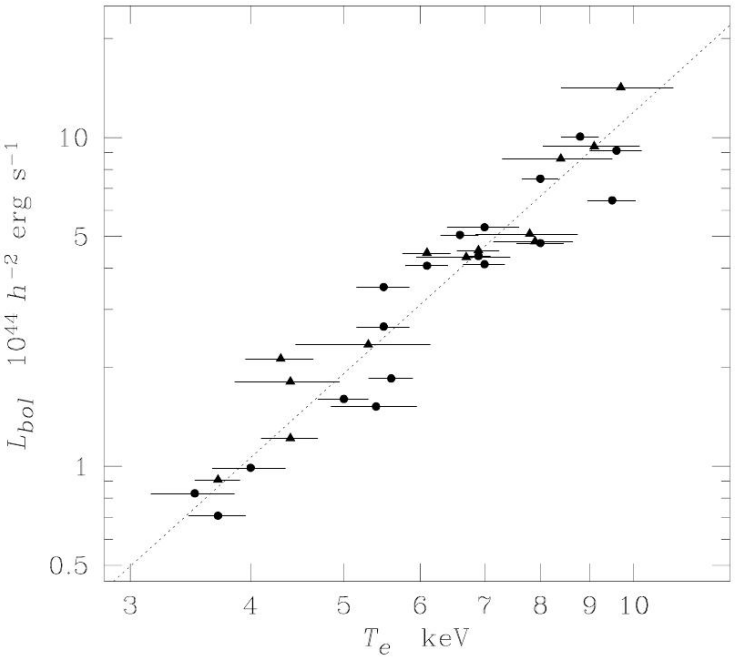

Figure 2.1: $L_X - T$ relation for a sample of observed galaxy clusters. Adopted from Markevitch (1998)

Slope	L_0 [10^{44} erg/s]	Reference
2.88 ± 0.15	10.14 ± 0.08	Arnaud & Evrard (1999)
2.64 ± 0.27	3.11 ± 0.27	Markevitch (1998)

Slope	$A_{200}[10^{14} M_\odot]$	Reference
1.49 ± 0.15	5.74 ± 0.3	Arnaud et al. (2005), largest
1.71 ± 0.09	5.34 ± 0.22	Arnaud et al. (2005), all

Table 2.1: $L_X - T$ (up) and $M - T$ (down) scaling relation from X-ray observations of galaxy clusters.

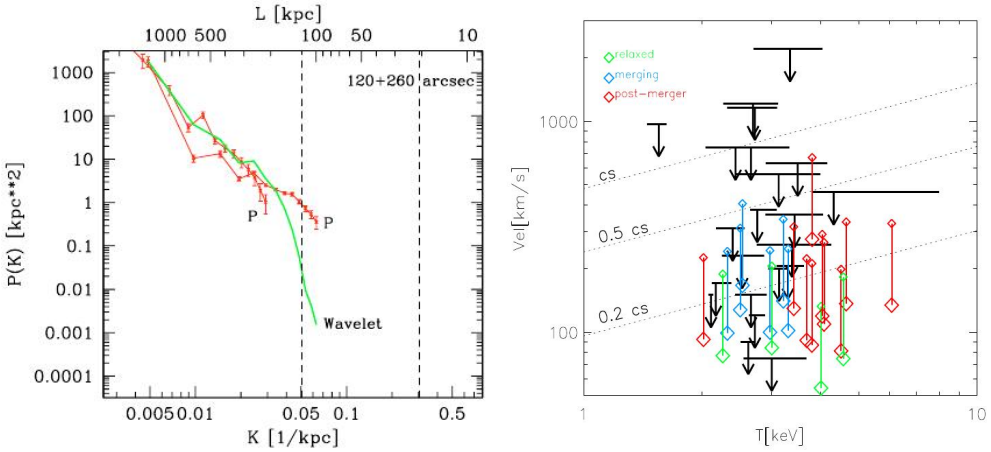

Figure 2.2: Left: power-spectrum of random motions derived from X-ray observations of Coma. Adopted from Schuecker et al. (2004). Right: velocity dispersion over cluster temperature in high resolution AMR simulations of galaxy clusters from (Vazza et al., 2011). Upper limits in black from Sanders et al. (2011).

2.1.1 Turbulence in Galaxy Clusters

Turbulence (Kolmogorov, 1941) in the cluster atmosphere is of central importance in this work. From direct observations little is known about the evolution of turbulence in the intra-cluster medium. So far the only viable way to observe random motions in the ICM is via pressure fluctuations, visible with X-ray telescopes. Alternative approaches based on Doppler line broadening, radial surface brightness distortions and resonant scattering have been proposed (Gilfanov et al., 1987; Sunyaev et al., 2003; Zhuravleva et al., 2010, 2011), but require the sensitivity and spectral resolution of next generation X-ray telescopes in order to become practical. So far only lower limits have been determined this way (Churazov et al., 2004; Werner et al., 2009; Sanders et al., 2011), which are consistent with findings from simulations.

Important theoretical work includes Koch (2009); Subramanian et al. (2006) and numerical studies using AMR and SPH codes (Sunyaev et al., 2003; Inogamov & Sunyaev, 2003; Dolag et al., 2005; Iapichino & Niemeyer, 2008; Vazza et al., 2009, 2010, 2011; Iapichino et al., 2010, 2011). Usually a Kolmogorov law for the spectrum of the random motions is found. This is in-line with observations of the magnetic field power-spectrum in Hydra A. Simulations also suggest that turbulence scales with cluster size (Vazza et al., 2011), which is supported by observations (Sanders et al., 2011). We reproduce that result in figure 2.2, right panel.

A seminal observational study was done by Schuecker et al. (2004), who used XMM-Newton observations of Coma to obtain pressure maps of the clusters hot gas (figure 2.3 and 2.2, left panel). In these studies major technical issues include the removal of substructure clumps and accounting for projection effects. The authors then use advanced wavelet techniques to obtain a spectrum of the pressure fluctuation in the intra-cluster gas

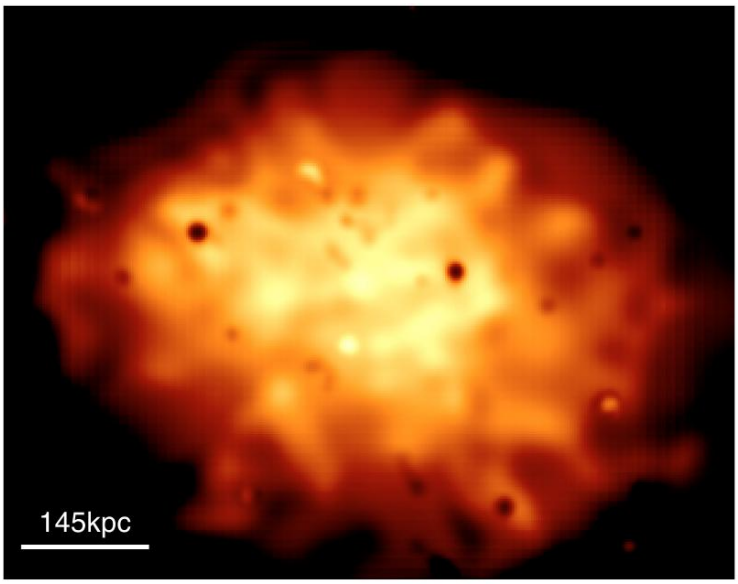

Figure 2.3: Pressure map obtained from XMM-Newton observation of Coma. Adopted from Schuecker et al. (2004).

(figure 2.3). The fluctuations roughly agree with a projected Kolmogorov power-law with less then 10% of the gas pressure in the form of turbulence.

2.2 Magnetic Fields in Galaxy Clusters

The quest for magnetic fields goes alongside with the problem of radio halos (Kim et al., 1990). The magnetic field in the intra-cluster medium and its scaling with density is an important ingredient in the formation of halos. On the other hand, halos can be used to measure magnetic fields under the assumption of equipartition of energy between CR electrons and magnetic fields (Tribble, 1991).

We will focus here on observations using the Faraday rotation (RM) measurement technique. In contrast to the radio halo (RH) method (Beck & Krause, 2005), this technique has the advantage of being independent of the cosmic-ray model assumed. This avoids inconsistencies, when modelling a CR electron population in a halo with its magnetic field inferred from different assumptions. Simple RH methods estimate the average magnetic field in the RH volume and give therefore smaller results than RM methods (Carilli & Taylor, 2002). Recent studies overcome this limitation by assuming a radial dependence of the field; both methods then give consistent field estimates (e.g. Vacca et al., 2010). Furthermore the fractional polarisation of RH can constrain the largest scales of the magnetic field power-spectrum (Bonafede et al., 2011).

The first excess rotation measure in a galaxy cluster was detected by Vallee et al. (1986). Today it is commonly assumed in the community that all clusters host a field of a few μG strength in their centre. This field usually assumed to follow a beta-model similar

to the density. These assumptions are also supported by cosmological MHD simulations (Dolag et al., 2005). It becomes more complicated when the spectral index of the field power spectrum is considered as well. Indeed spectral index and core field strength are degenerated parameters in RM observations.

A direct estimation of the spectral index comes from Vogt & Ensslin (2003, 2005), using advanced Bayesian techniques on the Hydra cluster. Alternatively, Murgia et al. (2004) propose a Monte-Carlo technique to model the field and its power spectrum from a number of RM observations. This method[1] was applied to a number of clusters (Coma (Bonafede et al., 2010), A2255 (Govoni et al., 2006), A2382 (Guidetti et al., 2008)), which we summarise in this section.

While there are a number of observations of magnetic fields in clusters, we still know relatively little about them. This is simply because inferring magnetic fields from observations is immensely difficult. Telescopes like LOFAR, ASKAP and SKA are expected to provide thousands of RM measurements, giving new insight into the field.

2.2.1 Technique

The Faraday rotation method to measure extra-galactic magnetic fields uses the magneto-optic Faraday effect. When polarised light travels through a medium containing a magnetic field, the polarisation vector changes angle (see figure 2.4 from Wikipedia (2011)). This can be easily understood, considering that linear polarised light can be thought of as a superposition of two circular polarised waves with fixed phase angle. The magnetic field changes the speed of both waves in the medium, therefore leading to a change in phase angle.

Quantitatively the phase angle is a function of the magnetic field and the electron density in the medium. Recently Mirnov et al. (2007) proposed relativistic corrections to the usual Faraday estimate, taking into account the effects of high temperatures in the magnetised medium. This effect is of the order of $\approx 5\%$, for large cluster. The Faraday rotation law then reads:

$$\phi = \frac{e^2\lambda^2}{2\pi m_\mathrm{e}^2 c^4} \int_0^{l_\mathrm{s}} n_\mathrm{e}(l) B_\parallel(l) \left(1 - \frac{2}{m_\mathrm{e}c^2} k_\mathrm{B} T\right) \mathrm{d}l + \phi_0, \tag{2.1}$$

where e and m_e are the electron charge and mass, respectively, λ - the wavelength, c - the speed of light, n_e - the electron density $B_\parallel$ - the magnetic field parallel to the line of sight, T - the gas temperature, ϕ - the rotation angle and k_B - the Boltzmann constant.

In the case of extra-galactic observations, a source of polarised light in or behind the cluster medium is chosen. It is then observed at a number of frequencies to remove the $n\pi$ ambiguity in angle[2]. The mean magnetic field along the line of sight can then be calculated

[1] See the Coma paragraph for more details on the method

[2] This can become problematic, in regions with low signal to noise. A solution to this was presented by Dolag et al. (2005); Vogt et al. (2005). They split the $n\pi$ ambiguity problem into a global and a local

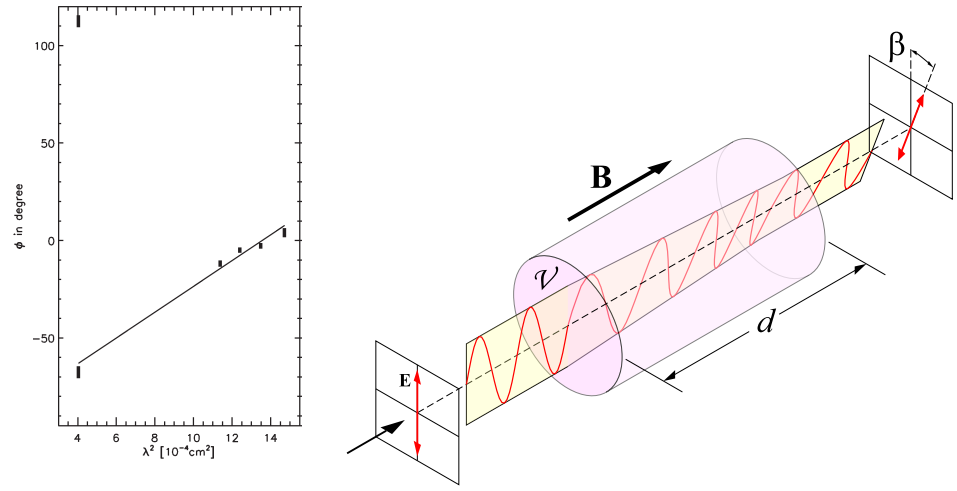

Figure 2.4: Left: Rotation angle over wavelength - $n\pi$ ambiguity solution from multi-frequency observations. Adopted from Vogt et al. (2005). Right: Cartoon of the magneto-optical Faraday effect. Adopted from Wikipedia (2011)

(Ruzmaikin & Sokoloff, 1979; Dennison, 1979; Lawler & Dennison, 1982), assuming a density model of the cluster atmosphere (usually a King law (e.g. Fusco-Femiano & Hughes, 1994)) and a distance. A recent development is the use of polarised multi-frequency observations to infer the three dimensional structure of magnetic field via "RM synthesis" (Brentjens & de Bruyn, 2005; Pizzo et al., 2011). So far radio telescopes barely match the sensitivity needed for this technique.

2.2.2 Observations

Early RM studies were done by (Kim et al., 1991; Clarke et al., 2001). They observed polarised sources in a sample of Abell galaxy clusters and saw excess Faraday rotation measure from these sources. We reproduce their radial profile of rotation measurements in figure 2.5. Both studies found a radial decline of the rotation measure, an indication for a radial decline of the magnetic field. A similar study was done for A119 by Feretti et al. (1999). They found RM values comparable to ones observed previously, indicating μG magnetic fields. Taylor et al. (2001) studied two RM sources in the cooling flow cluster 3C 129. This way they were able to constrain the rate of the cooling flow to $< 1.2\, M_{\odot}\mathrm{yr}^{-1}$.

This is already evidence that all clusters show similar magnetic fields and there is no bimodal distribution.

problem, where the global problem is solved in a reference region with high signal to noise ratio. The local problem can then be inferred from neighbouring pixels of the map, under the assumption of a smooth variation of the polarisation angle.

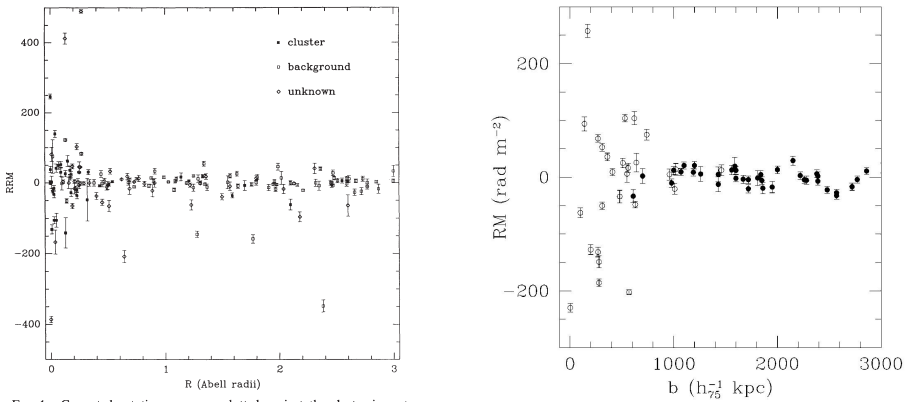

Figure 2.5: Left: RM radial profiles from a sample of Abell clusters. Adopted from Kim et al. (1991). Right: The same, but 10 years later. Adopted from Clarke et al. (2001)

Hydra A has been studied in great detail in a series of papers (Taylor & Perley, 1993; Vogt & Ensslin, 2003; Lane et al., 2004; Vogt & Ensslin, 2005; Vogt et al., 2005; Laing et al., 2008; Kuchar & Enßlin, 2011) over the last decades. The cluster is located at a redshift of $z = 0.0538$ (de Vaucouleurs et al., 1991) and hosts not only a radio halo, but also a spectacular AGN, jet and radio bubbles. The bubbles blown from the AGN form two lobes, which are not magnetised and emit polarised light. Their size and brightness make them ideal embedded sources for RM studies.

Taylor & Perley (1993) find a uniform field of $5.7\,\mu$G and a random field component of $30\,\mu$G. The dominance of the random component is the reason for the detailed investigation of this object in terms of magnetic field power spectra. This culminates in an article by Kuchar & Enßlin (2011), who use sophisticated Bayesian techniques to infer the underlying magnetic field power-spectrum from the observed RM distribution. Assuming density and magnetic field profiles for the ICM they find a Kolmogorov power-law distribution.

In figure 2.6 we reproduce the Faraday rotation measure obtained by Vogt et al. (2005) using the PACERMAN code for the northern and the southern lobe. In 2.7 we show the magnetic field power spectra, as inferred from two authors (Vogt & Ensslin, 2003; Kuchar & Enßlin, 2011).

The Hydra system is an excellent choice for studying magnetic field power spectra in the cluster environment. However it has to be noted that it is not a typical system, especially when considering radio halos.

Coma is the galaxy cluster receiving the most attention in the radio community. Magnetic fields are no exception to this rule (Kim et al., 1990; Feretti et al., 1995). Recently Bonafede et al. (2010) studied in detail the magnetic field in the Coma cluster via rotation measure analysis.

They observe a total of seven[3] polarised radio sources in the Coma cluster with the

[3]Commonly only a couple of sources are observable in other clusters.

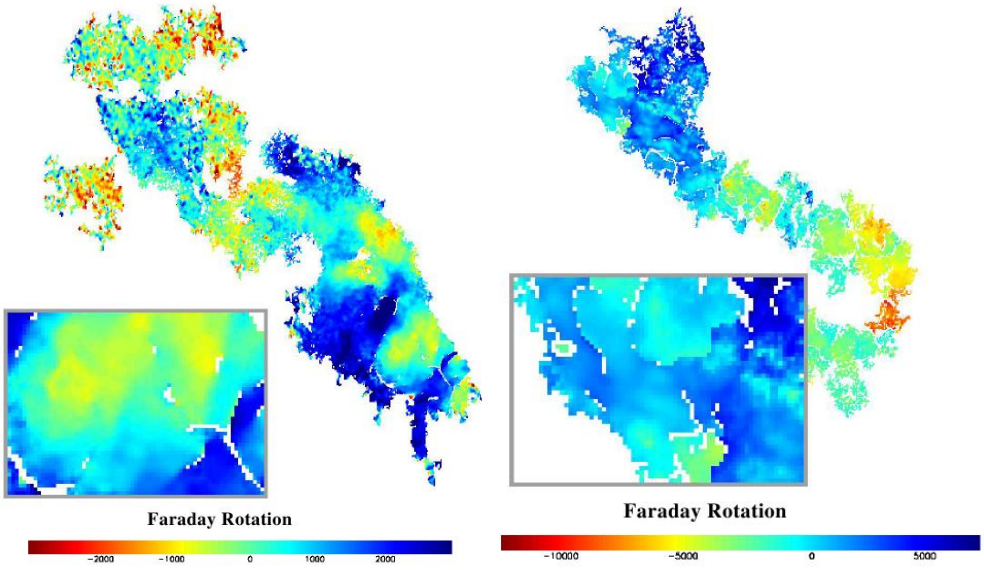

Figure 2.6: Left: Faraday rotation in the northern lobe of Hydra A. Right: Faraday rotation in the southern lobe of Hydra A. Adopted from Vogt et al. (2005)

VLA at 3.6, 6 and 20 cm wavelength. After deriving Faraday rotation measure for these sources the authors use a Monte Carlo procedure to simulate projected magnetic fields with different power spectra (Murgia et al., 2004) - A 3D magnetic field is set-up in a box with appropriate parameters in real and k-space (described below). Synthetic RM projections are then extracted and compared with the real ones via statistical methods.

They use a beta-model to fit the X-ray data and obtain the ICM density profile (Briel et al., 1992). The mean magnetic field profile $\langle \mathbf{B}(\mathbf{r}) \rangle$ is then expressed by the density profile $n_\mathrm{e}(r)$:

$$\langle \mathbf{B}(\mathbf{r}) \rangle = \langle \mathbf{B_0} \rangle \left(\frac{n_\mathrm{e}(r)}{n_0} \right)^\eta . \tag{2.2}$$

The magnetic field power spectrum is modelled as a power-law with spectral index between a minimum and a maximum scale. This approach yields five free parameters: Aside from spectral index η and central field strength $\langle \mathbf{B_0} \rangle$, largest and smallest scale of the fields power spectrum (Λ_0, Λ_1) and its slope n. Two of those are degenerate: η to $\langle \mathbf{B_0} \rangle$ and Λ_1 to n. For simplicity the authors assume a Kolmogorov spectral index and then find $\Lambda_0 \approx 2\,\mathrm{kpc}$, $\Lambda_1 \approx 34\,\mathrm{kpc}$. As the other two parameters are degenerate they give a range of 99% confidence of $B_0 = 3.9\,\mu\mathrm{G}, \eta = 0.4$ to $B_0 = 5.4\,\mu\mathrm{G}, \eta = 0.7$. The best fit yields $B_0 = 4.7\,\mu\mathrm{G}, \eta = 0.5$

In image 2.8 we reproduce in the left panel the χ^2 of the simulation fit to the data in the two parameters: average central magnetic field strength $\langle B_0 \rangle$ and spectral index η. The contours are 1,2 and 3 σ error-bars. The right panel shows a radial profile (pink) of

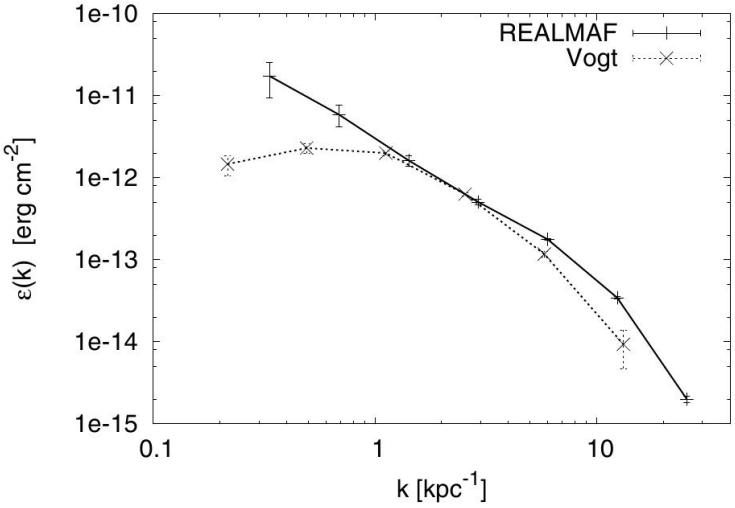

Figure 2.7: Magnetic field power spectrum of Hydra A inferred from a Bayesian analysis. Adopted from Kuchar & Enßlin (2011)

the best fit model of the average magnetic field strength in Coma with the fluctuations from the power spectrum in blue.

We make extensive use of these results in our work. Note that these observations do not clarify if the magnetic field scales with density as found in simulations or with the square-root of the density, i.e. the thermal energy density. However they constrain the field in Coma to be *not flat*, which is important for certain types of hadronic models of radio halos. The authors also conclude that adiabatic contraction is not sufficient to explain the field structure in the cluster. Additionally, turbulence has to act on the field to reach the final amplification levels. This is supported by cosmological MHD simulations (e.g. Donnert et al., 2009).

A2255 was investigated by Govoni et al. (2006) in a study where they observe four radio galaxies in the clusters atmosphere. Using the PACERMAN algorithm the authors obtain Faraday rotation measures for these galaxies. They then perform an analysis as described in Murgia et al. (2004). Simulated RM radio halo images are obtained and fit to observations, assuming specific 3D magnetic field models and using the gas density distribution from X-rays observations. This results in a best fit magnetic field model for both radio halo and RM sources.

In figure 2.9 we reproduce their two main results. The left panel shows the best fit power spectra at different distances from the centre. The right panel shows the best fit radial profile of magnetic field strength. Here the gray area marks the region of fluctuations due to the power spectra shown in the left panel.

The authors find a steepening of the magnetic field power spectrum towards the outskirts of the cluster (figure 2.9 left panel). This means that the cluster centre hosts magnetic fields, which are stronger at small scales, while at larger distances the larger scales

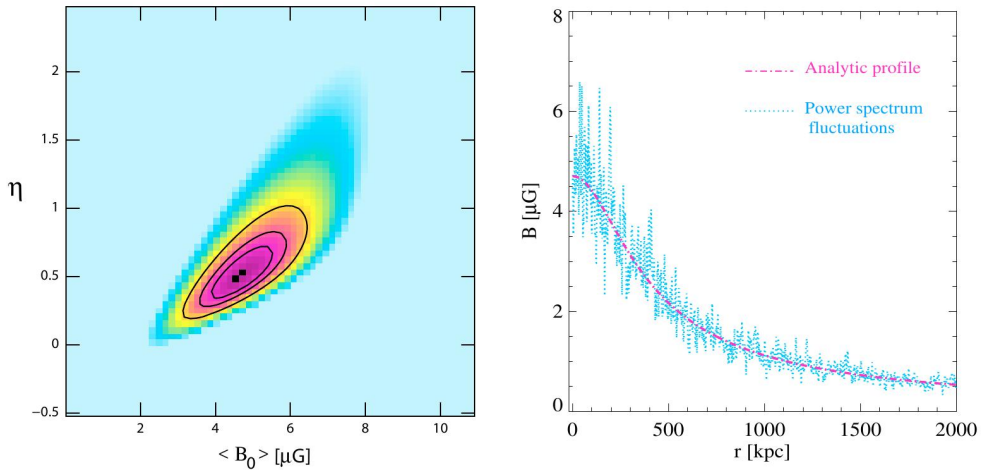

Figure 2.8: Left: χ^2 plane obtained from comparison of observations to Monte Carlo simulations of the magnetic field in Coma's ICM. Right: Derived radial profile of the magnetic field in the Coma cluster. Both adopted from Bonafede et al. (2010).

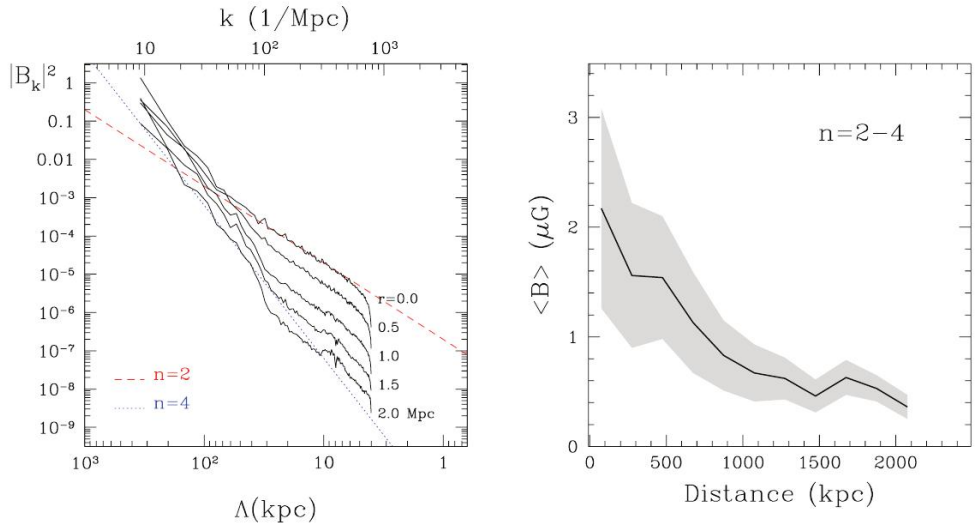

Figure 2.9: Left: Simulated magnetic field power spectra at different distances from the centre of A2255. Dashed and dotted power-laws with slope two and four respectively. Right: Radial profile of magnetic field strength for A2255. The gray area marks fluctuations from the random component assuming a power spectrum with slope two to four. Adopted from Govoni et al. (2006).

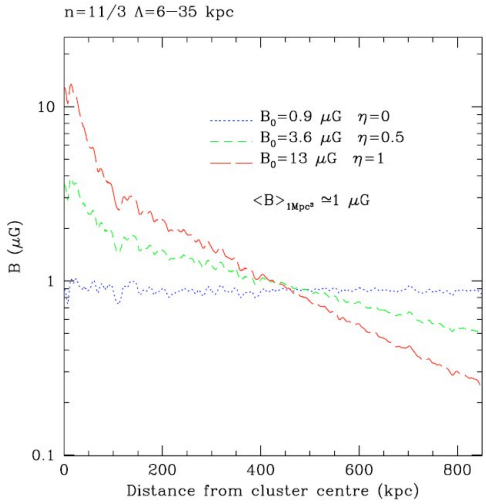

Figure 2.10: Radial profiles of magnetic field strength in A2382, depending on the scaling parameter η for power spectrum between 6 and 35 kpc. Adopted from Guidetti et al. (2008).

dominate. The average field strength at the centre is found to be about $2.5\,\mu$G with an average of $1.2\,\mu$G in a volume of $1\,\mathrm{Mpc}^3$. The authors also claim to find indications for a filamentary structure of the field.

A2382 was studied in a similar manner by Guidetti et al. (2008). They use VLA observations of two polarised sources in the cluster and the simulation method from Murgia et al. (2004) to estimate the magnetic field. In figure 2.10 we reproduce their main result - radial profiles of magnetic field strength for different scaling parameters. The authors are unable to resolve the degeneracy between scaling parameter η and centre magnetic field strength. Instead they show the reasonable range of possible parameter combinations. A Kolmogorov power spectrum is assumed for all profiles with an upper scale of 35 kpc and a lower scale of six kpc.

A665 was subject of a study by Vacca et al. (2010). The authors observes 26 radio galaxies with the VLA in the cluster and performed the analysis proposed by Murgia et al. (2004) in combination to fitting the observed radio halo (Tribble, 1991). They assumed a Kolmogorov-like magnetic field power spectrum, a minimal scale of four kpc and a field scaling parameter of $\eta = 0.47$. The CR electron population was modelled to have a power-law spectral index of three with a cutoff at $\gamma = 100$. They inferred a maximum scale of 450 kpc and a central field strength of $1.3\,\mu$G, by simultaneously fitting the radio halo and the RM sources. This was in-line with previous observations.

2.3 Observations of Radio Halos

Giant radio halos are observed to be diffuse Mpc-sized radio sources in the centre of merging galaxy clusters. They are associated with the X-ray bright intra-cluster medium (ICM). This and their low degree of polarisation sets them apart from radio relics discussed in section 2.5.1. The association with mergers and the sheer size distinguishes giant radio halos from mini-halos (section 2.5.2), which are found in relaxed cooling flow clusters almost exclusively.

The non-thermal spectrum of giant halos, a (broken) power-law, suggests synchrotron radiation to be the underlying emission mechanism. In this process a population of highly energetic electrons interacts with the ICM. The magnetic field present in that medium causes the electrons to emit radiation and lose energy (section 3.1.2). It is unclear (see section 3.2) how this CR electron population is maintained.

To make matters worse radio halos do not follow the self-similar model found from X-ray observations. They are present only in a fraction of galaxy clusters and associated with cluster mergers, i.e. a disturbed X-ray morphology. The upper limits for radio quite clusters are about a factor of 10 below radio loud clusters of the same mass. One can estimate that clusters have to become radio quiet within 1 Gyr (Brunetti et al., 2009).

This section is entirely devoted to the current observational status of giant radio halos in galaxy clusters. We begin with a gallery and a list of most of the well observed radio halos today. We will then focus on the Coma cluster (A1656) and the special role it plays to the research community today. It hosts most of the complexity found in clusters and can be considered a lucky coincidence to the researchers. We will turn to review a more detailed study on the connection between X-ray and radio surface brightness morphology. It challenges some models even seven years after its publication. These results are clarified by the statistical approaches presented in the following two sections. Correlations relate the observed radio properties of many clusters to thermal quantities like X-ray brightness and mass. We will finalise this section with a review of the newest results on ultra-steep sources, which present an outlook into the future of radio observations as it approaches with LOFAR and the SKA.

2.3.1 Known Halos

There are about 36 well observed radio halos known today. A list was compiled by Giovannini et al. (2009) and can be found in tables 2.2 and 2.3. We added a few recent observations, which are marked with negative citation numbers in column 9. The columns contain: name, redshift, angular to cluster conversion factor, radio flux at 1.4 GHz, error of that flux, log radio luminosity, largest linear size, X-ray luminosity, references to radio and X-ray luminosity, and notes.

We also compile a gallery of a few halos in image 2.11 observed at 1.4 GHz, if not stated otherwise. In the top left corner we reproduce a famous observation of A2163 by Feretti et al. (2001), which is still the most luminous cluster known today. At its largest extend the radio halo is over 2 Mpc in size. The top right features A1351 as observed by

(Giacintucci et al., 2009). The cluster is suspected to be part of a filament. The middle left panel shows A2744 from Govoni et al. (2001). The cluster also hosts a big relic, which is the large irregular structure in the north-west of the image. A low-frequency observation of RXCJ2003.5-2323 at 610 MHz by Venturi et al. (2007) can be found in the middle right panel. Due to their steep spectrum, clusters are significantly larger at this frequency than at the standard frequency of 1.4 GHz. A recent observation from Bonafede et al. (2009) is shown on the lower left panel. MACSJ J0717.5+3745 is in the top three of the largest clusters known today and a beautifully complex system. The authors mark a number of galaxies which were identified in the optical wave-band. The last halo is A523 as recently observed by Giovannini et al. (2011).

Quite a few famous clusters exhibit radio halos. The most prominent example is Coma, which we will discuss separately in chapter 2.3.2. The bullet cluster[4] 1E0657-56 also hosts a radio halo, as one would expect from an on-going massive merger. Two clusters (A3444 and J0717.5+3745) are claimed to host a filament - a gas bridge connecting two over-densities which is predicted by cosmological simulations. All clusters show a disturbed, irregular and highly complex X-ray morphology and many are host to radio relics as well. Radio halos have not been found to be significantly polarised. This points to a highly tangled magnetic field on scales below the beamsize[5]. Quite a few clusters show a steepening of their spectrum. This is expected in some theoretical models as an "ageing" of the clusters CR electron population. It is then on the transition to disappear from the $P_{14} - L_{\mathrm{X}}$ correlation presented in 2.3.5.

[4]Famous for having its gravitational potential as measured by weak lensing offset from the X-ray bright gas. Thus being an indirect observation of dark matter.

[5]In radio astronomy the beamsize corresponds to the point-spread function in optical astronomy. The Fourier transformed of the aperture of the telescope gives an estimate of the smallest structure resolvable by the instrument.

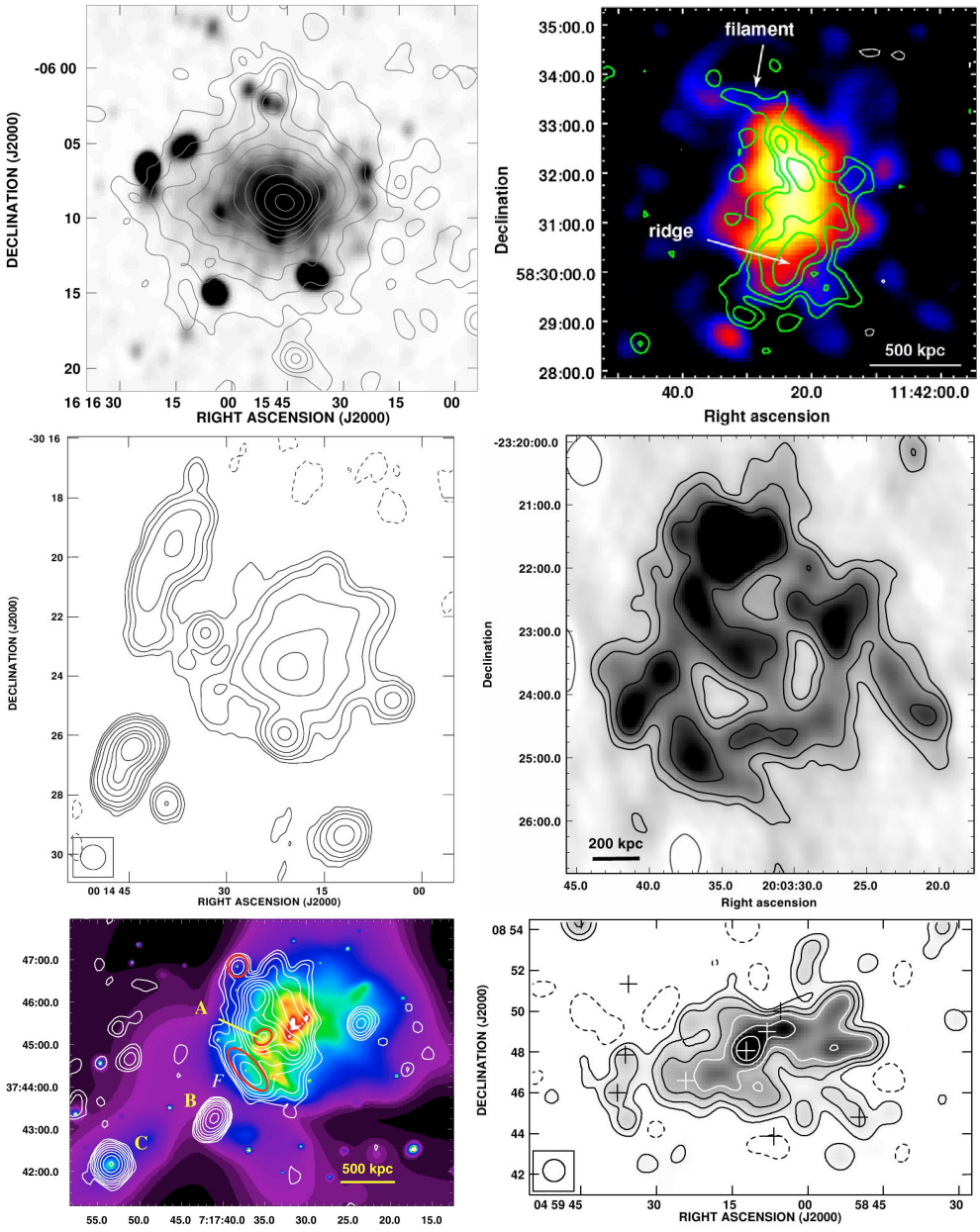

Figure 2.11: Gallery of radio halos at 1.4 GHz, if not stated otherwise. From top left to bottom right: A2163, radio in gray, X-ray in contours (Feretti et al., 2001); A1351, radio brightness in contours, X-ray in colour from (Giacintucci et al., 2009); A2744 from (Govoni et al., 2001); RXCJ2003.5-2323 at 610 MHz from (Venturi et al., 2007); MACSJ J0717.5 +3745, radio in contours, X-ray in colour (Bonafede et al., 2009); A523, radio brightness from (Giovannini et al., 2011).

Cluster Name	z	kpc/"	$S_{1.4}$ [mJy]	$\Delta S_{1.4}$ [mJy]	log $P_{1.4}$ [W/Hz]	LLS [Mpc]	L_X [10^{44} erg/s]	Ref. Radio	Ref. X-ray	Notes
A209	0.2060	3.34	16.9	1.0	24.31	1.40	6.17	0	21	a relic might be present
A401	0.0737	1.38	17.0	1.0	23.34	0.52	6.52	1	15	elongated and irregular
A520	0.1990	3.25	34.4	1.5	24.58	1.11	8.30	2	16	
A521	0.2533	3.91	5.9	0.5	24.05	1.17	8.47	0	21	relic
A523	0.10	1.82	59	5	24.17	1.3	1.07	-2	16	arXiv only
A545	0.1540	2.64	23.0	1.0	24.16	0.89	5.55	1	21	
A665	0.1819	3.03	43.1	2.2	24.59	1.82	9.65	3	16	
A697	0.2820	4.23	7.8	1.0	24.28	0.65	10.40	22	16	from NVSS
A754	0.0542	1.04	86.0	4.0	23.77	0.99	2.21	1	15	relic
A773	0.2170	3.48	12.7	1.3	24.23	1.25	7.95	2	16	
A781	0.3004	4.45	36	5	25.0	1.8	11	-3	16	substructure
A851	0.4069	5.40	3.7	0.3	24.33	1.08	5.04	0	17	
A1213	0.0469	0.91	72.2	3.5	23.56	0.22	0.10	0	18	asymmetric
A1300	0.3072	4.49	20.0	2.0	24.78	1.3	13.73	4,5	21	relic
A1351	0.3224	4.64	39.6	3.5	25.12	0.84	5.47	0	17	
A1656	0.0231	0.46	530.0	50.0	23.80	0.83	3.99	6	15	relic
A1758	0.2790	4.20	16.7	0.8	24.60	1.51	7.09	0	19	total diffuse emission H+R
			3.9	0.4	23.97	0.63		0		central halo
A1914	0.1712	2.88	64.0	3.0	24.71	1.04	10.42	1	15	

Table 2.2: Compilation of known radio halos from Giovannini et al. (2009), extended by PLCK G287.0 , MACSJ0717.5+3745, A523 and A773. References for radio halos: -4 = Bagchi et al. (2011), -3 = Govoni et al. (2011); -2 = Giovannini et al. (2011); -1 = Bonafede et al. (2009), 0 = Giovannini et al. (2009), 1 = Bacchi et al. (2003); 2 = Govoni et al. (2001); 3 = Giovannini & Feretti (2000); 4 = Venturi et al. (2009); 5 = Reid et al. (1999); 6 = Kim et al. (1991); 7 = Feretti et al. (2001); 8 = Govoni et al. (2005); 9 = Clarke & Ensslin (2006); 10 = Feretti et al. (1997); 11 = Venturi et al. (2003); 12 = Liang et al. (2000); 13 = Feretti et al. (2005); 14 = Giacintucci et al. (2009). References for X-ray data: 15 = Reiprich & Böhringer (2002); 16 = Ebeling et al. (1998); 17 = Böhringer et al. (2000); 18 = Ledlow et al. (2003); 19 = Ebeling et al. (1996); 20 = Wu et al. (1999); 21 = Böhringer et al. (2004); 22 = Ebeling et al. (2007).

Cluster Name	z	kpc/"	$S_{1.4}$ [mJy]	$\Delta S_{1.4}$ [mJy]	log $P_{1.4}$ [W/Hz]	LLS [Mpc]	L_X [10^{44} erg/s]	Ref. Radio	Ref. X-ray	Notes
A1995	0.3186	4.61	4.1	0.7	24.13	0.83	8.83	0	17	
A2034	0.1130	2.03	13.6	1.0	23.64	0.61	3.81	0	16	
A2163	0.2030	3.31	155.0	2.0	25.26	2.28	22.73	7	14	relic
A2218	0.1756	2.94	4.7	0.1	23.60	0.38	5.77	3	16	asymmetric
A2219	0.2256	3.58	81.0	4.0	25.08	1.72	12.19	1	16	
A2254	0.1780	2.98	33.7	1.8	24.47	0.92	4.55	2	16	irregular shape
A2255	0.0806	1.50	56.0	3.0	23.94	0.90	2.64	8	16	relic
A2256	0.0581	1.11	103.4	1.1	23.91	0.81	3.75	9	16	relic
A2294	0.1780	2.98	5.8	0.5	23.71	0.54	3.90	0	16	
A2319	0.0557	1.07	153.0	8.0	24.04	1.02	8.46	10	15	spectral steepening
A2744	0.3080	4.50	57.1	2.9	25.24	1.89	12.86	2	21	relic
A3444	0.2533	3.91	14.6	1.0	24.45	3.3	13.42	0	21	filament
A3562	0.0490	0.95	20.0	2.0	23.04	0.28	1.57	11	15	spectral steepening
1E0657-56	0.2960	4.38	78.0	5.0	25.33	2.1	22.59	12	21	bullet cluster
J1314.4-2515	0.2439	3.81	20.3	0.8	24.55	1.83	10.75	13	21	double relics
CL1446+26	0.3700	5.08	9.2	0.5	24.63	0.36	3.42	0	20	relic source
J2003.5-2323	0.3171	4.59	35.0	2.0	25.09	1.40	9.12	14	21	
MACS J0717.5	0.55	6.25	20.0	–	–	1.5	20.9	-1	22	filament
PLCK G287.0	0.39	5.29	–	–	–	–	17.2	-4	-4	3 relics, halo t.b.d.

Table 2.3: Compilation of known radio halos from Giovannini et al. (2009), extended by PLCK G287.0 , MACSJ0717.5+3745, A523 and A773. References for radio halos: -4 = Bagchi et al. (2011), -3 = Govoni et al. (2011); -2 = Giovannini et al. (2011); -1 = Bonafede et al. (2009), 0 = Giovannini et al. (2009), 1 = Bacchi et al. (2003); 2 = Govoni et al. (2001); 3 = Giovannini & Feretti (2000); 4 = Venturi et al. (2009); 5 = Reid et al. (1999); 6 = Kim et al. (1991); 7 = Feretti et al. (2001); 8 = Govoni et al. (2005); 9 = Clarke & Ensslin (2006); 10 = Feretti et al. (1997); 11 = Venturi et al. (2003); 12 = Liang et al. (2000); 13 = Feretti et al. (2005); 14 = Giacintucci et al. (2009). References for X-ray data: 15 = Reiprich & Böhringer (2002); 16 = Ebeling et al. (1998); 17 = Böhringer et al. (2000); 18 = Ledlow et al. (2003); 19 = Ebeling et al. (1996); 20 = Wu et al. (1999); 21 = Böhringer et al. (2004); 22 = Ebeling et al. (2007).

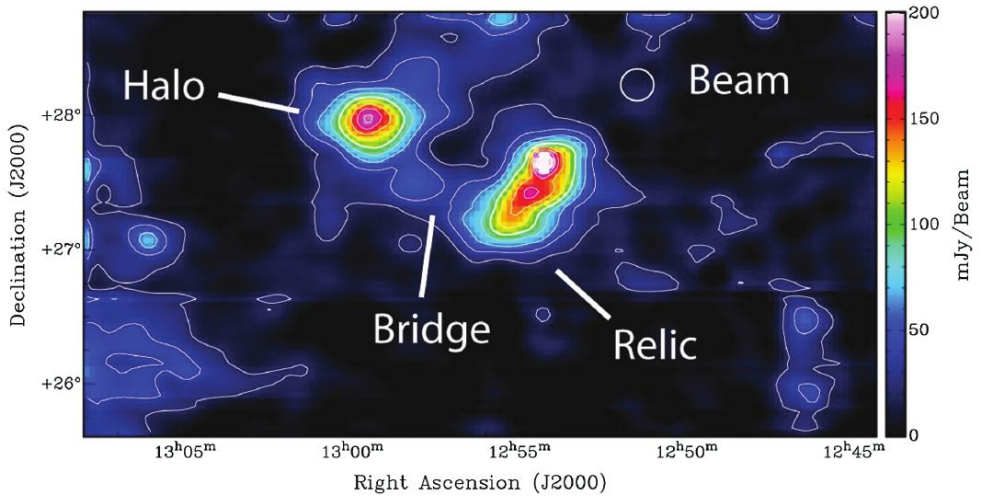

Figure 2.12: Radio surface brightness of the Coma cluster at 1.41 Ghz. Adopted from Brown & Rudnick (2011).

2.3.2 The Coma Cluster

From the beginning (Large et al., 1959) up to today (Brown & Rudnick, 2011), the Coma cluster (A1656) and its radio halo have been receiving a lot of attention. Due to its brightness of 530 mJy (Kim et al., 1991), Coma's ICM has been first discovered in the radio regime (Willson, 1970). Coma is probably the most studied system in existence. It is the prototype of this class of objects.

The Coma cluster is a system of two merging clusters at a redshift of $z = 0.0232$ or a distance of roughly $90\,h_{75}^{-1}$ Mpc (Thierbach et al., 2003). This corresponds to an angular scale of $26\,h_{75}^{-1}$ kpc/arcmin. The main cluster has a X-ray temperature of ≈ 9 keV (De Grandi & Molendi, 2002) and its X-ray derived ICM density profile is best fit with a beta profile with $\beta = 0.7$, $r_{\mathrm{core}} = 275$ kpc and $n_{e,0} = 0.0037\,\mathrm{cm}^{-3}$ (Mohr et al., 1999). On the other hand, Schuecker et al. (2004) found a highly disturbed X-ray morphology in the cluster using XMM-Newton, which questions the validity of the standard approach to model the cluster atmosphere with a King model.

Other X-ray telescopes have been used to observe the cluster: RXTE, INTEGRAL and Suzaku (Lutovinov et al., 2008; Wik et al., 2009, 2011), mostly to investigate the still heavily debated detection of the hard non-thermal X-ray excess claimed by (Fusco-Femiano et al., 1999; Rephaeli & Gruber, 2002; Fusco-Femiano, 2004). This excess is expected from inverse Compton scattering in the ICM, see also section 3.1.3.

Figures 2.12 and 2.13 show maps of the clusters radio emission at 1.41 GHz and 352 MHz, as recently observed with the Green Bank Telescope by Brown & Rudnick (2011). The radio halo and the radio relic are marked in both figures. The authors found a diffuse bridge between them in the high frequency observation 2.12 and indications for a shock front in the low frequency observation 2.13.

The size of the halo in figure 2.12 is approximately 1.3 Mpc at 1.4 GHz. Deiss et al.

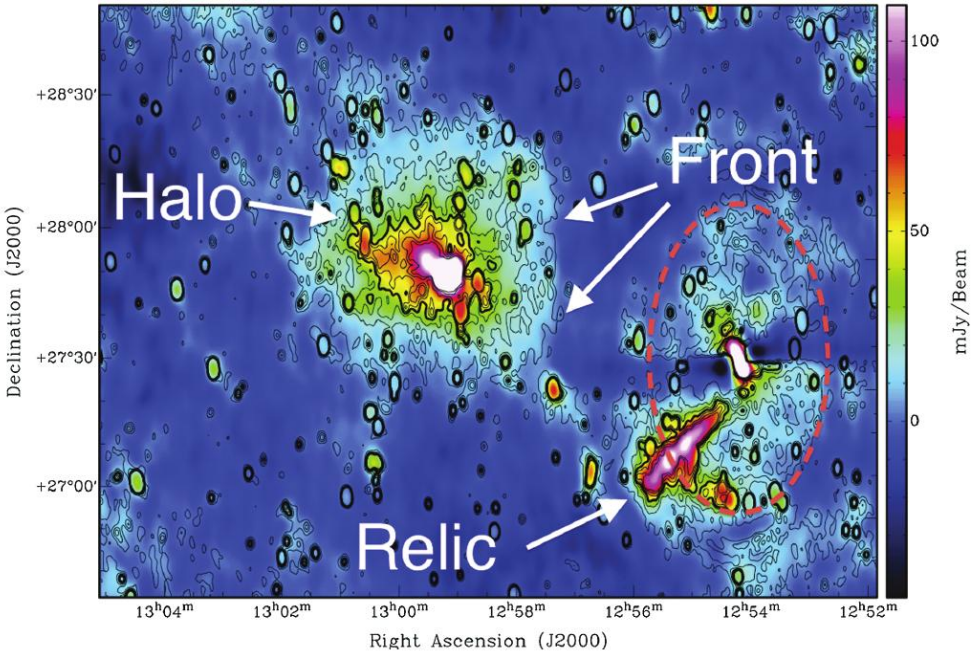

Figure 2.13: Radio surface brightness of the Coma cluster at 352 MHz. Adopted from Brown & Rudnick (2011).

(1997) show a surface brightness radial profile of the radio emission at 1.4 GHz, which we reproduce in figure 2.14. It is remarkably flat when compared to the usual density profile in clusters.

At a distance of a Mpc from the X-ray centre the cluster also features an extended relic of approximately 2 Mpc elongated size. The relic overlaps with the point source Coma A (3C 277.3), which renders data reduction especially tricky in this area.

The halo is highly unpolarised, while the relic shows a polarisation degree of 12-17 % at 1.41 Ghz (Brown & Rudnick, 2011).

Over the years the Coma halo has been observed at many frequencies in the radio band (see Thierbach et al., 2003). This allows to investigate the radio synchrotron spectrum of Coma, which is shown in figure 2.14. The spectrum follows a power-law with a spectral index of -1.35 up to its break at frequencies above 1.4 GHz.

Aside from the radio halo and relic, Kronberg et al. (2007) found large scale (4 Mpc) diffuse radio emission centred on the cluster, using combined data from Arecibo, the DRAO interferometer and the Effelsberg telescope. They attributed this to a combination of unknown foreground sources. This observation was later confirmed by Brown & Rudnick (2011) and its exact origin remains unclear.

Coma was also part of a detailed study to compare X-ray and radio morphology of a number of clusters and other statistical studies. We introduce these results in the next sections.

The cluster is an important test bed for the whole community and has so far not been

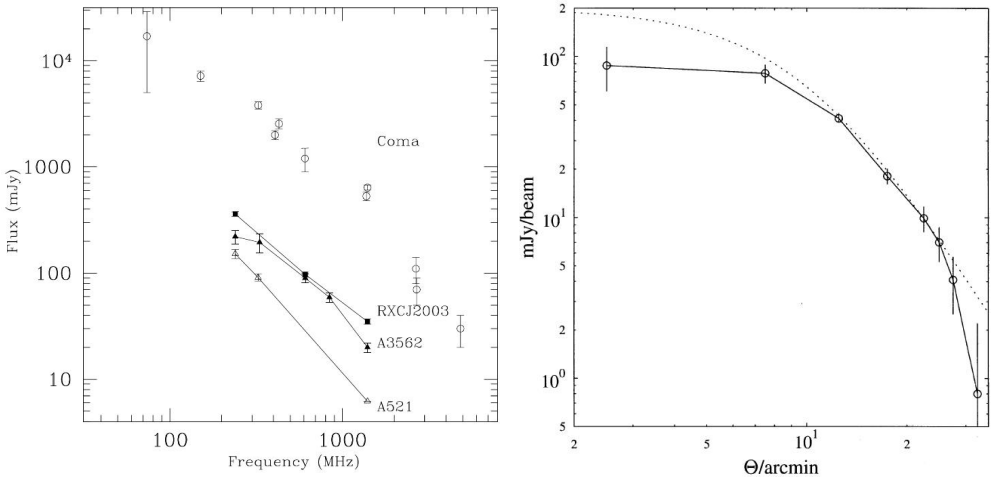

Figure 2.14: Left: Radio spectra of the clusters Coma, A521, A3562 and RXCJ2003. Adopted from Venturi et al. (2011), data from Thierbach et al. (2003); Dallacasa et al. (2009); Giacintucci et al. (2005, 2009). Right: Radial profile of the surface brightness of the halo at 1.4 GHz. Adopted from Deiss et al. (1997)

fully understood. However its radio halo and magnetic field distribution is most accurately known. We use the key observations from this cluster to test hadronic models in chapters 5 and 6

2.3.3 Morphology

A study of the morphological relation between X-ray and radio surface brightness in four clusters has been made by Govoni et al. (2001) and Feretti et al. (2001). They use data of the five clusters A2163, A1656 (Coma), A2255, A2319 and A2744 to investigate the relation in terms of patches and annuli around the clusters centre. This study is of special significance for hadronic models, where radio brightness intrinsically scales with cluster density squared and therefore X-ray brightness. See also our discussion in section 4.2.5.

In their study the authors tessellate radio and X-ray surface brightness maps with a grid of equally sized patches as shown for A2255 in figure 2.15, left panel. They then plot X-ray surface brightness F_{X} versus radio surface brightness F_{Radio} in the individual patches as shown in figure 2.15, right panel. They fit a power-law with normalisation a and spectral index b to the data:

$$\frac{F_{\mathrm{Radio}}}{\mathrm{mJy\,arcsec^{-2}}} = a \left(\frac{F_{\mathrm{X}}}{\mathrm{mCounts\,s^{-1}\,arcsec^{-2}}} \right)^{b} . \tag{2.3}$$

The best-fit parameters found for the five clusters are shown in table 2.4.

They find that three clusters show a strong sub-linear spectral index, implying that the *thermal scaling is broken*. For Coma this result has been confirmed by Brown & Rudnick (2011).

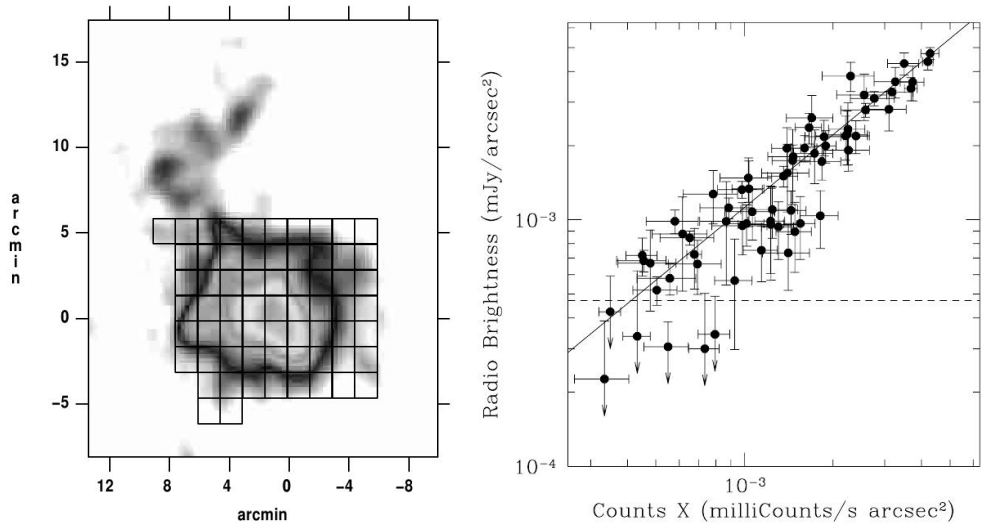

Figure 2.15: Left: Radio surface brightness of A2255 with grid overlayed. Right: F_{X} vers. F_{Radio} relation of A2255. Both adopted from Govoni et al. (2001).

Name	offset a	spectral index b
A2255	0.97 ± 0.25	0.98 ± 0.04
A2744	0.24 ± 0.07	0.99 ± 0.05
A2319	0.020 ± 0.004	0.82 ± 0.04
A1656	0.03 ± 0.01	0.64 ± 0.07
A2163	0.03 ± 0.01	0.64 ± 0.05

Table 2.4: Power-law fit parameters to X-ray versus radio brightness in five clusters, formula 2.3. Adopted from Feretti et al. (2001); Govoni et al. (2001).

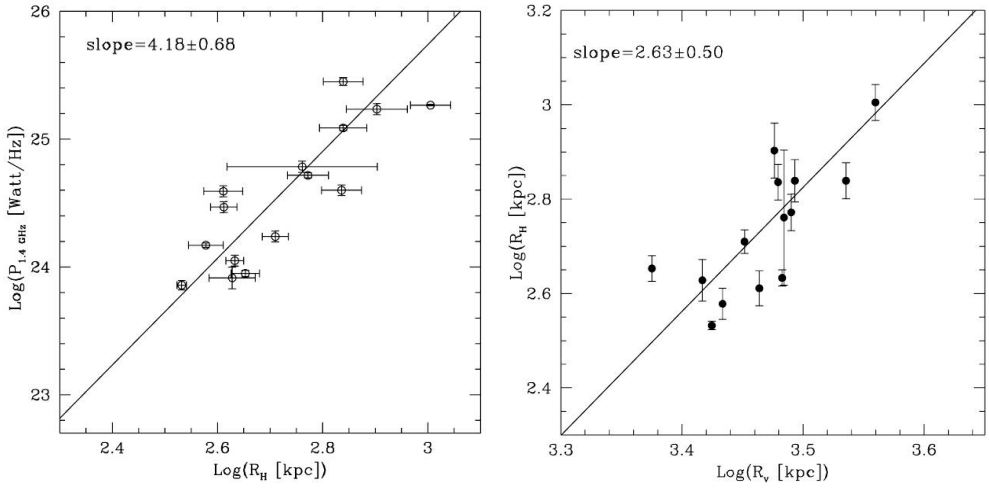

Figure 2.16: Non-thermal scaling relations for a sample of galaxy clusters with radio halos. Left: Total radio power at 1.4 GHz over radio halo radius. Right: R_{85} over cluster virial radius. Both adopted from Cassano et al. (2007).

As we show in section 4.2.5 this finding poses a strong challenge to many hadronic models.

2.3.4 Scaling Relations

Scaling relations are an important tool to infer dependencies of cluster variables and observables on one another. A number of thermal scaling relations of clusters lead to the self-similar model (see sections 2.1 and 3.7 for an overview).

A series of papers in the last decade (Kempner & Sarazin, 2001; Govoni et al., 2001; Ensslin & Röttgering, 2002; Feretti, 2003b; Cassano et al., 2006, 2007) systematically investigated scaling relations of non-thermal cluster parameters and their connection to thermal scalings.

In particular Cassano et al. (2007) investigated this connection in detail. We reproduce in figure 2.16 their scalings: radio power $P_{1.4}$ versus halo size and radio halo size[6] versus cluster size (virial radius). They estimate $R_{\rm H} \propto R_{\rm vir}^{2.63\pm0.5}$, which translates into (Kempner & Sarazin, 2001) $LLS \propto L_{\rm X}^{0.5}$.

For a thermal scaling one would expect a flatter relation $LLS \propto L_{\rm X}^{1/6}$ (Kempner & Sarazin, 2001), implying a *break in self-similarity* (compare chapter 6.4.4). That means as a cluster increases in size (and its mass, temperature, X-ray luminosity) the radio halo

[6]Because of the faint nature of the halo emission and the difficult treatment of noise in the data reduction, it is not straight forward to estimate the size of a radio halo from observations. To systematically treat this issue, Cassano et al. (2007) introduce R_{85} as a measure of the radio halo size. R_{85} is defined as the radius, where the integrated radial profile of the radio surface brightness reaches 85% of the total luminosity.

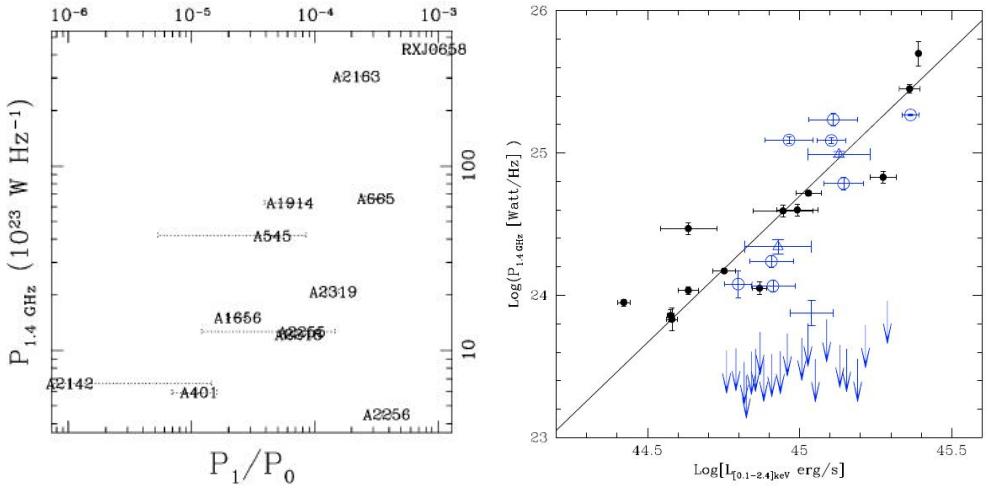

Figure 2.17: Left: Radio luminosity of cluster versus Dipole power ratio. Adopted from Buote (2001). Right: Radio power over X-ray luminosity. Blue circles mark clusters from a complete sample, arrows mark upper limits of non-detections. Adopted from Brunetti et al. (2009).

size and luminosity[7] increase over-proportionally. An intuitive way to understand this is to consider image 5.3, where a comparison of radial profiles of radio halos is done with respect to $r/r_{\rm vir}$. This is only possible because all cluster have comparable mass. Profiles of clusters with very different mass are *not* comparable if self-similarity is broken, i.e. the size cannot be scaled out anymore.

2.3.5 Power Ratio, $P_{14} - L_X$ Correlation and Bimodality

Radio halos have been linked to the disturbed dynamical state of their host cluster (Burns et al., 1995; Colless & Dunn, 1996). In a newer work the dynamical state of a galaxy cluster was estimated from X-ray observations by the so called dipole power ratio P_1/P_0 (Buote & Tsai, 1995, 1996). Here the surface brightness map is used to derive a projected gravitational potential, which is then analysed using a two-dimensional multi-pole expansion technique. P_i refers to the power in the i-th multi-pole. The dipole power ratio therefore measures the relative importance of the dipole to the monopole (spherically symmetric) moment. A disturbed cluster, out of hydrostatic equilibrium, is measured with a large power ratio.

Buote (2001) apply this technique to a sample of 15 clusters, observed with the ROSAT satellite. They find a rough correlation between dipole power ratio and radio luminosity of the clusters (figure 2.17).

A different approach was the first analysis of a complete X-ray selected sample of galaxy clusters regarding radio halos by Venturi et al. (2007, 2008). They confirmed the previous

[7] if it exists, see section 2.3.5 and 6.4.4

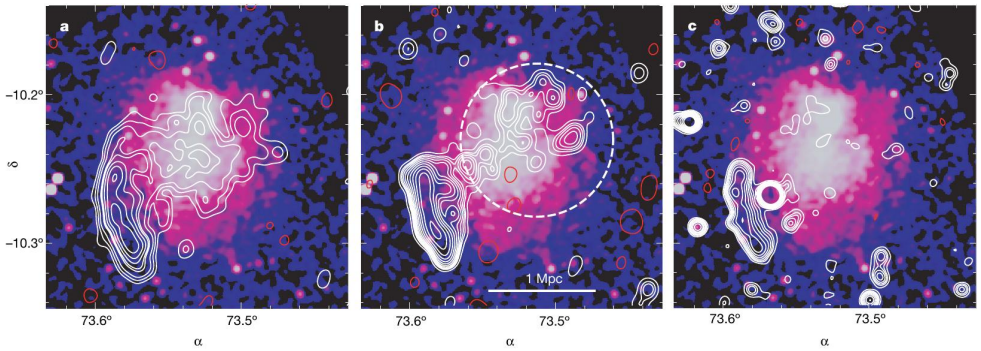

Figure 2.18: Surface brightness maps of X-ray (colour) and radio (contours) of A512 at 240 MHz, 610MHz and 1.4GHz as observed with GMRT. Adopted from Brunetti et al. (2008).

finding by Giovannini et al. (1999) that radio halos are more likely to occur in high mass - high temperature systems. But more importantly they found that only a fraction of all clusters in the complete sample host a radio halo ($\approx 38 \pm 13\%$). This is known as the *bimodality* in radio brightness (compare chapter 6.4.4). A plot of the bimodality is shown in figure 2.17, where we reproduce the $P_{1.4} - L_{\rm x}$ relation from Brunetti et al. (2009). Blue points and arrows mark detections/non-detections from the complete GMRT survey sample from Venturi et al. (2008). Black dots mark other clusters with halos. Using simple statistical arguments one can then show that the lifetime of radio halos on the correlation should roughly be $\approx 1.3\,$Gyr and the transition time $\approx 180\,$Myr (Brunetti et al., 2009). These are important constrains for reacceleration models.

Today it is well established that radio halos occur only in disturbed, merging systems and only in a fraction of all clusters. This has strong implications on models for these systems in a universe that is dominated by self-similar structures on the largest scales.

2.3.6 Ultra-Steep Sources

A sneak-peak into the future of low-frequency observations of radio halos was granted by observations of A512 by Brunetti et al. (2008) using the GMRT. We reproduce their observations in figure 2.18. They found for the first time a radio halo with a spectral index of $\alpha \approx 2.1$. Typically radio halos show $\alpha \approx 1.2$. These steep spectrum sources become detectable only with low-frequency instruments like LOFAR (Cassano et al., 2010) and present an important science goal and foreground source to these instruments.

Since then another steep spectrum halo has been found - A697 (Macario et al., 2010a).

Theoretical implications of these observations are very strong, as hadronic models run into problems with CR proton normalisation. The observed steep synchrotron spectrum implies even steeper CR electron and, in hadronic models, steep CR proton spectra. As steep spectrum halos have radii in the Mpc range at low frequencies this implies unphysical amounts of CR protons at the cluster outskirts. This class of "old" radio halos is expected to be ubiquitous at frequencies below 200 MHz.

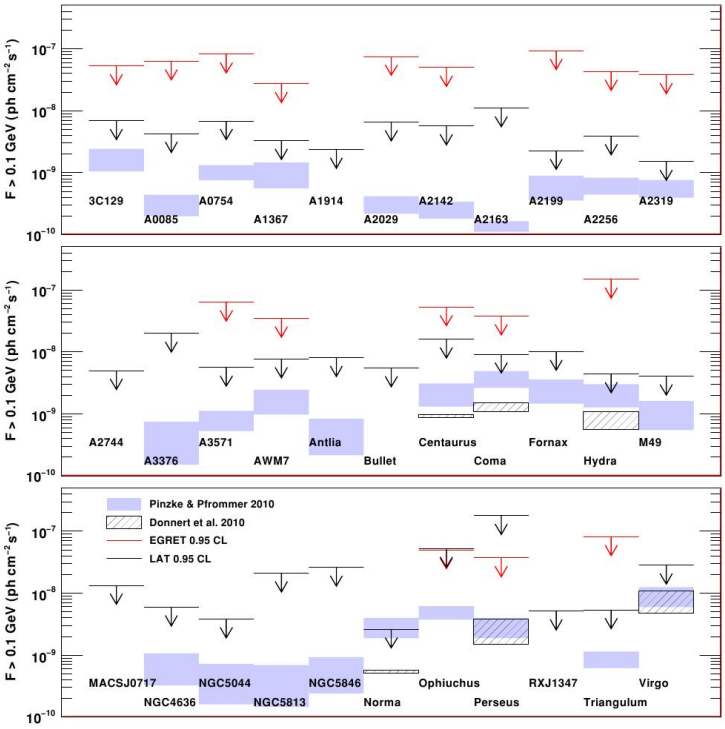

Figure 2.19: γ-ray upper limits for 33 galaxy clusters, as observed by the FERMI collaboration. Upper limits from simulations are included as well. Adopted from Ackermann (2010).

2.4 γ-ray Observations

Aside from observations in the radio regime, the brightness of clusters in γ-rays is of interest to this work as well. In secondary models the decay of neutral pions produced in CR proton-proton interactions is expected to produce γ-rays. Observations in this regime are therefore an independent measure of the CR proton content of clusters and are highly anticipated by the community.

There have been a number of attempts in the last years to detect clusters at energies $> 100\,\mathrm{MeV}$ with EGRET (Reimer et al., 2003), $> 100\,\mathrm{GeV}$ with VERITAS (Perkins, 2008). Recently the FERMI collaboration published new upper limits for a sample of 33 galaxy cluster, observed with the LAT instrument (Ackermann, 2010).

So far no galaxy cluster has been successfully detected in the γ-ray regime. In figure 2.19 we reproduce the newest results from the FERMI collaboration (Ackermann, 2010). In addition to the upper limits for the clusters they also show the upper limits obtained - from EGRET (Reimer et al., 2003) - from direct simulation of CR protons from a secondary model by (Pinzke & Pfrommer, 2010) and the results from chapter 6.

The authors selected the 33 most X-ray bright candidate clusters from the HIFLUCS flux-limited sample of the brightest X-ray clusters (Reiprich & Böhringer, 2002). They

added clusters with expected high CR proton populations, like the bullet cluster and MACSJ0717.5+3754. The observations then lead to constraints on the volume averaged ratio of CR-proton to thermal energy density of about $< 5 - 10\%$

No upper limit set by FERMI is below the predictions from simulations. For a few clusters like Coma, Hydra, Norma, and Virgo limits are within a factor of two to three and can be expected to be reached in the next years. It is remarkable to the observers that not even a faint detection using stacking methods has been reached with the LAT even for Norma and Hydra or the whole sample (Reimer priv. com.).

2.5 Other Non-Thermal Emission in Clusters

In this section we introduce two more classes of non-thermal sources in galaxy clusters. An informative review can be found in Ferrari et al. (2008). We begin with an introduction to radio relics showing exemplary the impressive relic CIZA J2242.8+5301. The second subsection comments on radio mini-halos.

2.5.1 Radio Relics

Another important class of objects, observed in the radio regime from clusters, are *radio relics*. Relics are Mpc-sized irregular shaped objects located in the cluster outskirts. Kempner et al. (2004) call them "radio gischt" to distinguish them from smaller objects ("radio phoenixes" and "AGN relics") related to radio galaxies.

Relics are partially polarised (usually 10-30%) and have been found to spatially coincide with large shocks (Kassim et al., 2001) in some cases. Commonly this class of objects is found in merging galaxy clusters. A wide variety in size, morphology and distance from the centre is observed.

In figure 2.20 we reproduce the recent observation of CIZA J2242.8+5301 by van Weeren et al. (2010). Here radio brightness at 1.4 GHz is shown in colours with X-ray emission in red contours. The dimension of the relic is 2 Mpc x 55 kpc (!) about 1.5 Mpc away from the cluster centre.

The formation mechanism of radio relics can be considered well understood: CR electrons and protons are injected at the shock front ahead of a large object falling into the cluster. The compression of the gas is expected to amplify and align the magnetic field in the shock front (sweep-up hypothesis). The resulting synchrotron radiation is then strongly polarised with a power-law spectral index. The electron population ages quickly behind the shock and the spectral index increases. Most models for well observed relics involve medium Mach numbers of $\lessapprox 3$, as found in e.g. A521 (Giacintucci et al., 2008), CIZA J2242.8+5301 (van Weeren et al., 2010) and A754 (Macario et al., 2011). Unfortunately only a few shocks have been clearly detected with present X-ray telescopes (Markevitch, 2010), however the connection is undisputed.

In the left panel of figure 2.21 we reproduce a zoom-in to the relic in CIZA J2242.8+5301 from van Weeren et al. (2010). Sub-panel A shows the spectral index distribution over the

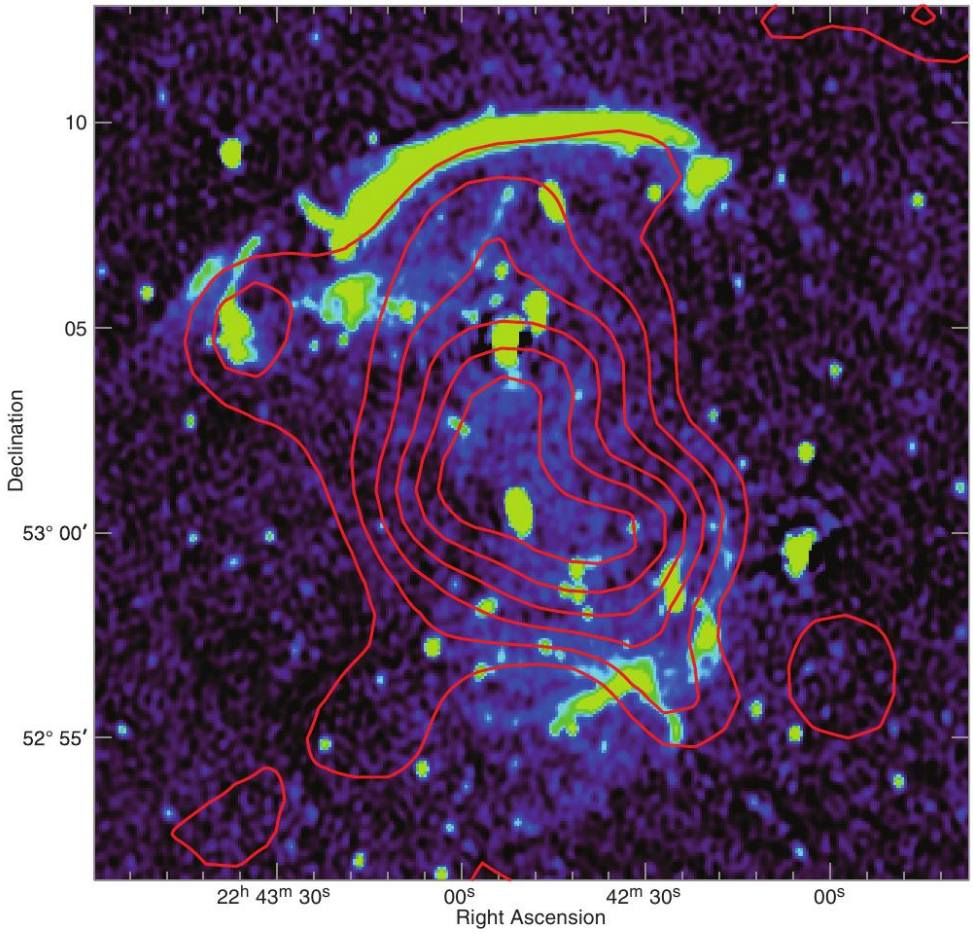

Figure 2.20: Radio relic in CIZA J2242.8+5301. Observation at 1.4 GHz in colours, X-ray surface brightness in red contours. The size of the image is about 4 x 4 Mpc. Adopted from van Weeren et al. (2010).

arc. It steepens from -0.75 at the front of the shock to nearly -2.0 in the post shock region. Sub-panel B shows the polarisation vectors of the radio emission. They are aligned perpendicular to the shock front. This indicates a magnetic field with a strong large scale component parallel to the shock front. The right panel of figure 2.21 shows an older simulation of a radio relic by Roettiger et al. (1999). The synthetic X-ray emission is displayed in contours and in gray the radio emission expected from injection of CRs at the shock front.

The injection of CR protons and electrons at the shock front is understood in terms of "Diffusive Shock Acceleration" (e.g. Krymskii, 1977; Malkov & O'C Drury, 2001; Blasi, 2010). In this theory particles from the supra-thermal tail of the distribution function are accelerated by bouncing back and forth through the shock, systematically gaining energy. The idea of this process dates back to Fermi (1949). Because the acceleration goes linear in the scatterers velocity (Eilek & Hughes, 1991), it is also called Fermi I acceleration.

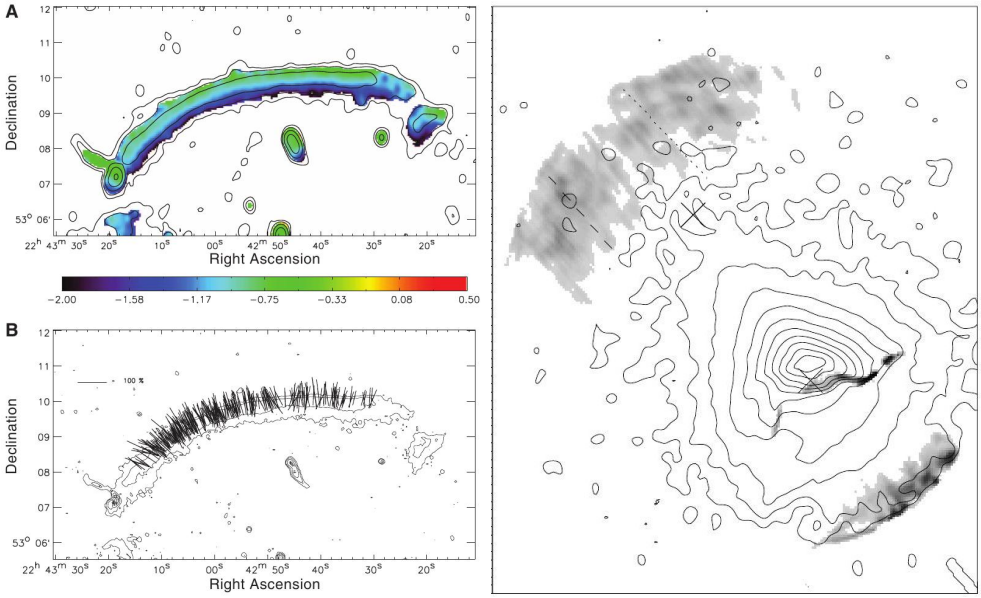

Figure 2.21: Left Panels: Observation of the relic in CIZA J2242.8+5301. Panel A shows the spatial distribution of spectral index of the radio emission and panel B - the direction of the polarised intensity, adopted from van Weeren et al. (2010). Right panel: Simulation of a radio relic in an idealised merger of two galaxy clusters. Synthetic X-ray emission in contours, radio emission in gray. Modified from Roettiger et al. (1999).

Recently particle-in-cell simulation are able to simulate this process, providing important parameters to the models (Spitkovsky, 2008).

Our work will not focus on this class of objects because they are comparatively well understood. However, the micro-physics, especially the injection efficiency of CR electrons and protons per Mach number, is an important parameter also in the context of our work (see Pfrommer et al., 2007).

2.5.2 Radio Mini Halos

As their name suggests, radio mini halos are diffuse radio sources in the centres of galaxy clusters of a few 100 kpc size. They are found around radio-loud brightest-cluster-galaxies (BCG) inside cooling core clusters. They are usually associated with that region and can, unlike their large counterpart, not be associated with major cluster mergers. These events would disrupt the core and stop the cooling of the cluster (Buote & Tsai, 1996).

Because of their size, faint nature and the association with a radio bright galaxy, radio mini halos are hard to detect. To date there are some five mini-halos known. Similar to giant radio halos, hadronic (Pfrommer & Ensslin, 2004) and reacceleration models (Gitti et al., 2002) have been proposed to model these sources. In the last years a connection to minor mergers in the presence of a cooling flow in clusters has been suggested (Gitti et al., 2007). In figure 2.22 we reproduce the observations of RX J1347.5-1145 at 1.4 GHz by Gitti

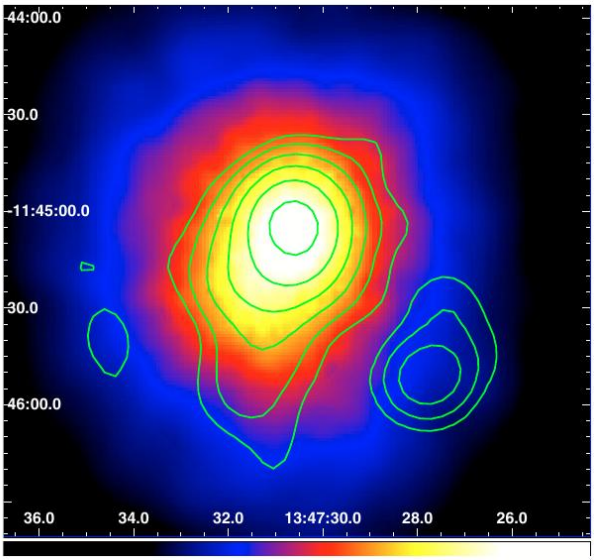

Figure 2.22: Radio mini halo in RX J1347.5-1145 at 1.4 GHz. The size of the image is 435 x 600 kpc at the clusters redshift and the total luminosity is 25.2 ± 0.3 mJy. Adopted from Gitti et al. (2007).

et al. (2007): in colours - the radio emission, in contours - the X-ray surface brightness. Two sub-clumps are visible in the X-ray regime. Furthermore they report that the cluster hosts two BCGs. This is another indication for a recent submerger event.

Mini halos are an interesting special case of non-thermal emission from galaxy clusters. At the moment it is unfortunately not feasible to attempt to investigate these rare objects numerically, as it is not clear how to simulate a cooling flow cluster with a BCG. They are therefore only of peripheral interest for our work.

Chapter 3

Theoretical Considerations

In this chapter we want to provide a motivation of the most important physical principles used later in this work. We start with the relevant emission processes for cosmic-rays in the ICM. The next section then provides a formulation of the actual problem of CR electron cooling in galaxy clusters and the formation of giant radio halos. Then we introduce the original and modern idea of CR transport in a cluster, followed by a derivation of a reacceleration coefficient. Section 3.6 gives an overview of the theory of secondary models and our derivation of the steady-state spectrum from the high energy approach used in Chapter 6. We finish this chapter with some thoughts on the physics of the ICM used in analytical and numerical approaches to the problem of cluster formation.

Most of this chapter is a collection of facts from textbooks, which are marked clearly as the source of the derivation. Exceptions to this are: Section 3.1.2 where we discuss the implications of low energy cut-off to the analytical synchrotron brightness formula; Section 3.6.3, the derivation of the steady-state electron distribution for secondaries in the high energy approximation; Parts of section 3.7.1, where we critically analyse parts of the assumptions that go into our numerical work on the ICM.

We do not further comment on primary models for radio halos (proposed in the early days) because they are essentially ruled out by estimates on the diffusion lengths and simulations of shocks in clusters and are not considered in the community anymore.

3.1 Emission and Loss Processes

Here we introduce the emission and energy loss processes of charged particles relevant for this work. We start with motivating the important energy loss terms for the Fokker-Planck equation which governs the CR dynamics. These are Coulomb, synchrotron and inverse Compton losses (Sarazin, 1999a). We neglect Bremsstrahlung losses here and in our calculations, because they are much less important at low energies (see 3.8 and Petrosian (2001)). Instead there is a strong focus on synchrotron radiation because it is of foremost importance. The last section is a short overview of the γ-ray emission from hadronic interactions of cosmic-ray protons in clusters.

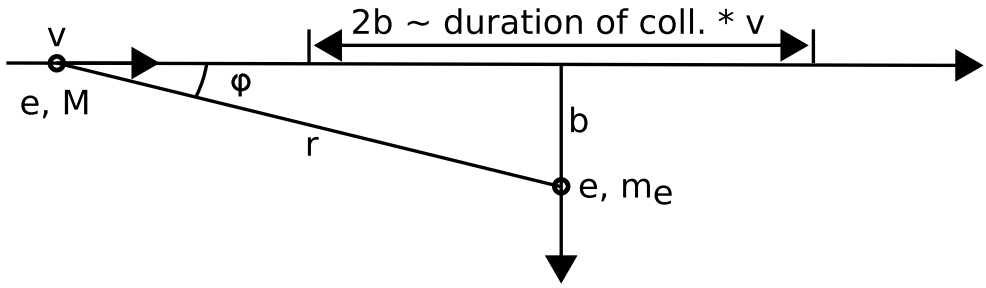

Figure 3.1: Schematic of the Coulomb collision of two electrons with mass M and m_e. From geometry : $\tan(\varphi) = b/x$ and $r = b/\sin(\varphi)$. After Longair (2010).

3.1.1 Coulomb losses

Charged particles (electrons) travelling at relativistic speed through an ionised plasma lose energy due to the Coulomb (electrostatic) interaction with the charge of the plasma particles. We motivate here the energy loss to the relativistic electrons due to this interaction. A more complete picture can be acquired from the standard literature on this topic, e.g. Gould (1972); Sarazin (1999a); Longair (2010). We follow the latter reference in our derivation of the classical loss rate for two particles carrying elemental charge (electrons).

The scattering of two charged electrons due to their Lorentz force is schematically drawn in figure 3.1: An electron with charge e and mass M moves with velocity $v \approx c$ from left to right. It encounters another electron with mass m_e at an impact parameter b. Furthermore at time t the incoming electron is at distance r at an angle of φ to the stationary one. We assume that this electrons stays at rest.

The force exerted on the incoming electron is perpendicular to its direction of movement as the parallel components cancel out over the time of the encounter,

$$F_\perp = \frac{e^2}{r^2}\sin(\varphi) \tag{3.1}$$

The total momentum loss is then given by the time integral over the force.

$$\Delta p = \int_\infty^\infty F_\perp \,\mathrm{d}t = \int_\infty^\infty F_\perp \,\frac{\mathrm{d}x}{v}, \tag{3.2}$$

where we neglect the change in velocity v.

This can be written as an integral over φ. Figure 3.1 suggests: $\tan(\varphi) = b/x$ and $r = b/\sin(\varphi)$. This leads to:

$$\mathrm{d}x = \frac{-b^2}{\sin^2(\varphi)}\,\mathrm{d}\varphi \tag{3.3}$$

$$\int_\infty^\infty F_\perp \,\frac{\mathrm{d}x}{v} = -\frac{2e^2}{bv}\int_0^\pi \sin(\varphi)\,\mathrm{d}\varphi \tag{3.4}$$

The total energy loss by the CR electron is then :

$$\frac{\Delta p^2}{2m_\mathrm{e}} = \frac{2e^4}{b^2 v^2 m_\mathrm{e}} \tag{3.5}$$

On *average* high energy electrons are going to encounter plasma electrons at all impact parameters. We therefore integrate equation 3.5 in cylindrical coordinates over all impact parameters:

$$-\frac{\mathrm{d}E}{\mathrm{d}x} = \frac{4\pi N_\mathrm{e} e^4}{v^2 m_\mathrm{e}} \int_{b_\mathrm{min}}^{b_\mathrm{max}} \frac{1}{b}\,\mathrm{d}b \tag{3.6}$$

$$\Rightarrow -\frac{\mathrm{d}E}{\mathrm{d}t} = \frac{4\pi N_\mathrm{e} c e^4}{\beta m_\mathrm{e}} \ln\left(\frac{b_\mathrm{max}}{b_\mathrm{min}}\right). \tag{3.7}$$

Here b_min and b_max are the maximum impact parameters encountered in the medium. $\ln\left(\frac{b_\mathrm{max}}{b_\mathrm{min}}\right) = \ln\Lambda = B$ is often called Coulomb logarithm or stopping number in literature.

A lot of physics can be done to estimate this parameter, a detailed discussion is beyond the scope of this work.

For the ICM the situation is complicated: The medium is fully ionised and the CR electrons have very high energies. From ionisation follows that for the maximum impact parameter the simple argument in Longair (2010) to compare the encounter time to the classical electron orbit frequency in an atom is not applicable. The latter statement suggests that we should have done a quantum mechanical calculation here[1], which we have not.

Gould (1972) found the correct expression for electrons[2]:

$$\begin{aligned} B_\mathrm{rel}(e^-) = \ln\left(\frac{\sqrt{\gamma-1}\beta m c^2\sqrt{2\delta}}{\hbar\omega_\mathrm{p}}\right) + \frac{1}{2}\left(1+\frac{2\gamma-1}{\gamma^2}\right) \\ \times \ln(1-\delta) + \frac{\frac{1}{2}\delta}{1-\delta} + \frac{1}{4}\left(\frac{\gamma-1}{\gamma}\right)^2 \delta^2 \end{aligned} \tag{3.8}$$

with the energy loss to maximum fractional energy loss ratio $\delta = (\Delta E_\mathrm{lab}/(p^2/2m)$, $\omega_\mathrm{p} = 4\pi n_\mathrm{e} e^2/m_\mathrm{e}$.

Petrosian (2001) sets the Coulomb logarithm to be 40 for the ICM. For our work we follow the ultra-relativistic approach of (Rephaeli, 1979; Sarazin, 1999a; Cassano & Brunetti, 2005) and approximate 3.8 for electrons and positrons, so the Coulomb loss term becomes:

$$\left(\frac{\mathrm{d}E}{\mathrm{d}t}\right)_\mathrm{coul} = -9.8\times10^{-19} n_\mathrm{e}\left[1+\frac{\ln(\gamma/n_\mathrm{e})}{75}\right] \tag{3.9}$$

[1] because of the very high energies involved

[2] he found it for positrons too, its just even more complicated

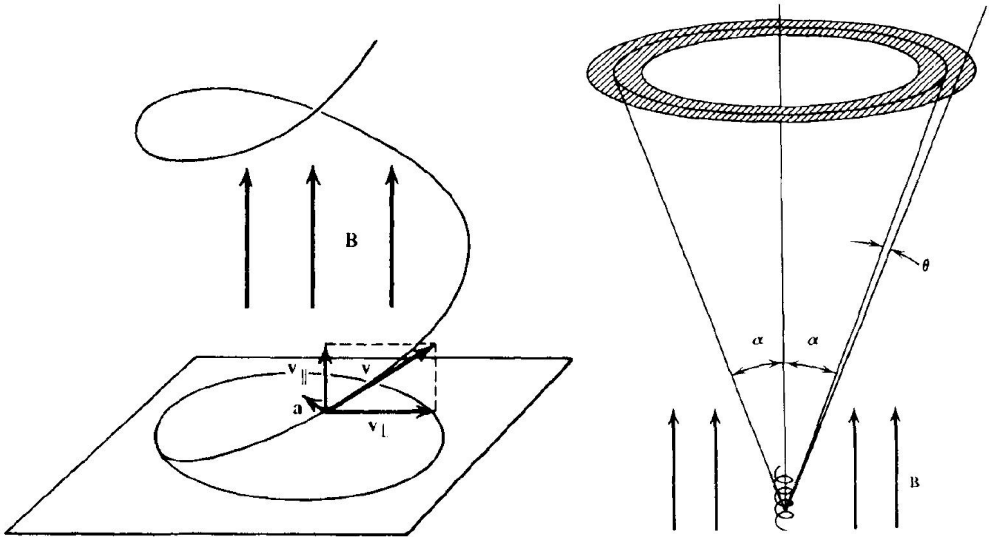

Figure 3.2: Left: Helical motion of a charged particle in an homogeneous magnetic field. Right: Synchrotron emission from a particle at pitch angle α confined to the gray region. Both adopted from Rybicki & Lightman (1986).

3.1.2 Synchrotron Radiation

Understanding the nature of relativistic magnetobremsstrahlung, or synchrotron emission, is key to understanding radio halos. We introduce here two important results, the emissivity from a population of electrons with a given spectrum and the subsequent energy loss rate. The former is needed later to build synchrotron maps or synthetic radio observations from our simulation. The latter makes the important cooling coefficient in the Fokker-Planck equation governing the dynamics of the spectrum in momentum space (see section 3.3). We will refrain from a detailed derivation of every formula, which exceeds the scope of this work and can be found in textbooks. The standard literature on this topic is Ginzburg & Syrovatskii (1965); Rybicki & Lightman (1986); Longair (2010), ordered historically and by inverse readability. We will start this section with a motivation of the Fokker-Planck coefficient for synchrotron losses, followed by a short paragraph about synchrotron emission from a single particle. Then we explain how the emission from a ensemble of electrons can be calculated. There are specific formulas for the emission from electrons governing a power-law spectrum. Here we point out a problem with these formulas, which we found undocumented in the literature. We will conclude with a note on our numerical implementation of a synchrotron solver.

Energy loss rate The emission mechanism of synchrotron emission is based on the helical motion of a charged particle in a magnetic field (figure 3.2). This is an accelerated movement (circular trajectory in the xy-plane) and therefore the electron emits radiation. The velocities involved do not have to be relativistic for this to work (cyclotron radiation).

With the Lorentz force the equation of motion is:

$$\gamma m_{\mathrm{e}} \frac{d\mathbf{v}}{dt} = \frac{e}{c}\mathbf{v} \times \mathbf{B} \tag{3.10}$$

from which follows the helical motion with the relativistic gyrofrequency:

$$\nu_{\mathrm{rel,g}} = \frac{eB}{\gamma m_{\mathrm{e}} c}. \tag{3.11}$$

The loss rate of an accelerated charged particle in a magnetic field can be obtained via the Liénard-Weichart potentials[3]:

$$\left(\frac{\mathrm{d}E}{\mathrm{d}t}\right)_{loss} = \frac{2e^2\gamma^4}{3c^3}\dot{v}^2 \tag{3.12}$$

and this can be combined with 3.10 to yield:

$$\left(\frac{\mathrm{d}E}{\mathrm{d}t}\right)_{loss} = \frac{2e^4B^2}{3c^3m_{\mathrm{e}}^2}\frac{v^2}{c^2}\gamma^2\sin^2(\alpha). \tag{3.13}$$

In the ultra-relativistic limit ($v/c \to 1$) and with integration over pitch angle α this yields (Dolag & Ensslin, 2000):

$$\left(\frac{\mathrm{d}E}{\mathrm{d}t}\right)_{\mathrm{synchro}} = \frac{4\sigma_{\mathrm{T}}}{3m_{\mathrm{e}}^2 c}\frac{B^2}{8\pi}\gamma^2, \tag{3.14}$$

with σ_{T} the Thomson cross-section (see section 3.1.3). This is the Fokker-Planck coefficient for synchrotron losses.

Synchrotron radiation from monoenergetic electrons One can use equation 3.10 and again the Liénard-Weichart potentials to calculate the total emitted power per solid angle from an arbitrarily moving relativistic electron. Choosing coordinates as shown in figure 3.2, "one can then battle away all the algebra to obtain the spectral distribution of the field components." Longair (2010, page 239). We will just quote the results here.

The radiation is found to be emitted in a narrow cone forward of the movement of the particle (figure 3.2). This effect is called relativistic beaming.

The total radiated power per frequency is given by the sum of the power radiated parallel and perpendicular to the magnetic field:

$$P_{\perp}(\nu) = \frac{\sqrt{3}e^3B\sin(\alpha)}{2m_{\mathrm{e}}c}\left(F(x) + G(x)\right) \tag{3.15}$$

$$P_{\parallel}(\nu) = \frac{\sqrt{3}e^3B\sin(\alpha)}{2m_{\mathrm{e}}c}\left(F(x) - G(x)\right), \tag{3.16}$$

[3]And this is where we would like to refer the reader to standard textbooks

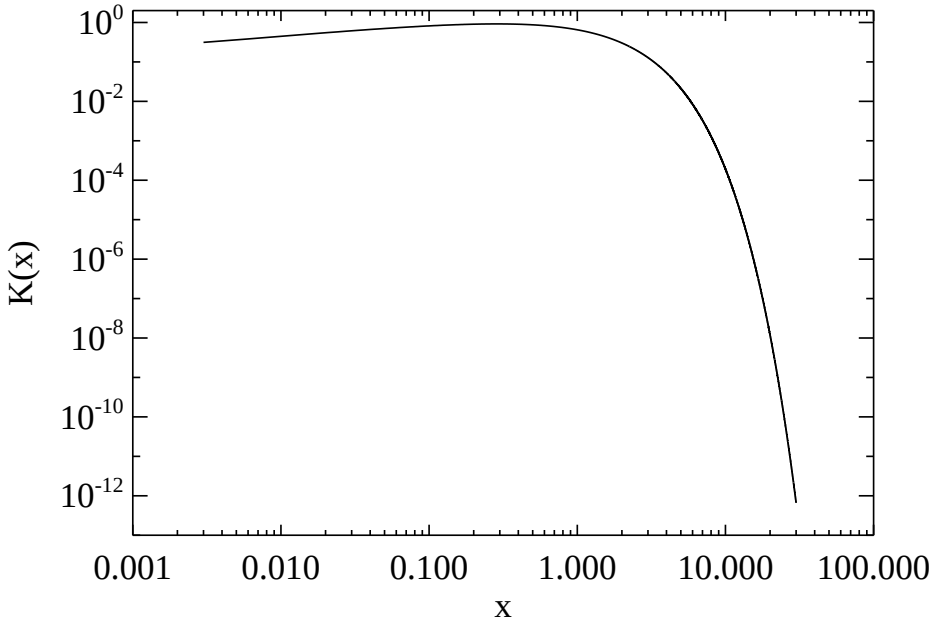

Figure 3.3: Synchrotron kernel F(x) as a function of $x = \nu/\nu_c$.

where α is the pitch angle between the magnetic field and the particle motion, $x = \nu/\nu_c$ the ratio between the frequency ν and the critical frequency ν_c:

$$\nu_c = \frac{3}{2}\gamma^3 \nu_{rel,g} \sin(\alpha), \tag{3.17}$$

and $F(x)$ and $G(x)$ the so called synchrotron kernels:

$$F(x) = x \int_x^\infty K_{\frac{5}{3}}(z)dz \tag{3.18}$$

$$G(x) = xK_{\frac{2}{3}}(x), \tag{3.19}$$

where $K_i(x)$ is the modified Bessel function of order i. The kernel function $F(x)$ is not an analytical function, even though a number of approximations exist (Schlickeiser et al., 1987). Thankfully a recent implementation in the GNU Scientific Library (Galassi, 2011) makes computation trivial and efficient these days. A plot of the kernel function $F(x)$ can be found in figure 3.3.

Synchrotron radiation from arbitrary electron distributions Having the radiated power of monoenergetic electrons, one can immediately obtain the emissivity of an ensemble of electrons as the integral over the spectrum $N(E)dE$ times the total radiated power per

particle (see chapter 6, equation 6.10):

$$j_\nu = \frac{\sqrt{3}\sin(\theta)e^3 B}{m_\mathrm{e}c^2} \int_{E_\mathrm{min}}^{E_\mathrm{max}} \mathrm{d}E_\mathrm{e}\, F\left(\frac{\nu}{\nu_c}\right) N_\mathrm{e}(E_\mathrm{e}) \tag{3.20}$$

$$j_\nu = \frac{\sqrt{3}e^3 B}{m_\mathrm{e}c^2} \int_{E_\mathrm{min}}^{E_\mathrm{max}} \int_0^{\frac{\pi}{2}} \mathrm{d}E_\mathrm{e}\mathrm{d}\theta\, \sin^2(\theta) F\left(\frac{\nu}{\nu_c}\right) N_\mathrm{e}(E_\mathrm{e}), \tag{3.21}$$

where equation 3.20 is the expression for a homogeneous magnetic field. Equation 3.21 includes pitch angle integration to give the emissivity for an isotropically tangled magnetic field.

The polarisation degree is defined as:

$$\Pi(\nu) = \frac{P_\perp(\nu) - P_\parallel(\nu)}{P_\perp(\nu) + P_\parallel(\nu)} = \frac{G(x)}{F(x)} \tag{3.22}$$

In the first case the radiation is strongly linearly polarised (73%). For a perfectly tangled magnetic field (second case) the linear polarisation is zero by definition, because $P_\perp(\nu) = P_\parallel(\nu)$. In reality a mixture of both cases is going to occur.

This explains immediately why the high polarisation degree in radio relics is an indication of a regular magnetic field pattern, which supports the sweep-up and shock hypothesis (see section 2.5.1). It is also clear that the absence of any significant polarisation in radio halos is an indication for irregular magnetic field patterns on scales below the beamsize[4].

The strong peak of the kernel function at $\nu \approx \nu_\mathrm{c}$ is often used to approximate the synchrotron spectrum of an electron to be monoenergetic at this frequency. Turning this argument around one can find the energy at which an electron distribution is going to be synchrotron bright:

$$\gamma = \sqrt{\frac{\nu m_\mathrm{e} c}{eB}}. \tag{3.23}$$

This gives for the "standard" frequency of radio halos 1.4 GHz the handy formula:

$$\begin{aligned}\gamma_{1.4\mathrm{GHz}} &\approx \frac{22}{\sqrt{B}} \\ &\approx 2.2 \times 10^4 \left(\frac{B}{1\,\mu\mathrm{G}}\right)^{-0.5}.\end{aligned}$$

This is the basis for the lifetime estimate in section 3.2.

[4]Here beam depolarisation makes it impossible to detect any polarisation on scales much below the beamsize.

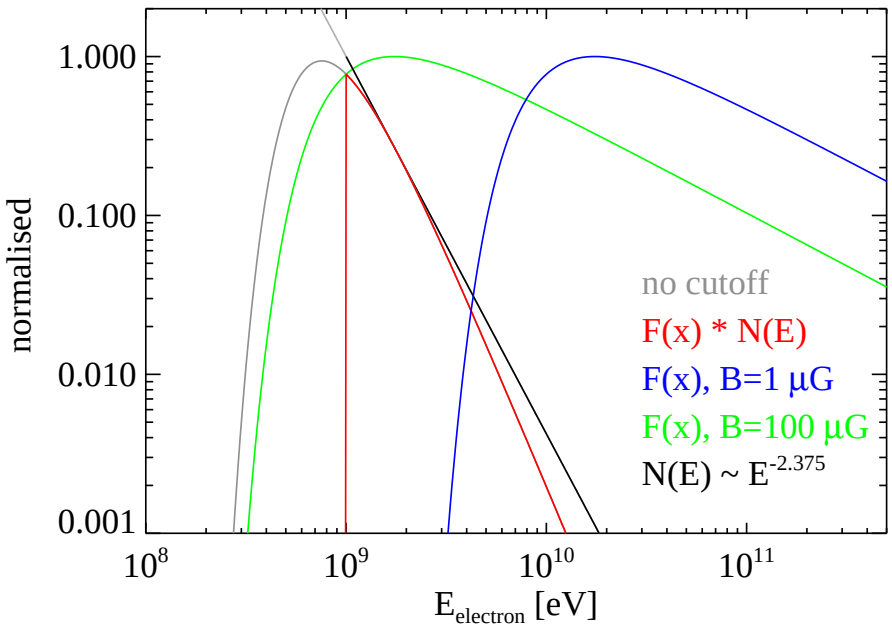

Figure 3.4: Synchrotron kernel in green (blue) at 1.4 GHz and 100 μG (1 μG). Power-law CR electron spectrum with cut-off at 1GeV in black. All were normalised for readability. The area under the red curve is proportional to the true synchrotron emissivity for 100 μG. However the analytical expression does not honour the cut-off and integrates the gray power-law spectrum. This gives a higher emissivity - the area under the gray curve.

Solution for power-law spectra One major complication in modelling radio halos is that no analytical expression exists for the synchrotron emissivity of an arbitrary electron spectrum. The only known solutions to equations 3.20 and 3.21 are for power-law electron distributions. This is a reason why secondary models, which predict power-laws can be handled well analytically.

The exact solutions for power-law spectra are derived elegantly in Longair (2010, page 251), which we do not reproduce here for brevity. More importantly assuming a power-law with spectral index s the emissivity scales as:

$$J(\nu) \propto N_0 B^{(s+1)/2} \nu^{-(s-2)/2}, \tag{3.24}$$

where the spectrum is usually normalised at a cut-off energy $E_0 = 1\,\mathrm{GeV}$ as:

$$\epsilon_{\mathrm{CRe}} = \int_{E_0}^{\infty} N_0 E^{-s+1} \mathrm{d}E, \tag{3.25}$$

where ϵ_{CRe} is the energy density in relativistic electrons. The choice of this cut-off at 1GeV is motivated from the injection of CR electrons in shocks, but still somewhat arbitrary.

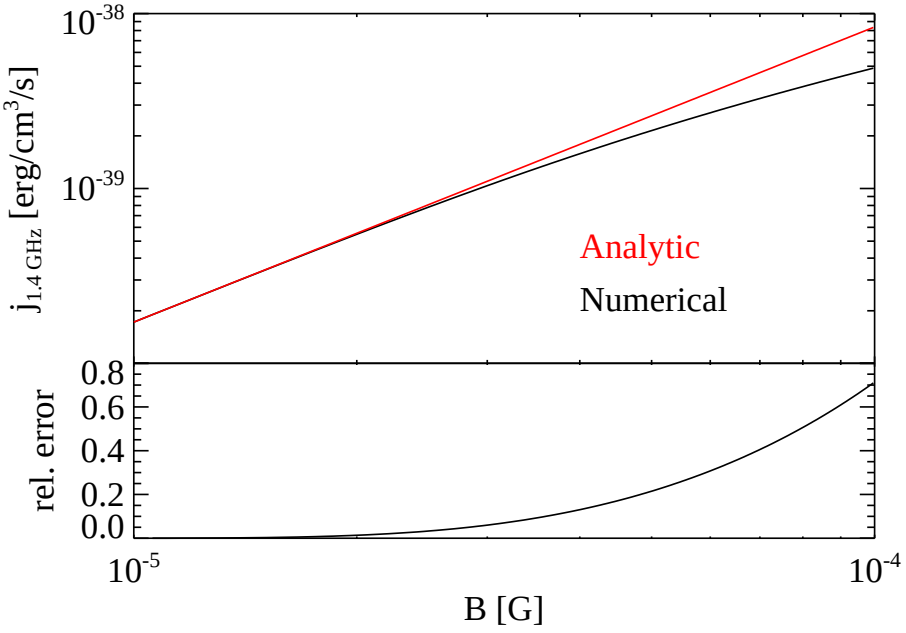

Figure 3.5: Synchrotron emissivity at 1.4 GHz from a power-law distribution of relativistic electrons over magnetic field strength. The analytical (wrong) solution is plotted in red, the numerical solution - in black. The relative error is given in the lower panel.

However one has to be careful when applying this formalism to distributions in regions with high magnetic fields or at low frequencies.

The solutions are based on the analytical integration of the integral 3.20 and 3.21, assuming the spectrum in equation 3.25. However this integration uses formula 11.4.22 from Abramowitz & Stegun (1972), (see also Rybicki & Lightman (1986)), which has the lower limit 0, not E_0. Therefore the analytical formula "does not know" about the cut-off assumed in equation 3.25 and will give wrong results if this region of the spectrum is probed by the synchrotron kernel.
We plot the situation in figure 3.4, where total emission is proportional to the product of the kernel and the spectrum. There we plot a power-law electron spectrum in black and two synchrotron kernels in green and blue. The two kernels correspond to 1.4 GHz and a magnetic field of $100\,\mu$G and $1\,\mu$G, respectively. One can see that in the $1\,\mu$G (blue) case no problem exists, at the spectral cut-off the kernel is basically zero. For the $100\,\mu$G however the kernel probes the cut-off of the spectrum and the true emission (area under the red curve) is overestimated by the analytical expression, which does not honour the cut-off (area under the gray curve). We show the dependency of the error with magnetic field at 1.4 GHz in figure 3.5, where we compare the emissivity from a numerical and the analytical solution of equation 3.20 in the upper panel. The relative error is shown in the lower panel and becomes significant for field strengths $B \geq 30\,\mu$G.

This effect is not mentioned in textbooks and can therefore be easily overlooked. It does not play a role for galaxy clusters, but might become important in galaxies and AGN, that reach the high field strengths required. This problem becomes even more severe at low frequencies (LOFAR), because of the frequency dependence of the brightest momentum (equation 3.23).

A numerical synchrotron solver For this work we need to extract synchrotron brightness maps from our simulation to compare with observations. On the other hand reacceleration models are expected to give significant deviations from the power-law behaviour found in secondary models. Therefore the analytical solution to eqn. 3.20 does not apply to our case and we have to solve the integral numerically.

We implemented analytical synchrotron formulae as well as a numerical synchrotron solver in our new projection program P-SMAC2. We use a trapezoidal algorithm to perform the numerical integration of equation 3.20 and 3.21. The integration is centred in energy on the brightest momentum from equation 3.23 with limits of one decade less and five decades more with 200 steps in energy and pitch angle. For a power-law distribution this gives an accuracy of a few percent. We directly use the kernel function provided by the GSL library which proofs to be fast enough for our purposes. This solver is used for all our synchrotron maps in this work.

3.1.3 Inverse Compton Scattering

Inverse Compton scattering (IC) is the up-scattering of low-energy photons by relativistic electrons. In this process the electrons *lose* energy, while the photons *gain* energy. In galaxy clusters this is expected to act on photons of the cosmic microwave background (CMB). The resulting up-scattered photons are expected in the hard X-ray regime. There is a debate in the community for years now, if this effect is detected in the COMA cluster or not (chapter 2.3.2, Fusco-Femiano et al. (2004)).

We will derive here the energy loss rate of relativistic electrons due to IC scattering with CMB photons. Standard literature on this subject include Blumenthal & Gould (1970); Rybicki & Lightman (1986); Longair (2010), in our derivation we follow the last of the three.

The energy of the incoming photon is much smaller than the energy of the relativistic electrons for CMB photons with wavelengths in the sub-centimetre regime, so Thomson scattering theory can be applied. The energy loss rate in the primed frame of the electron is then:

$$-\left(\frac{\mathrm{d}E}{\mathrm{d}t}\right)'_{\mathrm{IC}} = \sigma_{\mathrm{T}} c u'_{\mathrm{rad}}, \tag{3.26}$$

with the energy density of incoming radiation in the particle frame u'_{rad} and the Thomson

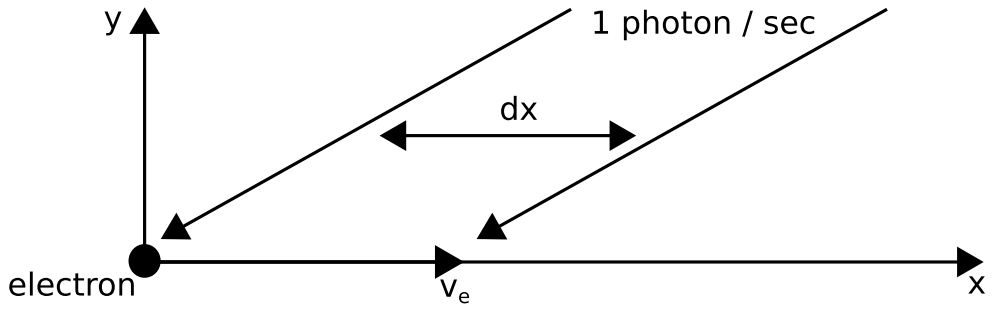

Figure 3.6: Illustration of the increase in the arrival rate of photons when transforming to a moving coordinate system. After Longair (2010).

cross-section:

$$\sigma_{\mathrm{T}} = \frac{8\pi}{3}\frac{e^4}{c^4 m_{\mathrm{e}^2}} \approx 6.6524 \times 10^{-25}\,\mathrm{cm}^2. \tag{3.27}$$

As the energy loss rate is independent of the frame of reference we have to estimate the energy density of radiation u'_{rad}. It is given by:

$$u'_{\mathrm{rad}} c = N\hbar\omega c, \tag{3.28}$$

where N is the number of incident photons.

We know from the relativistic Doppler formula (Einstein, 1905) how the energy transforms:

$$\hbar\omega' = \gamma\hbar\omega\left(1 + \beta\cos(\theta)\right), \tag{3.29}$$

where θ is the angle of the incoming photon.
One can show that the photon number N transforms the same way. This can be understood considering, that the arrival rate of photons on the trajectory of the particle is increased for two photons on parallel but separate trajectories. This is shown in figure 3.6: Considering 2 streams of photons along the diagonal arrows (a distance dx apart), that have an arrival rate of 1/sec and reach $y = 0$ with an delay of $\Delta t = dx/v_{\mathrm{e}}$. In the system of the moving electron the time difference between the arrival of both photons will be shortened, i.e. the arrival rate increased.

We can then combine this and integrate over solid angle $\mathrm{d}\Omega = 0.5\sin(\theta)\mathrm{d}\theta$ for the isotropic CMB photon field:

$$u'_{\mathrm{rad}} = u_{\mathrm{rad}} \int_0^{\pi} \gamma^2\left(1 + \beta\cos(\theta)\right)^2 \frac{1}{2}\sin(\theta)\mathrm{d}\theta \tag{3.30}$$

$$= \frac{4}{3}u_{\mathrm{rad}}\left(\gamma^2 - \frac{1}{4}\right). \tag{3.31}$$

Combining equations 3.26 and 3.30 we find the loss rate:

$$-\left(\frac{\mathrm{d}E}{\mathrm{d}t}\right)_{\mathrm{IC}} = \frac{4}{3}\sigma_{\mathrm{T}} c u_{\mathrm{rad}} \beta^2 \gamma^2. \tag{3.32}$$

This is remarkably similar to the loss rate due to synchrotron radiation, equation 3.14. Jackson (1998) argue that this can be understood by thinking of synchrotron radiation as IC scattering of the particle by virtual photons of the magnetic field.

It is common to express the energy density of the CMB as an magnetic field equivalent of $B_{\mathrm{CMB}} = 3.2\,\mu\mathrm{G} \times (1+z)^2$ and combine both formulas to (Dolag & Ensslin, 2000):

$$-\left(\frac{\mathrm{d}E}{\mathrm{d}t}\right)_{\mathrm{rad}} = \frac{4\sigma_{\mathrm{T}}}{3 m_{\mathrm{e}}^2 c}\left(\frac{B^2}{8\pi} + \frac{B_{\mathrm{CMB}}^2}{8\pi}\right)\gamma^2. \tag{3.33}$$

3.1.4 γ-ray Radiation from Hadronic CRp Interaction

Relativistic proton - thermal proton scattering in the ICM does not only produce charged pions[5] (see section 3.6), but neutral pions (π^0) as well. These decay via $\pi^0 \rightarrow 2\gamma$. The solid-angle integrated differential γ-ray source function $q_\gamma(E_\gamma)$ can then be found from the pion source function $q_{\pi^0}(E_{\pi^0})$ by (Mannheim & Schlickeiser, 1994):

$$q_\gamma(E_\gamma) = 2 \int\limits_{E_\gamma + [m_\pi^2 c^4/(4E_\gamma)]}^{\infty} \frac{q_{\pi^0}(E_{\pi^0})}{\sqrt{E_\pi^2 - m_\pi^2 c^4}}\,\mathrm{d}E_\pi \tag{3.34}$$

This leaves us with modelling the injection spectrum of neutral pions.

Here the original idea once again comes from Fermi (1950). In their "Fireball model" the relativistic protons interact with the thermal background protons to form a hot quark-gluon plasma, which eventually produces neutral (π^0) and charged ($\pi^\pm$) pions with multiplicities $\xi_{\pi^0} = \frac{1}{2}\xi_{\pi^\pm} = [E_{\mathrm{p}} - E_{\mathrm{th}}/\mathrm{GeV}]^{1/4}$, i.e. one out of five pions is a π^0. The threshold energy for pion production is $0.78\,\mathrm{GeV}/c$ (Mannheim & Schlickeiser, 1994) in this model.

Later Stecker (1970) extended this model to incorporate the production of $\Delta_{2/3}$ isobars[6], which carry parts of the energy and subsequently decay into pions (figure 3.7). Indeed at energies above 3 GeV ($\gamma > 3$ for CR protons) the authors argue this to be the dominant process. The mass distribution of the $\Delta_{2/3}$'s is taken to be a Breit-Wigner distribution, centered at the rest mass of the isobar with a width of 0.1 GeV. The normalised production spectrum of π^0 is found in Dermer (1986, eq. 7-10) and is not reproduced here for brevity.

For energies above 12 GeV Stephens & Badhwar (1981) proposed a model based on an empirical fit of the Lorentz invariant cross-section to accelerator data between 6 GeV and

[5] Pions are the lightest mesons, constituted from a quark-antiquark $(u, \bar{u}, d, \bar{d})$ pair. Having non-fractional spin they are Bosons.

[6] The $\Delta_{2/3}$ is a baryon made up of 3 quarks (u, d) and can be seen as an excited state of the proton. It has spin and isospin 2/3 and comes in 4 types $\Delta^{++}, \Delta^{+}, \Delta^{0}, \Delta^{-}$, all with a rest mass energy of $1.232\,\mathrm{MeV}/c^2$. In this channel only the Δ^+ is of interest for us.

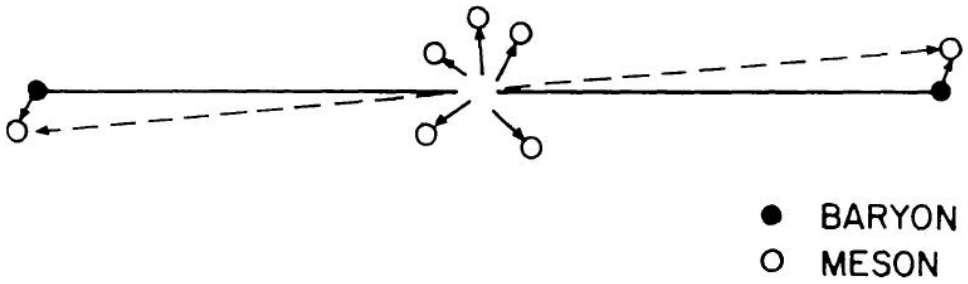

Figure 3.7: Centre of momentum distribution of secondary pions from proton-proton scattering according to Stecker's model. Adopted from Stecker (1970).

1.5 TeV (Badhwar et al., 1977). The authors then argue to scale the relativistic invariant cross-section to higher energies. Again the equations are found in Dermer (1986, eq. 11,12) and are not reproduced here.

A synthesis of both models was proposed by Dermer (1986). They compared the prediction from the two previous models to new (at that time) accelerator data and recalculate the γ-ray source functions for both models. Between the threshold energy and a few GeV (where most of the radiation is produced) Stecker's isobaric model was found to perform much better than the scaling approach. The authors therefore conclude, that at energies near the threshold the isobaric model should be used, while above 12.5 GeV the scaling model is applicable. At intermediate energies they propose a linear combination of both models.

For our work we follow the approach of Dermer (1986) and Pfrommer & Ensslin (2004). They introduce a shape parameter δ_γ to smoothly join isobaric and scaling model near the π^0 threshold. This yields:

$$q_\gamma(\mathbf{r}, E_\gamma)\,\mathrm{d}E_\gamma \mathrm{d}V \approx \sigma_{\mathrm{pp}} c n_{\mathrm{th}} \xi^{2-\alpha_\gamma} \frac{n_{\mathrm{CRp}}(\mathbf{r})}{\mathrm{GeV}} \times \frac{4}{3\alpha_\gamma} \left(\frac{m_{\pi^0}c^2}{\mathrm{GeV}}\right)^{-\alpha_\gamma} \left[\frac{2E_\gamma}{m_{\pi^0}c^2}^{+\delta_\gamma} + \frac{2E_\gamma}{m_{\pi^0}c^2}^{-\delta_\gamma}\right]^{-\alpha_\gamma/\delta_\gamma}, \tag{3.35}$$

where $\xi = 2$ is the pion multiplicity, n_{th} the thermal number density of proton, $n_{\mathrm{CRp}}(\mathbf{r})$ the number density of CR protons and

$$\alpha_\gamma = \frac{4}{3}\left(\alpha_{\mathrm{p}} - \frac{1}{2}\right) \tag{3.36}$$

$$\delta_\gamma = 0.14\alpha_\gamma^{-1.6} + 0.44 \tag{3.37}$$

$$\sigma_{\mathrm{pp}} = 32 \times (0.96 - \mathrm{e}^{4.4-2.4\alpha_\gamma}). \tag{3.38}$$

The authors note that both models have different energy dependence in the pion multiplicity and spectrum. The values for the shape parameter and the effective cross-section σ_{pp} were found using the COSMOCR code (Miniati, 2001) which follows an approach from Moskalenko & Strong (1998).

For a power-law distribution of CR protons this formalism yields the integrated γ-ray source density, equation 6.13.

3.2 The Cooling Problem

In this section we formulate the central theoretical problem inherent to the formation of giant radio halos.

Lifetime In the ICM cosmic-ray electrons are subject to the energy loss processes described in section 3.1. Given the energy loss rates derived for these processes (eqn. 3.33), one can then define an energy loss timescale (Jaffe, 1977; Petrosian, 2001):

$$\tau_{\rm loss} = -E/\dot{E}_{\rm loss}. \tag{3.39}$$

This timescale gives a rough estimation of the time needed for a CR electron to lose enough kinetic energy to be considered thermal. It is therefore a lifetime estimate of these electrons. Figure 3.8 shows the loss timescales for CR electrons in a cluster of 1 Mpc size over a wide range of energies. Synchrotron-, IC-, Bremsstrahlung- and Coulomb losses and combinations of those (see annotations) are considered. Hubble and escape time are marked as well and one can conclude that CR electrons at $\gamma \approx 200$ have a lifetime comparable to the age of the cluster.

Considering synchrotron radiation and a typical magnetic field strength of $1\,\mu$G it becomes clear (see 3.1.2), that electrons with $\gamma > 2 \times 10^3$ emit the synchrotron radiation in radio halos. Their lifetime is $\tau_{\rm loss} \approx 10^8\,$yr.

Injection On the other hand cosmic-rays are injected into the ICM through shocks and outflows. This may happen in large scale shocks observed as radio relics on the outskirts of many clusters (see section 2.5.1). Another possibility are shocks driven by AGN or super novas in galaxies on small scales and the subsequent diffusion into the ICM. This outflow mechanism is also believed to transport metals (Tornatore et al., 2004) and magnetic fields (Kronberg et al., 1999; Donnert et al., 2009) into the cluster atmosphere. In any case, the microphysics employed is diffusive shock acceleration (Fermi, 1949; Blasi, 2010) and the injection is *localised* to a few kpc.

Diffusion Speed The diffusion of cosmic-rays in the intra-cluster medium is unfortunately not as straight forward as it may seem. It has been realised early on that the diffusion speed of CR electrons is not close to the speed of light as one might naively expect. Instead, the presence of a magnetic field causes the particles to excite MHD waves (streaming instability), that back react on the particle population and reduce the streaming

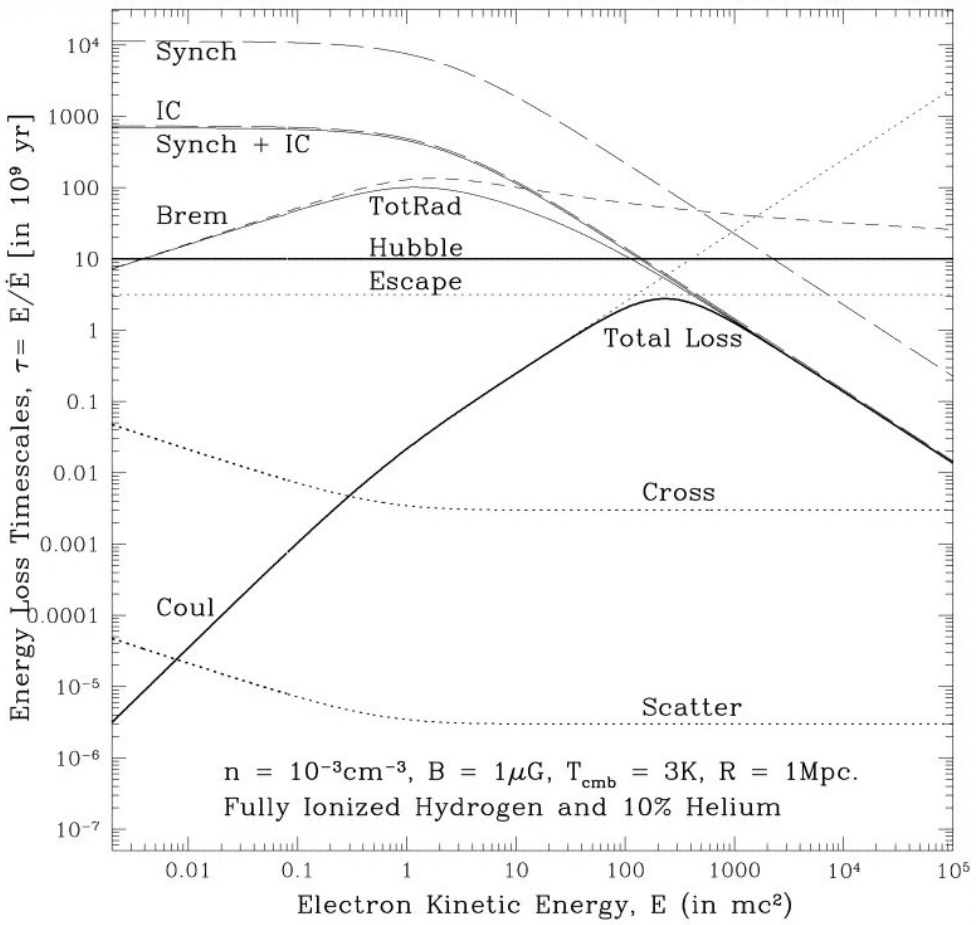

Figure 3.8: Energy loss timescale over kinetic energy for a population of CR electrons in the ICM. For radio halos the important population is at $E > 1000\,\mathrm{m_e c^2}$. Adopted from Petrosian (2001).

rate to approximately the Alvén speed in the ICM (Wentzel, 1974):

$$v_{\mathrm{Alven}} = \frac{|\mathbf{B}|}{\sqrt{4\pi n_{\mathrm{th}} m_{\mathrm{p}}}} \tag{3.40}$$

$$\approx 100\,\mathrm{km/s}. \tag{3.41}$$

Here n_{th} is the thermal number density of protons with mass m_{p}. The MHD waves act as "scattering agents" and the CR electrons perform a random walk through the cluster atmosphere.

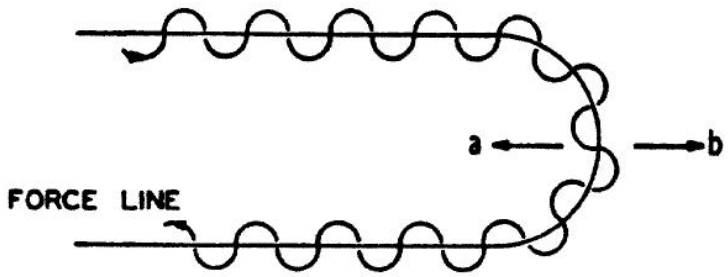

Figure 3.9: Scattering of a relativistic particle by a magnetic field reversal. The field reversal is either moving towards the particle (a) or overtaking the particle (b). While the momentum change for a given velocity is the same, case (a happens more often. On average a net momentum gain is achieved. Adopted from Fermi (1949).

Problem Given the last 3 paragraphs one can calculate the effective diffusion length of CR electrons in the ICM as:

$$l_{\text{diffusion}} = v_{\text{Alven}} \times \tau_{\text{loss}} \tag{3.42}$$

$$\approx 10\,\text{kpc}. \tag{3.43}$$

This is a very small number given that radio halos extend for several Mpc. Their size proofs the presence of CR electrons in the whole inner cluster volume.

> Given the locality of the primary cosmic-ray injection it is not clear how a synchrotron bright population of CR electrons is maintained throughout the cluster volume to produce a giant radio halo.

This was first realised by Jaffe (1977). A number of ways out of this dilemma have been proposed, which we will introduce in the next sections.

3.3 Cosmic Ray Transport Equation

Before we start with the modern theory of particle transport in the ICM, we will summarise the original idea for particle acceleration. We will then give a motivation of the modern theory of particle transport in a magnetised plasma.

3.3.1 The Classical Idea

In their seminal paper Fermi (1949) introduce the idea of random scattering of relativistic particles of magnetic irregularities in the interstellar medium. At that time magnetic fields in the ISM were not observed, but Alvén had introduced his velocity of waves in a magnetised liquid. Still it was unclear how relativistic particles were injected.

From the observations of molecular Calcium lines and their Doppler broadening, it was assumed that there was proper motion of "magnetic clouds" in the ISM. The authors concluded that weak fields would be adverted with the flow which would not only result in a tangled shape of the field, but also let cosmic-rays scatter off these irregularities, similar to a magnetic bottle (figure 3.9).

For a particle with velocity $v = \beta c$ and clouds in random motion with velocity V and average separation L, the rate of collision is then:

$$\nu_{\pm} = \frac{v \pm V}{L}, \tag{3.44}$$

where the ν_+ is for forward, head-on (a, figure 3.9) collision and ν_- for backward (b, figure 3.9) collision. Even though the energy gain/loss for a cloud with velocity V is the same, head-on collisions are more probable than backward collisions. This results in a net energy gain of the CR particle by this stochastic process (see also Eilek & Hughes, 1991). With a mean momentum change $\Delta p = \gamma m V$ and $v \approx c$, this energy gain is then

$$\frac{\mathrm{d}E}{\mathrm{d}t} = (\nu_+ - \nu_-)\gamma m c V \tag{3.45}$$

$$\approx \frac{2V^2}{Lc} E. \tag{3.46}$$

This is second order in V and is therefore called *second order Fermi acceleration*. In the case of only head-on collisions:

$$\frac{\mathrm{d}E}{\mathrm{d}t} = \nu_+ \gamma m c V \tag{3.47}$$

$$\approx \frac{V}{L} E. \tag{3.48}$$

we have *first order Fermi acceleration*, the basis for shock acceleration and subsequent CR injection. In the modern case this process is buried in the collision integral of the Boltzmann equation, as we will see in the next chapter.

3.3.2 The Modern Theory

In what follows we will introduce the basic equations governing our description of the evolution of cosmic-rays in the ICM. There are extensive discussions of this in the literature (e.g. Melrose, 1980; Eilek & Hughes, 1991; Schlickeiser, 2002; Brunetti, 2004a), especially instructive is the article by Eilek & Hughes. We follow Lifshitz & Pitaevskii (1981); Blandford (1986) in our derivation, which is sloppy in some parts. A more strict derivation from the Vlasov-Maxwell system is found in Schlickeiser (2002), but is far beyond the scope of this work. Specific models, i.e. application of the theory to galaxy clusters and radio halos, are subject of the next sections.

In statistical physics one recognises the inability to describe a complex (classical) system in all details, e.g. the trajectory of every particle of a many body system like a gas. Instead,

one turns to a statistical description of the system by a distribution function $f(\mathbf{r}, \mathbf{p}, t)$[7], usually under the assumption of quasi-ergodicity[8].

It follows then, that the total number of particles in phase space Ω is:

$$N_{\text{total}}(t) = \int\limits_{\Omega} f(\mathbf{r}, \mathbf{p}, t)\, \mathrm{d}\mathbf{r}\, \mathrm{d}\mathbf{p} \tag{3.49}$$

The fundamental evolution equation is given by the Boltzmann equation:

$$\frac{\partial f}{\partial t} + \dot{\mathbf{x}} \cdot \frac{\partial f}{\partial \mathbf{x}} + m\ddot{\mathbf{x}} \cdot \frac{\partial f}{\partial \mathbf{p}} = \left(\frac{\partial f}{\partial t}\right)_{\text{collision}} + \left(\frac{\partial f}{\partial t}\right)_{\text{diffusion}}, \tag{3.50}$$

which describes changes due to drift and external forces (second + third term), effects due to collision (fourth term) and effects due to diffusion (last term). In a Lagrangian description we can neglect the second term. For our application gravity and large scale electric fields do not play a role and we treat magnetic fields as scattering agents[9], so we set $\ddot{\mathbf{x}} = 0$.

The collision term then carries most of the physics relevant for our application. Following Lifshitz & Pitaevskii (1981) the collision term describes the rate of change of the distribution function in a volume element of phase space. Formally this is expressed by the collision integral, which is gains - losses for a 6-dim. volume element[10]:

$$\left(\frac{\partial f}{\partial t}\right)_{\text{collision}} = \int (w' f' f_1' - w f f_1)\, \mathrm{d}^3q\, \mathrm{d}^3p'\, \mathrm{d}^3q', \tag{3.51}$$

where $f(t, \mathbf{p})$ and $f_1(t, \mathbf{q})$ are the distribution functions of the two scattering agents (CR electrons and photon, MHD waves, etc) before and after (primed) scattering and d^3q the volume element in momentum space of species 1. $w(\mathbf{p}, \mathbf{q})$ marks the probability per unit time to change the momentum $\mathbf{p} \rightarrow \mathbf{p} - \mathbf{q}$ of the particles in the distribution function $f(\mathbf{p})$. We can simplify this further by assuming that there is no back-reaction on the scattering agents distribution function $f_1(\mathbf{q})$, i.e. it remains unchanged by the collision. Equation 3.51 then simplifies to:

$$\left(\frac{\partial f}{\partial t}\right)_{\text{collision}} = \int \left(w(\mathbf{p}+\mathbf{q}, \mathbf{q}) f(t, \mathbf{p}+\mathbf{q}) - w(\mathbf{p}, \mathbf{q}) f(t, \mathbf{p})\right)\, \mathrm{d}^3q \tag{3.52}$$

[7] which can be understood just as a histogram of all particles in 6 dimensional phase space

[8] We do not comment on that here, but refer the reader to the textbooks.

[9] This is where Schlickeiser (2002) does much better, for the price of filling pages with 25 coefficients of a non-linear PDE.

[10] This requires the concept of detailed balance. We refer the reader to Lifshitz & Pitaevskii (1981)

Assuming that changes of the distribution function due to scattering are small, we can use a Taylor expansion:

$$w(\mathbf{p}+\mathbf{q},\mathbf{q})f(t,\mathbf{p}\approx w(\mathbf{p},\mathbf{q})f(t,\mathbf{p})+\mathbf{q}\cdot\frac{\partial}{\partial\mathbf{p}}w(\mathbf{p})f(t,\mathbf{p}) + \frac{1}{2}q_\alpha q_\beta\frac{\partial^2}{\partial p_\alpha\partial p_\beta}w(\mathbf{p},\mathbf{q})f(t,\mathbf{p}), \tag{3.53}$$

where α and β refer to the two scattering species. So :

$$\begin{aligned}\frac{\partial f}{\partial t} &= \frac{\partial}{\partial p_\alpha}\left[A_\alpha f+\frac{\partial}{\partial p_\beta}\left(B_{\alpha\beta}f\right)\right]\\ &= \frac{\partial}{\partial p_\alpha}\left[\left(A_\alpha+\frac{\partial B_{\alpha\beta}}{\partial p_\beta}\right)f+B_{\alpha\beta}\frac{\partial f}{\partial p_\beta}\right] \qquad (3.54)\\ A_\alpha &= \int q_\alpha w(\mathbf{p},\mathbf{q})\,\mathrm{d}^3q \qquad (3.55)\\ B_{\alpha\beta} &= \frac{1}{2}\int q_\alpha q_\beta w(\mathbf{p},\mathbf{q})\,\mathrm{d}^3q. \qquad (3.56)\end{aligned}$$

Equation 3.54 can be understood as the divergence of a vector in α and is a continuity equation in momentum space. We can understand the coefficients A_α and $B_{\alpha\beta}$ by means of time average characteristics:

$$\begin{aligned}A_\alpha &= \sum q_\alpha/\delta t \qquad (3.57)\\ B_{\alpha\beta} &= \sum q_\alpha q_\beta/(2\delta t), \qquad (3.58)\end{aligned}$$

as a first and second order loss or gain term to the particles or their distribution function f. The sums are to be understood over a large number of collisions during time δt. This way A_α can be identified with the first order systematic energy loss terms from sections 3.1.1, 3.1.2 and 3.1.3. $B_{\alpha\beta}$ describes a second order process that gives a systematic energy change and another non-linear term. This part of equation 3.54 can be identified with a diffusion equation with $B_{\alpha\beta}$ the diffusion coefficient.

This can be understood considering that the first term on the RHS of 3.54 induces a *systematic* energy gain/loss of the particle distribution. For example a translation of the spectrum to higher or lower momenta (if the term is chosen appropriately), figure 3.10 upper right. The second stochastic term in 3.54 induces a *broadening* of the spectrum (figure 3.10 lower left). As $B_{\alpha\beta}$ acts on both terms a stochastic momentum gain will always be coupled with a systematic momentum gain. This is the principle of reacceleration (figure 3.10, lower right).

The spatial diffusion term is formally given similar to the second part on the right side of 3.54 :

$$\left(\frac{\partial f}{\partial t}\right)_{\text{diffusion}} = \frac{\partial}{\partial x_\alpha}\left[K_{\alpha\beta}\frac{\partial f}{\partial x_\beta}\right], \tag{3.59}$$

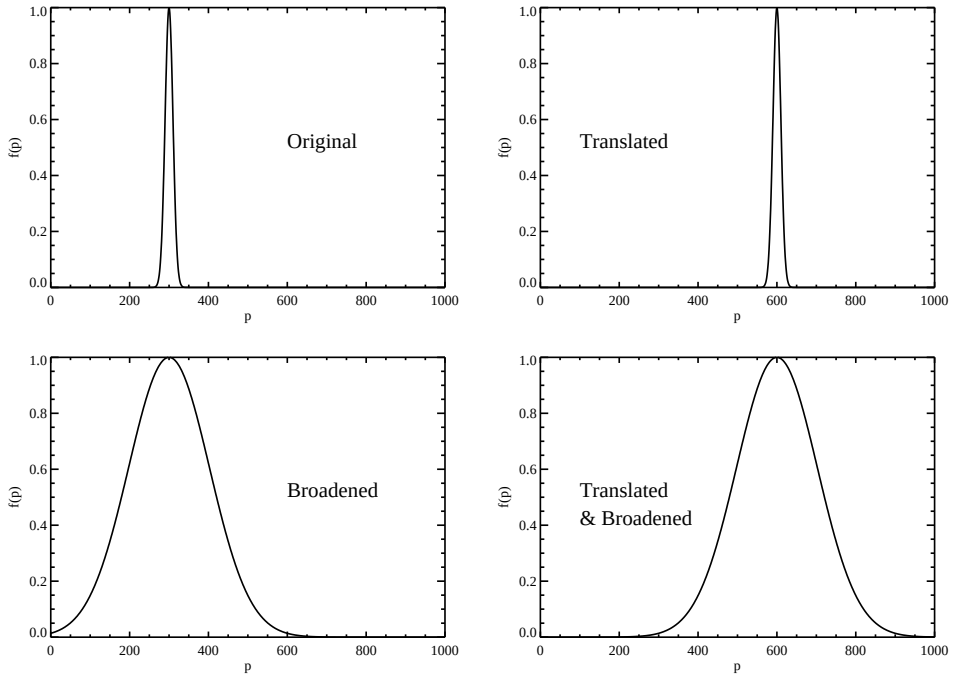

Figure 3.10: Upper left: Gaussian spectrum, Upper right: Translated Gaussian spectrum by a systematic momentum gain. Lower left: Broadened Gaussian spectrum by stochastic momentum gain. Lower right: Translated and broadened spectrum by systematic and stochastic momentum gain.

where $K_{\alpha\beta}$ is the spatial diffusion coefficient. It is often modelled so that:

$$\left(\frac{\partial n(E,t)}{\partial t}\right)_{\text{diffusion}} = Q_{\text{e}}(E,t) - \frac{T_{\text{e}}(E,t)}{n(E,t)}. \tag{3.60}$$

This is a simple description for particle addition $Q_{\text{e}}(E,t)$ and particle removal $T_{\text{e}}(E,t)$ from a Lagrangian volume element. These two terms are also referred to as injection function and catastrophic loss function.

The Fokker-Planck Equation: The important assumption we made so far is the one of no back-reaction on the scattering agents and the Taylor expansion (eqn. 3.53). These premises are equivalent with demanding *quasi-linear behaviour* of the transport process.

We will now make the second assumption of *isotropy of the distribution function* and write $n(E,t) = 4\pi p^2 f(\mathbf{p},t)\,\mathrm{d}p/\mathrm{d}E$. We then combine this with eqn. 3.54, 3.50 and 3.59,

identify $B_{\alpha\beta} = D_{\rm pp}$ and obtain:

$$\frac{\partial n(E,t)}{\partial t} = \frac{\partial}{\partial E}\left[n(E,t)\left(\left|\frac{\mathrm{d}E}{\mathrm{d}t}\right|_{\rm rad} + \left|\frac{\mathrm{d}E}{\mathrm{d}t}\right|_{\rm coul} - \frac{2}{E}D_{\rm pp}(E)\right)\right] + \frac{\partial}{\partial E}\left[D_{\rm pp}(E)\frac{\partial n(E,t)}{\partial E}\right] + Q_{\rm e}(E,t) - \frac{T_e(E,t)}{n(p,t)}, \tag{3.61}$$

Equation 3.61 is a *Fokker-Planck equation* (Fokker, 1914; Planck, 1917), which describes the CR electron transport in the ICM. One way or the other all CR models have to deal with it. The numerical solution of this equation is a central problem in the second part of this work. We have not made any assumption about the coefficients yet, that is left for the specific models to do.

General solutions to the equation are scarce and do not exist for our specific problem. A good overview can be found in Park & Petrosian (1995) who calculate a number of analytical solutions for Fokker-Planck type equations in the context of CR astrophysics.

The numerical solution of the equation can be done elegantly (Chang & Cooper, 1970; Park & Petrosian, 1996) and is described together with our implementation in chapter 7.

3.4 The Reacceleration Coefficient $\mathbf{D_{pp}}$

"This is highly speculative physics."
(Brunetti, 2009, priv.com.)

Even though this quote is not very optimistic[11], we will motivate the modern view on wave-particle coupling here.

The physics entering the coefficient $D_{\rm pp}$ describes the stochastic momentum gain by a particle distribution due to any kind of scattering agent in the ISM. In practice what we mean with scattering agent is turbulence, more specific of the coupling of the particle population to turbulent MHD modes. Turbulence is a stochastic process, so to first order the net momentum gain may be neglected ($\rightarrow$ secondary models), which is a good approximation for some astrophysical environments. It is the point of chapter 7 to demonstrate that this is not true for galaxy clusters. These processes are observable in the solar wind (Jokipii, 2010). However this system still differs greatly from the ICM.

The MHD description[12] predicts a magnetised plasma to host three principle types of waves: Alvèn, fast and slow magnetosonic waves. Alvèn waves can be thought of as longitudinal waves along the magnetic field line, while magnetosonic waves travel exclusively at non-zero angle relative to the field. They are the equivalent to sound waves in MHD.

[11] and certainly not what a PhD student wants to hear

[12] If this is fully applicable for the cluster atmosphere on all scales of interest is a complicated topic

In principle CR protons and electrons can couple (resonantly and non-resonantly) to all of these waves (and they probably do). We will restrict our derivation to fast magnetosonic waves here. There are two important reasons for this:

1. Reacceleration due to fast magnetosonic waves is expected to be inefficient. That makes it a good starting point for models that want to establish the relevance of this process. Every other process would be even more effective than this one, if there is enough turbulence in that kind of wave.

2. Alvèn waves are tightly coupled to CR protons. A treatment of Alvènic reacceleration must include CR protons and their modification of the turbulent spectrum on the scales of coupling, the wave-proton-boiler (Brunetti et al., 2004). This is beyond our scope.

Very little is known about turbulence in the ICM (see section 2.1.1). The amount of turbulent energy per type of MHD wave is pure speculation. The approach described above ensures that we take the worst case scenario. In our work we usually set $\eta_{\rm MS} = 0.25$, which is equivalent to 25% of the turbulent energy in fast magnetosonic waves. As we will see, the process does not depend strongly on that parameter (essentially every value above a few percent is probably fine).

There is extensive literature on this subject (Kulsrud & Ferrari, 1971; Blandford, 1986; Eilek & Hughes, 1991; Schlickeiser & Miller, 1998; Schlickeiser, 2002; Brunetti & Blasi, 2005; Brunetti & Lazarian, 2007). We will motivate here one way to derive the reacceleration coefficient, that is not especially strict, but instructive. In chapter 7 we use a different expression from Brunetti & Lazarian (2007), which is more complicated to derive. For the full formalism see Schlickeiser (2002).

Our derivation follows Cassano & Brunetti (2005):

We consider the resonant coupling of compressible and incompressible fast magnetosonic MHD waves to relativistic particles. Here the turbulent wave introduces a net electric field in the reference frame of the gyrating CR electron (Melrose, 1980). The relevant resonance condition reads:

$$\omega - k_{\parallel} v_{\parallel} - n\frac{\omega}{\gamma} = 0, \tag{3.62}$$

where ω is the wave frequency, $k_{\parallel}$ and $v_{\parallel}$ are the wave-vector and the particle velocity parallel to the magnetic field. $n = 0, \pm 1, \pm 2, \ldots$ is the harmonic number of the resonance[13]. We discuss here the $n = 0$ resonance, which is the component of the compressible wave along the magnetic field line. This is called *transit-time damping* (Barnes, 1968; Fisk, 1976).

[13]Brunetti & Lazarian (2007) argue that in general these waves might actually not be present at the relevant scales in the ICM. At these small scales the ICM might actually be a low beta plasma, i.e. random motion perpendicular to the magnetic field might be strongly suppressed, rendering the $n > 0$ channels useless.

This type of acceleration acts only along the magnetic field and therefore needs efficient isotropisation of the CR electron momenta to be effective. For this motivation we trust the zoo of plasma instabilities believed to act in the ICM to do the isotropisation for us. A discussion can be found in Brunetti & Lazarian (2007).

For our derivation we assume, that the magnetosonic wave spectrum $W_{\rm k}$ follows a diffusion equation:

$$\frac{\partial W_{\rm k}(t)}{\partial t} = \frac{\partial}{\partial k}\left(D_{\rm kk}\frac{\partial W_{\rm k}(t)}{\partial k}\right) - \sum_{i=1}^{\rm n}\Gamma^i(k)W_{\rm k}(t) + I_{\rm k}(t), \tag{3.63}$$

where $D_{\rm kk} = k^2/\tau_{\rm s}$ is the diffusion coefficient for wave-wave coupling with the energy transfer time $\tau_{\rm s}$ (cascading in Kolmogorov's theory). $\Gamma^i(k)$ is the wave-damping coefficient due to any type i of damping, and $I_{\rm k}(t)$ is the injection function for turbulence (Cassano & Brunetti, 2005):

$$\int_{k_{\rm min}}^{k_{\rm max}} I_0 k^{-\alpha}\,{\rm d}k = \eta_{\rm MS}\frac{E_{\rm turb}}{\tau_{\rm turb}V_{\rm turb}}, \tag{3.64}$$

where I_0 is the norm of the injection spectrum and $E_{\rm turb}$ is the turbulent energy in a volume $V_{\rm turb}$ of gas inject over time $\tau_{\rm turb}$.

We can then estimate the reacceleration coefficient by the principle of detailed balancing: assuming that at the momentum gain of the particle distribution function is equal to the turbulent energy damped away by the particles on all scales (Eilek, 1979):

$$\int {\rm d}^3 p E_{\rm e}\left(\frac{\partial n_{\rm e}}{\partial t}\right) = \int {\rm d}\mathbf{k}\Gamma_{\rm e}W(\mathbf{k}), \tag{3.65}$$

which can be written as (Eilek, 1979):

$$D_{\rm pp}(p,t) \approx 4.45\pi^2\frac{v_{\rm M}^2}{c}\frac{p^2}{B^2}\int_{k_{\rm min}}^{k_{\rm max}} kW_{\rm k}^{\rm B}(t)\,{\rm d}k. \tag{3.66}$$

Given stationarity in the turbulent diffusion and damping only by CR electrons, equation 3.63 can be rewritten as:

$$W_{\rm k} \approx \frac{I(k)}{\Gamma^{\rm e}(k)k}. \tag{3.67}$$

We now "only" need an expression for the damping rate $\Gamma_{\rm e}(k)$ which can be estimated as

(Cassano & Brunetti, 2005):

$$\Gamma_{\rm e}(k) = \sqrt{32\pi^3} n_{\rm th} \sqrt{m_{\rm e} k_{\rm b} T} \left(\frac{v_{\rm MS}}{B}\right)^2 \frac{W_{\rm k}^{\rm B}}{W_{\rm k}} I(x) k \tag{3.68}$$

$$I(x) = 2 \int_1^\infty {\rm d}x \left(\frac{1}{x^2} - \frac{1}{x^3}\right) \exp\left[-x^2 a\right] \tag{3.69}$$

$$= \left(1 + a^2\right) E_1(a^2) - \exp\left(-a^2\right) \tag{3.70}$$

$$a = \left(\frac{v_{\rm MS}}{v_{\rm th}}\right)^2, \tag{3.71}$$

where E_1 is the exponential integral, $v_{\rm MS}$ - the magnetosonic velocity, and $W_{\rm k}^{\rm B}$ - the turbulent magnetic energy density.

These can be combined to give:

$$D_{\rm pp}(p,t) \approx \frac{4.45\pi^2}{\sqrt{32\pi^3} c} n_{\rm th}^{-1} (m_{\rm e} k_{\rm b} T)^{-1/2} I(x)^{-1} \int_{k_{\rm min}}^{k_{\rm max}} I(k)\, {\rm d}k. \tag{3.72}$$

Note that reacceleration is a process that goes quadratic with the cumulative turbulent energy in a certain scale range. That is why turbulence is so effective in switching halos on and off in this model.

3.5 Reacceleration Models

Given the previous two sections we can now introduce reacceleration models.

In general these models assume injection of turbulence by major cluster mergers. Coupling of the dormant longer-lived CR electron population around 0.1 GeV then leads to a stochastic momentum gain of the particles. This momentum gain makes the CR electrons synchrotron bright. As turbulence is a transient phenomenon in galaxy clusters, reacceleration predicts transient radio halos. Broken synchrotron spectra are produced naturally by aging of the CR electron population (see Schlickeiser et al., 1987, for a good example), which results in a steepening of the CR electrons and subsequently the synchrotron spectrum starting at high energies/frequencies. In contrast steep synchrotron spectra pose a problem to hadronic models, which require unphysically large CRp fractions to explain them.

We summarise the published work on this type of model in chapter 4.1.

The first ever inclusion of a reacceleration model in astrophysical simulations and its application to radio halos is presented in chapter 7.

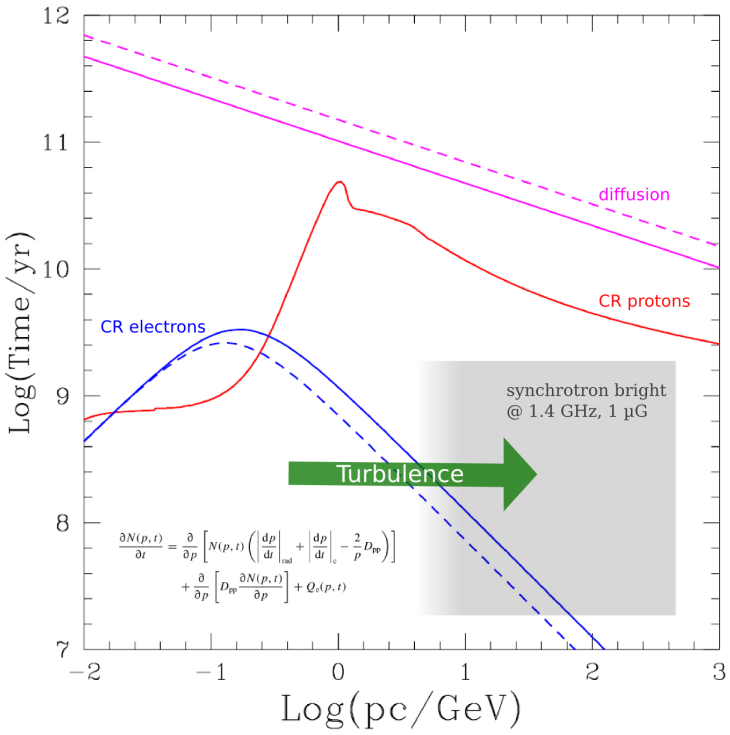

Figure 3.11: Reacceleration of mildly relativistic CR electrons, dormant at $\gamma \approx 100$. Coupling to turbulence leads to diffusion to synchrotron bright momenta at $\gamma \approx 10^4$. Modified from Blasi et al. (2007).

3.6 Secondary/Hadronic Models

Here we will give an introduction to secondary models for radio halos. Many groups have worked on this type of model, mostly because it allows a number of convenient simplifications in the theory.

3.6.1 Basic Principle

Hadronic models were first proposed by Dennison (1980) and have been studied extensively from then on (Schlickeiser et al., 1987; Blasi & Colafrancesco, 1999). In the past ten years the focus has shifted from purely analytical models to numerical work, basically because Schlickeiser's paper on the subject exhausted the predictive power of the model in an analytical approach (and came to a negative conclusion).

The basic idea of secondary/hadronic models is to use the long lifetime of CR protons of $> 10^9$ years (Blasi et al., 2007) and their subsequent decay into CR electrons to solve the cooling problem (section 3.2). As protons do not suffer from radiative losses as electrons do, they can diffuse throughout the whole cluster (figure 3.12). Scattering with thermal protons can then inject synchrotron bright CR electrons in the whole cluster and produce

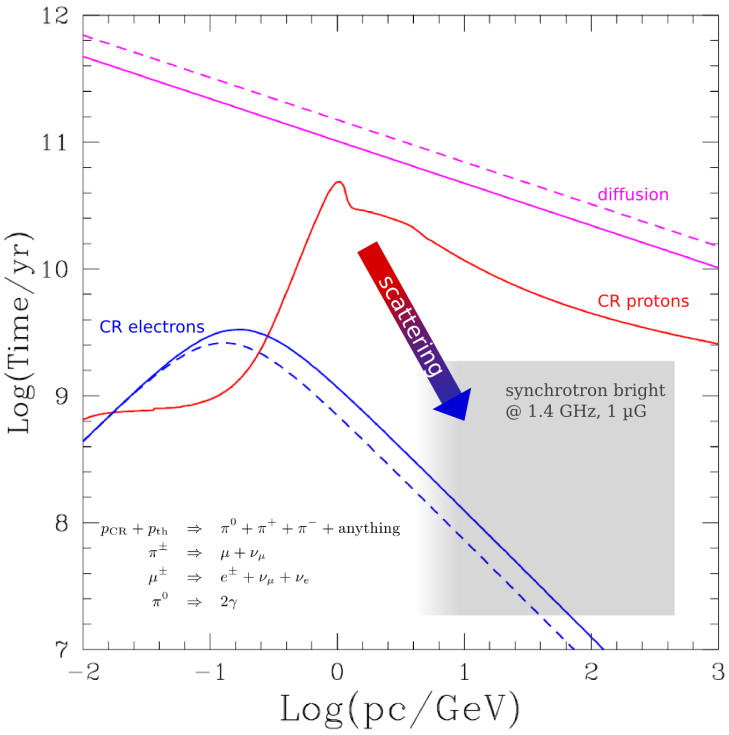

Figure 3.12: Cluster wide in-situ injection of synchrotron bright CR electrons by hadronic interaction of CR protons with thermal protons. The CR proton lifetime is long enough for diffusion throughout the whole cluster. Modified from Blasi et al. (2007).

a radio halo. Conveniently CR protons are usually injected in shocks and therefore to first approximation their spectrum might follow a power-law. The CR electrons distribution produced from these CR protons follows a power-law with steeper spectral index, allowing the authors to use the simplified formulas for the synchrotron emissivity derived above.

Pure secondary models neglect the influence of magnetic turbulence on the particle spectra, setting $D_{pp} = 0$ in equation 3.61. Catastrophic losses are neglected as well. For the steady state of the CR proton spectrum $T_e = \infty$ is assumed and the Fokker-Planck equation 3.61 becomes (Dolag & Ensslin, 2000):

$$\frac{\partial n(E,t)}{\partial t} = 0$$
$$\Rightarrow -\frac{\partial}{\partial E}\left(\dot{E}_e(\mathbf{x}, E_e) n_e(\mathbf{x}, E_e)\right) = Q_e(\mathbf{x}, E_e), \tag{3.73}$$

where we write radiative cooling terms like equation 3.33. Coulomb losses do not play a role in this regime (see eq. 3.23). This is solved by:

$$n_e(\mathbf{x}, E_e) = \left|\dot{E}_e(\mathbf{x}, E_e)\right|^{-1} \int_{\infty}^{E_e} Q_e(\mathbf{x}, E'_e)\, \mathrm{d}E'_e. \tag{3.74}$$

We are left with the integral over the injection function of CR electrons from hadronic interaction of CR protons with thermal protons of density $n_{\rm th}$. Expressions for the injection function, given CR protons with a power-law distribution, are given in Mannheim & Schlickeiser (1994); Dolag & Ensslin (2000) and Brunetti & Blasi (2005).

3.6.2 The Simple Hadronic Model

An instructive example for a secondary model can be found in Dolag & Ensslin (2000). They follow the simple model from Mannheim & Schlickeiser (1994) for the injection function. The treatment runs similar to the γ-ray source function in section 3.1.4, but one uses the $\pi^{\pm}$ source function as:

$$p_{\rm CR} + p_{\rm thermal} \rightarrow \mu^{\pm} + \nu_{\mu}/\bar{\nu}_{\mu} \rightarrow e^{\pm} + \nu_{\rm e}/\bar{\nu}_{\rm e} + \nu_{\mu} + \bar{\nu}_{\mu} \tag{3.75}$$

The *proton spectrum* with slope $\alpha_{\rm p}$ can be normed as a fraction $X_{\rm CRp}$ of the thermal energy density $\epsilon_{\rm th}$, so:

$$n_{\rm p}(\mathbf{x}, E) = N_{\rm p} E_{\rm p}^{-\alpha_{\rm p}} \tag{3.76}$$

$$X_{\rm CRp}\epsilon_{\rm th} = \int\limits_{E_{\rm p,min}}^{\infty} E' n_{\rm p}(\mathbf{x}, E')\,{\rm d}E' \tag{3.77}$$

The injection function is calculated from the formalism in Mannheim & Schlickeiser (1994). Simply speaking here one has to calculate the pion source function $q_{\pi^{\pm}}$ from the pion production rate $P_{\pi^{\pm}}(E_{\pi}, E_{\rm p})$ of the proton-proton collision times the proton spectrum by integrating over all proton energies:

$$q_{\pi^{\pm}} = \frac{1.26}{E_{\pi}} \int\limits_{1}^{\infty} {\rm d}E_{\rm p}\, n_{\rm p} P_{\pi^{\pm}}(E_{\pi}, E_{\rm p}) \tag{3.78}$$

$$q_{\rm e^{\pm}} = \frac{m_{\pi}}{70 m_{\rm e}} q_{\pi^{\pm}} \left(\frac{E_{\pm}}{70}\right) \tag{3.79}$$

$$\approx 2^6 \sigma_{\rm pp} c n_{\rm th} N_{\rm p} \left(24 E_{\rm e}\right)^{-\frac{4}{3}(\alpha_{\rm p}-\frac{1}{2})}, \tag{3.80}$$

where $\sigma_{\rm pp} = 32 \times 10^{-26}\,{\rm cm}$ is the inelastic proton-proton cross-section. For details on the pion production spectrum we refer the reader to Mannheim & Schlickeiser (1994). We want to stress that the pion production rate used here is an approximation, which gives an error that grows logarithmically with energy. I.e. the power-law index is too small (see next section).
With this the steady-state CR electron spectrum from equation 3.74 has a power-law index $\alpha_{\rm e} = \frac{4}{3}\alpha_{\rm p} + \frac{1}{3}$ and is given by:

$$n_{\rm e} = N_{\rm e} E_{\rm e}^{-\alpha_{\rm e}} \tag{3.81}$$

$$N_{\rm e} = \frac{2^7 3^2 \pi 24^{\frac{4}{3}\alpha_{\rm p}+\frac{1}{2}}}{4\alpha_{\rm p} - 5} \frac{\sigma_{\rm pp} m_{\rm e}^2 c^4}{\sigma_{\rm T}} \frac{n_{\rm p} N_{\rm p}}{B^2 + B_{\rm CMB}^2}. \tag{3.82}$$

With the analytical expression for the synchrotron emissivity of power-law electrons (Longair, 2010) and section 3.1.2 one finds:

$$j_\nu \propto X_{\mathrm{CRp}} n_{\mathrm{p}} \epsilon_{\mathrm{th}} \frac{B_\perp^{\alpha_\nu+1}}{B^2 + B_{\mathrm{CMB}}^2} \nu^{-\alpha_\nu} \tag{3.83}$$

$$\alpha_\nu = \frac{1}{2}(\alpha_{\mathrm{e}} - 1) = \frac{1}{3}(2\alpha_{\mathrm{p}} - 1)\,. \tag{3.84}$$

The exact relation is found in Dolag & Ensslin (2000). Most arguments for hadronic models use this scaling of the CR proton to synchrotron spectral index to "fit" observations. The last relation between synchrotron and CRp spectral index results in the normalisation problem of CRp in steep spectrum halos.

These basic equations are commonly used because they allow an easy estimation of the synchrotron brightness, without solving the full Fokker-Planck equation.

3.6.3 Steady State Spectrum in the High Energy Approximation

For our work with secondary models we use the more complicated model of Brunetti & Blasi (2005) to obtain a more accurate CR electron spectrum. The main motivation to do so was, that this model does imply a steeper electron spectrum compared to the simple one described before. This was important to not underestimate the CR proton normalisation, required to fit Coma radio halo (see chapter 5). There we use this formalism with an additional correction factor (≈ 1.7, Brunetti, priv.com.) to the electron normalisation to obtain our results.

However this choice complicates the model given before in that the synchrotron integral is not analytically solvable, because the CR electron spectrum is *not* a pure power-law anymore. Because the formalism presented in the paper is nebulous, we give here the steady state spectrum obtained by solving integral 3.74 for the high energy approximation from Brunetti & Blasi (2005). This is an unpublished result and is implemented in our projection program P-SMAC2. We show a plot of the steady-state spectrum for $n_{\mathrm{th}} = 10^{-3}, T = 10^7\,\mathrm{K}, B = 1\,\mu\mathrm{G}, \alpha_{\mathrm{p}} = 2.375, X_{\mathrm{CRp}} = 0.01$ in figure 3.13.

$$N_{\mathrm{e}^\pm}(E_{\mathrm{e}}) = \frac{3 m_{\mathrm{e}} c^3}{4\sigma_{\mathrm{T}}} \left(\frac{B^2 + B_{\mathrm{CMB}}^2}{8\pi}\right)^{-1} A(s) n_{\mathrm{th}} N_{\mathrm{p}} E_{\mathrm{e}}^{-1-s} \tag{3.85}$$

$$\times \left[\frac{P_1}{s-1} + \frac{P_2}{(s-1)^2}\left((s-1)\ln\left(\frac{aE_{\mathrm{e}}}{64\mathrm{GeV}}\right) + 1\right) - \frac{P_3}{\frac{3}{2} - s}\sqrt{\frac{aE_{\mathrm{e}}}{\mathrm{GeV}}}\right] \tag{3.86}$$

with the definitions from the original injection function:

$$A(s) = 64 \times 10^{-27} c \times a^{1-s}$$

$$a = \frac{2m_\pi^2}{m_\pi^2 + m_\mu^2}$$

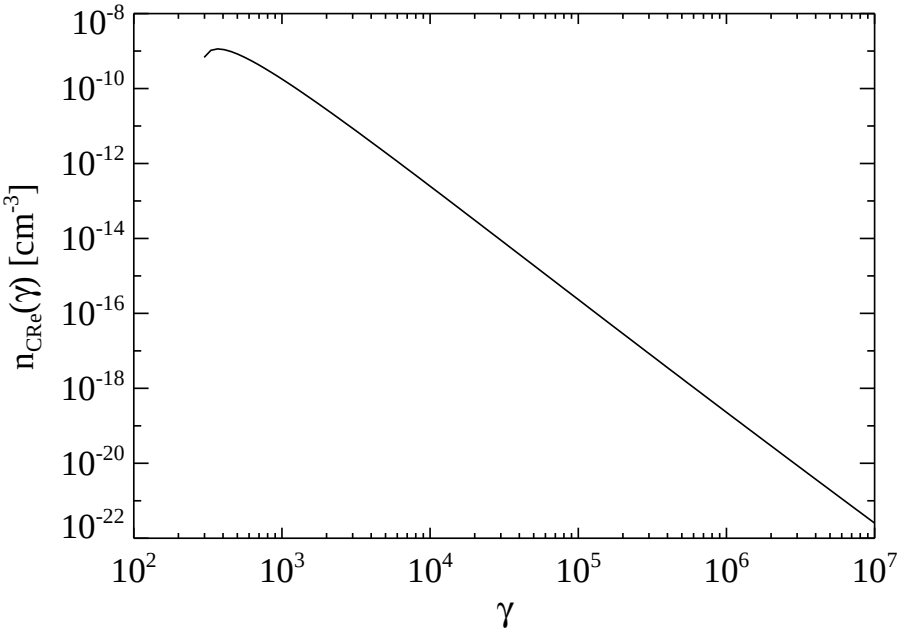

Figure 3.13: Steady state CR electron spectrum for a blob of gas with: $n_{\rm th} = 10^{-3}, T = 10^7\,{\rm K}, B = 1\,\mu{\rm G}, \alpha_{\rm p} = s = 2.375, X_{\rm CRp} = 0.01$.

and $c_1 = 1.22$ and $c_2 = 0.92$ in

$$
\begin{aligned}
P_1 &= \left[\frac{\bar{a}}{s^2} + \frac{\bar{b}}{(s+2)^2} + \frac{\bar{c}}{(s+3)^2}\right] I_0 \\
&\quad - \left[\frac{\bar{a}}{s} + \frac{\bar{b}}{s+2} + \frac{\bar{c}}{s+3}\right] I_1 \\
P_2 &= \left[\frac{\bar{a}}{s} + \frac{\bar{b}}{s+2} + \frac{\bar{c}}{s+3}\right] I_0 \\
P_3 &= \frac{3}{2}\left[\frac{\bar{a}}{s+\frac{1}{2}} + \frac{\bar{b}}{s+\frac{5}{2}} + \frac{\bar{c}}{s+\frac{7}{2}}\right] I_2
\end{aligned}
$$

and

$$
\begin{aligned}
\bar{a} &= \frac{5}{12}\left[1 + \frac{1}{5}(a^2-1)\frac{1+(m_\mu/m_\pi)^2}{1-(m_\mu/m_\pi)^2}\right] \\
\bar{b} &= -\frac{3}{4}\left[1 + (a^2-1)\frac{1+(m_\mu/m_\pi)^2}{1-(m_\mu/m_\pi)^2}\right] \\
\bar{c} &= \frac{1}{3}\left[1 + 2(a^2-1)\frac{1+(m_\mu/m_\pi)^2}{1-(m_\mu/m_\pi)^2}\right]
\end{aligned}
$$

and

$$I_0 = \int_0^1 \frac{\mathrm{d}x \ln(x)}{x^{2-s}} \left[c_1(1-x)^{7/2} + c_2 \exp(-18x)\right]$$

$$I_1 = \int_0^1 \frac{\mathrm{d}x}{x^{2-s}} \left[c_1(1-x)^{7/2} + c_2 \exp(-18x)\right]$$

$$I_2 = \int_0^1 \frac{\mathrm{d}x \ln(x)}{x^{3/2-s}} \left[c_1(1-x)^{7/2} + c_2 \exp(-18x)\right].$$

We found that the values given for the numeric integrals I_0, I_1 and I_2 in Brunetti & Blasi (2005) are not accurate enough to give a stable result.

3.7 The Intra-Cluster Medium

Many publications start with: "Galaxy clusters are the largest virialised objects in the universe". While this is certainly true, to many astrophysist these objects were rather simple ones. Unlike in galaxies, stars and star formation play only a minor role in clusters. Those are formed by a central, spherical symmetric potential made from dark matter. The dark matter probably follows the NFW-law[14] (Navarro et al., 1996):

$$\frac{\rho_{\mathrm{DM}}(r)}{\rho_{\mathrm{crit}}} = \frac{\delta_{\mathrm{c}}}{(r/r_{\mathrm{s}})(1+r/r\_\mathrm{s})^2} \tag{3.87}$$

$$\delta_{\mathrm{c}} = \frac{200}{3} \frac{c^3}{\ln(1+c) - c/(1+c)} \tag{3.88}$$

with the concentration parameter c and the critical density of the universe $\rho_{\mathrm{crit}} = 3H^2/8\pi G$.

To form the ICM, which we observe in the X-rays so beautifully, the baryonic matter settles in this potential. The physics of the ICM is commonly described to follow the (magneto-)hydrodynamic equations. They describe the evolution of the macroscopic quantities density, energy, momentum, and magnetic field in the form of conservation laws and can be derived from kinetic theory by taking moments of the Boltzmann equation. Usually the ideal gas law is used as a closure relation, which is a good first order approximation for the intra-cluster-medium. We refrain from a derivation here, which can be found in every standard textbook[15].

The common hydrostatic model for the ICM is the King model or isothermal beta-model (King, 1966; Cavaliere & Fusco-Femiano, 1978):

$$n(r) = n_0 \left(1 - \frac{r^2}{r_{\mathrm{c}}^2}\right)^{-3/2\beta} \tag{3.89}$$

[14] One of only a view real results predicted from simulations first

[15] The author recommends Goossens (2003)

with central density n_0, core radius r_c, and spectral index β. Consider the equation of hydrostatic equilibrium and ideal gas law:

$$\frac{\mathrm{d}p}{\mathrm{d}r} = -\frac{G\rho M(r)}{r^2} \tag{3.90}$$

$$p = nk_\mathrm{B}T \tag{3.91}$$

and $\rho = n\mu m_\mathrm{p}$, where μ is the effective mass per proton (to account for He fraction). Given observations of the thermal emission from the ICM, i.e. a spectral fit from X-ray telescopes, one can derive the mass profile:

$$M(r) = -\frac{k_\mathrm{B}Tr}{G\mu m_\mathrm{p}}\left(\frac{\mathrm{d}\ln n}{\mathrm{d}\ln r} + \frac{\mathrm{d}\ln T}{\mathrm{d}\ln r}\right) \tag{3.92}$$

This gives a direct handle on cluster mass, radius and temperature from X-ray observations. This model is strictly valid only in the isothermal, static and undisturbed case. This however does not hinder X-ray observers to fit its projected surface brightness to everything that looks like a cluster. Surprisingly they are quite successful with this approach - this might mean that cluster atmospheres rarely experience major disturbance once the object reaches a mass of a few $10^{14}\,\mathrm{M}_\odot$.

From the theory of cosmological structure formation one can derive the slope of the M - T relation for clusters. The mass density in an isothermal sphere can be written in terms of the velocity dispersion σ:

$$\rho(r) = \frac{\sigma^2}{2\pi G r^2}. \tag{3.93}$$

At the overdensity $\delta = 200$ one usually defines the virial radius:

$$M = \frac{4}{3}\pi r^3_{200,\mathrm{vir}}\rho_{200} \tag{3.94}$$

so the velocity dispersion is:

$$\sigma = M^{\frac{1}{3}}\left(H(z)^2\delta G^2/16\right)^{\frac{1}{3}}. \tag{3.95}$$

This allows us to write down the M-T relation, assuming the ideal gas law:

$$M = \left(\frac{16G^2}{\mu m_\mathrm{p}\delta^3}\right)^{\frac{3}{2}} H(z)^{-1}T^{3/2}, \tag{3.96}$$

which predicts a slope of 1.5, as observed in the X-rays, see section 2.1. This is the *self-similar model*.

This self-similar model is very successful. Weak lensing, X-ray, and SZ[16] data are prescribed well with these models. Additionally the theory of structure formation prescribes

[16]The Sunyaev-Zeldovich effect describes the increase in microwave flux through up-scattering of CMB photons of the thermal gas in the ICM.

the hierarchical build-up of clusters from a cosmological model (Press & Schechter, 1974) and lets us understand the statistical properties of the cluster distribution.

To this end cosmological simulations of structure formation reproduce most of these properties surprisingly well. Apart from this, problems still remain, one of which is the cooling-flow problem (Sijacki et al., 2007).

3.7.1 Extending our View of the ICM

As mentioned before, simulations of clusters from cosmological initial conditions are very successful in reproducing thermal properties of the ICM, globally and locally. These simulations usually assume a fluid model for the baryonic matter in the universe - the most advanced ones also follow magnetic fields.

However consider that in a galaxy cluster $n_{\rm th} \approx 10^{-3}\,\mathrm{particles/cm^3}$ and $T_{\rm ICM} \approx 10^8\,\mathrm{K}$. What does this imply for the thermal gas ?

Let us assume that the main interaction of charged particles in a plasma is Coulomb scattering. Following section 3.1.1 we can rewrite the total energy loss per particle from Coulomb collisions in the thermal gas (eq. 3.5) for protons and electrons as:

$$\Delta v_\perp = \frac{2e^2}{bvm_{\rm e}}, \tag{3.97}$$

which now gives the change in velocity by Coulomb scattering in the ICM. To get the mean square of velocity perpendicular to the motion of the incoming particle distribution per second we have to integrate over impact parameter again, which gives:

$$\begin{aligned} \left\langle \Delta v_\perp^2 \right\rangle &= \int_{b_{\rm min}}^{b_{\rm max}} \left(\frac{2e^2}{bvm_{\rm e}} \right)^2 2\pi b N v \,\mathrm{d}b \\ &= \frac{4e^4 N}{m_{\rm e}^2 v} \ln\Lambda. \end{aligned} \tag{3.98}$$

This means for the total velocity that, approximately:

$$\begin{aligned} \left\langle \Delta v_\perp^2 \right\rangle t_{\rm c} &= v^2 \\ &= 3\frac{k_{\rm B}T}{m_{\rm e}}. \end{aligned} \tag{3.99}$$

We can now combine 3.98 and 3.99 to estimate the *self-collision time* of protons and electrons in the ICM ($\ln\Lambda \approx 40$):

$$t_{\rm c} = \frac{\sqrt{m_{\rm e}}(3k_{\rm B}T)^{3/2}}{2\pi e^4 N \ln\Lambda}. \tag{3.100}$$

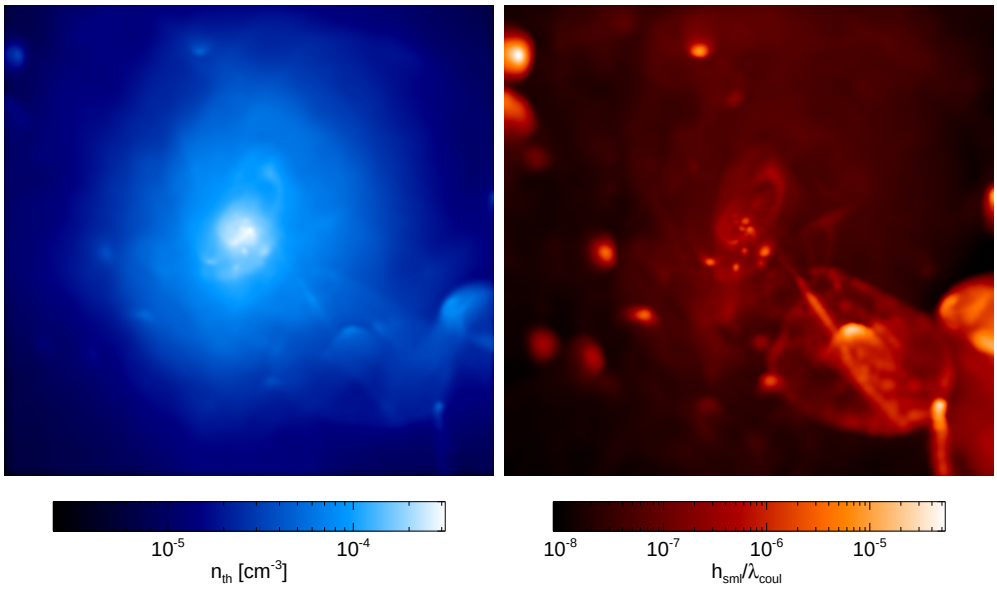

Figure 3.14: Left: Gas density projection of the ICM in a galaxy cluster (g72) from a cosmological simulation. The image size is $1.4 \times 1.4\,\mathrm{Mpc}$. Right: particle scale $2h_{\mathrm{sml}}$ over collisional mean free path from Coulomb interactions of the thermal plasma. Data from Dolag et al. (2006).

More importantly the mean free path is then (Spitzer, 1956; Sarazin, 1988):

$$\lambda_{\mathrm{e}} = \frac{3^{3/2}(k_{\mathrm{B}}T)^2}{4\sqrt{\pi}n_{\mathrm{th}}e^4 \ln\Lambda} \tag{3.101}$$

$$\approx 23\,\mathrm{kpc}\left(\frac{T_{\mathrm{ICM}}}{10^8\,\mathrm{K}}\right)^2\left(\frac{n_{\mathrm{th}}}{10^{-3}\,\mathrm{cm}^{-3}}\right)^{-1} \tag{3.102}$$

This result is most surprising: *Coulomb scattering is not sufficient to establish collisionality in the ICM on scales of even below a kpc.*

However without collisionality every fluid description *must* break down. Without collisional relaxation there is no temperature in a fluid element, no well defined pressure, etc. We will now explore what that means for simulations.

In figure 3.14 we show an example of a simulated galaxy cluster from cosmological initial conditions. On the left we show a projection of the number density distribution with a side length of 1.4 Mpc. The right panel shows the SPH particle scale over the collisional mean free path (eq. 3.102). The SPH smoothing length is a rough proxi of the resolved scale in the simulation. The fraction reaches values of $< 8 \times 10^4$. This is equivalent to the mean free path being 1000 times larger than the numerical resolution.

This shows that, considering only Coulomb interactions, the fluid model is formally not applicable on the scales of the simulation. In this case the equilibration of the thermal gas particles, a fluid element on scales of the simulation would not feel pressure, temperature

would not be definable, etc. On these scales the gas particles should be collisionless, as dark matter particles are.

We want to stress here that this is not a problem of the simulation or numerics, but of the physics assumed. In the derivation of the fluid equations from the kinetic equations, one assumes that in a fluid element[17] collisional timescales and lengths are sufficiently smaller than in the macrophysical system of interest.

However numerical simulations of clusters are a huge success, the fluid description is valid in clusters. This has to mean that Coulomb scattering is *not* the dominant process of equilibration in the ICM. Note that this is known for a long time (Sarazin, 1988).

Considering this quick investigation it is not surprising that the cooling problem in clusters exists in simulations. One has to ask, what does this mean to the thermal conductivity of the ICM (Dolag et al., 2004)? What is the actual mechanism that establishes collisionality on scales below the Spitzer value? What is the role of magnetic fields in this process?

Non-thermal cluster physics probably holds the answer. A recent paper points out collective plasma effects might be responsible for the reduced mean free path (Brunetti & Lazarian, 2011b). With the upcoming telescopes we will be able to probe the ICM and its non-thermal components with unprecedented precision. This will open doors to test and model plasma physics in a regime not accessible before.

[17] An SPH particle should be made up of more than one of these elements

Chapter 4

Preamble to the Papers

In this section we will provide an overview of the theoretical articles published on radio halos in the past decade. We consider reacceleration models, followed by hadronic models. We keep the discussion of reacceleration models relatively short because a detailed discussion is beyond the scope of this work.

4.1 Reacceleration Models

The word "reacceleration model" is used in the community for every model that is not based solely on CR protons and their hadronic interactions or primary CR electrons, directly injected at shocks. In the last years this distinction became increasingly meaningless because this type of models often include hadronic injection of CR electrons. A nomenclature similar to "more complete" would be therefore more appropriate.

A variety of articles examine reacceleration models for radio halos analytically or semi-analytically. The classic work on Coma comes from Schlickeiser et al. (1987). In the 1990's, even though there was growing evidence for on-going merger activity in Coma and other halo clusters (Colless & Dunn, 1996; Burns et al., 1995), most authors argued against it (e.g. Enßlin et al., 1999).

The model got more attention in the beginning of the new millennium (Petrosian, 2001; Brunetti et al., 2001). From then on only one group has been following a more complete approach to this problem. The work includes analytical work on reacceleration by compressible magnetosonic turbulence (Brunetti et al., 2001; Brunetti & Lazarian, 2007, 2011a), Alvénic reacceleration of CR electrons and protons (Brunetti & Blasi, 2005) and coupling of these models with a stochastic model for cluster mergers (Cassano & Brunetti, 2005).

Critique: A general critique on this type of model is (and must be clearly) the large number of ill constrained parameters that go into it. Turbulence in the ICM is not well constrained from observations. Numerical simulations point into the direction of a few 100 km/s on the injection scale. However as we have shown before, these simulations do not

catch all of the relevant micro-physics (e.g. Brunetti & Lazarian, 2011b). The nature of the reacceleration coefficient and the detailed plasma physics at work, when turbulence is damped on small scales by CR protons and electrons is not known very well.

Specifically, magnetosonic reacceleration requires efficient particle isotropisation to work. While it is true that a number of instabilities might do this in the ICM it is speculative at best how this is achieved. Furthermore CR damping occurs on scales of a few kpc and below, much smaller than the turbulent injections scale. Here magnetic field strengths in the μG range are strong enough to suppress motions perpendicular to the field and subsequently prevent magnetosonic turbulence.

In such a situation where a complicated model with weakly constrained parameters is used to fit the observations the validity of its predictions are doubted by many authors in the community (e.g. Ensslin, 2005).

4.2 10 Years of Hadronic Models

In what follows we review the most important papers in the field of secondary models to radio halos published in the last decade. A very instructive purely analytical work was presented early by Schlickeiser et al. (1987).

4.2.1 Dolag & Ensslin (2000)

The authors use a cosmological simulation of galaxy clusters with magnetic fields and the simple secondary model reproduced in section 3.6.2. The magnetic field of the cluster is shown to be within bounds from observations of Faraday rotation measurements.

In post-processing the authors obtain synchrotron brightness maps for a set of ten clusters with different masses. They show radial profiles in radio emission, P_ν-P_X morphology plots and the P_{14} - L_X correlation. To fit the total flux of Coma they need $4\% < X_\mathrm{CR} < 14\%$. They found the radial profile of one cluster to fit the Coma cluster in one projection. The whole simulated sample showed consistently too steep profiles. The morphology comparison was found to be steeper in simulations when compared to observations. The P_{14}-L_X correlation was fitted sufficiently, polarisation and γ-ray properties stay below constrains from observations at that time.

Critique: From today's point of view the CR proton normalisation is problematic. 14% relativistic protons means an equal amount of non-thermal pressure, which should be detectable with modern X-ray satellites, esp. in the Coma cluster. The discrepancy in steepness of the morphology plot is a first hint to the break in self-similarity found later in observations (see 2.3.4). As argued also by the authors they find consistently too steep radial profiles of radio synchrotron emission. A result we confirm in this work.

4.2.2 Miniati et al. (2001)

were the first to implement CR proton physics into cosmological simulations (Miniati, 2000, 2001; Miniati et al., 2001; Miniati, 2003). At first they focused on primary CR proton and electron acceleration in accretion shocks, i.e. radio relics from their grid code. Miniati et al. (2001) investigated the combined primary and secondary CR electron population and the resulting EUV, HXR, γ-ray, and synchrotron emission from a galaxy cluster.

They numerically solve the evolution of CR protons and primary electrons for power-law spectra without coupling to turbulence. Their secondary model is based on Moskalenko & Strong (1998), which is a more accurate treatment of the process than presented in section 3.6.2. The magnetic field is inserted by hand to give a volume-averaged value of $3\,\mu$G.

The authors find that the EUV emission from their simulation fails to explain observations discussed at that time. The same is true for the HXR emission from secondaries, which would hit the γ-ray limits available from EGRET. The authors claim, that their model explains radio synchrotron luminosity, polarisation and morphology found in observations. The spectral index obtained from the simulation did not fit the observations. However they succeeded to reproduce radio relics, only limited by their numerical resolution.

Critique: The Mach number found by the authors in earlier work for the cluster centre was consistently too high (Miniati et al., 2000). We know today, that turbulence in the cluster centre is mostly subsonic and shocks do not exceed Mach numbers of 3-4 (e.g. Vazza et al., 2009). Therefore primary electrons were largely overestimated. Anyway in this early work regarding radio relics the limited spatial resolution of the simulation does not allow proper detailed predictions. Radio halos inferred from a combined primary/secondary model may fill the outer regions of the cluster with primary emission, where there is none expected from observations. Eventually they assumed essentially flat magnetic field profiles for the their emission. This is in contrast to observations and findings from simulations (Dolag et al., 2005; Miniati & Martin, 2011).

4.2.3 Ensslin et al. (2007) and Others

Extensive work has been done in the five years on the subject of hadronic + primary models coupled to cosmological SPH simulations. Based on the model presented in Ensslin et al. (2007), articles by Jubelgas et al. (2008); Pfrommer & Ensslin (2004); Pfrommer et al. (2007, 2008); Pfrommer (2008), and Pinzke & Pfrommer (2010) use the SPH code GADGET (Springel, 2005) and a prescription for shock finding (Pfrommer et al., 2006) to model the CR proton feedback and primary injection in simulations. They derive relevant observables in the radio and γ-ray regime.

The CR proton theory outlined in Ensslin et al. (2007) is based on the assumptions that CR protons are the dominating relativistic particle population in clusters, and these CR protons follow a power-law distribution in momentum space (a direct prediction from primary shock acceleration). This proton spectrum is then described by spectral index,

cut-off and normalisation, from which the macroscopic quantities energy, particle number and non-thermal pressure can be derived. The theory is "tuned" towards SPH simulations as this spectrum can be prescribed in an adiabatically invariant (Lagrangian) way:

$$f(p) = Cp^{-\alpha_{\mathrm{CRp}}}\Theta(p-q) \tag{4.1}$$

$$q(p) = (\rho/\rho_0)^{1/3}\, q_0 \qquad \text{and} \qquad C(\rho) = (\rho/\rho_0)^{\frac{2}{3}\alpha_{\mathrm{CRp}}}\, C_0 \tag{4.2}$$

where q_0 and C_0 are the Lagrangian cut-off and normalisation. They then provide a prescription how to obtain the macroscopic variables energy, temperature and pressure from these quantities and how to evolve the microscopic variables under the assumption of a constant or variable spectral index α_{CRp}. Neglecting particle acceleration by turbulence, one can then derive the SPH equations of motion with the adiabatic invariant CR proton variables.

Ensslin (2002) propose the spectral break found in Coma to be an observational artifact from the SZ-decrement in the cluster[1].

This model was first implemented by Jubelgas et al. (2008) in GADGET-2 and supplemented with a shock finder (Pfrommer et al., 2006), applied and extended by Pfrommer et al. (2007, and subsequent papers).

This formalism is applied in a number of papers using a sample of simulated galaxy clusters to establish predictions for non-thermal observables. The authors show the expected non-thermal pressure from CR protons and their spatial distribution[2] together with the Mach number distribution (Pfrommer et al., 2007). They find a small contribution of CR protons to the non-thermal pressure in non-radiative simulations, and a significant contribution in radiative runs. In non-radiative runs the contribution is small in the cluster centre and rises up to the virial radius, in radiative runs it is flatter. The CR proton pressure is found to be strongly enhanced in merging clusters, due to the primary shock injection.

In Pfrommer et al. (2008) and Pfrommer (2008) the authors then derive non-thermal observables from the cluster sample. They show radio synchrotron emission at different frequencies, assuming magnetic field scaling as $B \propto \rho^{0.5}$ and complete the picture with IC and γ-ray maps.

Critique: The main motivation for parts of this thesis was the unclear status of the predictions of secondary models when compared directly with observations. This is true especially for the work discussed here, that claims a unified model for the formation of radio halos. A few points have to be kept in mind as well:

- The work discussed uses a composite model for the formation of radio halos, primary injection/emission in shocks at $r > 0.1r_{\mathrm{vir}}$ and secondary emission further inward. They achieve a good match with observations when two projections are compared "by eye". However, in the simulation shocks are usually broadened over 2-3 SPH

[1] We show in section 5 that this is not correct.

[2] We used these results in chapters 5 and 6

particles due to the smoothing nature of the algorithm. This is going to lead to a smoothing of the emission in the outskirts of the radio halo as well, which is going to compensate for the steep decline in emission predicted for all emission models that scale with density. In contrast, shocks are believed to be very narrow[3], as seen in observations (chapter 2.5.1) and numerical simulations with grid codes (Vazza et al., 2008). This questions the ability of a composite model to "fill the gap" of radio emission at radii above $0.1 r_{\rm vir}$ and provide the break in self-similarity seen for the largest cluster in correlations.

- The amount of CR protons in the ICM depends strongly on the injection efficiency in intermediate shocks of Mach number ~ 3. However this parameter is highly uncertain, available only from PIC simulations (Spitkovsky, 2008) and rather high in the work discussed here.

- It is unclear how a model based on a pure power-law description of CR particles in ISM can reproduce the spectral properties of the Coma cluster. This was convincingly demonstrated early on by Schlickeiser et al. (1987).

- This work as all hadronic models predicts radio halos to be present in all galaxy clusters. This follows directly from the long life-time of CR protons and their ubiquitous injection.

4.2.4 Kushnir et al. (2009)

In their work Kushnir et al. (2009) point out that the bimodality observed in radio halos (see section 2.3.5) can be resolved assuming high magnetic fields in galaxy cluster. They argue that magnetic field amplification by turbulence is sufficient to boost the radio luminosity from the radio quiet region to the P_{14} - $L_{\rm x}$ correlation. They estimate from the present correlation that:

$$\frac{\nu L_\nu^{\rm synch}}{L_{\rm X}} \approx 1.1 \times 10^{-5} \frac{\beta_{\rm core}}{10^{-4}} \frac{\sqrt{T}}{10\,{\rm keV}}, \tag{4.3}$$

where $\beta_{\rm core}$ is the scaling of CR proton energy density to thermal energy density. In their model the synchrotron luminosity can then be approximated by:

$$j_\nu = 10^4 \sqrt{\frac{\nu_{\rm radio}}{1.4\,{\rm GHz}}} \left(\frac{B}{B_{\rm CMB}} \right)^{-1/2}. \tag{4.4}$$

Based on this result they derive that a magnetic field suppression to $B < 1\,\mu{\rm G} = B_{\rm CMB}/3$ corresponds to a suppression in emissivity by a factor of 10. This may explain the bimodality.

[3] in an astrophysical context

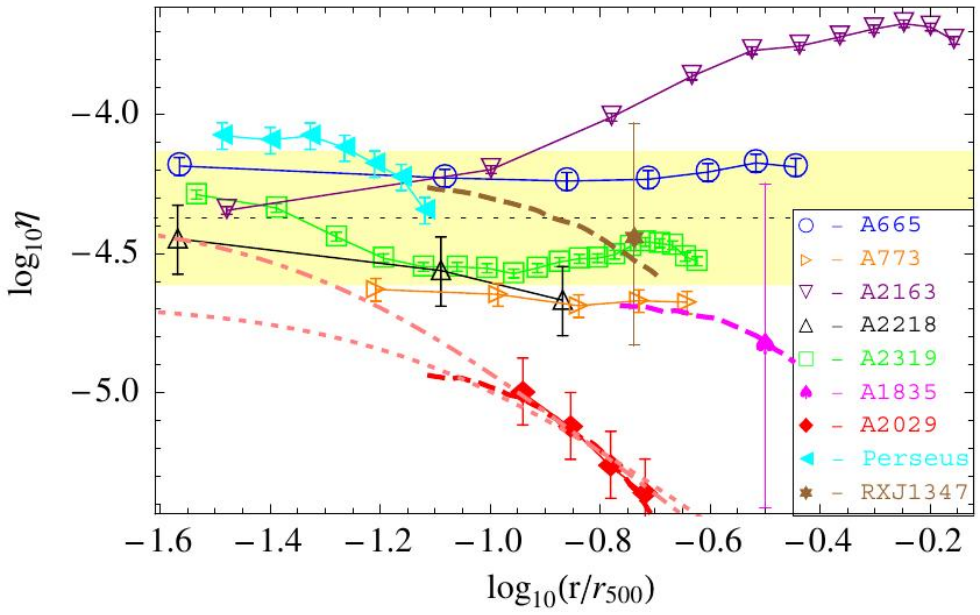

Figure 4.1: η for a number of clusters. Adopted from Keshet & Loeb (2010).

Critique: The main point here is that neither high magnetic fields of $B \gg 3\,\mu$G are observed in clusters, nor is a bimodality in Faraday RM observed in surveys (see 2.2). In contrast, simulations of magnetic fields in clusters (Dolag et al., 1999, 2002) and observations (Kim et al., 1991; Bonafede et al., 2011) point to magnetic fields being of the order of a view μG and not a highly transient phenomenon[4].

Furthermore the presented model does not solve the riddle of the spectral break in Coma nor does it explain the break in self-similarity in the correlations. In contrast it assumes self-similarity to derive equation 4.3.

4.2.5 Keshet & Loeb (2010)

In a recent work Keshet & Loeb (2010) propose a unified scheme for radio halos and radio mini halos based on the dimensionless ratio between radio and X-ray luminosity:

$$\eta(r) = \frac{\nu I_\nu(1.4\,\mathrm{GHz})}{F_{\mathrm{x}[0.1-2.4]}}, \tag{4.5}$$

which they claim to be constant over radius and similar in a majority of clusters, hosting radio halos and mini halos. We reproduce their findings in figure 4.1. Following Kushnir et al. (2009) they propose a universal radio mechanism based on magnetic field values $B \gg B_{\mathrm{CMB}}$. According to their model, radio halos are universally characterised by these high field values of $B_{\mathrm{central}} \geq 10\,\mu$G in the radio bright region. The bimodality arises

[4]Magnetic field diffusion is happening in clusters, but not to this extend

when the field value drops below the CMB equivalent magnetic field due to reconnection or diffusion of the field (Kushnir et al., 2009). The same is true for the morphology, where the brightness drops steeply at the radius where $B \approx B_{\mathrm{CMB}}$. In this model the spectral break in Coma can be explained by a drop in the proton-proton cross-section.

Critique:

- Referring to observations of four clusters by Govoni et al. (2001), one can calculate η from their correlation (see equation 2.3 and table 2.4, reproduced in this work). After some elementary algebra η can be written as:

$$\eta = \frac{10^{-3}}{T_{10}} a \cdot \left(\frac{F_{\mathrm{x}}}{1.4 \times 10^{-14} \frac{\mathrm{erg}}{\mathrm{cm}^2 \mathrm{sec}} \mathrm{arcsec}^{-2}} \right)^{b-1}, \tag{4.6}$$

  where $T_{10} \approx const$ among clusters of the same size (self-similarity of thermal properties).
  From this it is immediately clear that for values of $b(r) \neq 1$, η differs among clusters and is not universal. In table 2.4 we find 2 clusters which clearly do not show this behaviour (Coma, A2163) and a third one on the edge (A2319). This is not surprising, as the break in self-similarity is well established (Cassano et al., 2007).

- Observations of RM in clusters are not compatible with fields of the required strength (see section 2.2). Fields of that strength would make the ICM plasma a low beta plasma, the magnetic field would start to dominate thermal motions and the non-thermal pressure would be dominating. That is not compatible with X-ray observations (see 2.1.1).

- It has been shown that the bimodality can not be easily explained by magnetic field decay (Brunetti et al., 2009). Even if the field would have to decay to just below B_{CMB}, it is not clear where the magnetic energy is going into on the short timescale.

Chapter 5

Radio Halos From Hadronic Models I: The Coma cluster

J. Donnert, K. Dolag, G. Brunetti, R.Cassano, A. Bonafede

ABSTRACT

We use the results from a constrained, cosmological MHD simulation of the Local Universe to predict the radio halo and the γ-ray flux from the Coma cluster and compare it to current observations. The simulated magnetic field within the Coma cluster is the result of turbulent amplification of the magnetic field during build-up of the cluster. The magnetic seed field originates from star-burst driven, galactic outflows. The synchrotron emission is calculated assuming a hadronic model. We follow four approaches with different distributions for the cosmic-ray proton (CRp) population within galaxy clusters. The radial profile of the radio halo can only be reproduced with a radially increasing energy fraction within the cosmic-ray proton population, reaching >100% of the thermal energy content at $\approx$ 1Mpc, e.g. the edge of the radio emitting region. Additionally the spectral steepening of the observed radio halo in Coma cannot be reproduced, even when accounting for the negative flux from the thermal SZ effect at high frequencies. Therefore the hadronic models are disfavoured from present analysis. The emission of γ-rays expected from our simulated Coma is still below the current observational limits (by a factor of $\sim$6) but would be detectable by FERMI observations in the near future.

Accepted to MNRAS 3 Sep 2009; **Published** in volume 401, Jan 2010

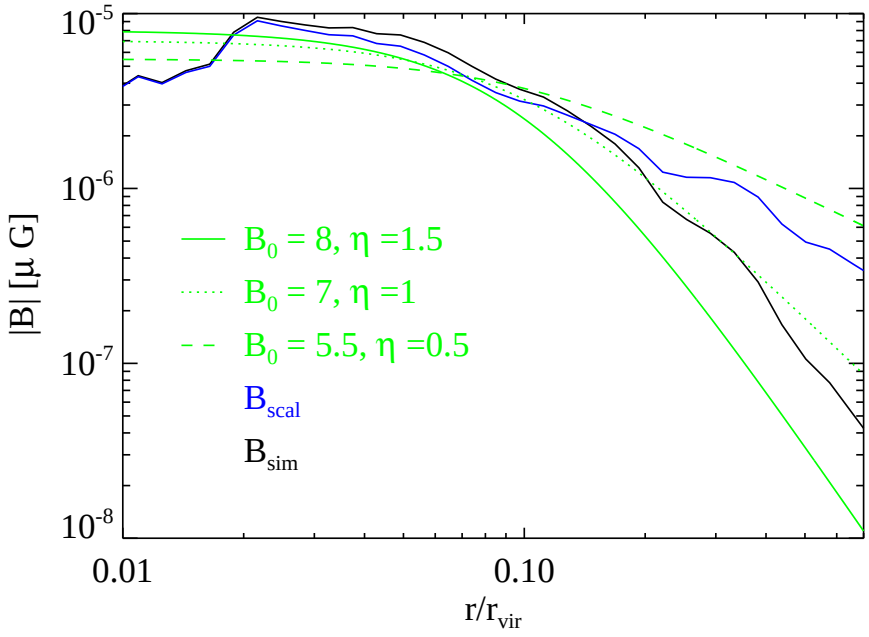

Figure 5.1: Comparison of the radial profile of the magnetic field in the simulated Coma cluster (black), the scaled version for *Model 3* (blue) and the class of models inferred from the observations. See text for more details.

5.1 Introduction

Galaxy clusters are the largest gravitationally bound objects in the Universe. The thermal gas, which forms the dominant component in the Intra-Cluster-Medium (ICM), is mixed with magnetic fields and relativistic particles, as seen by radio observations that detected Mpc-sized diffuse radio sources, radio halos and relics, in a fraction of X-ray luminous galaxy clusters in merging phase (e.g. Feretti, 2003b; Ferrari et al., 2008). A fraction of the energy dissipated during cluster mergers may be channelled into the amplification of the magnetic fields (e.g. Dolag et al., 2002; Subramanian et al., 2006) and into the acceleration of relativistic, primary electrons (CRe) and protons (CRp) via shocks and turbulence (Ensslin et al., 1998; Blasi, 2001; Brunetti & Lazarian, 2007). CRp have long life-times and remain confined within clusters for a Hubble time (e.g. Blasi et al., 2007, and ref. therein). Consequently they are expected to be the dominant non-thermal particle component in the ICM.

Primary and secondary particles in the ICM are expected to produce a complex emission spectrum from radio to γ-rays (see Petrosian et al., 2008; Brunetti, 2009; Cassano, 2009, for recent reviews).

Giant radio halos are presently detected in a fraction of massive galaxy clusters at low and intermediate redshifts (e.g. Cassano et al. 2008) and their origin is still not fully un-

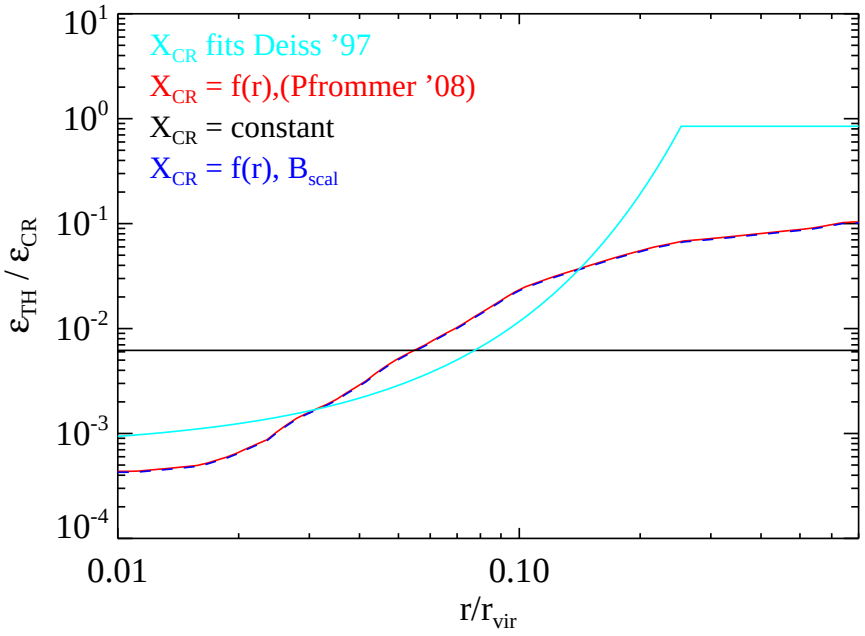

Figure 5.2: This panel shows the energy density fraction of the CRp as function of radius for the different models as indicated in the plot. See text for more details.

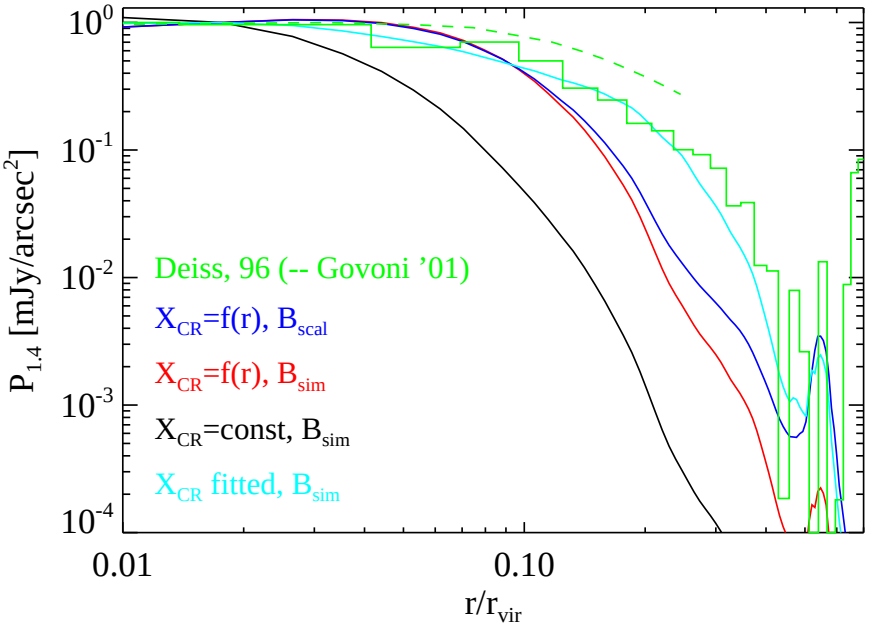

Figure 5.3: We show the radial profile for the radio emission resulting from the different models compared with the observed profile. See text for more details.

derstood. Extended and fairly regular diffuse synchrotron emission may be produced by secondary electrons injected during proton-proton collisions, since the parent relativistic protons can diffuse on large scales (e.g. hadronic or secondary models; Dennison (1980); Blasi & Colafrancesco (1999); Dolag & Ensslin (2000)). Alternative models assume relativistic electrons to be re-accelerated in-situ by MHD turbulence generated in the ICM during cluster-cluster mergers (e.g. re-acceleration models; Brunetti et al. (2001); Petrosian (2001)).

Unavoidable gamma ray emission, due to the decay of the neutral pions that are generated through proton-proton collisions, is expected in the context of hadronic models (e.g. Blasi, Gabici, Brunetti 2007 for review). Gamma ray emission is also expected from those re-acceleration models that account for the general situation where both relativistic protons and electrons (including secondaries) interact with MHD turbulence (Brunetti & Blasi, 2005), yet in this case the level of gamma rays is expected to be lower than that from standard hadronic models (Brunetti, 2009; Brunetti et al., 2009).

Only upper limits to the γ-ray emission from clusters have been obtained so far (Reimer et al., 2003; Aharonian et al., 2009), although the FERMI telescope will shortly provide the chance to obtain the first γ-ray detections of clusters and/or to put stringent constraints to the energy density of the CRp. Future deep observations with high energy Cerenkov arrays are expected to provide complementary constraints. Most importantly, in a few years the Low Frequency Array (LOFAR) and the Long Wavelength Array (LWA) will observe clusters at low radio frequencies with the potential to discover the bulk of the cluster-scale synchrotron emission in the Universe (Ensslin & Röttgering, 2002; Brunetti et al., 2008; Cassano et al., 2006).

The theoretical picture for the generation of non thermal cluster-emission is very complex and modern numerical simulations provide an efficient way to obtain expectations to compare with present and future observations. Advances in this respect have been recently obtained by including aspects of cosmic-ray physics into cosmological Lagrangian simulations (Pfrommer et al., 2007, 2008), mostly focussing on the acceleration of CRe and CRp at shocks and on the production of secondary electrons from such a CRp population.

Hadronic models are based on a well known physical process, the production of secondary particles through proton-proton collisions at relatively high energies. Thus they can be adequately implemented into cosmological simulations and compared with observations, provided the properties of the population of parent CRp are modelled correctly. On the other hand, turbulent re-acceleration is based on complex processes that happen at small scales, often unresolved in present simulations, and a correct implementation of this scenario would require complex sub-grid modelling which is presently not available. In this paper we investigate the non-thermal emission from secondary particles in a Coma–like cluster extracted from a cosmological simulation and, for the first time, compare numerical predictions and observations.

5.2 The Simulation

We use results from one of the constrained, cosmological MHD simulations presented in Donnert et al. (2009) from which we select the simulated counterpart of the Coma cluster. The initial conditions for a constrained realization of the local Universe were the same as used in Mathis et al. (2002). Briefly, the initial conditions were obtained based on the the IRAS 1.2-Jy galaxy survey (see Dolag et al., 2005, for more details). Its density field was smoothed on a scale of 7 Mpc, evolved back in time to $z = 50$ using the Zeldovich approximation and used as an Gaussian constraint (Hoffman & Ribak, 1991) for an otherwise random realization of a ΛCDM cosmology ($\Omega_M = 0.3$, $\Lambda = 0.7$, $h = 0.7$). The IRAS observations constrain a volume of ≈ 115 Mpc centred on the Milky Way. In the evolved density field, many locally observed galaxy clusters can be identified by position and mass. The Coma cluster in particular can be clearly identified by its global properties and gives an excellent match to the observed SZ decrement, especially in the non-radiative simulations used in this paper (Dolag et al., 2005). The similarity in morphology of the simulated and observed Coma cluster is coincidental, as this structure is far below the constrains originally imposed by the IRAS galaxy distribution. The original initial conditions were extended to include gas by splitting dark matter particles into gas and dark matter, obtaining particle of masses 6.9×10^8 $M_\odot$ and 4.4×10^9 $M_\odot$ respectively. The gravitational softening length was set to 10 kpc.

Our MHD simulation follows the magnetic field through the turbulent amplification driven by the structure formation process. For the magnetic seed fields a semi-analytic model for galactic winds was used. Here we used the result of the *0.1 Dipole* simulation (Donnert et al., 2009), which gives a reasonable match to the observed magnetic field in the Coma cluster. In figure 5.1 we compare the magnetic field profile predicted for the Coma cluster from our simulations with models that best reproduce the Rotation Measure observed in five extended sources within the Coma cluster (Bonafede et al., 2010) with a magnetic field radial profile:

$$\langle B(r) \rangle = B_0 \left[\frac{n_{\rm gas}(r)}{n_0} \right]^\eta$$

and η in the range [0.5 -1.5]. Our simulations are in good agreement with $\eta \approx 1.0$. This profile gives an average magnetic field over the central Mpc^3 of $\sim 1.9\mu$G, which is consistent with the equipartition estimate derived from the radio halo emission (Thierbach et al., 2003).

5.3 Secondary Electrons in Galaxy Clusters

In this paper we focus on hadronic models that can be implemented reasonably well in present simulations, providing a chance to test this scenario in the case of the Coma cluster.

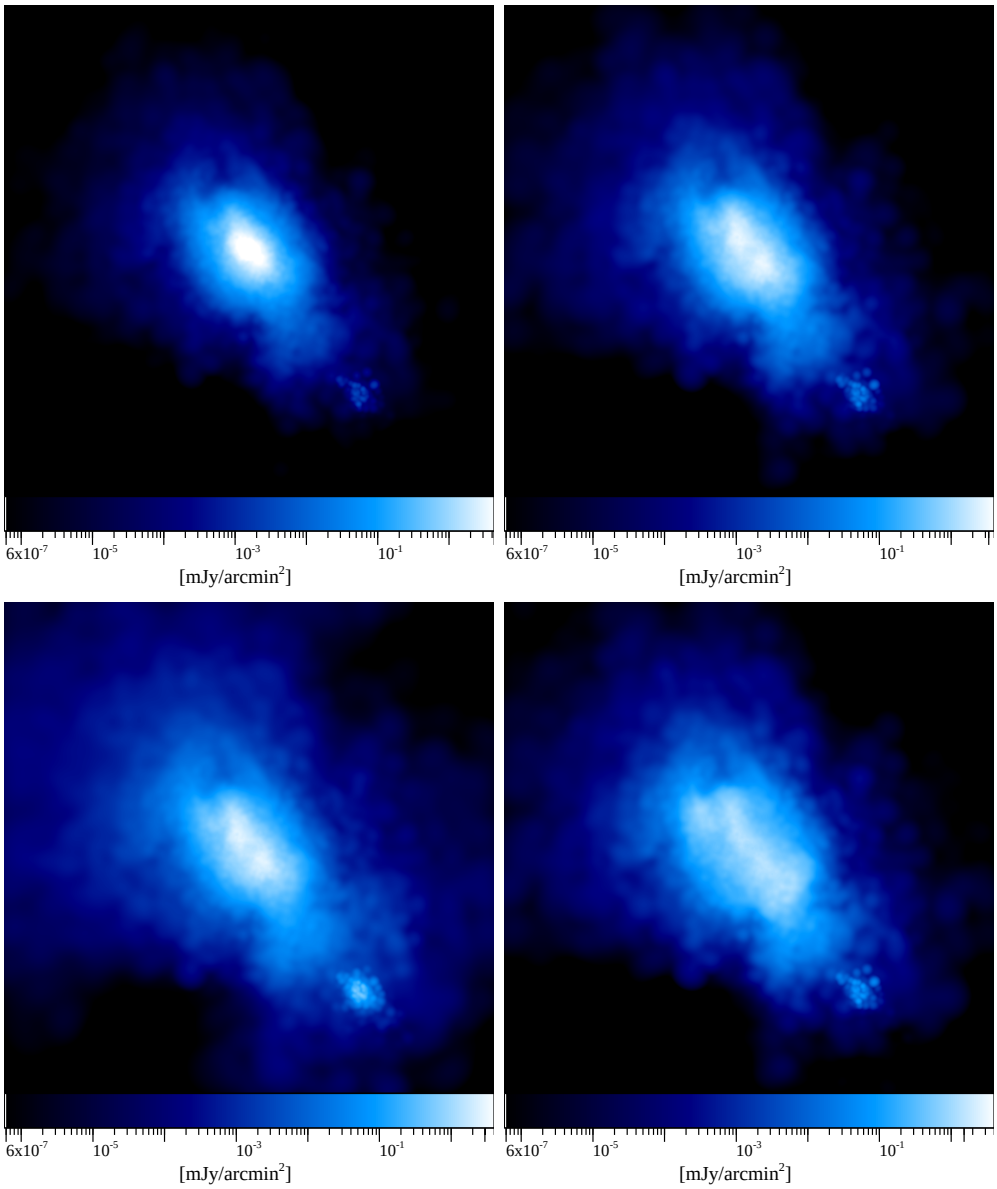

Figure 5.4: Synthetic synchrotron maps of the simulated Coma cluster (4 Mpc a side) at 1.4 GHz. The four models displayed from left to right are: constant CRp energy fraction (*Model 1*), scaled CRp energy fraction (*Model 2*), scaled magnetic field (*Model 3*) and fitted CRp energy fraction (*Model 4*). The overall normalisation of the CRp energy fraction is chosen to match the observed total radio luminosity of Coma.

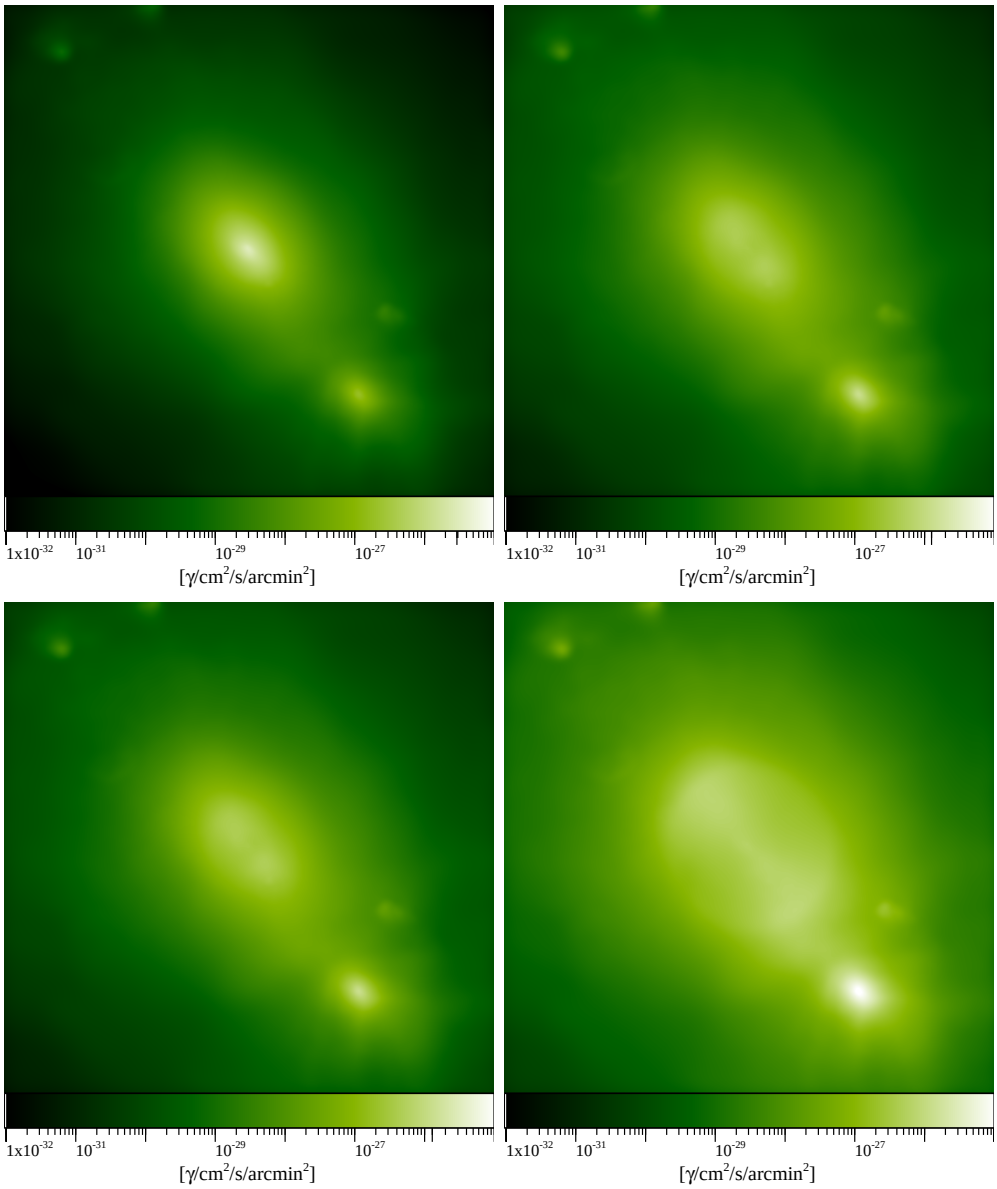

Figure 5.5: Synthetic γ-ray maps of the simulated Coma cluster (4 Mpc a side) at $E_\gamma > 100\,\mathrm{GeV}$. The four models displayed from left to right are: constant CRp energy fraction (*Model 1*), scaled CRp energy fraction (*Model 2*), scaled magnetic field (*Model 3*) and fitted CRp energy fraction (*Model 4*). The overall normalisation of the CRp energy fraction is chosen to match the observed total radio luminosity of Coma.

The spectrum of CRp was taken to be a power law, $N(E) = K_p E^{-\alpha_p}$, and the spectrum of the secondary electrons resulting from p-p collisions was calculated under stationary conditions considering synchrotron and inverse Compton losses (Brunetti & Blasi, 2005, and ref. therein). Following Dolag & Ensslin (2000) we adopted the slope of the spectral index of the Coma halo, $\alpha = 1.25$, obtained with $\alpha_p = 2.6$ for the hadronic models (this also accounts for the logarithmic increase of the p-p cross-section with proton energy). Such CRp collisions also produce γ-rays from the decay of secondary neutral pions, which are a direct measure of the CRp and of the unavoidable secondary electron injection process into the ICM. We calculate the γ-ray flux from our simulated Coma cluster by adopting $\alpha_p = 2.6$ and the formalism described in Pfrommer & Ensslin (2004).

There are several potential sources of CRp in the ICM, including shocks, AGN and galaxies (Ensslin et al., 1998; Völk & Atoyan, 1999; Ryu et al., 2003). An adequate modelling of the CRp-injection process by all these sources in simulations is challenging and consequently we treat the spatial distribution of CRp in our MHD simulations as a free parameter. Thus we follow four approaches chosen to encompass a range suggested by theoretical and observational findings, but restrict to large magnetic fields in the ICM that provide the most favourable case for hadronic models as it minimises the CRp-energy requirement necessary to generate a fixed synchrotron luminosity. In *Model 1* we assume that the energy density of the CR protons is a constant fraction of the thermal energy density of the ICM. In *Model 2* we adopt a radius-dependent ratio between CRp and thermal energy density following results from cosmological simulations of CRp acceleration at structure formation shocks by Pfrommer et al. (2007). In both these models, we use the magnetic field strength and spatial distribution from our MHD simulations of the Coma cluster. In *Model 3* we adopt the radius-dependent energy density of CRp as in *Model 2* and *an artificial* magnetic field by assuming a radial scaling of the field strength in the form $B \propto \sqrt{\rho}$ within the radio emitting region (figure 1). In the last model, *Model 4*, we used the magnetic field from our MHD simulations, but fit the radial profile of the CRp energy density in the simulated cluster to match the synchrotron brightness profile measured for the Coma radio halo; in this case we limit the CRp energy density so that is stays smaller than the thermal energy density of the ICM at large radii.

For these models the overall normalisation of the CRp energy density is chosen to match the observed radio luminosity of the Coma radio halo at 1.4 GHz, 7.76×10^{23} W/Hz (Deiss et al., 1997).

5.4 The Radio Halo of Coma

The Coma cluster hosts the prototype of giant radio halos (eg. Giovannini et al. 1993), and in this section we compare the radio properties from the simulated Coma cluster with the observed ones. We calculate simulated radio images by using a map–making algorithm (Dolag et al., 2005), that allows us to project the predicted emission of every SPH particle along the line of sight, considering an integration depth of $\pm$4Mpc around the centre of the simulated Coma cluster. The resulting images of radio emission for our models are shown

in Figure 5.4.

5.4.1 Radial Profile and Cosmic-Ray Energy Budget

The radial distribution of the fraction between the energy density of CRp and thermal gas for *Models 1–4* is reported in figure 5.2. Provided that the magnetic field strength in the central cluster regions is sufficiently large (i.e. $> 5\mu$G, as in our cases), *Models 1–3* generate enough synchrotron luminosity at 1.4 GHz to match that of the Coma halo with reasonable requests in terms of energy density in the CRp (about 1 to 10 % of that of the thermal gas).

However, a drawback of hadronic models, that was already discussed in the literature, is that the radial distribution of the synchrotron emission generated from secondary electrons is expected to be much steeper than observed in radio halos, with most of the radio luminosity generated in the cluster-core region (e.g. Brunetti, 2004b). Figure 5.3 shows a comparison of the simulated and observed radial profile of the radio emission from the Coma cluster. In line with previous simulations (Dolag & Ensslin, 2000) and analytical expectations (e.g. Brunetti, 2004b) we obtained a radial profile that is far too steep assuming that CRp contain a constant fraction of the energy density of the thermal pool (*Model 1*). Flatter radial profiles of the radio emission, and thus fairly extended radio halos, are generated only by *Models 2* and 3, yet the expected radio brightness at 0.5-1 Mpc distance from the cluster centre is still >10 times fainter than observed in the Coma halo. This picture also arises from the point-to-point scatter plot between radio surface brightness and the X–ray brightness from thermal emission (figure 5.6); the solid line is the observed correlation obtained by Govoni et al. (2001). To reproduce the radial profile as measured at 1.4 GHz by Deiss et al. (1997) out to 0.5-1 Mpc distance, we allow the energy density of CRp to vary with distance from the cluster center in *Model 4*. The resulting radial distribution of CRp energy relative to that of the thermal pool is shown in figure 5.2 and highlights an expected energetic problem of hadronic models: to considerably increase the synchrotron emissivity at large distance from cluster centre, where the generation of secondary particles is inefficient due to the small number density of (target) thermal protons, a secondary model requires the energy density of CRp be extremely large, comparable with (or even larger than) the thermal pool. Considering the profile measured with high sensitivity by Westerbork observations at 330 MHz (green, dashed line in figure 5.3, Govoni et al., 2001) makes this point even more problematic.
As a matter of fact the observed radial profile of the Coma halo drops smoothly by less than a factor 10 at 0.3 $r_{\rm vir}$. We expect this also considering results from simulations that attempt to combine secondaries and shock-accelerated electrons, which does not help significantly, as can be seen by comparing the shape of the observed profile (fig. 5.3) with those in Pfrommer et al. (2008) (their Figure 9).[1]

[1] Also note that the upturn in the profile of Figure 9 in Pfrommer et al. (2008). is due to the presence of a very bright shock-like feature south-east of the centre of their simulated cluster (see their Figure 8) and is not indicative of an upturn in the distribution of the truly diffuse halo-emission. On the other hand our fig. 5.3 refers to the observed brightness of the diffuse Coma halo emission, that is smooth and fairly

Mission Model	Veritas (diffuse) (> 0.1TeV)	($r < 1.3$ Mpc) (> 0.1TeV)	Egret (> 0.1GeV)
observed	$< 2.0 \times 10^{-12}$	—-	$< 3.8 \times 10^{-8}$
Model1	6.3×10^{-14}	6.6×10^{-14}	1.1×10^{-9}
Model2	6.3×10^{-14}	7.8×10^{-14}	1.2×10^{-9}
Model3	6.4×10^{-14}	8.0×10^{-14}	1.3×10^{-9}
Model4	1.6×10^{-13}	3.7×10^{-13}	6.0×10^{-9}
Spectrum1	$< 1.6 \times 10^{-14}$	$< 1.7 \times 10^{-14}$	$< 2.8 \times 10^{-10}$
Spectrum2	$< 1.6 \times 10^{-14}$	$< 1.9 \times 10^{-14}$	$< 3.0 \times 10^{-10}$
Spectrum3	$< 1.6 \times 10^{-14}$	$< 2.0 \times 10^{-14}$	$< 3.3 \times 10^{-10}$

Table 5.1: The upper part quotes the limits in different energy ranges ($E < 1$ TeV), corresponding to recent experiments together with the expected γ-ray emission from the simulated Coma cluster in $\gamma/\mathrm{s}/\mathrm{cm}^2$ (always excluding the substructure on the lower right) for the different models. Below we quote the upper limits for the γ-ray emission for combined primary and secondary models (assuming that the total emission at 4.85 GHz is of hadronic origin, see text for details.

5.4.2 The Spectrum

The radio spectrum of the Coma halo shows a steepening at higher frequencies (Thierbach et al., 2003) that has been interpreted as a signature of stochastic reacceleration of the emitting electrons (Schlickeiser et al., 1987; Brunetti et al., 2001). On the other hand, it has also been argued that the steepening is due to incorrect estimation of the flux of the radio halo at the highest frequencies due to the Sunyaev-Zeldovich (SZ) decrement (e.g. Ensslin, 2002). The latter results in a flux reduction of the cosmic microwave background photons in the cluster region by Compton scattering with the cluster-thermal electrons, which diminishes the radio flux at higher frequencies, although other authors conclude that this is not sufficient to explain the spectral steepening in the Coma halo (Reimer et al., 2004; Brunetti, 2004b).

Our numerical simulations can be used to investigate the SZ-decrement on the synchrotron spectral properties. Figure 5.7 shows the radio and inverse Compton spectrum from the SZ effect inside the cluster gas. The red line is the prediction of the total flux from our models, where the SZ signal is extracted from the region of the radio halo at 1.4 GHz, ≈500 kpc in radius. The deviation from a pure power law at higher frequencies is due to the SZ flux decrement (the dotted line marks the corresponding power law with $\nu^{-1.25}$), while the flattening at lower frequencies is due to the energy-dependent cross-section of p-p collisions. We plot the absolute of the IC flux, although it corresponds to negative flux at frequencies smaller than $\approx 2 \times 10^5$ MHz. In black we show observations from Thierbach et al. (2003) and Battistelli et al. (2002) of the Coma cluster in the radio and microwave band, respectively. We also evaluate the fluxes integrated over the relevant sizes according

symmetric

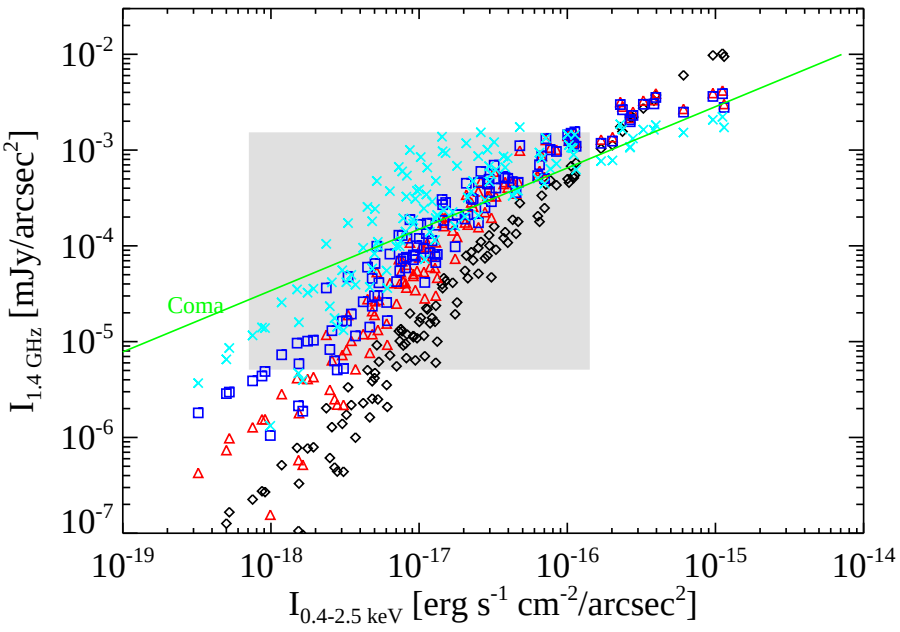

Figure 5.6: We show the Radio Flux of the simulated Coma cluster at 1.4 GHz versus X-ray surface brightness. We plot the constant model in black, the model with scaled CRp in red, the one with scaled MF and CRp in blue and the one with fitted CRp in magenta. The solid line is taken from the observations by Govoni et al. (2001). The gray rectangle marks where their observed data lies.

to the individual observations (red symbols). The observed shape of the radio spectrum, with the steepening at 2×10^3 MHz, cannot be explained by our secondary models, even including the SZ decrement for these frequencies, although the simulated SZ signal almost perfectly fits observations in the microwave regime. The blue dashed line shows the inverse Compton decrement, assuming an isothermal beta model for the thermal gas of Coma with emission region of 5 Mpc radius (as done in Ensslin (2002)), which would be needed to cause the steepening at 5 GHz. This size is about one order of magnitude more extended than the radio emission. Additionally we show in green the expected spectrum from stochastic electron-acceleration (Schlickeiser et al., 1987).

5.5 γ-ray Spectrum and Limits

Maps of the predicted γ-ray emission from our simulated Coma cluster are shown in Figure 5.5. In figure 5.8 we show the differential and integral γ-ray flux as function of energy of the photons. Here we also included the observed limits from VERITAS and EGRET (Reimer et al., 2003; Perkins, 2008), see Table 5.1.

We find that the γ-ray emission produced in the case of *Model 4*, that allows a reasonable

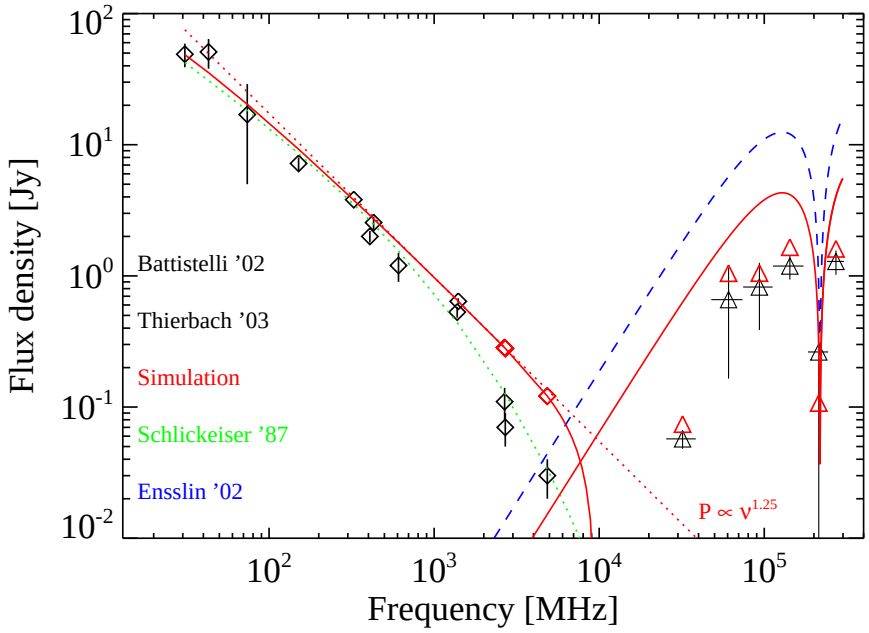

Figure 5.7: Observed spectrum of the Coma cluster (synchrotron emission: black diamonds, Thierbach et al. (2003); inverse Compton: black triangles, Battistelli et al. (2002)). Red lines are from the simulation and the red symbols are evaluated within the same aperture as the according observations. See text for more details.

match at least with the Deiss et al. profile of the Coma halo (for $<$ 0.7-1 Mpc distance from cluster centre), is a factor $\sim$6 below present upper limits. As well, matching the radial profile of the Coma halo as measured by high sensitivity observations at 330 MHz would require an even larger energy budget of CRp with respect to that in *Model 4* and consequently a larger γ-ray emission. Thus as soon as future γ-ray observations will reach sensitivities slightly deeper than present upper limits they will allow complementary tests to the hadronic origin of the radio emitting electrons in the Coma cluster. For instance, the expected sensitivity of the Fermi γ-ray Telescope will be sufficient to constrain *Model 4* after 1 year observations.

An alternative possibility is that particle acceleration in the Coma cluster is due to MHD turbulence in the ICM, remarkably the steepening of the synchrotron spectrum in Figure 7 is in line with expectations from this scenario (e.g., Schlickeiser et al. 1987; Brunetti et al. 2001). A possibility is that relativistic protons and their secondary products are accelerated by MHD turbulence (Brunetti & Blasi 2005), in which case gamma ray emission from neutral-pion decay is still expected but the ratio between gamma rays and synchrotron emission is substantially smaller than in the standard secondary-model case (Brunetti et al., 2009). Following Reimer et al. (2004), we adopt a simple approach to obtain an upper limit to the expected gamma ray emission from the Coma cluster: we

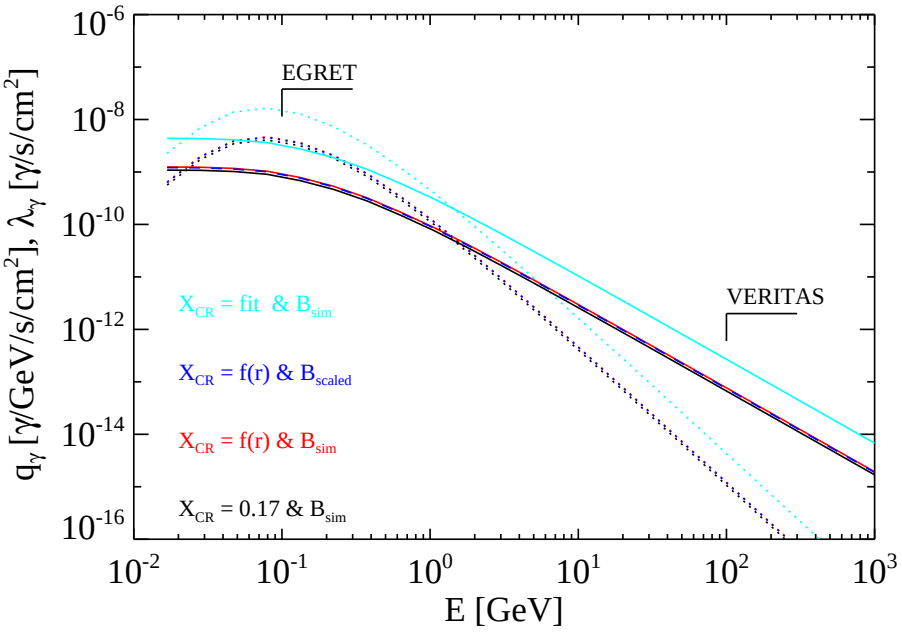

Figure 5.8: Expected γ-ray spectrum (dotted lines) for $E < 1$ TeV, from the simulated Coma cluster for the different models of CRp distribution (*Model1*: black, *Model2*: red, *Model3*: blue, *Model4*: light blue) and the integrated (solid lines) γ-ray spectrum (within $r < 1.3$ Mpc) with the current upper limits from EGRET and VERITAS (Reimer et al., 2003; Perkins, 2008), for limits at $E > 1$ TeV see The HESS Collaboration: F. A. Aharonian (2009).

limit the synchrotron emission produced through a standard secondary electron model to that measured at high frequencies, 4.85 GHz, and assume that the emission at lower frequencies is amplified by the effect of turbulent acceleration. Results are given in Table 5.1 that reports the upper γ-ray fluxes obtained in such scenario, that are about a factor 4 below those expected in the case of the hadronic model.

5.6 Conclusions

The hadronic model for the origin of radio haloes is based on the rate of secondary products generated through collisions between high energy CRp and thermal protons in the ICM, and present numerical simulations provide a way to compare model predictions with observations. Based on a constrained, cosmological MHD simulation of the local universe we investigated the predicted properties of the radio halo of the Coma cluster within the framework of the hadronic model. We follow four approaches, chosen to span the reasonable range suggested by theoretical and observational findings, and focusing on the case of high magnetic field values that represents the most favourable way for hadronic models.

Our main conclusions are:

- In agreement with previous findings, hadronic models may produce the synchrotron radio luminosity of the Coma halo with energy densities of CRp between 1–10% of the thermal ICM. However the radial brightness profile of the generated synchrotron emission is much steeper than seen in observations of the Coma halo, consequently the simulated radio halos come out much smaller than the observed one. This also leads to a slope in the thermal X–ray vs. radio brightness point-to-point correlation that is significantly steeper than the observed one.

- The observed flat radial brightness profile and the fairly large extent of the observed radio halo can only be obtained with hadronic models by strongly increasing the CRp energy density outside the core of the cluster. In this case, however, the resulting CRp energy density at $\approx$ 1Mpc (e.g. the rim of the observed radio halo) would equal (or exceed) that of the thermal ICM.

- Our simulated Coma cluster matches almost perfectly the observed SZ decrement. But this SZ decrement is still not enough to explain the spectral steepening observed in the spectrum of the radio halo at large frequencies; contrary to previous claims in literature.

In summary, we find that a purely hadronic model is disfavoured by current observations of the Coma cluster. In principle the energy problem might be alleviated if the magnetic field strength were almost constant with cluster radius up to the rim of the observed radio halo (see Pfrommer & Ensslin, 2004), however such models are not among the best-fitting ones inferred from present RM observations.

At the same time we have shown that hadronic models cannot explain the spectral steepening of the Coma radio halo: regardless of the model assumptions, an SZ effect matching observations produces a negligible SZ decrement at 2.7 and 5 GHz in the region of the halo.

The γ-ray flux generated by the hadronic interaction in case of *Model 4*, which alone roughly matches the radial profile of the halo, at least that measured at 1.4 GHz, is only a factor $\sim$6 below the current limits, thus incoming γ-ray observations will shortly provide additional constraints to the models.

Given the difficulties encompassed by the hadronic scenario to reproduce present observations of the Coma halo, we conclude that most of the radio emission we observe should originate from relativistic electrons accelerated by other mechanisms. One possibility is that electrons are re-accelerated in-situ by MHD turbulence within the ICM. It is well known that this scenario provides a unique way to explain the steepening of the radio spectrum of the halo at higher frequencies (Figure 7), yet in this case predictions of the gamma ray flux from the Coma cluster are more difficult (Brunetti et al., 2009). The presence of the spectral steepening at high frequency limits the contribution from secondary electrons that should produce a flatter spectral shape. Thus following Reimer et al.(2004), an upper limit to the gamma ray emission expected from the Coma cluster

may be estimated by requiring that the emission from secondaries does not outweigh the flux measured at 4.85 GHz. Such constrain leads to upper limits to the expected gamma rays about 4 times below the expectations in the case of pure hadronic models.

As a final comment we also stress that the energy requirements of CRp derived for hadronic models and the predicted gamma ray emission depend on the value of the magnetic field in the Coma cluster. As already stressed we assume relatively large values of B in the ICM, yet both the energy density of CRp and the gamma ray emission depend on:

$$\left\langle \frac{B^2 + B^2_{\rm cmb}}{B^{1+\alpha}} \right\rangle \tag{5.1}$$

where $< .. >$ indicates averaged quantities (weighted for $X_{\rm cr}\,\rho^2$) in the synchrotron emitting volume. Consequently, if the magnetic field outside the cluster core of the Coma cluster (where $B^2 < B^2_{\rm cmb}$, Figure 1) is $\sim 50\%$ smaller than that assumed, the CRp energy density and the expected gamma ray emission would result about 1.5–2 times larger.
This, combined with the fact that larger γ–ray fluxes are expected if the profile of the Coma halo at 330 MHz is adopted, implies that a non detection of the Coma cluster with FERMI after 1 year of observations would further strengthen our conclusions that disfavour purely hadronic models for the origin of the radio halo.

5.7 Acknowledgements

We would like to thank the referee for helpful comments on our paper. J.Donnert kindly acknowledges the support of ESF/Astrosim Exchange grant 2065 and thanks the INAF/IRA in Bologna for its hospitality. GB, RC and AB acknowledge partial support from PRIN-INAF2007 and ASI-INAF I/088/06/0.

Chapter 6

Radio Halos From Hadronic Models II: The Scaling Relations

J. Donnert, K. Dolag, R.Cassano, G. Brunetti

ABSTRACT

We use results from a constrained, cosmological MHD simulation of the Local Universe to predict radio halos and their evolution for a volume limited set of galaxy clusters and compare to current observations. The simulated magnetic field inside the clusters is a result of turbulent amplification within them, with the magnetic seed originating from star-burst driven, galactic outflows. We evaluate three models, where we choose different normalisations for the cosmic-ray proton population within clusters. Similar to our previous analysis of the Coma cluster (Donnert et al., 2010), the radial profile and the morphological properties of observed radio halos can not be reproduced, even with a radially increasing energy fraction within the cosmic-ray proton population. Scaling relations between X-ray luminosity and radio power can be reproduced by all models, however all models fail in the prediction of clusters with no radio emission. Also the evolutionary tracks of our largest clusters in all models fail to reproduce the observed bi-modality in radio luminosity. This provides additional evidence that the framework of hadronic, secondary models is disfavoured to reproduce the large scale diffuse radio emission. of galaxy clusters. We also provide predictions for the unavoidable emission of γ-rays from the hadronic models for the full cluster set. None of such secondary models is yet excluded by the observed limits in γ-ray emission, emphasising that large scale diffuse radio emission is a powerful tool to constrain the amount of cosmic-ray protons in galaxy clusters.

Accepted to MNRAS 18 May 2010; **Published** in volume 407, Sep 2010

6.1 Introduction

The thermal gas, that is the dominant component in the Inter-Galactic-Medium (IGM), is mixed with magnetic fields and relativistic particles, as proven by radio observations which detected Mpc-sized diffuse radio emission from the IGM, in the form of radio halos and relics (e.g. Feretti, 2003a; Ferrari et al., 2008). These Mpc-scale radio sources are found in a fraction of massive clusters with complex dynamics, which suggests a connection between non-thermal emission and cluster mergers (e.g. Buote, 2001; Venturi et al., 2008; Brunetti et al., 2009). Cluster mergers are the most energetic events in the universe and a fraction of the energy dissipated during these mergers may be channelled into the amplification of the magnetic fields (e.g. Dolag et al., 2002; Subramanian et al., 2006; Ryu et al., 2008) and into the acceleration of relativistic, primary, electrons and protons via shocks and turbulence (e.g. Ensslin et al., 1998; Sarazin, 1999b; Brunetti et al., 2001, 2004; Brunetti, 2004b; Petrosian, 2001; Gabici & Blasi, 2003; Ryu et al., 2003; Cassano & Brunetti, 2005; Pfrommer et al., 2006; Brunetti & Lazarian, 2007; Vazza et al., 2009).

Relativistic protons in the IGM have long life-times and remain confined within galaxy clusters for a Hubble time (e.g. Völk et al., 1996; Berezinsky et al., 1997). As a consequence they are expected to be the dominant non-thermal particle component. Collisions between these relativistic protons and the thermal protons in the IGM generate secondary particles that combined with the primary relativistic particles are expected to produce a complex emission spectrum from radio to γ-rays (e.g. Blasi, 2001; Brunetti, 2009). Only upper limits to the γ-ray emission from galaxy clusters have been obtained so far (Reimer et al., 2003; Perkins & the VERITAS Collaboration, 2006; Aharonian, 2009b,a; The MAGIC Collaboration & Aleksić, 2009) however the FERMI Gamma-ray telescope will shortly allow a step forward, having a chance to obtain first detections of galaxy clusters or to put stringent constraints on the energy density of the relativistic protons. Most importantly, in a few years the Low Frequency Array (LOFAR) and the Long Wavelength Array (LWA) will observe galaxy clusters at low radio frequencies with the potential to discover the bulk of the cluster-scale synchrotron emission in the Universe (e.g. Ensslin & Röttgering, 2002; Cassano et al., 2006).

The emerging theoretical picture is very complex and modern numerical simulations provide an efficient way to obtain detailed models of non thermal emission from galaxy clusters to compare with present and future observations. Advances in this respect have been recently obtained by including aspects of cosmic-ray physics into cosmological Lagrangian hydrodynamical simulations mostly focussing on the acceleration of relativistic particles at shocks and on the relative production of secondary electrons (e.g. Pfrommer et al., 2008). In this work we investigate the non-thermal emission from secondary particles in galaxy clusters extracted from cosmological Lagrangian MHD simulations and, most important for the first time, we report on an adequate comparison between our expectations and observations.

6.2 Simulations

The simulation was done using the cosmological simulation code GADGET-2 (Springel, 2005) with a treatment for magnetic fields. It features an entropy conserving formulation of Smooth Particle Hydrodynamics (SPH) (Springel & Hernquist, 2002), which is supplemented with the formulation of ideal MHD presented in Dolag & Stasyszyn (2009). The implementation follows the induction equation and computes the back reaction of the magnetic field using a symmetric formulation of the Lorentz force. We used a divergence cleaning scheme presented in Børve et al. (2001), which reduces numerical noise in shocks by subtracting the magnetic force which is proportional to the divergence of the field. It also helps to suppress the clumping instability particle based MHD codes encounter in regions with small plasma β (i.e. where magnetic pressure considerably exceeds thermal pressure).

In non radiative simulations like ours, regions with small plasma β are rare. Only the strong shocks in cores of galaxy clusters during major mergers produce enough compression to amplify the field to become dynamically dominant. These mergers are relatively brief events and are handled more accurately with our new numerical treatment (see Dolag & Stasyszyn, 2009, for details).
Borgani et al. (2006) have shown that non radiative simulations over predict the gas density in cores of galaxy clusters. This affects our simulation as well and can be seen in density and magnetic field profiles as well as in X-ray luminosities. As cosmological MHD SPH simulations lack physical dissipation, radiative SPH MHD simulations are not feasible at the moment. On the other hand secondary models have difficulties reproducing the outer parts of radio haloes correctly. Therefore our main focus lies on these regions, where the simulations are not affected by the overpredicted gas density.

6.2.1 Initial Conditions

We used a constrained realisation of the local universe (see Dolag et al. (2005) and references therein). The initial conditions are similar to those used in Mathis et al. (2002) to study the formation of the local galaxy population. They were obtained based on the IRAS 1.2-Jy galaxy survey. Its density field was smoothed on a scale of 7 Mpc, evolved back in time to $z = 50$ using the Zeldovich approximation and assumed to be Gaussian (Hoffman & Ribak, 1991). The IRAS observations constrain a volume of ≈ 115 Mpc centred on the Milky Way. It was sampled with dark matter particles and embedded in a periodic box of ≈ 343 Mpc comoving. Outside of the inner region, the box is filled with dark matter particles with 6 times the mass (i.e. 1/6th of the resolution), to cover for long range gravitational tidal forces arising from the low-frequency constrains.
In the evolved density field, many locally observed galaxy clusters can be identified by position and mass. Especially the Coma cluster (see Donnert et al., 2010) shows remarkable similarities in morphology. A fly-through of the simulation can be downloaded from the

MPA Website[1].
The initial conditions were extended to include gas by splitting dark matter particles in the high resolution region into gas and dark matter particles of masses 0.69×10^9 $M_\odot$ and 4.4×10^9 $M_\odot$ respectively. Therefore the biggest clusters are resolved by about a million particles. The gravitational softening length was set to 10 kpc. This is comparable to the inter-particle separation found in the centre of the largest clusters.

6.2.2 Magnetic Fields from Galactic Outflows

The origins of magnetic fields in galaxy clusters are still under debate. It is assumed that some kind of early seed magnetic field is amplified by structure formation through adiabatic compression, turbulence and shear flows to values observed today ($\approx 1 - 10\,\mu$G in clusters). Three main classes of models for the seed field exist: At first the seed fields can be created in shocks through the "Biermann battery " (Kulsrud et al., 1997; Ryu et al., 1998; Miniati et al., 2001). A second class of models invokes primordial processes to predict seed fields that fill the entire volume of the universe. The coherence length of these fields strongly depends on the details of the model (see Grasso & Rubinstein, 2001, for a review). Finally the seed can be produced by AGN (Ensslin et al., 1997; Furlanetto & Loeb, 2001) or starbursting galaxies (Völk & Atoyan, 2000) at high redshift ($z \approx 4 - 6$), whose outflows contaminate the proto-cluster region.

Cosmological simulations using SPH (Dolag et al., 1999, 2002, 2005) and grid based Adaptive Mesh Refinement (AMR) codes (Brüggen et al., 2005; Dubois & Teyssier, 2008; Li et al., 2008) were able to show that observed Faraday rotations are compatible with a cosmological seed field of $\approx 10^{-11}$ G. They also suggest that spatial distribution and structure of cluster magnetic fields are determined by the dynamics in the velocity field caused by structure formation (Dolag et al., 1999, 2002).

For this work we follow Donnert et al. (2009) in terms of magnetic field origin. They use a semi analytic model for galactic winds (Bertone et al., 2006) to seed magnetic fields in a constrained cosmological MHD SPH simulation. The continuous seeding process is approximated with an instantaneous seed at $z \approx 4$. As they were able to show, the main properties of magnetic fields obtained in clusters were not influenced by that approximation.

The wind model used assumes adiabatic expansion of a spherical gas bubble with homogeneous magnetic energy density around every galaxy below a certain mass threshold. The magnetic bubble can be characterised by radius and field strength. The galaxy injects gas into the bubble carrying frozen-in magnetic field from the disc into the bubble over the star-burst timescale. Its final size is determined by the wind velocity, which is a function of the star formation rate and the properties of the ISM. Bertone et al. (2006) give an evolution equation for the magnetic energy in the bubble depending on the star-burst timescale. The energy is converted into a dipole moment and seeded once at a chosen redshift. The magnetic field is then amplified by structure formation to μG level. For details on the

[1] http://www.mpa-garching.mpg.de/galform/data_vis/index.shtml#movie12

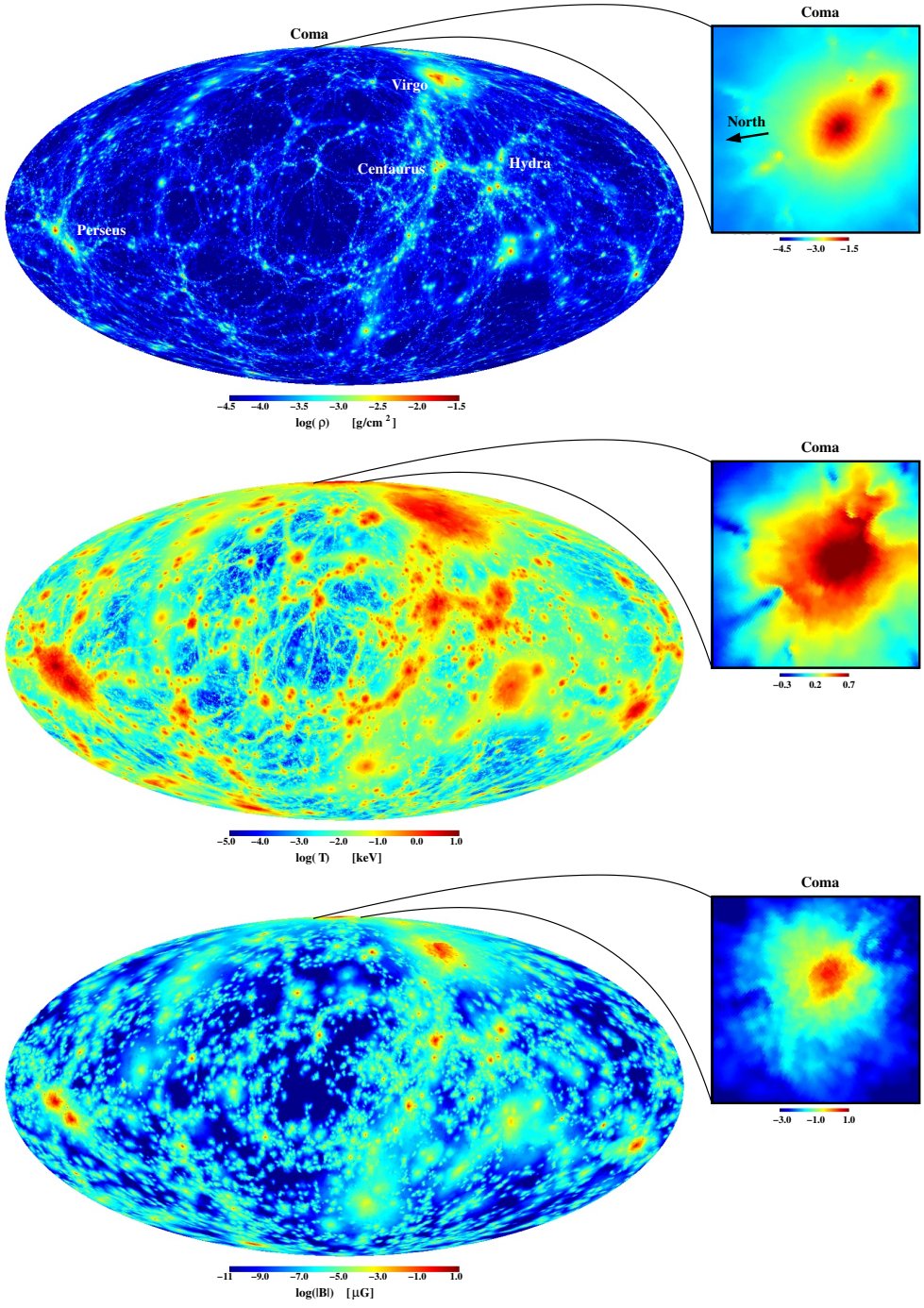

Figure 6.1: Full sky maps of the simulation in galactic coordinates. From top to bottom, electron density, temperature and magnetic field, projected through the whole box. The inlay shows a zoom onto a 3×3 degree region around the Coma cluster, respectively. In the upper most map, the most prominent clusters of the local universe are labelled and the arrow in the inlay points towards north.

Parameter	Value	Source
R_0	400 pc	(Klein et al., 1988)
B_0	$5\,\mu$G	(Donnert et al., 2009)
$B_{\rm G}$	$3\,\mu$G	(Donnert et al., 2009)
$\dot{M}_\star$	$10\,{\rm M}_\odot/{\rm yr}$	(de Grijs, 2001)
$t_{\rm sb}$	150 Myr	(de Grijs, 2001)
$M_{\rm ISM}$	$< 300 \times 10^{12}{\rm M}_\odot$	from simulation

Table 6.1: Summary of the parameters used for the wind model. This corresponds to the *0.1 Dipole* simulation in (Donnert et al., 2009), which fits best to observations of Faraday rotation.

wind model refer to Bertone et al. (2006); Donnert et al. (2009). Figure 6.1 shows full sky maps produced from the simulation, projecting the electron density, temperature and the magnetic field. The magnetic field closely follows the density distribution. The magnetic field is more patchy in the filaments compared to a cosmological seed because the seeding by individual galaxies does not overlap.

The simulation used in this work is based on the *0.1 Dipole* parameter set from Donnert et al. (2009), shown in table 6.1. It represents the best fit to observations of Faraday rotation presented in Donnert et al. (2009). There the parameter space was explored based on observations from the wind in M82. It was demonstrated that the resulting magnetic field does not critically depend on the exact choice of the parameters.

6.3 Modelling Hadronic Secondary Electrons in Clusters

In secondary models proposed for the origin of radio halos (Dennison, 1980; Blasi & Colafrancesco, 1999), the emitting cosmic-ray electrons (CRe) are a product of cosmic-ray proton collisions (CRp) with thermal protons in the cluster. Possible mechanisms for the injection of CRp in the IGM include shock waves caused by cluster accretion and mergers (e.g. Gabici & Blasi, 2003; Ryu et al., 2003; Pfrommer et al., 2006; Vazza et al., 2009) outflows from radio galaxies (AGN) (e.g. Ensslin et al., 1998; Rachen, 2008) and supernova driven winds (Völk et al., 1996). The resulting CRp spectrum from these theoretical scenarios is a power law in particle momentum (e.g. Schlickeiser, 2002), that is also consistent with observations of galactic cosmic-rays. We assume a power law spectrum of CRp in the IGM and calculate the spectrum of high-energy secondary electrons under stationary conditions by considering only synchrotron and inverse Compton losses and by neglecting re-acceleration processes in the IGM (Section 6.3.1). Throughout the first two of our models, we use the magnetic fields obtained from the constrained cosmological simulation described in section 6.2.2. In a third model we increased the magnetic field, especially at larger distances to the centre, by up-scaling the magnetic field in our simulation to be $B \propto \sqrt{\rho}$, which allows for better comparison with results obtained in previous literature,

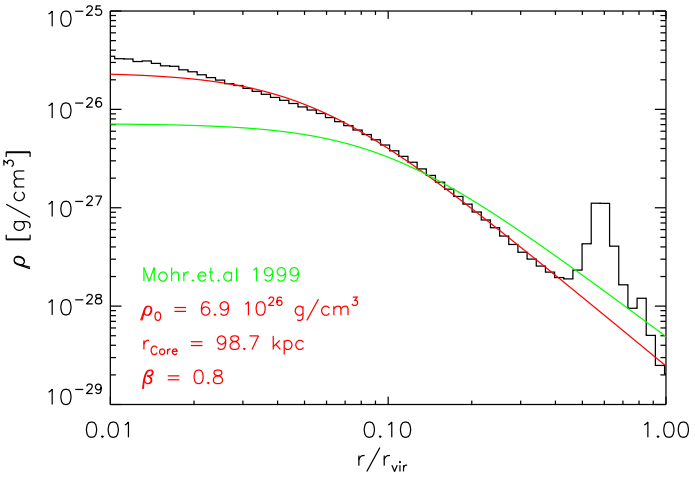

Figure 6.2: Radial profile of the density in our simulated Coma cluster. In red we plot the best fit beta model ($\rho_0 = 6.4 \times 10^{15}, \beta = 0.8, r_{\rm core} = 0.06$), excluding the density bump at 0.6 $R_{\rm vir}$. A fit to observations of Coma by Mohr et al. (1999) is shown in green. Due to the non-radiativity of our simulation the gas density is overestimated by a factor of 5 in the centre

as there such a relation is often used (as for example in Pfrommer et al. (2008)).

6.3.1 Synchrotron Emission from Secondary Models

We consider a spectral distribution of the population of relativistic CRp described by a power law in energy $E_{\rm p}$:

$$N(E_{\rm p}) = K_{\rm p} E_{\rm p}^{-\alpha_{\rm p}} \, ; \tag{6.1}$$

if not stated otherwise, we use a spectral index $\alpha_{\rm p} = 2.6$. The normalisation $K_{\rm p}$ is model dependent and is defined in the next Sections.

The main channel of hadronic interaction between the CR protons and the ambient medium is multi-pion production (Blasi & Colafrancesco, 1999):

$$\begin{aligned} p_{\rm CR} + p_{\rm th} &\Rightarrow \pi^0 + \pi^+ + \pi^- + \text{anything} \\ \pi^{\pm} &\Rightarrow \mu + \nu_{\mu} \\ \mu^{\pm} &\Rightarrow e^{\pm} + \nu_{\mu} + \nu_e \\ \pi^0 &\Rightarrow 2\gamma \end{aligned}$$

In this case the injection spectral rate of secondary $e^{\pm}$ is (e.g. Brunetti & Blasi, 2005):

$$Q_e(E) = \int_{E_\pi} Q_\pi(E_\pi) dE_\pi \times \\ \times \int dE_\mu F_e^{\pm}(E_\pi, E_\mu, E_e) F_\mu(E_\mu, E_\pi), \tag{6.2}$$

where $F_e^{\pm}(E_e, E_\mu, E_\pi)$ is the spectrum of electrons and positrons from the decay of a muon of energy E_μ produced in the decay of a pion with energy E_π (taken from Blasi & Colafrancesco (1999), $F_\mu(E_\mu, E_\pi)$ is the muon spectrum generated by the decay of a pion of energy E_π (e.g. Moskalenko & Strong, 1998), and the pion injection rate due to p-p collisions is (e.g. Dermer, 1986; Blasi & Colafrancesco, 1999; Brunetti & Blasi, 2005):

$$Q_\pi(E_\pi) = n_{th} c \int dE_p N(E_p) \beta_p F_\pi(E_\pi, E_p) \times \\ \times \sigma_{pp}(E_p) \sqrt{1 - (\frac{m_p c^2}{E_p})^2}, \tag{6.3}$$

where n_{th} is the number density of thermal protons, σ_{pp} is the p-p cross-section, and F_π is the spectrum of pions from the collision between a CRp of energy E_p and thermal protons (e.g. Moskalenko & Strong, 1998; Blasi & Colafrancesco, 1999; Brunetti & Blasi, 2005).
The observed synchrotron emission in radio halos at frequencies of $\approx$ GHz requires energies of the secondary particles of several GeV, considering field strengths of $\approx \mu$G typical of the IGM (e.g. Carilli & Taylor, 2002). In this case a scaling model is appropriate to describe the pion-spectrum from p-p collisions, and we calculate $Q_e(E)$ from Eqs. 6.2–6.3 following Brunetti & Blasi (2005) and using a pion-spectrum:

$$F_\pi(E_\pi) = \frac{1}{2E_\pi} \left[c_1 (1 - \frac{E_\pi}{E_p})^{3.5} + c_2 \exp(-18 \frac{E_\pi}{E_p}) \right] \tag{6.4}$$

where c_1=1.22 and c_2=0.92 (Berezinskii & Kudriavtsev, 1990).
The resulting electron source function can be approximated by:

$$Q_{e^\pm}(E) = c\, n_{\rm th} K_{\rm p} E^{-\alpha_{\rm p}} f(E, \alpha_{\rm p}) \tag{6.5}$$

where $f(E, \alpha_{\rm p})$ accounts for the log–scaling of the p-p cross–section at high energies and causes the spectral shape to be slightly flatter than $E^{-\alpha_{\rm p}}$; an analytical expression for the asymptotic form of f (for $E_\mu >> m_\mu c^2$, $E_\pi >> m_\pi c^2$, $E_p >> m_p c^2$) is derived in Brunetti & Blasi (2005).

The steady state spectrum of high energy electrons in the IGM is given by (e.g. Dolag & Ensslin, 2000):

$$N_{\rm e}(E) \;\; = \;\; \left| \dot{E}(E) \right|^{-1} \int_E^\infty dE'\, Q_{e^\pm}(E') \tag{6.6}$$

where the relevant cooling processes involve synchrotron and inverse Compton losses:

$$\dot{E}(E) = -\frac{4\sigma_{\rm T}c}{3m_{\rm e}^2c^4}\left(\frac{B^2}{8\pi}+\frac{B_{\rm CMB}^2}{8\pi}\right)E^2, \tag{6.7}$$

B is the local magnetic field strength and $B_{\rm CMB}^2/8\pi$ gives the energy density of the CMB expressed as an equivalent magnetic field.
We calculate the electron spectrum from Eqs. 6.2–6.4 and 6.6–6.7; this can be approximated by :

$$N_{\rm e}(E) = \frac{6\pi m_e^2c^4}{\sigma_T} n_{th} K_p E^{-(1+\alpha_{\rm p})} \frac{g(E,\alpha_{\rm p})}{B^2+B_{\rm CMB}^2} \tag{6.8}$$

where g is related to f in Eq. 6.5 via:

$$\begin{aligned} g(E,\alpha_{\rm p}) &= \frac{1}{E^{1-\alpha_{\rm p}}}\int_E dX X^{-\alpha_{\rm p}} f(X,\alpha_{\rm p}) \\ &\propto E^{\Delta} \end{aligned} \tag{6.9}$$

and $\Delta \approx 0.2$ for $E \approx$ few GeV.
The radio emissivity is:

$$j_\nu = \frac{\sqrt{3}e^3B}{m_{\rm e}c^2}\int_{E_{\rm min}}^{E_{\rm max}}\int_0^{\frac{\pi}{2}} {\rm d}E_{\rm e}{\rm d}\theta\, \sin^2\theta F\left(\frac{\nu}{\nu_c}\right) N_{\rm e}(E) \tag{6.10}$$

where $\nu_{\rm c} = (3/4\pi)p^2eB\sin\theta/(mc)^3$ is the critical frequency and F the integral over the synchrotron kernel:

$$F(x) = x\int_x^\infty K_{\frac{5}{3}}(\xi)\,{\rm d}\xi. \tag{6.11}$$

Here $K_{\frac{5}{3}}$ denotes the modified Bessel function of order 5/3.
For a power law spectrum of CRp, $N_p(E_p) \propto E_p^{-\alpha_{\rm p}}$, the resulting synchrotron emission from secondary electrons is $j_\nu \propto \nu^{-(\alpha_{\rm p}-\Delta)/2}$.

6.3.2 γ-rays from Hadronic Interactions

As already mentioned before, CRp - proton collisions produce neutral pions, which in turn decay to 2 photons. γ-rays are a direct measure of the CRp and provide a complementary constraint to the injection process of secondary electrons.
In order to allow for a prompt comparison with recent results we follow the formalism described in Pfrommer & Ensslin (2004) to estimate the γ-ray flux from CR in our simulations.

The γ-ray source function is:

$$q_\gamma(E_\gamma) \approx \frac{2^{4-\alpha_\gamma}}{3\alpha_\gamma}\frac{\sigma_{\rm pp} c n_{\rm th} K_p}{\alpha_{\rm p}-1}(E_{\rm p,min})^{-\alpha_{\rm p}}\frac{E_{\rm p,min}}{\rm GeV}\times \\ \times\left(\frac{m_{\pi^0}c^2}{\rm GeV}\right)^{\alpha_\gamma}\left[\left(\frac{2E_\gamma}{m_{\pi^0}c^2}\right)^{\delta_\gamma}+\left(\frac{2E_\gamma}{m_{\pi^0}c^2}\right)^{-\delta_\gamma}\right]^{-\alpha_\gamma/\delta_\gamma} \quad (6.12)$$

where $\alpha_\gamma \simeq \alpha_{\rm p}$ is the asymptotic slope of the γ-ray spectrum, which resembles the slope of the proton spectrum (Dermer, 1986). The shape parameter, which describes the semi-analytic model near the pion threshold, is $\delta_\gamma = 0.14\alpha_\gamma^{-1.6} + 0.44$ by using an effective cross-section $\sigma_{\rm PP} = 32 \times (0.96 + \exp(4.4 - 2.4\alpha_\gamma))$ mbarn. The integrated γ-ray source density λ_γ is then obtained by integrating the source function over energy (Pfrommer & Ensslin, 2004):

$$\lambda_\gamma = \int_{E_1}^{E_2} {\rm d}E_\gamma q_\gamma(E_\gamma) \\ = \frac{\sigma_{\rm pp} m_\pi c^3}{3\alpha_\gamma\delta_\gamma}\frac{n_{\rm th}K_{\rm p}}{\alpha_{\rm p}-1}\frac{(E_{\rm p,min})^{-\alpha_{\rm p}}}{2^{\alpha_\gamma-1}}\frac{E_{\rm p,min}}{\rm GeV}\left(\frac{m_{\pi_0}c^2}{\rm GeV}\right)^{-\alpha_\gamma}\times \\ \times\left[\mathcal{B}_{\rm x}\left(\frac{\alpha_\gamma+1}{2\delta_\gamma},\frac{\alpha_\gamma-1}{2\delta_\gamma}\right)\right]_{x_2}^{x_1} \quad (6.13)$$

where $\mathcal{B}_{\rm x}(a,b)$ denotes the incomplete beta-function and $[f(x)]_b^a = f(a) - f(b)$.

6.3.3 The Three Models

To investigate the dependence of the predicted properties of non thermal emission of clusters on the underlying assumptions, we investigate 3 models for the distribution of magnetic fields and cosmic-rays in clusters. They are chosen to encompass the reasonable range suggested by theoretical and observational findings.
We keep the spectral index fixed to $\alpha_{\rm p} = 2.6$ in order to be able to match the typical spectrum of giant radio halos, $\alpha \sim 1.2 - 1.3$ (e.g. Ferrari et al., 2008), although a fraction of presently known halos has a steeper spectrum (e.g. Brunetti et al., 2008; Giovannini et al., 2009; Macario et al., 2010b). Also, a spectral index $\alpha_{\rm p} = 2.6$ allows to fit the spectral shape of the Coma halo at $\nu \leq 1.4$ GHz, although also in this case the spectrum steepens at higher frequencies (e.g. Thierbach et al., 2003; Donnert et al., 2010).

Model 1: Constant $X_{\rm CR}$

In our first model the energy density of the CR protons is taken as a constant fraction of the thermal energy density. This is reasonable if a constant fraction of the energy that is channelled into the IGM to heat the gas goes into the acceleration of CRp.

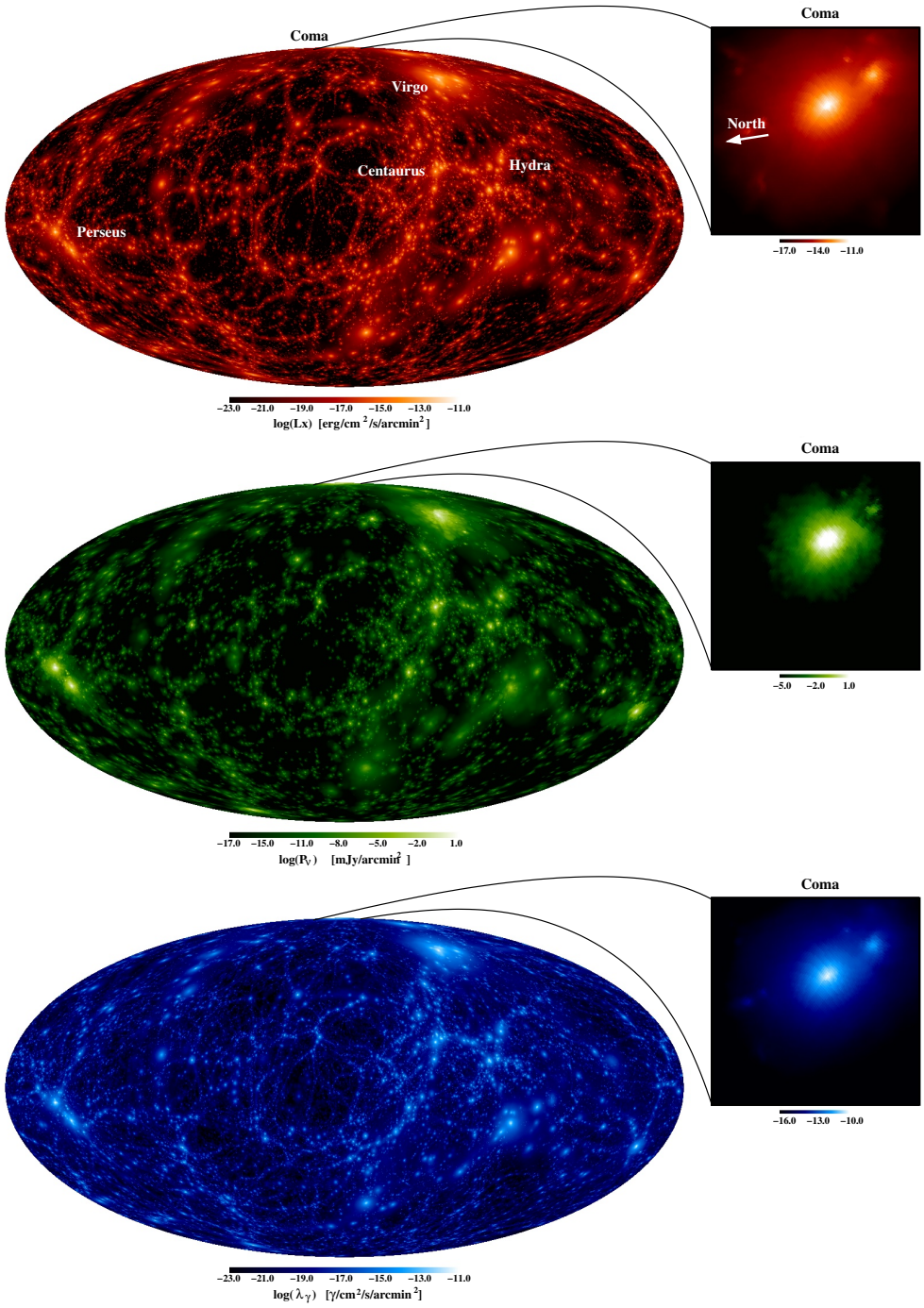

Figure 6.3: Full sky maps of the simulation in galactic coordinates. From top to bottom, X-ray, radio and γ-ray surface brightness are shown. For the radio and γ-ray emission the model with the constant cosmic-ray energy fraction was chosen. The γ-ray emission is evaluated for VERITAS (e.g. $E > 100\,GeV$). The inlay shows a zoom onto a 3×3 degree region around the Coma cluster. In the upper most map, the most prominent clusters of the local universe are labelled and the arrow in the inlay points towards north.

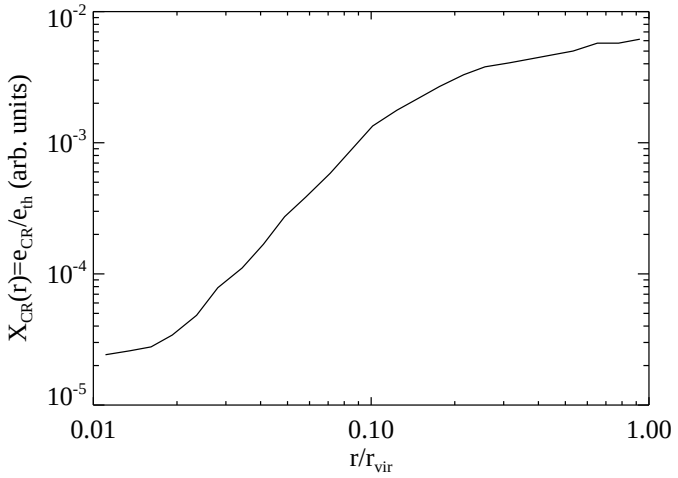

Figure 6.4: Energy in cosmic-ray protons relative to thermal energy over cluster radius, inferred from Pfrommer et al. (2007). The dependence was derived assuming a linear relation between pressure and energy density.

Therefore, in this model, the normalisation K_p is chosen to have a constant fraction, $X_\mathrm{p} = \mathrm{const}$, of kinetic CRp energy density ϵ_p to thermal energy density ϵ_th of the IGM:

$$\epsilon_\mathrm{p} = X_\mathrm{p}\,\epsilon_\mathrm{th} \tag{6.14}$$

$$= \frac{K_\mathrm{p}}{\alpha_\mathrm{p}-2}\,(E_\mathrm{p,min})^{2-\alpha_\mathrm{p}} \tag{6.15}$$

For the magnetic field distribution within the IGM we take directly the magnetic field extracted from the simulations.

Model 2: Varying $X_\mathrm{CR}(r)$

In a second model we adopt a radius dependent cosmic-ray energy density fraction, $X_\mathrm{CR}(r)$, as obtained from simulations of CR acceleration in structure formation shocks by Pfrommer et al. (2007). We also assume a constant CRp spectral index over the whole cluster volume, $\alpha_\mathrm{p} = 2.6$.

Pfrommer et al. (2008) simulated the injection of CR protons by merger shocks during structure formation. They find that cosmic-ray pressure increases relative to thermal pressure with increasing distance to the cluster centre. Assuming an ideal gas this directly translates into a radially increasing cosmic-ray energy density fraction $X_\mathrm{CR}(r) = \epsilon_\mathrm{th}/\epsilon_\mathrm{p}$. We use these results to infer a radially varying normalisation, so that Eq. 6.14 becomes:

$$\epsilon_\mathrm{p}(\mathbf{r}) = X_\mathrm{p}(r)\,\epsilon_\mathrm{th}(\mathbf{r}) \tag{6.16}$$

$$= \frac{K_\mathrm{p}(r)}{\alpha_\mathrm{p}-2}\,(E_\mathrm{p,min})^{2-\alpha_\mathrm{p}}\,. \tag{6.17}$$

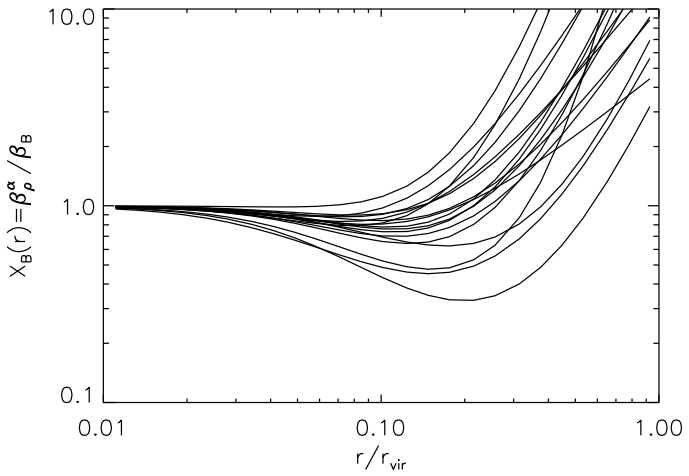

Figure 6.5: Scaling functions $f_{\rm scal}(r)$ of all clusters. It modifies the magnetic field globally, so that its magnetic energy scales linear with thermal energy.

Figure 6.4 shows the radial dependence of the fraction used in agreement with the average over two cool core clusters, as shown in Pfrommer et al. (2008). The fraction increases by more than 2 orders of magnitude in the cluster external regions. This is expected to increase the extension of the diffuse radio emission generated by secondary electrons with respect to model 1. For the magnetic field distribution within the IGM we again use the magnetic field extracted from the simulations.

Model 3: Scaling $B \propto \sqrt{\rho}$

In our third model we modify the magnetic field originally obtained from the cosmological simulations.

The main reason for this is that the magnetic energy density, $\epsilon_{\rm B,0}$, of the IGM is often modelled to follow thermal energy density, $\epsilon_{\rm th}$, which implies $B \propto \sqrt{\rho}$. In contrast to that we find $B \propto \rho$ in the outer regions of our simulated clusters. To allow a comparison with models that assume $B \propto \sqrt{\rho}$, we construct in our third model a function $f_{\rm scal}(r)$ which scales the simulated magnetic field to follow $B \propto \sqrt{\rho}$ globally. This allows us to alter the dependence of the field with thermal density without loosing its inherent structure which is a result of our simulations.

To construct the scaling function, we fit beta models $n_\beta = n_0(1 + r^2/r^2_{\rm core})^{3\beta/2}$ to spherically averaged density and magnetic field profiles. The scaling function is then:

$$f_{\rm scal}(r) \;=\; \frac{\left(\rho_0(1 + r^2/r^2_{\rm core,\rho})^{3/2\beta_\rho}\right)^{1/2}}{B_0(1 + r^2/r^2_{\rm core,B})^{3/2\beta_{\rm B}}} \tag{6.18}$$

and is shown in figure 6.5 for every cluster in the sample. This changes the field strength

at $r > 0.2R_{vir}$ without strongly affecting the field in the innermost regions.

For the cosmic-ray distribution in this model, $X_{\rm p}(r)$, we use the same radially dependent profile as in our model 2.

6.4 Application to the Cluster Sample

Having the diffuse synchrotron emission from secondary electrons in our simulated clusters under control, the aim of this Section is to compare the simulated properties with the most relevant observational properties of radio halos.
We use an unprecedented sample of fairly-massive simulated clusters made by the 16 most massive objects extracted from our simulations. This allows for a statistical comparison with the main observational properties of radio halos obtained from studies of volume limited samples of radio halos in galaxy clusters. In addition our sample (as well as the observational samples) contains the Coma cluster, so that we can calibrate K_p in all our models to match the observed radio luminosity of the Coma halo where needed.

6.4.1 The Magnetic Field in our Cluster Set

The magnetic field obtained for our simulated Coma cluster is consistent with the one inferred from modelling Faraday Rotation Measures of the Coma cluster, as shown in (Donnert et al., 2010).
To compare the "statistical" properties of the magnetic field in the complete set of simulated clusters with observations and to show the effect of re-scaling the field (model 3), we plot in figure 6.6 radial profiles of Faraday Rotation. Here we bin all clusters with gas mass $M > 3 \times 10^{14}\, M_{\odot}$ in radius and take the median in each bin. In green we plot the field profile from simulations, and in red the scaled field profile (model 3). To compare we over-plot observations of a sample of Abell clusters from Kim et al. (1991); Clarke et al. (2001), observations of A119 from Feretti et al. (1999) and observations of the Coma cluster (Feretti et al., 1995). Because of the small number of points, the error from the Abell clusters was estimated using a bootstrapping technique. For every bin we generate several samples, by selecting every data point a random number of times and computing the median of this subsample. We then compute the standard deviation of all samples to get an estimate of the error in each bin.

6.4.2 Radial Profile of the Radio Emission

Since both the target thermal-protons and the expected magnetic field strength in the IGM decrease with distance from the cluster centre, most of the synchrotron luminosity emitted by secondary electrons should be produced in the cluster-core region. This causes the radial profile of secondary-generated radio halos to be substantially steeper than those of the observed halos (e.g. Brunetti, 2004b), although formally this discrepancy may be

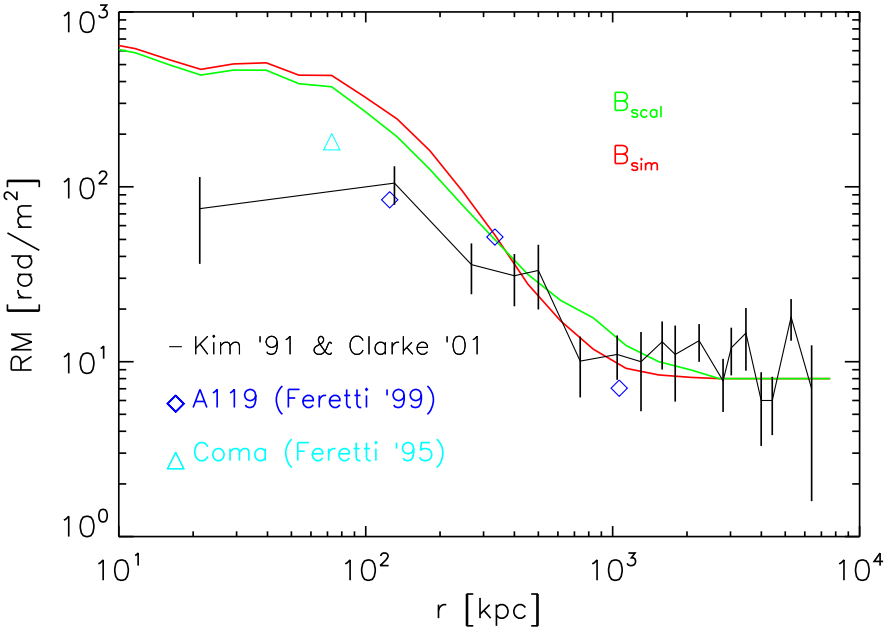

Figure 6.6: Faraday rotation over radius for a mass selected subsample of our simulated clusters. Shown are the original (green) and upscaled (red) median over the whole sample in every radial bin. We also plot observations from Coma (turquoise), A119 (blue) and a sample of Abell clusters (black) (Kim et al., 1991; Clarke et al., 2001; Feretti et al., 1995, 1999). The errors in Abell cluster sample were estimated using a bootstrapping technique (see text).

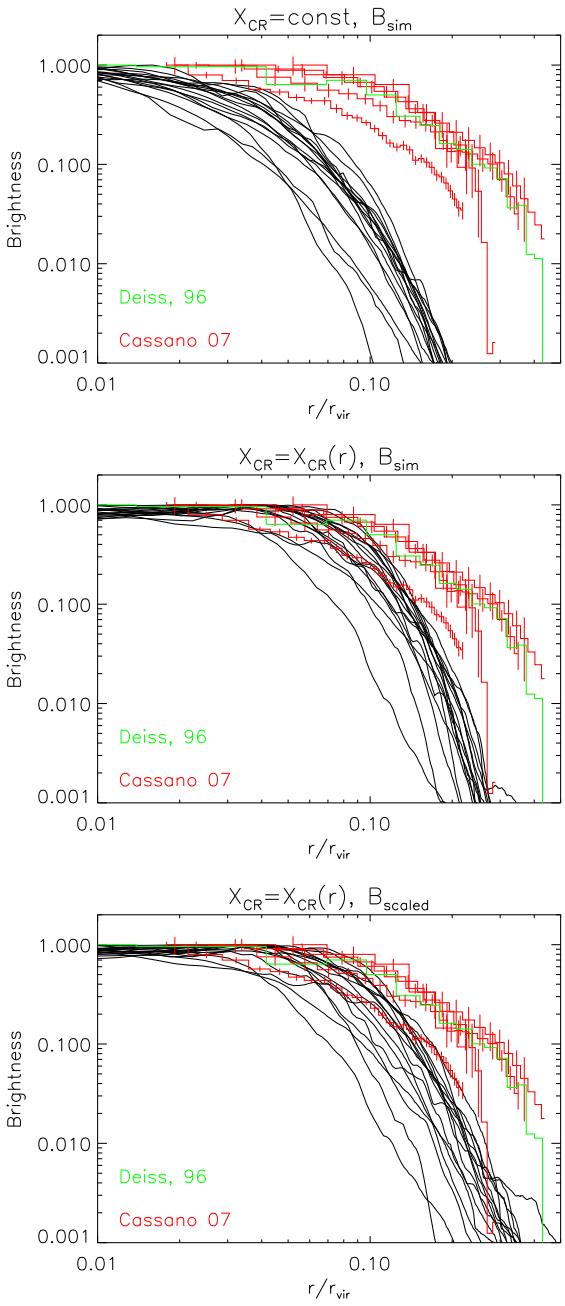

Figure 6.7: Normalised radial profiles of radio emission from 17 simulated clusters (black). In the left panel the CRe population was modelled using a constant $X_{\rm P}$. The middle one uses the radius dependent CR to thermal energy fraction (fig. 6.4) adopted from Pfrommer et al. (2008). Additionally we modified (fig. 6.5) the magnetic field in the right panel to be $\propto \sqrt{\rho}$ (right panel). We add observations of A2744, A2319, A545, A2163 and A2255 from (Cassano et al., 2007) as red curves with error bars, Coma (green) is taken from Deiss et al. (1997).

alleviated by assuming that both the magnetic field and CRp have flat spatial distributions (Pfrommer & Ensslin, 2004).

Cassano et al. (2007) report radial profiles of the radio emission of 5 well studied radio halos. We convolve our synthetic radio maps with a Gaussian using the typical beam size (43 kpc) of the observations, and in figure 6.7 compare these profiles with the observed ones. Both simulated and observed profiles were normalised to one. We also include the radial profile of the Coma halo from Deiss et al. (1997).

In all cases (models 1–3), Figure 6.7 shows that the radial profiles of the secondary-generated radio halos in our simulated clusters are considerably steeper than the observed ones. In agreement with Brunetti et al. (2004), by assuming a constant $X_{\rm P}$ (first panel), the simulated radio emission (black) for $r \geq 0.15 R_{\rm vir}$ is about 100 times below that measured in real radio halos (red, green).

By allowing $X_{\rm P}$ to increase with radius as in 6.3.3 results in an increase of the simulated emission for larger radii (figure 6.7, middle panel), but still expectations account for $< 10\%$ of the observed emission in real radio halos at $r \geq 0.15 R_{\rm vir}$. Additional up-scaling of the magnetic field (model 3) further increases the size of the simulated halos, especially at very large distances from the cluster centre, where our MHD simulations would predict a steeper scaling of the magnetic field with gas density. However this up-scaling only mildly increases the level of the expected emission at intermediate distances, $r \approx 0.1 - 0.3 R_{\rm vir}$, where the radio brightness of radio halos is constrained by present observations.

In a recent paper Pfrommer et al. (2008) claim that, according to cosmological simulations, the combined synchrotron emission from secondary electrons and primary electrons accelerated at large scale shocks may produce diffuse emission with a fairly broad spatial distribution. Based on our results, the contribution from primary electrons (even assuming Pfrommer et al. (2008) results[2]) is not expected to solve the discrepancy between models and observations in Fig.6.7. Indeed, our model 3 is thought to mimic the secondary-generated emission in Pfrommer et al. (2008) and, based on their Figure 9, the contributions from primary electrons at $r \approx 0.2 R_{\rm vir}$ is (at best) comparable with that of the secondary electrons leaving expectations well below observations[3].

In principle, for each cluster, it would be possible to allow the energy density of CRp to further increase at large distances from the cluster centre and find an *ad hoc* spatial distribution of CRp that allows for matching the brightness profiles of radio halos. However this would imply the untenable scenario in which CRp store very large energy budget outside the cluster core, for example in the case of the Coma halo the energy density of CRp at $r \approx 0.2 - 0.3 R_{\rm vir}$ should be comparable to that of the thermal ICM (Donnert et al., 2010).

[2] Which are based on the optimistic assumption that 10 percent of the energy of shock accelerated particles are channelled into CR electrons.

[3] it is more difficult to evaluate the ratio of secondary to primary electrons at $r \approx 0.3\, R_{\rm vir}$ from Figure 9 in Pfrommer et al. due to the presence of a very bright shock-like spot southest of the centre of their simulated cluster (see their Figures 7 and 8) that affects the azimuthal brightness profile, but that is not indicative of an upturn in the distribution of the truly diffuse halo-emission

Cluster	M1	M2	M3
0	1.09	1.04	0.87
PERSEUS	1.33	1.10	0.90
COMA	1.54	1.18	0.98
4	1.21	1.01	0.94

Table 6.2: Slopes of the Radio vers. X-ray surface brightness correlation from patches for our three models and the four largest clusters. Govoni et al. (2001); Feretti et al. (2001) find slopes of Coma & A2163: b=0.64, A2391: b=0.98 and, A2255: b=0.82

6.4.3 Morphology of the Radio Emission

A complementary approach to compare expectations from simulations with observations is to derive a point-to-point plot between radio and X-ray brightness. A number of clusters indeed show morphological correlations between X-ray and radio surface brightness (Govoni et al., 2001). This provides a complementary approach to the comparison of the radial profiles and is not affected by the morphological asymmetries and possible imperfect alignment of the emission centres (Govoni et al., 2001). In Figure 6.8 we show the luminosity in $(166\,\mathrm{kpc})^2$ sized square patches of our synthetic radio maps of the four biggest simulated clusters in our sample as a function of the same patches in the X-rays. The three panels again show constant (model 1, left), increased cosmic-ray scaling (model 2, middle) and cosmic-rays scaled combined with magnetic fields scaled (model 3, right).

We include the observed scaling for three clusters (Coma and the steepest halo A2255) from Govoni et al. (2001) (dashed lines) and add the correlations found from best fits to the simulated data, calculated inside the region corresponding to the range of observed radio - X-ray brightness (dashed dotted lines). In table 6.2 we include the slopes from a best fit model to the simulations inside the observed region for the four largest clusters. We find that the models produce too steep scaling with only the third model approaching the sub-linear regime, where haloes are found in observations. Still no model produces substantially sub-linear scalings, which are typical for very extended haloes, like e.g. Coma, A2163 and A2744, which have a scaling slope $b = 0.6$ (Govoni et al., 2001; Feretti et al., 2001; Murgia et al., 2009). This reflects the point raised in the previous Section, i.e. that the slope of the radial distribution of the synchrotron emission in our secondary-generated radio halos is too steep.

6.4.4 Scaling Relations

There are several observed correlations for radio halos that relate thermal and non-thermal properties of the IGM: those between the radio power at 1.4 GHz, $P_{1.4}$, and the X-ray luminosity, L_X, temperature, and cluster mass (Liang et al., 2000; Govoni et al., 2001; Cassano et al., 2006). In addition, by making use of a sample of 14 giant radio halos, Cassano et al. (2007) found new scaling relations that connect the radio power, P_{R}, of halos to the size of the emitting region, R_{H} (see also Murgia et al., 2009), and to the total

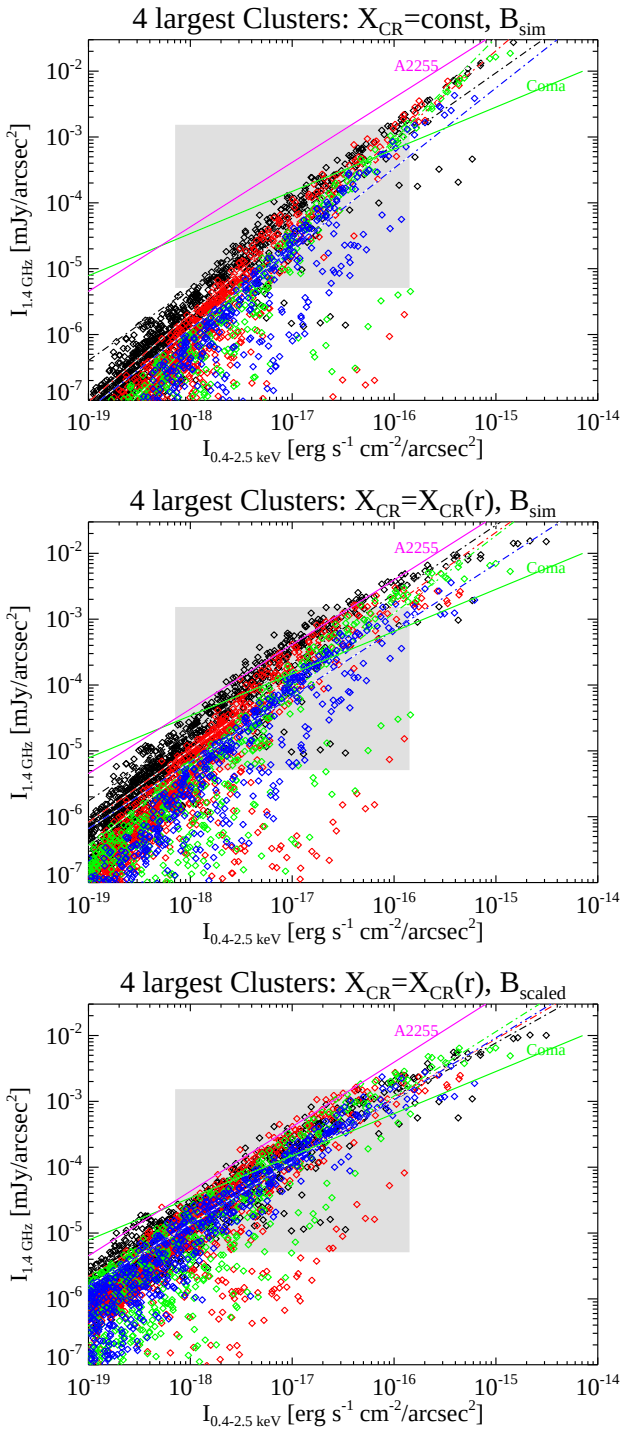

Figure 6.8: Radio vers. X-ray surface brightness in patches with 166 kpc side length, with the radio flux normalised to Coma. We also plot a fit to observations from Govoni et al. (2001) (red, $b = 0.64$ for COMA and A2255 in purple, $b = 0.98$). The gray box indicates the observed region from Govoni et al. (2001).

cluster mass within $R_{\rm H}$, $M_{\rm H}$; a geometrical scaling was also found between $M_{\rm H}$ and $R_{\rm H}$. The observed scalings from Cassano et al. (2007) are:

$$P_{\rm R} \propto R_{\rm H}^{4.18\pm0.68} \tag{6.19}$$

$$P_{\rm R} \propto M_{\rm H}^{1.99\pm0.22} \tag{6.20}$$

$$M_{\rm H} \propto R_{\rm H}^{2.17\pm0.19} \tag{6.21}$$

Specifically, $M_{\rm H}$ was computed from X-ray observations under the assumption of hydrostatic equilibrium and spherical symmetry. Radio haloes are found exclusively in disturbed, merging clusters, where these assumptions break down to some degree. Therefore, this procedure may lead to errors as large as 40% in mass (Rasia et al., 2006) which are expected to be not dependent on cluster mass, so that these errors might introduce considerable scatter without affecting the real trend of the correlation. $R_{\rm H}$ was measured on the radio img2s, $R_{\rm H} = \sqrt{R_{\rm min} \times R_{\rm max}}$, where $R_{\rm min}$ and $R_{\rm max}$ are the minimum and maximum radii measured on the 3σ radio isophotes. We stress that $R_{\rm H}$ provides a simple, but viable estimate of the physical size of radio halos, indeed a one-to-one correlation has been found between $R_{\rm H}$ and the size containing the 85% of the radio halo flux, R_{85}, derived from the observed brightness profiles of halos (Cassano et al., 2007).

A scaling was also found between the size of radio halos and the virial radius of clusters(Cassano et al., 2007) [4]:

$$R_{\rm H} \propto R_{\rm vir}^{2.63\pm0.50}. \tag{6.22}$$

Given that massive clusters are almost self similar (e.g. Rosati et al., 2002) one might have expected that $R_{\rm H}$ scales with $R_{\rm vir}$ and that the radial profiles of the radio emission are self-similar. On the contrary, this result proves that self-similarity is broken in the case of the non-thermal cluster components, as first noted by (Kempner & Sarazin, 2001).

As the synchrotron power depends on both magnetic field scaling and CRe scaling with density, it is unclear what is responsible for the break in the observed properties. On the other hand we know from previous works (Donnert et al., 2009) that the magnetic field scaling (with temperature or mass) flattens out for the largest clusters in our simulation, that would imply an expected break of self similarity in the thermal vs non-thermal properties of our simulated clusters.

Cassano et al. (2007) showed that all the correlations explored so far for radio halos can be derived by combining the $R_H - R_v$ and $P_{1.4} - R_H$ scalings. This suggests that there are two main scaling relations that carry out the leading information on the physics of the non-thermal components in galaxy clusters.

In what follows we shall investigate whether the properties of our simulated secondary-radio halos are consistent with the observed scalings.

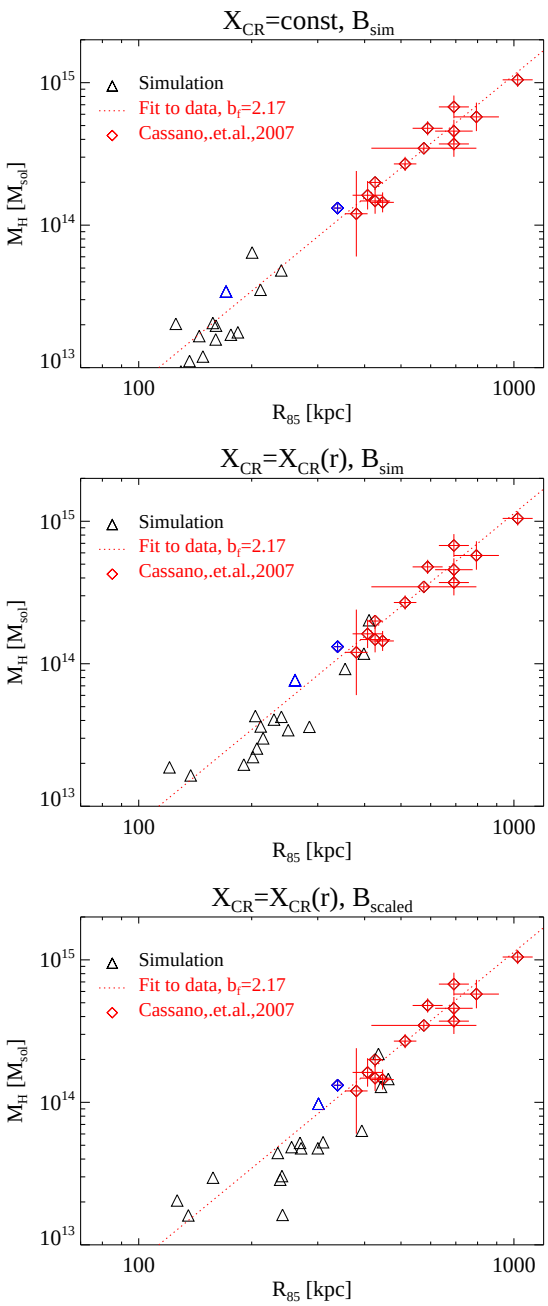

Figure 6.9: Total gravitational mass inside the radio emitting region over radius of the same region. We plot the correlation for all three models, constant and varying CR fraction and varying CR fraction and upscaled magnetic field (from left to right). We also plot observations of 14 galaxy clusters from (Cassano et al., 2007) and the best fit correlations. Due to uncertainties in the mass estimation from X-ray data the observations may show systematic errors. For both, simulations and observations the coma cluster is marked in blue.

Mass vs. Size

As a first step, before comparing the observed scalings with those derived for our simulated clusters, we check whether our clusters inherit the same mass distribution of real clusters with radio halos. We compare the observed and simulated scaling between the total mass inside $R_{\rm H}$ (M_{85}) and R_{85}, that provides a geometrical scaling on the halo-region. Therefore we plot in Figure 6.9 $M_{\rm H}$ versus R_{85} for simulated (open triangles) and observed (diamonds) clusters, together with the best fit power law to the observed scaling from Cassano et al. (2007).

The three models define different values of R_{85} and consequently different volumes where the scaling can be tested. We find that in all cases simulated clusters lie on the thermal scaling described by observed clusters, although, as expected (Sects.6.4.2–6.4.3), simulations populate a region in the $M_{\rm H}$–R_{85} diagram with smaller values of R_{85}.

The Size vs. Size Relation

As stated in Section 6.4.4, observations of clusters with radio halos show that the size of halos scales not linearly with the cluster virial radius, suggesting that the non-thermal component in clusters is not self-similar.

In figure 6.10 we plot the radius containing 85% of the clusters emission over virial radius for all three models. We include data from Cassano et al. (2007) and the fits to the simulated clusters-distribution obtained for models 1–3 at $z = 0$. We find a correlation between R_{85} and $R_{\rm vir}$ for our simulated hadronic-halos. Results suggest that self-similarity is preserved in the non-thermal components of simulated clusters, as the increase of the halos' radius is roughly proportional to the virial radius of the hosting clusters; the slopes of the correlations are $b_{\rm f} = 0.8$, 1.2 and 1.3 for models 1, 2 and 3, respectively.
This is not in line with observations: the expected correlations are flatter than the observed one and we predict halos systematically smaller than the observed ones. In contrast this is expected considering results reported in section 6.4.2 and confirms that it is challenging to reproduce the spatial extension of the observed radio halos with hadronic models, even by adopting a profile of the magnetic field that is flatter than that from our MHD simulations and by assuming a flat profile of the spatial distribution of CRp (model 3).
Donnert et al. (2010) have shown that matching the radio emission of the Coma halo at distance $\approx 0.2 - 0.3\,R_{vir}$ with hadronic models (by further increasing the CRp energy content at larger radii, see also section 6.4.2) would require the energy content of CRp to be roughly similar to the content of the thermal ICM at these distances (at least when constraints on the magnetic field from RM observations of the Coma cluster are used). The scalings found in figure 6.10 make the situation possibly more challenging, because they show that even more energy in the form of CRp would be required in the case of more massive clusters where the differences, between R_{85} of our hadronic-halos and that of the observed ones, are larger.

[4] We stress that the error in the slope of this scaling, as well as those in eqn. 6.19 and following accounts for both intrinsic scatter and measured errors in the data points in both variables.

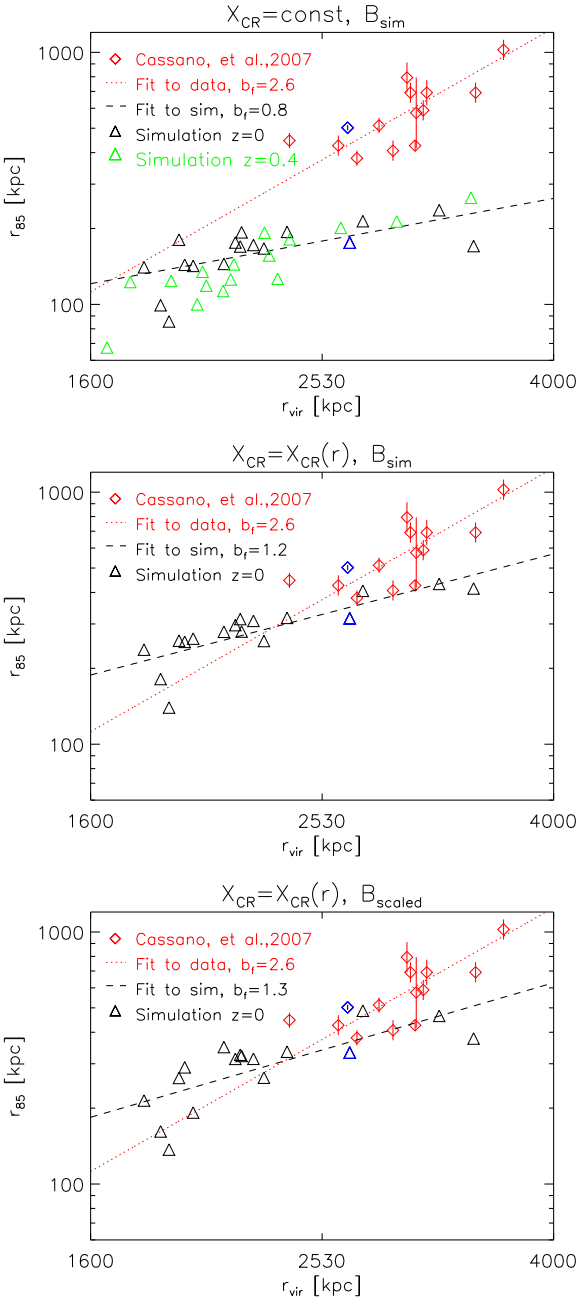

Figure 6.10: Radius of the radio emitting region as function of the virial radius of the cluster. We plot, left to right, the correlation for all three models and include the best fit ($\chi^2 = 0.54$, 0.29, 0.86, respectively) . We also plot observations of 14 galaxy clusters from (Cassano et al., 2007) and the best fit correlation. For both, simulations and observations the Coma cluster is marked in blue. For model 1 we include the include the correlation at redshift 0.4.

The observed clusters are in a range of redshifts, $z = 0 - -0.4$, while hadronic-halos are extracted from the simulations at $z = 0$. For this reason in figure 6.10a we also plot the distribution of simulated clusters obtained at $z = 0.4$ in the case of model 1 (marked green). We find that the correlation between R_{85}–R_{vir} in hadronic simulated haloes does not show significant change in slope at higher redshift.

The X-ray Luminosity vs. Radio Power Relation and the Evolution of Radio Halos

Radio halos follow a correlation between the monochromatic radio luminosity at 1.4 GHz, $P_{1.4}$, and the X-ray luminosity of the hosting clusters, L_X (e.g. Liang et al., 2000; Ensslin & Röttgering, 2002; Bacchi et al., 2003; Cassano et al., 2006). Recent radio observations of a statistical sample of X-ray selected galaxy clusters, the "GMRT radio halo survey", (Venturi et al., 2007, 2008) allow to study the distribution of clusters in the $P_{1.4} - L_X$ diagram. These observations suggest that the distribution of clusters in the $P_{1.4} - L_X$ diagram is *bi-modal*: radio-halo clusters trace the $P_{1.4} - L_X$ correlation, while the majority of clusters are found "radio quiet" with the limits to their radio luminosities about 10 times smaller than the radio luminosities of halos.
In order to investigate the behaviour of our simulated clusters in the $P_{1.4} - L_X$ diagram, in Fig.6.11 we plot our simulated clusters together with observed clusters (from Venturi et al. (2008); Brunetti et al. (2009, 2007)). The synthetic radio luminosities of our simulated clusters are scaled in order to have the simulated Coma cluster matching the observed one.

According to secondary models a correlation between radio luminosity and cluster X–ray luminosity (or temperature) is expected (e.g. Dolag & Ensslin, 2000; Miniati, 2001; Dolag et al., 2005; Pfrommer et al., 2008). We qualitatively confirm these expectations and in all three models find that the largest simulated clusters would naturally approach the observed correlation. In all three models the smallest systems are significantly more scattered in radio power than the largest clusters. This is expected as the magnetic field in the central regions of our simulated clusters (where most of the synchrotron emission is generated) is found to be tighly correlated with cluster thermal properties only in the case of massive clusters, while only a steep trend is found for smaller systems (figure 9 in Donnert et al., 2009).

The most relevant difference with respect to observations is that according to all three models (as for every secondary model) the synchrotron luminosity of the massive simulated clusters is equivalent to that of typical radio halos, at least if the radio luminosity of the simulated Coma cluster is normalised to that of the real Coma halo. This is inconsistent with observations which, on the other hand, found radio halos in only about 1/3 of massive clusters.
Most important, no radio *bi–modality* is expected in our simulated secondary–halos. Hadronic halos in simulated massive systems would follow a tight correlation, while those in less massive systems would be more broadly distributed.
One possibility to reconcile the hadronic scenario with the observed halo–merger connection

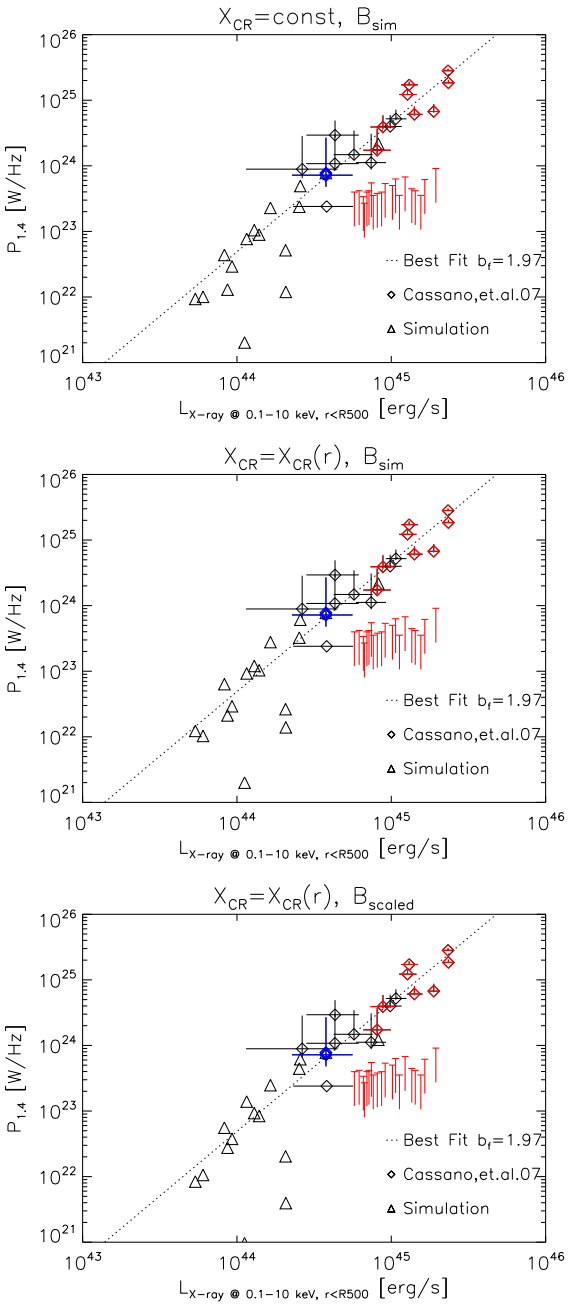

Figure 6.11: Radio power per frequency at 1.4 GHz over X-ray luminosity in erg/s from our simulated clusters using all three models (triangles, ltr.: constant fraction, scaled fraction,scaled fraction and scaled field). Observed scalings by Cassano et al. (2007) (diamonds, $z > 0.2$: red diamonds) and non-detections in red (Venturi et al., 2007, 2008). For both, simulations and observations the Coma cluster is marked blue.

and with the *bi–modal* distribution of clusters in the $P_{1.4} - L_X$ diagram is to admit that the observed *bi–modality* is driven by the amplification and dissipation of the magnetic field in the merging and post–merging phase, respectively (Brunetti et al., 2007; Pfrommer et al., 2008; Kushnir et al., 2009). However, Brunetti et al.(2009) have shown that the degree of amplification/dissipation of the magnetic field and the time–scale of this process that would be necessary to explain observations are difficult to reconcile with the observed properties of magnetic fields in the ICM (namely the field intensity and coherence scales from Rotation Measurements), and appear also disfavoured by energetic arguments.
The amplification of the magnetic field during cluster mergers is followed by our MHD cosmological simulations that offer a complementary approach to highlight this issue. To show the effect of magnetic field evolution and investigate the *bimodality* we plot the time evolution of the simulated radio haloes in figure 6.12. Shown is the radio luminosity over X-ray luminosity of the simulated sample for redshift $z < 0.48$ (big triangles: z=0, small triangles and black line: earlier redshifts); We highlight the path of the largest simulated cluster in cyan. Further we show the radio power vers. temperature correlation and evolution in the Appendix. No hint of a *bi–modality* is found, simply because magnetic field amplification in massive systems is a gradual process that happens in a time–scale comparable with the life–time of clusters themselves. For example, cluster 0 (cyan in img2 6.12) increases its mass by a factor 1.5 in the redshift range, staying close to the correlation. The evolution of magnetic field is reflected in the broad/scattered distribution of clusters in the $P_{1.4} - L_X$ diagram, especially in the case of smaller systems. These smallest clusters approach the lower end of the correlation with rather large scatter because the magnetic field is not saturated yet in their central regions and even smaller mergers yield a significant field amplification resulting in an increased radio luminosity. Although one would expect this behaviour to be slightly dependent on numerical resolution, increasing the numerical resolution would make the situation even more stringent. Resolving smaller gas motions leads to increase the amplification of the magnetic field, specially at early times. Having a larger magnetic field the changes in the magnetic field due to merger activity will be suppressed as the magnetic field is already closer to saturation effects. Therefore we would expect the clusters (especially the smaller, less resolved systems) to evolve even more along the correlation, and the spread around it would be further decreased.

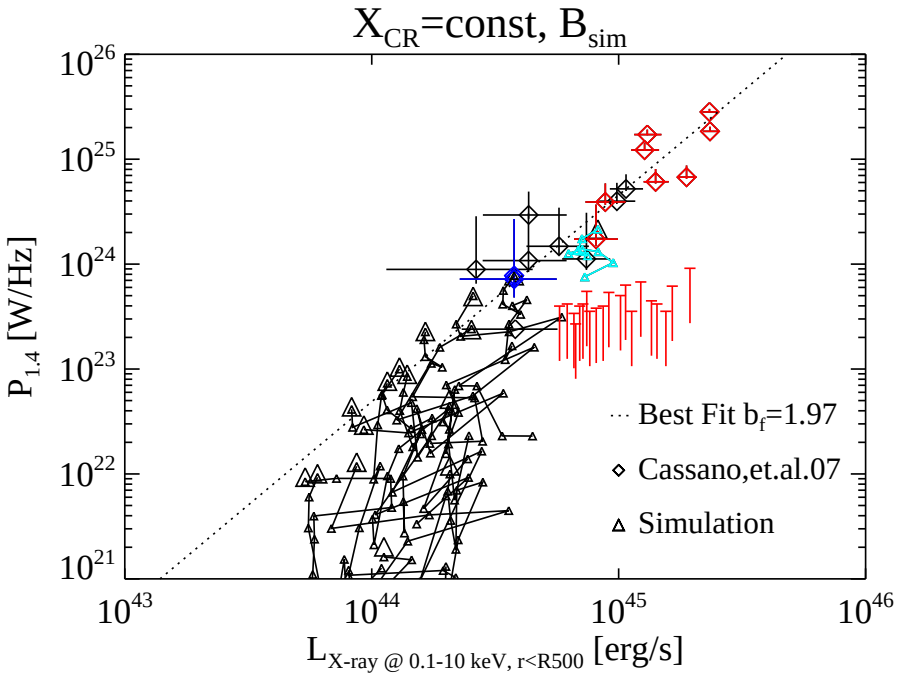

Figure 6.12: Radio power per frequency at 1.4 GHz over X-ray luminosity in erg/s from our simulated clusters using the constant model. Observed scalings by Cassano et al. (2007) (diamonds, $z > 0.2$: red diamonds) and non-detections in red (Venturi et al., 2007, 2008). We also include the time evolution of clusters for $z < 0.48$ (black lines), and highlight the largest cluster of the simulated sample (0) cyan.

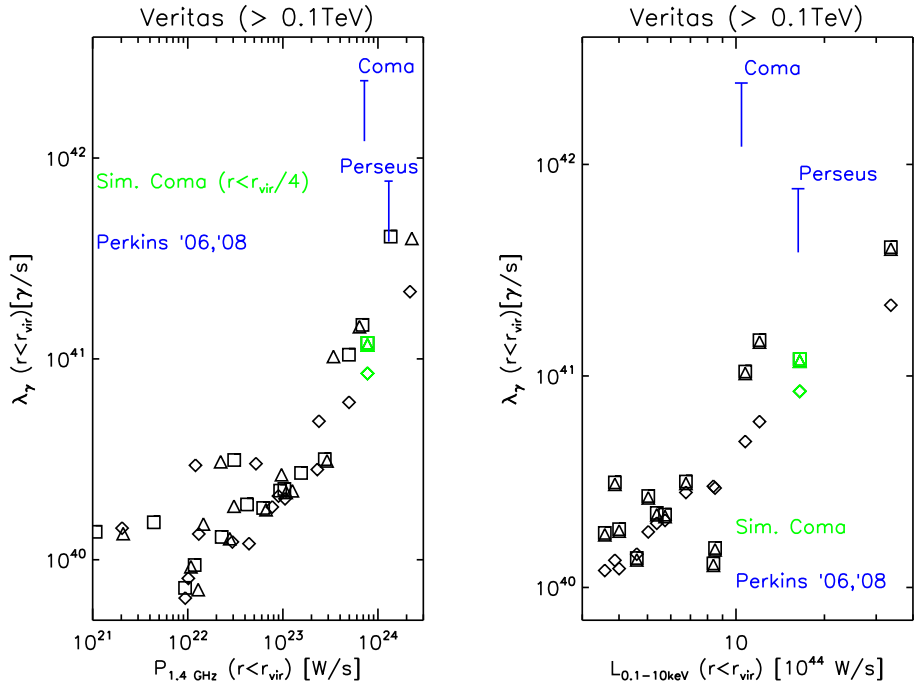

Figure 6.13: γ-ray luminosity ($E > 0.1$ Tev, e.g. VERITAS) over radio luminosity (at 1.4 GHz,left) and bolometric X-ray luminosity of all cluster at redshift z=0.We plotted the three models as different symbols (diamonds - model 1, triangles - model 2, boxes - model 3) and include upper limits from Perkins (2008); Perkins & the VERITAS Collaboration (2006) in blue. The Coma cluster is marked green.

6.5 γ-ray Emission from Simulated Clusters

We use the formalism in section 6.3.2 to compute predictions for the γ-ray luminosity of the simulated clusters according to all three models. Of interest are the two energy bands of Cerenkov telescopes, $E > 0.1$ TeV, and FERMI/EGRET telescopes, $E > 0.1$ GeV.
In table 6.3 (6.4) we present fluxes for the simulated sample in the VERITAS (FERMI) energy band. None of the clusters is in the observable range of the VERITAS experiment, however the largest ones (0, Coma, Virgo, Perseus, Centaurus) have a chance to be detected by FERMI in the next few years, at least for models with radially increasing CRp normalisation (model 2 and 3).

In the left panel of figures 6.13 and 6.14 we plot the simulated clusters in γ-ray vers. radio luminosity at 1.4 GHz for the 3 models. Following the previous Section we normalise the radio luminosity of the sample so the simulated Coma cluster fits the observed luminosity from the Coma halo. We also report available limits from VERITAS observations (Perkins, 2008; Perkins & the VERITAS Collaboration, 2006) (figure 6.13). Further we include (figure 6.14) newest preliminary results from the FERMI experiment (Mori, 2009) on the upper limit of the γ-ray flux from the Coma cluster. A scaling between γ-ray and

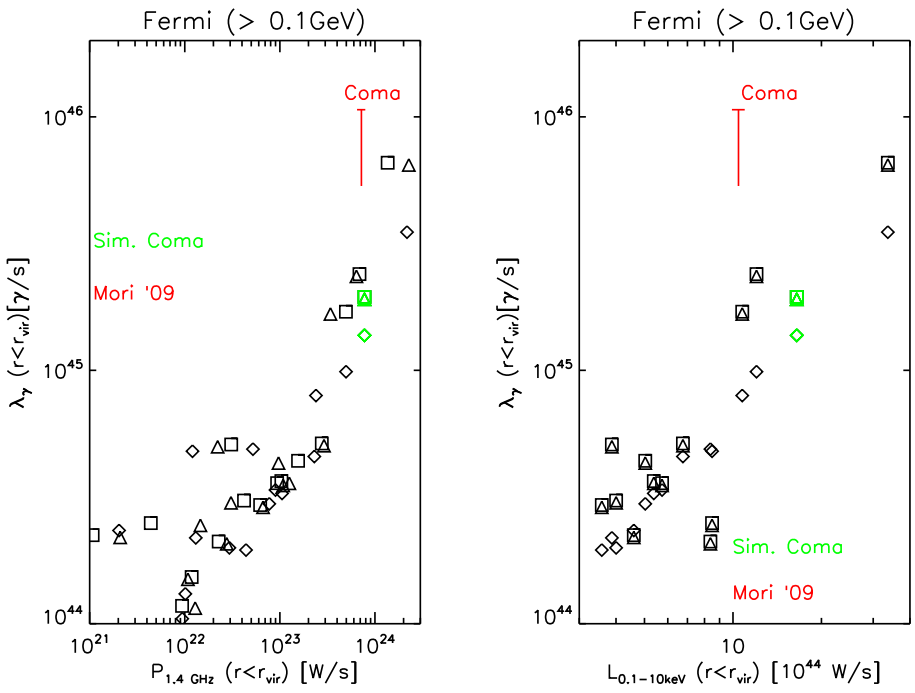

Figure 6.14: γ-ray luminosity ($E > 0.1$ Gev, e.g. FERMI, EGRET) over radio luminosity (at 1.4 GHz,left) and bolometric X-ray luminosity of all cluster at redshift z=0.We plotted the three models as different symbols (diamonds - model 1, triangles - model 2, boxes - model 3) . We add preliminary results from the first year FERMI data (Mori, 2009) in red. The Coma cluster is marked green.

Cluster	M1	M2	M3
0	3.2×10^{-13}	5.8×10^{-13}	6.0×10^{-13}
HYDRA	6.9×10^{-14}	3.3×10^{-14}	3.4×10^{-14}
2	2.4×10^{-14}	1.0×10^{-14}	1.0×10^{-14}
3	1.7×10^{-14}	2.5×10^{-14}	2.5×10^{-14}
4	9.9×10^{-14}	2.0×10^{-13}	2.1×10^{-13}
5	1.7×10^{-14}	2.6×10^{-14}	2.6×10^{-14}
COMA	6.7×10^{-14}	9.4×10^{-14}	9.6×10^{-14}
7	8.6×10^{-15}	9.8×10^{-15}	1.0×10^{-14}
8	1.8×10^{-14}	2.0×10^{-14}	2.1×10^{-14}
VIRGO	2.9×10^{-13}	6.7×10^{-13}	6.9×10^{-13}
A3627	3.2×10^{-14}	3.3×10^{-14}	3.4×10^{-14}
11	1.4×10^{-14}	2.1×10^{-14}	2.1×10^{-14}
12	4.5×10^{-14}	4.2×10^{-14}	4.3×10^{-14}
PERSEUS	9.7×10^{-14}	2.3×10^{-13}	2.3×10^{-13}
CENTAURUS	5.3×10^{-14}	5.8×10^{-14}	5.9×10^{-14}
15	5.0×10^{-15}	5.5×10^{-15}	5.6×10^{-15}

Table 6.3: Fluxes ($\gamma/\mathrm{cm}^2/\mathrm{s}$) in the VERITAS energy range ($E > 100$ GeV) from $1\,R_{\mathrm{vir}}$ for all Clusters from the simulations using the three different models.

radio luminosity is expected for the 3 models because p–p collisions generate both secondary electrons and neutral pions, the scaling is sub–linear since the radio luminosity is further boosted by the increase of the magnetic field in more massive clusters.

In the right panel of figure 6.13 and 6.14 we plot the emission of our clusters in γ-ray vers. X-ray luminosity for the 3 models. Also in this case we show two γ-ray upper limits from VERITAS (Poulain et al., 1992) and preliminary FERMI (Mori, 2009) observations respectively. A quasi–linear correlation is predicted, and is found less scattered than that between γ-ray and radio luminosities since it compares two purely thermal quantities (also in the case of models 2 and 3 CRp are scaled with thermal energy according with the profile in Figure 6.4).
The FERMI results are still consistent with the models for CRp presented in this paper. However, as shown by Donnert et al. (2010), the expected γ-ray flux increases substantially if we consider a spatial distribution of CRp that would the simulated radio emission to fit the observed profiles of radio haloes. We therefore expect a rejection or confirmation of these models in the very near future.

6.6 Conclusions

We use a constrained, cosmological MHD SPH simulation with a semi-analytic model for galactic magnetic outflows, to obtain a sample of 16 galaxy clusters with thermal prop-

Cluster	M1	M2	M3
0	5.2×10^{-9}	9.5×10^{-9}	9.7×10^{-9}
HYDRA	1.1×10^{-9}	5.5×10^{-10}	5.6×10^{-10}
2	3.9×10^{-10}	1.6×10^{-10}	1.7×10^{-10}
3	2.8×10^{-10}	4.1×10^{-10}	4.1×10^{-10}
4	1.6×10^{-9}	3.4×10^{-9}	3.4×10^{-9}
5	2.8×10^{-10}	4.2×10^{-10}	4.3×10^{-10}
COMA	1.1×10^{-9}	1.5×10^{-9}	1.5×10^{-9}
7	1.4×10^{-10}	1.6×10^{-10}	1.6×10^{-10}
8	3.0×10^{-10}	3.3×10^{-10}	3.4×10^{-10}
VIRGO	4.7×10^{-9}	1.0×10^{-8}	1.1×10^{-8}
A3627	5.2×10^{-10}	5.4×10^{-10}	5.5×10^{-10}
11	2.3×10^{-10}	3.4×10^{-10}	3.5×10^{-10}
12	7.4×10^{-10}	6.9×10^{-10}	7.0×10^{-10}
PERSEUS	1.5×10^{-9}	3.7×10^{-9}	3.8×10^{-9}
CENTAURUS	8.7×10^{-10}	9.5×10^{-10}	9.7×10^{-10}
15	8.1×10^{-11}	9.0×10^{-11}	9.2×10^{-11}

Table 6.4: Fluxes ($\gamma/\mathrm{cm}^2/\mathrm{s}$) in the EGRET/FERMI energy range ($E > 0.1$ TeV) from $1\,R_{vir}$ for all Clusters from the simulations using the three different models.

erties similar to clusters in the Local Universe. Further we assume 3 different models for secondary cosmic-rays motivated by simulations (Pfrommer et al., 2007) using the proper high energy approximation for the pion cross-section. In the first model we assume a constant CRp normalisation relative to the thermal density and the simulated magnetic field. In the second model we keep the magnetic field and introduce a radius dependent CRp normalisation inferred from non-radiative simulations by Pfrommer et al. (2007). The third model uses the same CRs and flattens the simulated magnetic field to be $B \propto \sqrt{\rho}$.

Although our simulations do not include a (internally) self-consistent treatment of CRp as done in other simulations (e.g. Pfrommer et al., 2007), contrary to previous work they allow us to properly simulate the properties of the magnetic field in the ICM which is important for modelling the cluster-scale synchrotron emission.

For the first time, we carry out a detailed comparison between the observed properties of giant radio haloes and those of simulated halos according to secondary models and under different assumptions for the spatial distribution of CRp. In an earlier paper we presented a detailed comparison of the simulated Coma cluster (Donnert et al., 2010). In this work we focus on global sample properties and compare with recent observations.

In particular, as a first step, we show that:

- The radial profiles of Faraday rotation of the median of our cluster sample is in line with that obtained from a number of observations of different clusters. This confirms

that the properties of the cluster's magnetic fields in our simulations are similar to the observed ones.

- The normalised radial profiles of the radio emission at 1.4 GHz of our simulated hadronic-halos show a deficit at radii $\geq 0.1 r_{\rm vir}$ with respect to the synchrotron profiles observed for a sample of well studied radio halos. This is in line with previous claims based on semi-analytic calculations in the context of the hadronic model (Brunetti, 2004b). In addition our results show that, even by assuming a flat profile for both the magnetic field and CRp spatial distributions (Model 3), secondary electrons may account for less than about 10 % of the observed emission at radii 0.15 - 0.3 $r_{\rm vir}$.

- A Point to Point comparison of radio vs. X-ray emission, obtained for the 4 largest clusters of our sample, confirms the results obtained for the profiles showing that the radial distribution of radio emission is too steep. All three models do not fit the observations over the whole range. Furthermore an excess in radio emission of the innermost patches suggests that haloes from the simulation are too centrally peaked.

As a second step we compare scaling relations obtained for the hadronic-halos in our simulated cluster sample with those given in (Cassano et al., 2007) that are obtained from a sample of observed radio halos. We find that:

- The geometrical correlation between the radius of radio halos and the cluster-mass contained within this radius is well reproduced by all three models. Due to the expected self-similarity of cluster in thermal properties this result implies that -at least- the simulated and observed clusters share similar thermal properties.

- A quasi self-similar behaviour is found for the non-thermal properties of our simulated clusters. In particular the radius of our hadronic halos is found to scale (approximately) with the virial radius of the simulated clusters. This is contrary to observations that found a steeper correlation between halo-radius and virial radius of the hosting clusters and implies that our simulated halos are systematically smaller than the observed ones.

- A correlation between the monochromatic luminosity of our hadronic halos and the X-ray luminosity of the simulated hosting-clusters is found. As soon as the population of our hadronic halos is normalised, by scaling the radio luminosity of the simulated Coma halo with that of the observed one, the correlation is similar to that observed for radio halos. However, since at this point all the simulated clusters show radio emission at the level of the observed halos, we find that the cluster radio *bi-modality*, observed for X-ray selected clusters, cannot be reproduced. A radio *bi-modality* in the radio – X-ray diagram would require a fast ($<$ Gyr) evolution of the radio luminosity in connection with cluster mergers, on the other hand, we find that the time evolution of our simulated massive-clusters in this diagram happens on cosmological, long, time-scales. Finally, we show that once the radio – X-ray correlation is approached at low

X-ray luminosities, during their evolution clusters follow the correlation closely due to the saturation of the magnetic field.

As a final point we calculate the γ-ray emission from our simulated clusters once the radio luminosity of the simulated Coma halo is anchored to that of the observed one (essentially by scaling the number density of CRp in simulated clusters). We find that:

- The γ-ray emission expected from our simulated clusters is well below the sensitivity of present Cerenkov Arrays, e.g. the VERITAS experiment, for all the adopted models for hadronic halos. The γ-ray fluxes at > 100 MeV expected from our simulated clusters would allow for a marginal detection by the FERMI telescope in next years, at least by assuming Models 2 and 3.

- The integrated γ-ray flux from our simulated clusters is expected to scale with their radio emission, although with rather large scatter. On the other hand, a tight correlation is found between γ-ray and X-ray fluxes, in which case (due to the scalings between thermal and non-thermal CRp in Models 1–3) the correlation is essentially driven by the density of the thermal gas in our simulated clusters.

Considering all these results, as well as the outcome from our earlier work on the Coma cluster (Donnert et al., 2010), we conclude that hadronic models alone are not able to explain the observed properties of giant radio haloes, in terms of their radial extension, observed cluster's radio *bi-modality*, scaling relations and spectral properties. Therefore we conclude that radio emission observed in galaxy clusters in form of giant radio halos is a powerful tool to infer the amount of cosmic-ray protons within galaxy cluster, confirming previous results that the energy content of cosmic-ray protons in clusters can not exceed percent level (e.g. Brunetti et al., 2007; Churazov et al., 2008).

The problem of halo's extension could be alleviated in *extended* hadronic models, where the contribution from primary (shock accelerated) electrons at the cluster outskirts is combined in the simulations with that from secondary electrons (Pfrommer et al. (2008)). However, as shown in Sect. 6.4.2, the problem of the halo profiles arises at distances 0.1 – 0.3 $R_{\rm vir}$ from cluster centres where, even based on the same simulations, the contribution to the diffuse synchrotron emission from these shock accelerated electrons is not yet dominant. Further we would like to note that the detailed morphology of the radio emission caused by electrons injected at shocks (e.g. Vazza et al., 2010; Roettiger et al., 1999) [5] will be significantly different from the morphology of giant radio halos and therefore is in general not able to mimic large scale, truly diffuse cluster centric radio emission. Thus additional physical processes are required to explain observations.

The problem of the radio *bi-modality* in massive clusters can be alleviated by assuming that MHD turbulence (and the RMS magnetic field) decays as soon as clusters approach a relaxed state after a major merger (Brunetti et al., 2009; Kushnir et al., 2009). In this

[5]These are base on Eulerian simulation, which are most appropriate to describe the morphology of shocks outside the cluster core.

case it might also be thought that CRp in these relaxed clusters would undergo less scattering on magnetic field irregularities escaping from the cluster volume and reducing the source of secondary electrons. All these processes are not properly included in our MHD cosmological simulations. However, Brunetti et al. (2009) have shown that the fast decay of the RMS field in galaxy clusters, that is necessary to explain the observed *bi-modality*, would imply a *rather unphysical* situation where the magnetic field power spectrum peaks at the smaller scales, and leads to the consequence that an *extremely* large flux of energy in clusters goes into magnetic field amplification/dissipation. In addition, because turbulent cascade should start to decay on largest scales, which are resolved by Faraday rotation measurements, this scenario would predict a *bi-modality* in rotation measures and depolarisation in largest clusters, which is not observed (Govoni et al. 2010).

The discovery of giant radio halos with *very* steep spectrum ($\alpha \sim 1.8 - 2$) in merging clusters (Brunetti et al., 2008; Giovannini et al., 2009; Macario et al., 2010b) proves that *inefficient* particle acceleration mechanisms are responsible for the origin of these sources and, based on simple energy arguments, disfavours hadronic models (Brunetti et al., 2008). Observations of the best studied halo, in the Coma cluster, have shown that its spectrum steepens at higher frequencies (Thierbach et al., 2003), due to the competition between energy losses and acceleration of the emitting particles, in which case the particle acceleration time-scale would be of the order of 0.1 Gyr. More recently we have shown that the steepening cannot be a result of the inverse Compton (SZ) decrement (Donnert et al., 2010), confirming these previous finding and supporting a scenario of *inefficient* particle acceleration mechanisms at the origin of the halo.

Particle acceleration due to micro-turbulence in merging galaxy clusters has been proposed for the origin of radio halos (e.g. Brunetti et al., 2001; Petrosian, 2001). In this case *gentle* particle acceleration mechanisms would generate radio halos in connection with (massive) cluster mergers, while the radio emission would decay as soon as clusters approach a relaxed state, due to dissipation of (at least a fraction of) this turbulence and the fast electron radiative cooling. It will therefore be interesting to consider these processes in future simulations used to study radio halos. That includes an estimation of the locally merger injected turbulence as well as a more detailed description of CR electron spectra.

6.7 Acknowledgements

We thank the referee for the helpful comments.
J. D. kindly acknowledges the support of ESF/Astrosim Exchange grant 2065 and thanks the INAF/IRA in Bologna for the hospitality.
K. D. acknowledges the supported by the DFG Priority Programme 1177.
R. C. and G. B. acknowledge partial support from PRIN-INAF 2007 and 2008, and from ASI-INAF I/088/06/0.

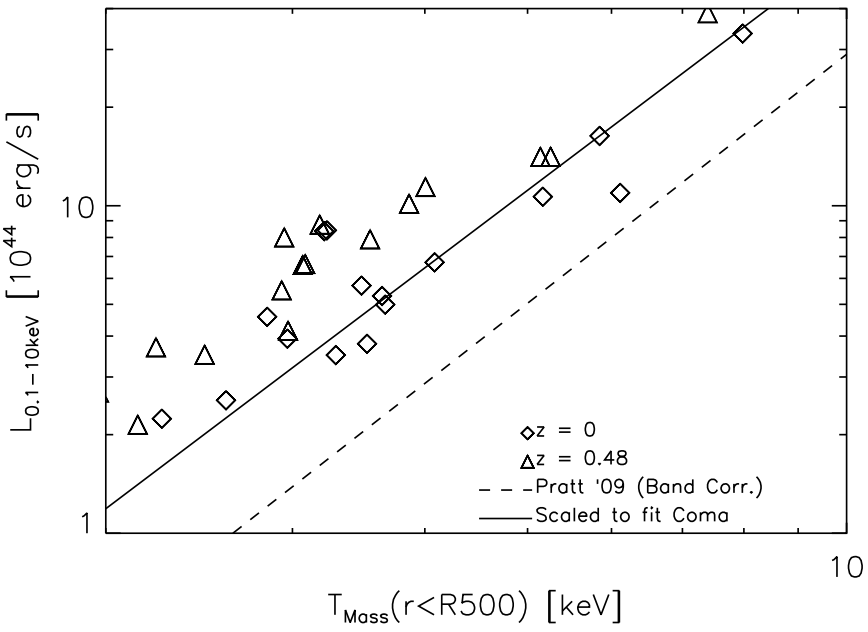

Figure 6.15: Bolometric X-ray luminosity over temperature of all cluster at redshift z=0 (diamonds) and z=0.48 (triangles). We also plot the observed correlation from Pratt et al. (2008).

6.8 Additional Scaling Relations

Here we provide additional scaling relations to substantiate the scalings shown before.

6.8.1 X-ray luminosity - Temperature relation

In figure 6.15 we show bolometric X-ray luminosity over mass weighted temperature for the simulated cluster sample at redshift zero (diamonds) and 0.48 (triangles). We include band-corrected the observed relation from Pratt et al. (2008) (broken line) and a the same correlation normalised to the simulated Coma cluster (black line). It is well known that non radiative simulations tend to over predict the X-ray luminosity by a fair amount (see for example (Borgani et al., 2006)). In addition the effect of K-correction can be seen in comparison with the cluster at high redshift.
Still, after re-normalising the X-ray luminosity there is a reasonably good agreement of with observations We therefore conclude, that our simulated clusters sample shows similar thermal properties than the observations.

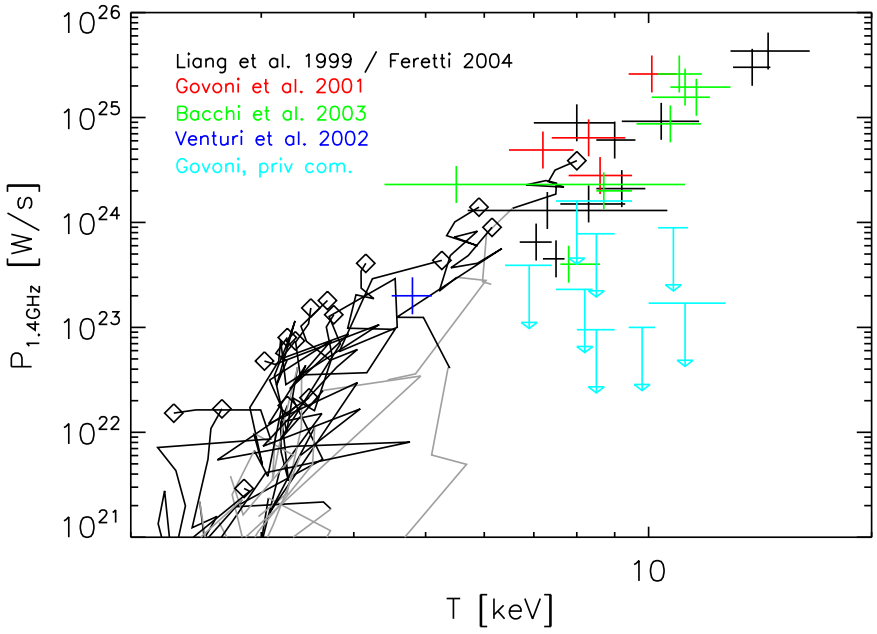

Figure 6.16: Radio power at 1.4 Ghz over mass weighted temperature inside $0.1r_{\rm vir}$ for all clusters. We include various observations from the literature. The evolution of the simulated clusters is plotted as lines in black (gray) for $z < 0.48$ ($z > 0.48$), while the points correspond to $z = 0$.

6.8.2 Radio luminosity - Temperature relation

In figure 6.16 we present the scaling of radio power at 1.4 GHz over cluster temperature as obtained from e.g. X-ray observations for constant CRp scaling (model 1). We include the evolution of the emission with time as lines in black (gray) for $z < 0.48$ ($z > 0.48$). Further we plot a number of recent observations. The sample follows the correlation closely at redshift zero, and only two clusters show significant deviation from the correlation at temperature larger than 5 keV, and only at high redshift.
In simulations, temperature is a less merger sensitive mass estimator compared to the X-ray luminosity, in terms of cluster mergers. We therefore conclude, that the bimodality observed in large clusters is not a result of biased mass estimation.

Chapter 7

Reacceleration of Cosmic Ray Electrons in Cluster Mergers

J. Donnert, K. Dolag, R.Cassano, G. Brunetti

ABSTRACT

We attempt to for the first time simulate the evolution of CR electrons in the intra-cluster medium, including stochastic reacceleration by compressible magnetosonic turbulence. We present a prescription to estimate turbulence in SPH simulations based on the RMS velocity dispersion of neighbours inside the SPH kernel. Using idealised simulations of sub- and supersonic turbulence, we show that this indeed gives similar results as prescriptions in Fourier space. We present a novel MPI parallel implementation of CR electron physics, including reacceleration, to be used in post-processing with the SPH code GADGET. We use the Chang & Cooper method to efficiently solve the underlying Fokker-Planck equation. We demonstrate accuracy and convergence of our implementation in comparison with analytical results. In addition, we present a novel implementation of an SPH projection algorithm based on the gather approach, which features a numerical synchrotron solver for arbitrary CR electron spectra.

We apply our novel prescription to a simulation of an idealised cluster collision. The two halos with mass ratio of 10 are modelled using Hernquist profiles. CR electron injection is treated as a hadronic process, normalised as a fraction of the thermal energy density. This way we are for the first time able to demonstrate that reacceleration indeed plays an important in the formation of giant radio halos. The time evolution of our simulated system reproduces the bimodality expected from observations. Further its synchrotron spectrum fits nicely to the observed spectrum from the Coma cluster.

In preparation to be submitted to MNRAS;

7.1 Introduction

Since over three decades radio observations reveal Mpc-sized diffuse radio emission in a number of merging galaxy clusters (Willson, 1970; Cane et al., 1981; Venturi et al., 2008). This emission is associated with the hot intra-cluster medium (ICM) seen in the X-ray regime (Sarazin, 1988). The non-thermal nature of the diffuse radio emission (giant radio halos) points to synchrotron emission from a population of relativistic electrons present in the cluster. Consequently the ICM is made up of hot thermal gas, magnetic fields and relativistic electrons and protons interacting with each other (Petrosian, 2001).

It has been realised early on, that the size of giant radio halos poses a problem on the injection and transport of CR electrons (CRe). While being injected locally by shock or galactic outflows, CR electrons suffer substantial losses while diffusing through the ICM. As their streaming velocity is limited to the Alvén velocity their lifetime is too short to remain radio synchrotron bright and diffuse through the whole cluster volume at the same time.

Two models have been discussed extensively in the past years to solve the problem:

- *Hadronic models* (Dennison, 1980; Schlickeiser et al., 1987; Dolag & Ensslin, 2000; Miniati et al., 2001; Ensslin et al., 2007; Pfrommer, 2008) explain the presence of the CRe by the in-situ injection through hadronic interaction of cosmic-ray protons (CRp) with the thermal gas. CRp are injected with CRe and have lifetimes comparable to the Hubble-time. The can diffuse through the cluster volume and scatter with thermal protons, which injects CR electrons through a Pion-Muon cascade.

- *Reacceleration models* (Jaffe, 1977; Schlickeiser et al., 1987; Brunetti et al., 2001, 2004; Brunetti & Lazarian, 2007) attempt to explain the abundance of CRe via the injections of MHD turbulence during major merger events. The injected plasma waves couple to mildly relativistic CRe. This leads to momentum diffusion of population to synchrotron bright momenta.

Recently a number of authors found hadronic models to be disfavoured by observations (Brunetti et al., 2007, 2008, 2009; Donnert et al., 2010). Additionally there is growing evidence for a sufficient injection of turbulence in the ICM by major mergers from simulations (Dolag et al., 2005; Vazza et al., 2011). Furthermore the expected arrival of low-frequency observations from new observatories like LOFAR makes it timely to investigate reacceleration models in detail.

We attempt here to for the first time couple CR electron momentum transport self-consistently to astrophysical simulations of galaxy clusters. To do so we develop a novel model for local turbulent energy in the SPH formalism (section 7.2). Using idealised simulations of sub- and supersonic turbulence we show that our approach is indeed a good description of turbulence in SPH. In section 7.3 we show our model of compressible magneto-sonic turbulence used later in this work. We proceed to present an implementation of CR electron physics based on the method proposed by Chang & Cooper (1970) in section 7.4. Using a number of test cases we show that our implementation is converged and

accurate on a small number of grid points and therefore suitable for the application to SPH simulations with millions of particles. In section 7.5 we comment on the extraction of non-thermal observables from the simulations. In section 7.6 we apply our formalism to an ideal simulation of a high-mass cluster merger. Our conclusions are drawn in section 7.7.

7.2 Local Turbulence in SPH

Recent studies of turbulence in particle simulations suggest good agreement between codes (Kitsionas et al., 2009; Price & Federrath, 2010). However, these studies are usually targeted at driven *supersonic* turbulence and do not investigate the effects below the kernel scale of SPH simulations ($k_{\rm hsml} = (2h_{\rm hsml})^{-1}$). For our CRe sub-grid model we need to measure local *subsonic* turbulence in SPH and need to understand to what extend the SPH kernel influences the estimate directly.

We use the root-mean-square velocity dispersion around the kernel mean to estimate the turbulent velocity of the flow. For a particle i this is given by:

$$v^i_{\rm RMS} = \left(\sum_{j=0}^{N_{\rm ngb}} (v^j - \bar{v}^i)^2 / N_{\rm ngb} \right)^{1/2}, \tag{7.1}$$

where $N_{\rm ngb}$ is the number of neighbours of particle i, and $\bar{v}^i$ is the velocity mean of all particles inside i's kernel.

The velocity dispersion measures the amount of turbulence, i.e. velocity divergence and rotation on the kernel scale $h_{\rm sml}$, directly from the particle distribution. This can be easily understood considering figure 7.1, where we show a cartoon of two SPH particles with high and low velocity dispersion. However it is not obvious to what extend the SPH approximation indirectly influences the velocity distribution inside the kernel. In SPH the velocities are not computed using kernel smoothing, but the forces are calculated using the SPH approximation. Note that the SPH kernel is mostly affecting scales below half the smoothing scale $2h_{\rm hsml}$, where the kernel is large. These are marked gray in figure 7.2, where we plot the standard 3D normalised SPH kernel. Another issue is the sampling noise, introduced by the finite number of particles inside the kernel. We use 64 neighbours in our simulations to minimise this effect. Assuming a sufficiently steep turbulent spectrum, where the largest scales are dominant in terms of the turbulent energy it is reasonable to assume little influence of the force smoothing on the turbulent energy measured via equation 7.1.

Nonetheless we test our turbulence model against the standard FFT based method of estimating local turbulence in a particle simulation in the next section.

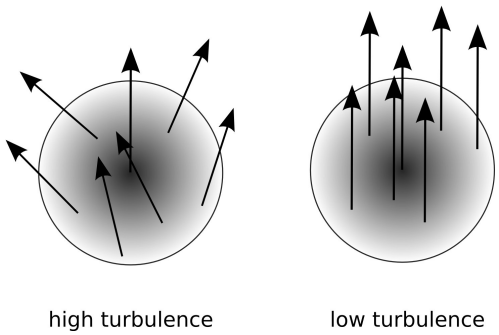

Figure 7.1: Cartoon depicting the SPH representations of a laminar flow (right), i.e. low turbulence and a turbulent flow (left). Every arrow marks the velocities of a particle at its base.

Quantity	Subsonic	Supersonic
Volume [Mpc]	3000^3	3000^3
Density [g/cm]	4.9×10^{-28}	4.9×10^{-28}
Temperature [K]	8×10^6	8×10^6
Therm Energy [erg]	1.3×10^{63}	1.3×10^{63}
Hsml [kpc]	60.5	60.5
$X_{\rm turb}$	0.1	0.5

Table 7.1: Physical quantities used to set up an idealised simulation of cluster turbulence. $X_{\rm turb}$ marks the fraction of thermal energy in turbulence.

7.2.1 Simulations of Idealised Turbulence

To investigate the correctness of the RMS method, we use idealised simulations of subsonic turbulence. This allows us to compare the turbulent energy, estimated by the RMS method, with an estimate of the same energy in Fourier space.

Initial Conditions

We set up initial conditions in a periodic box, mimicking physical conditions of a galaxy cluster (see table 7.1). Positions are set using a glass file with 100^3 particles to achieve a homogeneous Poisson sampling of the volume. To initialise particle velocities we set up a random vector field on a grid with 100^3 grid-points, assuming a Kolmogorov-like power spectrum with a spectral index of $-11/3$. This vector field is then mapped to the particles using the nearest grid-point method (Hockney & Eastwood, 1988). The simulation is evolved for a few Gyr.

The particle velocities of the outputs are then mapped in a mass weighted way to a grid of equal resolution, using the cloud-in-cell technique.

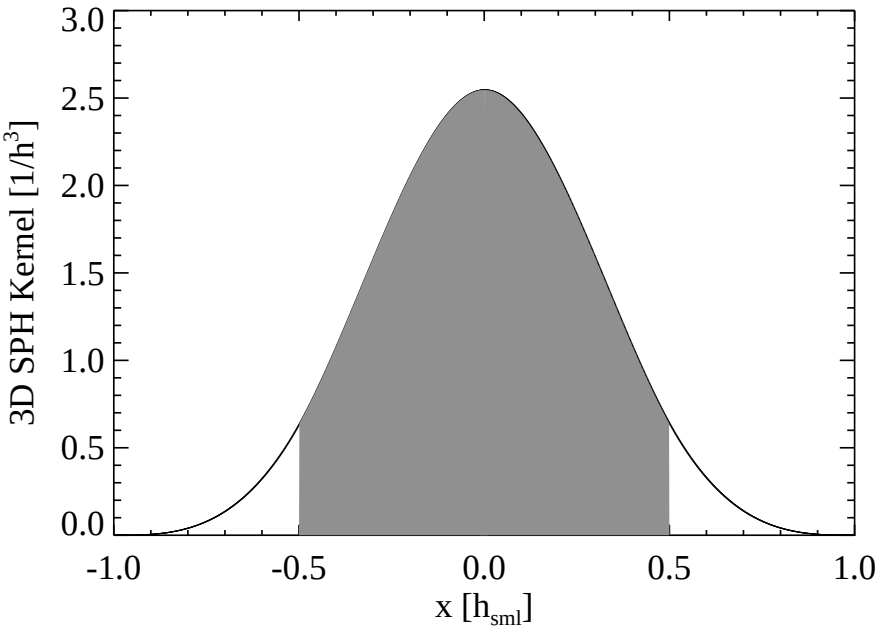

Figure 7.2: Standard spline SPH kernel, as implemented in GADGET. Scales with strong smoothing are marked gray.

Errors

The procedure described above introduces considerable errors to the final velocity grid, which modify the power spectrum from the initial grid on smallest scales. As we are interested in these scales, we have to carefully treat most of them:

1. The mapping procedure from the initial grid to the particles involves a kernel estimate, which modifies the power spectrum near the grid scale. We found that we can minimise this effect by using the Nearest-Grid-Point (NGP) method. It is of no importance to the energy estimate, because this spectrum is measured by the RMS method as well as the Fourier method. However, it explains why we are not recovering exactly the seeded Kolmogorov law everywhere.

2. The positions have to be homogeneous, isotropic and Poisson-like to properly sample the smallest scales. A grid-like particle distribution is unsuitable for these purposes. We use a glass to achieve best results.

3. The finite amount of particles introduces the shot-noise error below the SPH kernel scale. This effect can be accounted for (Jing, 2005) in the case of homogeneous sampling.

4. The particle mapping to the final grid involves another kernel estimate that acts on the power-spectrum as well as the shot-noise. This can be accounted for by

deconvolving with the kernel Fourier transform in k-space, which is given for the cloud-in-cell (CIC) kernel in e.g. Hockney & Eastwood (1988).

Power Spectra

In figure 7.3 and 7.4 we show velocity power spectra of the sub/supersonic simulations at different times. In each panel we plot the seeded power spectrum (black), the uncorrected power spectrum from the grid (blue), the deconvolved power spectrum (red, 7.2.1, point 4), and the deconvolved, shot noise correct spectrum (green). As red, red dashed lines we mark the mean,min and max hsml scale in the simulation, respectively. In addition we over-plot in the first panel ($t = 0$) the CIC kernel (black, dashed) and the shot noise (black, dashed dotted).

After correcting for CIC kernel and shotnoise (green) the initial power spectrum follows the seeded power spectrum (black) very well. Slight differences arise below the kernel scale. We attribute this to the NGP mapping of the seeded power spectrum to the particles. At this point due to the homogeneous sampling the effect of kernel and shot noise correction on the power spectrum are rather small. Due to the higher energy content the effect of the shot-noise on the power spectrum is less prominent in the supersonic case.

As the simulations evolve, the power spectrum becomes increasingly shot noise dominated on the smallest scales, until after one sound-crossing time, when the whole kernel scale is shot noise dominated. Again the effect is more prominent in the subsonic case.

Above the hsml scale the spectrum steepens with time. Additionally, at intermediate times the spectrum shows wiggles near the maximum kernel scale, i.e. in the most underdense regions. The supersonic simulation shows a larger density contrast than the subsonic case, which leads to a less wiggly spectrum at intermediate times.

In both cases the increasing importance of the shot noise suggests that on smallest scales correction terms become dominant with time. Additionally the density contrast in the box and inhomogeneity of the sampling increases, as shown by the spread in hsml. That makes the sampling noise spatially dependent and our shotnoise correction more and more incorrect. Therefore we conclude that any estimation of the power spectrum or the turbulent energy on smallest scales via a grid/FFT based technique becomes more uncertain with higher density gradients. This has to be kept in mind, when comparing a particle based methods with FFT/grid based methods. So far there is no way to correct for spatially inhomogeneous shot noise in Fourier space.

Energy Evolution

In figure 7.5 we show the evolution of the turbulent energy on the mean kernel scale inside the box, the RMS method (green) and the FFT method (purple). We correct the RMS velocity dispersion for the spread in hsml. Using Parsevals theorem and assuming a Kolmogorov power-law, $v_{\rm rms}$ scales like:

$$v^2_{\rm rms,0} = v^2_{\rm rms,hsml} \left(\frac{k_0}{k_{\rm hsml}} \right)^{-2/3}, \tag{7.2}$$

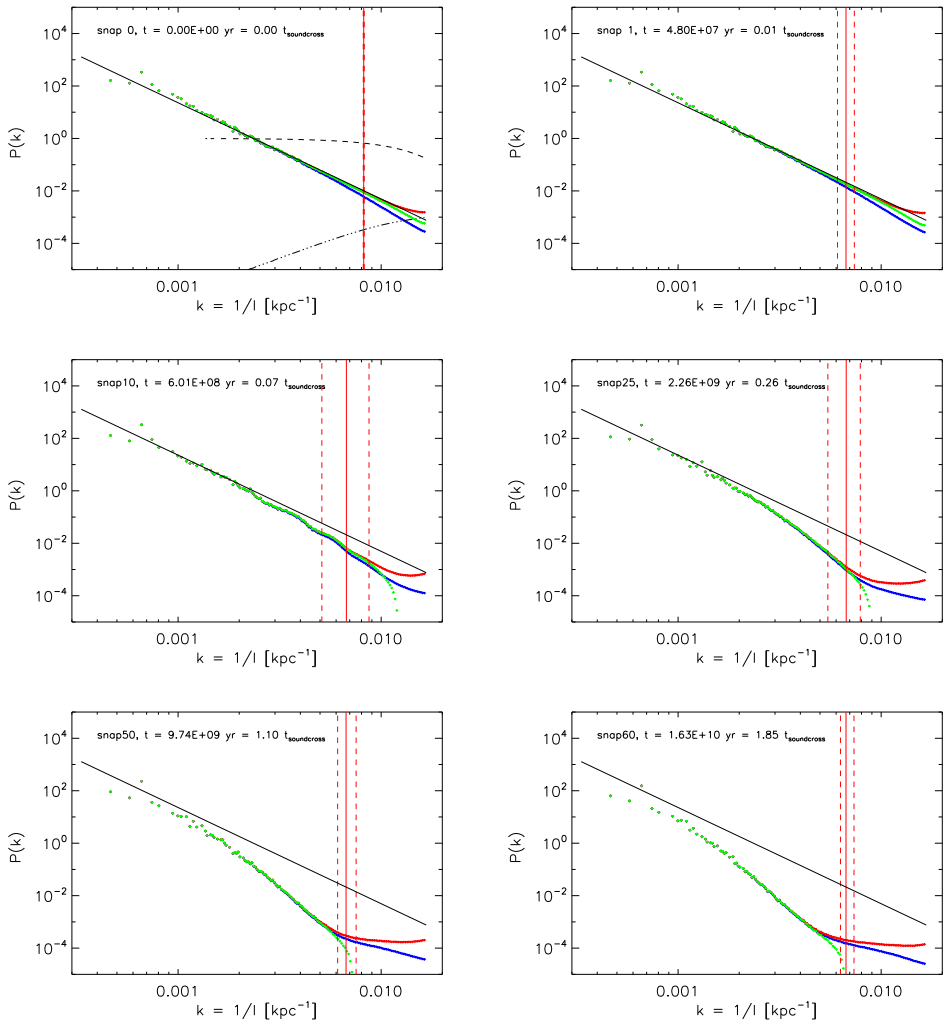

Figure 7.3: Power spectra of simulations of ideal subsonic turbulence $E_{\rm turb} = 0.1 E_{\rm thermal}$. We plot the seeded power spectrum (black), the uncorrected spectrum (blue), the deconvolved spectrum (red) and the deconvolved and shot noise corrected spectrum (green). We also over-plot the CIC kernel (black dashed) and Poisson shot noise term (black, dotted dashed) in the first panel. The red vertical lines represent the kernel scale and its maximum/minimum.

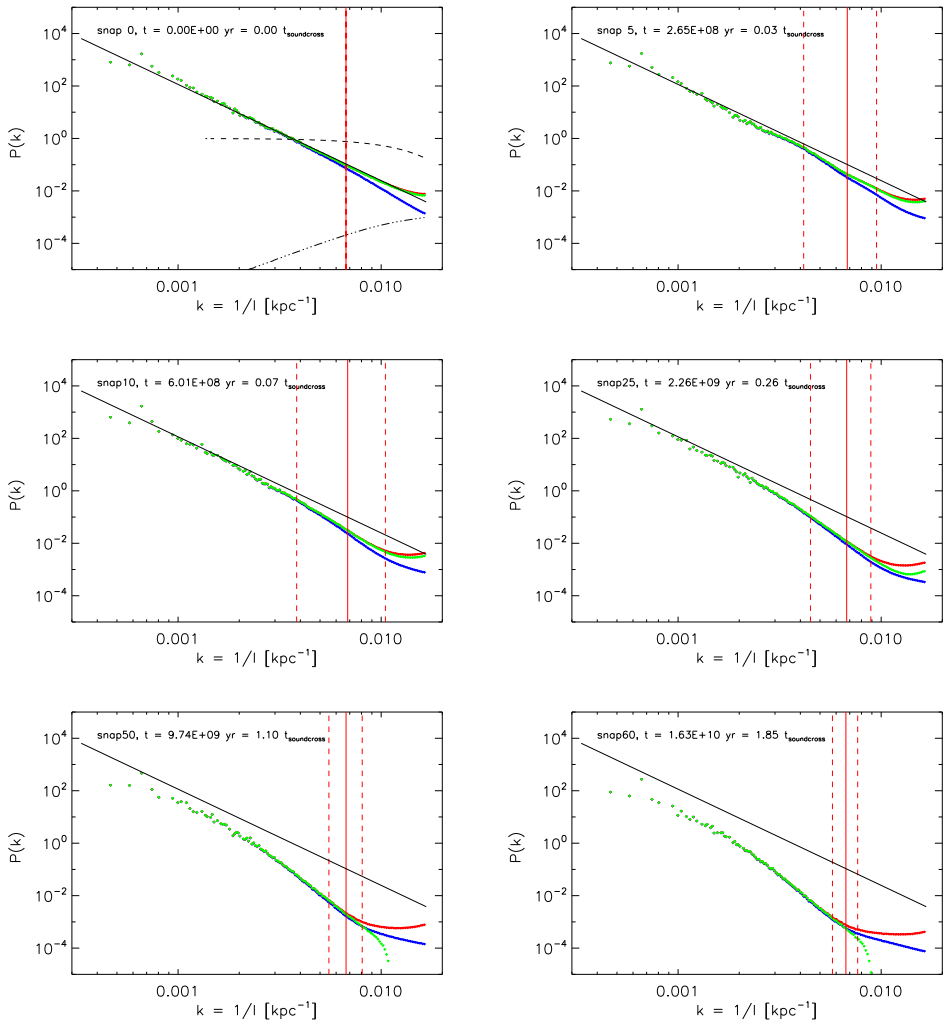

Figure 7.4: Power spectra of simulations of ideal supersonic turbulence ($E_{\rm turb} = 0.5E_{\rm thermal}$). We plot the seeded power spectrum (black), the uncorrected spectrum (blue), the deconvolved spectrum (red) and the deconvolved and shot noise corrected spectrum (green). We also over-plot the CIC kernel (black dashed) and Poisson shot noise term (black, dotted dashed) in the first panel. The red vertical lines represent the kernel scale and its maximum/minimum.

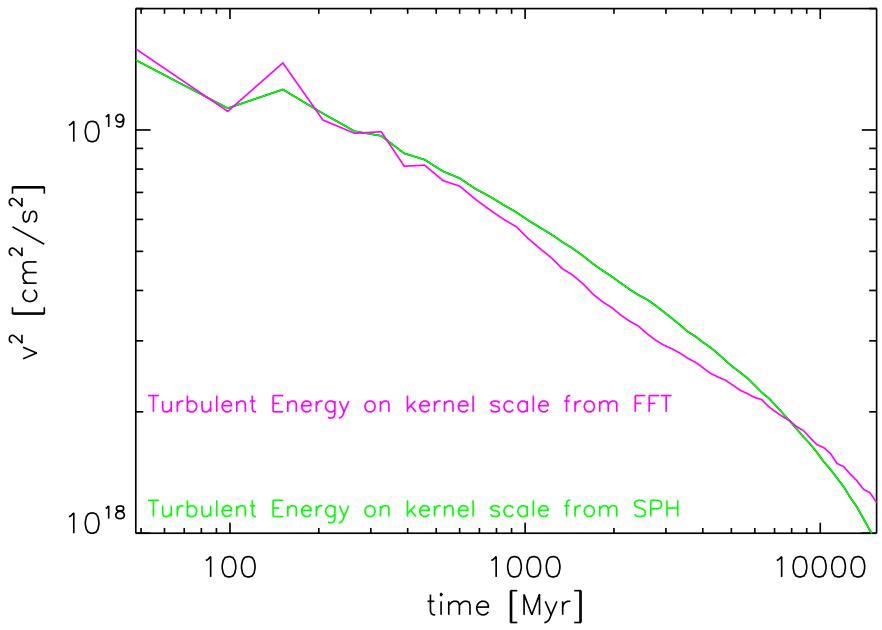

Figure 7.5: Time evolution of the turbulent energy on mean kernel scale in a simulation of ideal subsonic turbulence. In green we plot the measured turbulent energy using the particle based RMS approach. In purple we plot the same, but measured using the standard Fourier transform approach.

where the index 0 is to the reference scale and the index "hsml" refers to the particle scale. While this correction can be significant for the velocity dispersion of a single particle, it is only a few percent of the total energy in the simulated volume.

To estimate the turbulent energy in Fourier space, we bin the mass weighted particle velocity to a grid of the same size as the particle number. Similar to the previous section, we Fourier transform the grid and correct for the CIC kernel and the shot noise of a *homogeneous* particle distribution in k-space. The resulting power grid is then filtered, using an ideal high pass filter, and the total energy in all modes k_{hsml} is calculated.

Over about ten Gyr, the turbulent energies on the kernel scale agree reasonably well, as measured by both techniques. This is remarkable, considering the increasing uncertainties regarding corrections to the power on the grid in Fourier space. We found the relative error between both methods to be between 4% at early times and 20 % at late times. Given the discussion above, we attribute these errors to the uncertainties in the velocity grid and the inhomogeneous sampling. We conclude that the local turbulent energy in an SPH simulation can be measured reasonably well by the velocity dispersion around the kernel mean.

7.3 Particle Acceleration Model

In galaxy clusters CR electrons are subject to interaction with turbulent MHD waves injected by cluster infall and mergers. These provide a stochastic scattering agent, which energises trans-relativistic particles to relativistic energies. In addition CR electrons are subject to a number of systematic energy losses due to interaction with the thermal plasma, the CMB and the magnetic field in the ICM. Several mechanisms are believed to inject (trans-)relativistic electrons in the ICM, among the collisionless shocks, galactic outflows, AGN, and hadronic CR proton interactions.

The equations, governing the time evolution of an ensemble of CR electrons, can be derived from kinetic theory (Melrose, 1980; Eilek & Hughes, 1991). This yields:

$$\frac{\partial n(p,t)}{\partial t} = \frac{\partial}{\partial p}\left[n(p,t)\left(\left|\frac{\mathrm{d}p}{\mathrm{d}t}\right|_{\mathrm{rad}} + \left|\frac{\mathrm{d}p}{\mathrm{d}t}\right|_{\mathrm{c}} - \frac{2}{p}D_{\mathrm{pp}}(p)\right)\right] + \frac{\partial}{\partial p}\left[D_{\mathrm{pp}}(p)\frac{\partial n(p,t)}{\partial p}\right] + Q_{\mathrm{e}}(p,t), \tag{7.3}$$

where $n(p,t) = 4\pi f(\mathbf{p},t)$ is the isotropic number density of CR electrons. For a magnetic field $B_{\mu G}$ in μG, synchrotron and inverse Compton losses can be modelled as (Petrosian, 2001; Cassano & Brunetti, 2005):

$$\frac{\mathrm{d}p}{\mathrm{d}t}_{\mathrm{rad}} = -4.8\times10^{-4}p^2\left[\left(\frac{B_{\mu G}}{3.2}\right)^2 + (1+z)^4\right] \tag{7.4}$$

and ionisation and Coulomb losses as:

$$\frac{\mathrm{d}p}{\mathrm{d}t}_{\mathrm{i}} = -3.3\times10^{-29}n_{\mathrm{th}}\left[1+\ln\left(\frac{\gamma}{n_{\mathrm{th}}}\right)/75\right], \tag{7.5}$$

where $\gamma = p_e/m_e c$ is the relativistic gamma factor and n_{th} - the number density of thermal gas. $D_{\mathrm{pp}}(p)$ is the reacceleration coefficient which describes the interaction of the spectrum with the turbulent waves in the plasma.
Equation 7.3 takes the form a Fokker-Planck equation, where turbulence provides systematic (first $D_{\mathrm{pp}}(p)$ term) and stochastic (second term) energy gain to the particle spectrum.

We limit our model to compressible (magnetosonic) MHD waves because this interaction represents a lower limit to particle acceleration in clusters. In the theory of resonant particle interaction with magnetosonic turbulence CR electrons are accelerated by the electric field of the mode via gyroresonant interaction. Again we limit our interest to the zeroth order interaction for which the resonance condition (e.g. Eilek, 1979; Brunetti & Lazarian, 2007, and references therein) reads:

$$\omega - k_{\parallel}v_{\parallel} = 0, \tag{7.6}$$

here ω is the frequency, $k_{\parallel}$ and $v_{\parallel}$ are the speed and wavenumber components of the particles and waves parallel to the magnetic field. This interaction is known as transit time damping (TTD). Because this changes only the particle momentum parallel to the

magnetic field, TTD damping requires an efficient isotropisation of the particle momenta (Schlickeiser & Miller, 1998). Anisotropies lead to strongly decreased efficiency of this mechanism. There are a number of isotropisation mechanism discussed in the literature (Brunetti & Lazarian, 2007), which may act on scales relevant to us. We will therefore assume TTD is efficient in clusters.

One can then derive the reacceleration coefficient $D_{\rm pp}$, considering the simple energy argument that a fraction η of the turbulent energy below a scale $h_{\rm sml}$ is channelled into CR electrons (Eilek, 1979). Brunetti & Lazarian (2007) derive an expression (their equation 47) for the reacceleration coefficient which can be further simplified assuming a Kraichnan type turbulent spectrum to yield:

$$D_{\rm pp} \approx 9 \times 10^{-8} p^2 \eta \frac{c_{\rm s}}{h_{\rm sml}} \left(\frac{v_{\rm turb}}{c_{\rm s}} \right)^4, \tag{7.7}$$

where $c_{\rm s}$ is the speed of sound, $h_{\rm sml}$ - the minimum scale of turbulence considered and $v_{\rm turb}$ the turbulent velocity measured.

7.4 Fokker-Planck Solver

To account for the reacceleration of electrons in astrophysical simulations, we have to solve equation 7.3 for every particle in the dense gas in the computational domain. However the contribution of a single particle to the total synchrotron emission of a cluster is likely small. We therefore need a numerical method which is fast enough to be used on the majority of the particles ($n_{\rm part} > 10^6$), but in turn does not have to be highly accurate.

In this paragraph we will describe the implementation and test of our Fokker-Planck solver. We will start with the numerical method, comment on boundary conditions and continue by applying the code to known test cases to show correctness and convergence.

7.4.1 Numerical Method

We use the finite difference scheme proposed by Chang & Cooper (1970). Using no-flux boundary conditions, it ensures positivity, particle conservation and correctness of the equilibrium solution by construction. Furthermore it is unconditionally stable and well suited for logarithmic grids, which allows us to use a comparatively small number of gridpoints and speed-up the calculation.

Equation 7.3 can be written as:

$$\frac{\partial n(p)}{\partial t} = \frac{\partial}{\partial p} \left[H(p) n(p) + D_{\rm pp} \frac{\partial n(p)}{\partial p} \right] - \frac{n(p)}{T_{\rm e}(p,t)} + Q_{\rm e}(p,t), \tag{7.8}$$

where we introduced the generalised cooling function $H(p)$ for simplicity:

$$H(p) = \left|\frac{dp}{dt}\right|_{\rm rad} + \left|\frac{dp}{dt}\right|_{\rm c} + \frac{2}{p} D_{\rm pp} \tag{7.9}$$

and added a term for catastrophic losses $T_{\rm e}(p,t)$.
We use a logarithmic momentum grid with N points:

$$p_{\rm i} = p_{\rm min} 10^{i p_{\rm step}}, \qquad i = \{0 \ldots N-1\}, \tag{7.10}$$

$$p_{\rm step} = \frac{1}{N-1} \log_{10}\left(\frac{p_{\rm max}}{p_{\rm min}}\right), \tag{7.11}$$

$$\Delta p_i = \frac{1}{2}(p_{i+1} - p_{i-1}), \tag{7.12}$$

$$\Delta p_{i+1/2} = p_{i+1} - p_i, \tag{7.13}$$

so that for a quantity A(p):

$$A_i = A(p_i), \qquad A_{i+\frac{1}{2}} = \frac{1}{2}(A_i + A_{i+1}), \tag{7.14}$$

and the time dependence:

$$n_i^j = n(p_i, t_j). \tag{7.15}$$

So far we have implemented only constant, universal timesteps.
Following (Park & Petrosian, 1996) we discretise equation 7.8 as:

$$\frac{n_i^{j+1} - n_i^j}{\Delta t} = \frac{F_{i+1/2}^{j+1} - F_{i-1/2}^{j+1}}{\Delta p_i} - \frac{n_i^{j+1}}{T_i} + Q_i. \tag{7.16}$$

The Chang & Cooper method exploits the degree of freedom introduced when discretising the cooling function in the flux F_i^j, so the method is adaptively 'upwind', towards the steady-state solution:

$$\begin{aligned} F_{j+1}^{i+1/2} &= (1-\delta_{i+1/2}) H_{i+1/2} n_{i+1}^{j+1} + \delta_{i+1/2} H_{i+1/2} n_i^{j+1} \\ &\quad + D_{{\rm pp},i+1/2} \frac{n_{i+1}^{j+1} - n_i^{j+1}}{\Delta p_{i+1/2}} \end{aligned} \tag{7.17}$$

$$= \frac{D_{{\rm pp},i+1/2}}{\Delta p_{i+1/2}} \left[W_{i+1/2}^{+} n_{i+1}^{j+1} - W_{i+1/2}^{-} n_m^{j+1} \right], \tag{7.18}$$

with

$$w_i = \frac{H_i}{D_{\mathrm{pp},i}} \Delta p_i, \qquad \delta_i = \frac{1}{w_i} - [e^{w_i} - 1]^{-1} \tag{7.19}$$

$$W_i^+ = \frac{w_i}{1 - e^{-w_i}}, \qquad W_i^- = \frac{w_i}{e^{w_i} - 1}. \tag{7.20}$$

which can be calculated very efficiently.

Combining equations 7.16 and 7.18 leads to a tridiagonal system of equations:

$$-A_i n_{i+1}^{j+1} + B_i n_i^{j+1} + C_i n_{i-1}^{j+1} = r_i \tag{7.21}$$

$$A_N = C_0 = 0 \tag{7.22}$$

with

$$A_i = \frac{\Delta t}{\Delta p_i} \frac{D_{\mathrm{pp},i+1/2}}{\Delta p_{i+1/2}} W_{i+1/2}^+ \tag{7.23}$$

$$B_i = 1 + \frac{\Delta t}{\Delta p_i} \left[\frac{D_{\mathrm{pp},i-1/2}}{\Delta p_{i-1/2}} W_{i-1}^+ + \frac{D_{\mathrm{pp},i+1/2}}{\Delta p_{i+1/2}} W_{i+1}^- \right] + \frac{\Delta t}{T_i} \tag{7.24}$$

$$C_i = \frac{\Delta t}{\Delta p_i} \frac{D_{\mathrm{pp},i-1/2}}{\Delta p_{i-1/2}} W_{i-1/2}^- \tag{7.25}$$

$$r_i = \Delta t Q_i + n_i^j. \tag{7.26}$$

The tridiagonal system is then solved using a TDMA[1] (e.g. Press et al., 1992).

7.4.2 Boundary Conditions

Proper treatment of boundary conditions is essential for the analytical as well as the numerical solution of Fokker-Planck type equations. Under no-flux boundary conditions, the Chang & Cooper method can be shown to conserve the particle number (e.g. Park & Petrosian, 1996), which makes this choice useful for code tests. The no-flux condition is equivalent to setting all Fokker-Planck coefficients equal zero at the two momentum bins next to the boundary.

However for our application we need to allow flux through the low momentum boundary, to avoid an unphysical pile-up of particle at the domain edge. This can be done (Borovsky & Eilek, 1986) by truncating the spectrum at a momentum p_{cut} near the boundary and extrapolating $n(p)$ up to the boundary. I.e. every timestep we set $n(p < p_{\mathrm{cut}}) = 0$ and then extrapolate $n(p)$ for a few momentum bins as a power-law. This region usually spans around five to ten gridpoints, depending on the problem.

[1] TriDiagonal Matrix Algorithm

7.4.3 Hard Sphere Equation

To test our implementation it is useful to compare its numerical solution to analytical solutions of the Fokker-Planck equation. Unfortunately time dependent solutions to equation 7.4 are not known. However there have been extensive studies on a similar type of Fokker-Planck equation (Jones, 1970; Schlickeiser, 1984; Park & Petrosian, 1995). In the "hard-sphere approximation" the interaction of a thermal plasma with magnetic turbulence is described similar to elastic collisions between hard spheres considering Coulomb and Fermi interactions (Parker & Tidman, 1958). We follow the analysis of Park & Petrosian (1995, 1996) to test our code against a Hard-sphere equation with the addition of a general power-law term and first order process (eq. 62 in Park & Petrosian (1995)). This equation also includes catastrophic losses and constant particle injection at a single momentum:

$$\frac{\partial n(p)}{\partial t} = \frac{\partial}{\partial p}\left(p^2 \frac{\partial n(p)}{\partial p} - apn(p) + bp^r n(p)\right) - \theta n(p) + \delta(p - p_0)\Theta(t). \tag{7.27}$$

Here $n(p)$ is the isotropic distribution function of CR electrons, a describes advection, b is the loss coefficient, r is the spectral index of the power-law loss terms (for synchrotron radiation $r = 2$), θ is the catastrophic loss coefficient and p_0 the momentum at which particle injection takes place. We implicitly assume an advection coefficient of $D = 1$.

Equation 7.27 is singular at $p = 0$ and $p = \infty$. Its time-dependent solution is not known, however the steady state solution can be found using a Greens function approach (Park & Petrosian, 1995). The corresponding boundary value problem can then be solved by transforming the equation to Kummers equation. See Park & Petrosian (1995) for details. Neglecting catastrophic losses, the steady-state solution can be understood in terms of the dominant timescales acting on each momentum bin. Defining advection, diffusion and loss timescales as:

$$\tau_D = 1/D, \qquad \tau_A = \tau_D/|a|, \qquad \tau_b = \tau_D p^{-\alpha}/|b| \tag{7.28}$$

one finds the critical momentum, where advection and losses are equal:

$$p_c = \left(\frac{|b|}{|a|}\right)^{-1/\alpha}. \tag{7.29}$$

Without loss of generality and for a fixed value of $a = 1$, r and $b \cdot D$ determine the shape of the solution. See (Park & Petrosian, 1995) for a more detailed discussion.

We compare our numerical steady-state solution to the analytical solution for the three cases where advection and losses are dominant on the right or left side of p_c, respectively. We assume $\lambda = 0$, $a = \theta = 1$, $x_0 = 0.1$ and $b \in [-1, 1]$, $r \in [0, 2]$, which leads to $x_c = 1$.

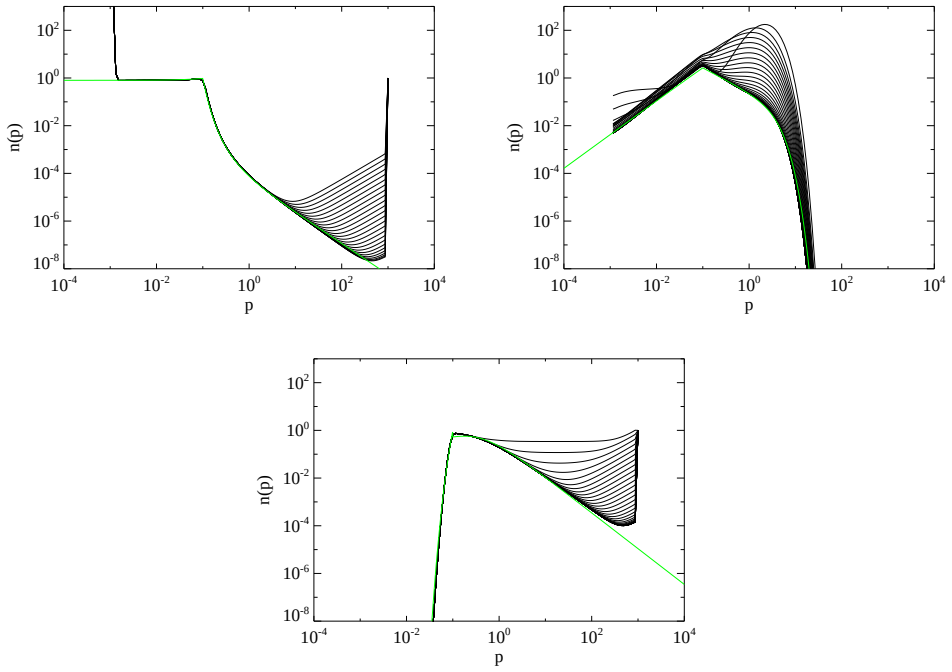

Figure 7.6: Numerical (black) and analytical steady state (green) solutions of the Hard-Sphere Fokker-Planck equation 7.27 (see Park & Petrosian, 1995, for a discussion). In all plots we set $\lambda = 0$, $a = \theta = 1$ and $x_0 = 0.1$. In the upper left: $b = 1, r = 0$; the upper right: $b = 1, r = 2$ and down: $b = -1, r = 0$.

We apply no-flux boundary conditions, which corresponds to setting all coefficients to zero at the domain edges. The simulation is evolved until $t = 20$ with a timestep of $\Delta t = 0.04$.

Our results are shown in figure 7.6, where the analytical solution is plotted in green and the numeric solutions are $\Delta t = 0.5$ apart. In all three cases, the numerical steady state solution agrees well with the analytical solution. Boundary effects are clearly visible at the edges of the computational domain, as expected. These can be dealt with by allowing loss through the boundary using the expansion technique described in section 7.4.2. We conclude that our code is able to properly handle advection, diffusion and cooling in the hard-sphere case.

7.4.4 Convergence

It is known from previous studies (Park & Petrosian, 1996), that the Chang & Cooper method performs very well even for a small number of momentum bins. This is essential for astrophysical applications, where gas dynamics is often sampled with millions of particles/cells. Only a coarse momentum grid over a wide range of particle momenta is going to give the speed-up needed to perform large simulations.

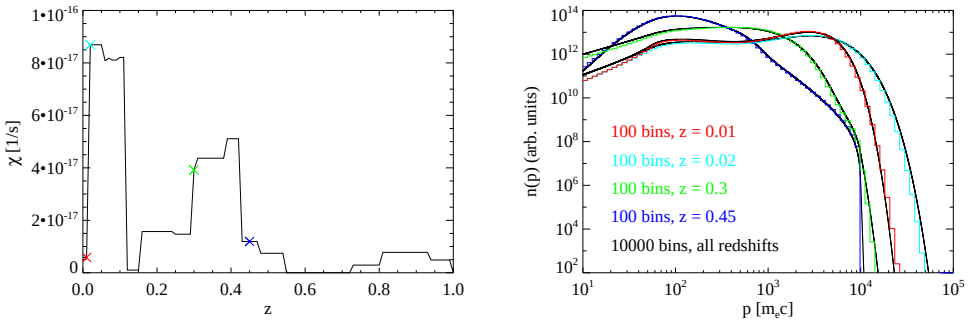

Figure 7.7: Left panel: Evolution of the systematic energy gain with redshift for a cluster as given in Cassano & Brunetti (2005). Output times are marked with crosses and are colour coded. Right panel: CR electron spectra of the same cluster at different redshifts, simulatated on a logarithmic momentum grid with 10000 (black) and 100 (colour coded) points. The colours correspond to crosses in the left panel.

To verify and test the situation for radio halos we use data from Cassano & Brunetti (2005) to follow the evolution of the CR electron spectrum in a galaxy cluster with mass $10^{15}\,M_{\odot}$ from redshift 1 to 0. They use the Press-Schechter formalism to obtain the turbulent energy injected by cluster mergers and subsequently the time evolution of the cluster wide reacceleration coefficients.

In figure 7.7 we show (left panel) the value of the systematic energy gain with redshift as given in Cassano & Brunetti (2005). We mark the spectra shown in the right panel with crosses. Further we assume a number density $n_{\rm th} = 10^{-4}\,{\rm cm}^{-3}$ and a magnetic field of 1μG. Using a power-law injection spectrum with spectral index -1.5 and open boundary conditions, we calculate the time evolution of the clusters CR electron spectrum, assuming a logarithmic momentum grid with 100 and 10000 grid points. We plot the spectra at four different redshifts in the right panel of figure 7.7 (high resolution spectra in black, low resultion in green).

A comparison of the spectra with Cassano & Brunetti (2005) yields a good agreement for momenta larger than $2\,{\rm m_e c}$. At lower momenta our treatment of the boundary condition impacts the spectra and leads to differences which are not relevant for the synchrotron brightness of the cluster.
The differences between the low resolution run (colours) and the high resolution run (black) are within the range expected from the difference in grid spacing. We therefore conclude that our code is converged at 100 logarithmic momentum bins.

7.5 Synchrotron Solver and Map Making

Synthetic observations are very useful to study the astrophysical objects and compare predictions from simulations with observations. These usually come in the form of projections of physical quantities and their derivatives. The increasing complexity of the astrophysical

phenomena and their simulations poses ever growing demand on computational power in extracting these maps from the data. In our case we have to compute thermal and non-thermal quantities from millions of particles for several hundred snapshots. In particular, the calculation of the synchrotron emission from arbitrary CR spectra in an isotropically tangled magnetic field is computationally demanding. The emissivity of a volume of gas, containing a population of CR electrons, is given by (e.g. Ginzburg & Syrovatskii, 1965; Longair, 1994):

$$j_\nu = \frac{\sqrt{3}e^3 B}{m_\mathrm{e}c^2} \int_0^\infty \int_0^{\frac{\pi}{2}} \mathrm{d}E_\mathrm{e}\mathrm{d}\theta \, \sin^2\theta F\left(\frac{\nu}{\nu_c}\right) N_\mathrm{e}(E), \tag{7.30}$$

where B is the magnetic field, e and m_e are electron charge and mass, θ is the pitch angle, $F(x)$ is the synchrotron kernel, ν and ν_c are the frequency and critical frequency, and $N_\mathrm{e}(E)$ is the electron spectrum.

To match the growing computational demand we implemented a new MPI-parallel map making code P-SMAC2 in C. It uses the gather approach (Dolag et al., 2005) to accurately compute the contribution of every particle to a given pixel. We make extensive use of function pointers to modularise the code and allow for easy extension and implementation of additional emission models. So far the code projects a number of thermal and non-thermal quantities:

- Gas and dark matter density, velocity and temperature
- Bolometric X-ray luminosity
- Magnetic field, Faraday rotation measurements and Alvén velocity
- Thermal and kinetic Sunyaev Zeldovich effect, Compton Y-parameter
- γ-ray emission from hadronic CR interactions via pion decay
- Synchrotron emission, polarised intensity, Stokes parameters, polarisation degree and angle from a secondary model (Brunetti & Blasi, 2005) and arbitrary CR electron spectra
- Synchrotron emission, polarised intensity, Stokes parameters, polarisation degree and angle from power-law CR electrons, using analytical formulas
- Ionised Hydrogen and Helium fractions from radiative transfer simulations (Petkova & Springel, 2009)

The code reads GADGET format 2 (Springel, 2005) and PIERNIK (Hanasz et al., 2008) snapshots and features a serial tree for neighbour finding.

We use a simple trapezoidal integration rule with 200 steps in energy and pitch angle in the synchrotron solver. We logarithmically integrate over six decades in energy with

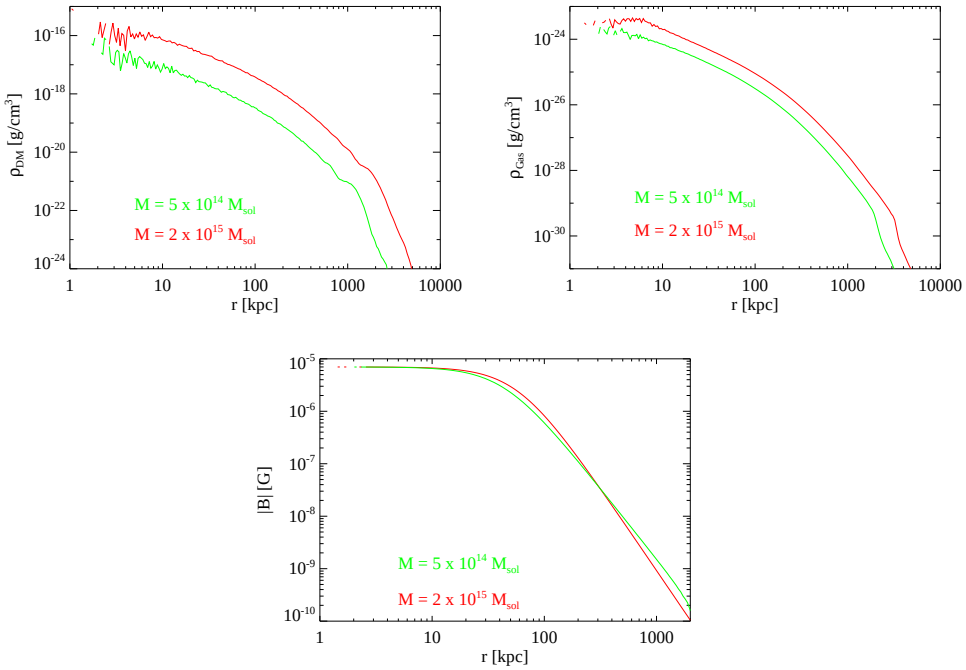

Figure 7.8: Profiles of dark matter density (top left), gas density (top right) and magnetic field strength (bottom) of both cluster in the collision. The larger one is marked red, the small one green.

the second decade centred on the brightest particle energy. For a power-law distribution of CR electrons this corresponds to an accuracy of the solver of about 3%.

We apply the code to our idealised simulation of a cluster merger in the next section.

7.6 Cluster Merger

As a first application of our code we run an idealised MHD simulation of a galaxy cluster merger using GADGET-3 (Springel & Farrar, 2007; Dolag & Stasyszyn, 2009). This setting gives us control over all basic parameters of the merger as well as a firm expectation on the evolution of the thermal gas. It does not have to be calculated in comoving space so we can apply the formalism developed in section 7.4.1 without any changes in post-processing.

7.6.1 Setup

We set up a collision of two halos with a Hernquist profile (Hernquist, 1990) with a scale length of 500 kpc. We use a baryon fraction of 0.17 and a total number of 256^3 DM and gas particles. The total mass of the system is $2.5 \times 10^{15} M_\odot$, with a mass ratio of the clusters of 1:4. We sample the distribution function out to r_{200} and set the temperature of the gas simply via $u(r) = 3/2\sigma^2_{\rm 1D}(r)$, where $\sigma_{\rm 1D}$ is the one dimensional velocity dispersion of

the dark matter particles. This places the SPH particles only in approximate hydrostatic equilibrium, thus we evolve both clusters in isolation for a few Gyrs without magnetic fields to allow the gas to settle.

Both clusters are then set for a head-on collision (Ricker & Sarazin, 2001) on a zero energy orbit at a distance equal to the sum of their r_{200}. The box is centred on the centre of mass of the system. We initialise a divergence free, large scale magnetic field on a coarse grid by realizing a random magnetic potential on the grid. We use a central difference scheme to compute the rotation of the potential on every grid point. We choose a cellsize of five times the mean particle distance (here ≈ 100 kpc) to avoid undersampling of the field by the SPH particles in low density regions. The field strength was set to approximately follow the gas density with a central field strength of $7\,\mu$G, as found by Bonafede et al. (2010) for the Coma cluster. In figure 7.8 we plot radial profiles of the dark matter density, gas density and magnetic field of both clusters.

We evolve the merger simulation for 3.65 Gyr using the standard GADGET-3 viscosity scheme and magnetic diffusion (Bonafede et al. in prep). Afterwards we run our Fokker-Planck code in postprocessing on the 210 output snapshots to evolve CR electron spectra on 100 logarithmic bins running from $p_{\rm min} = 5\,m_{\rm e}{\rm c}$ to $p_{\rm max} = 10^7\,m_{\rm e}{\rm c}$. We use the reacceleration model described in section 7.3 with $\eta = 0.25$. This was shown by Cassano & Brunetti (2005) to be a reasonable choice. These authors argue that the exact value of η does not have a strong influence on their results. As a complete treatment of the subscale plasma physics is beyond the scope of this paper, we consider this choice a conservative estimate. Other mechanisms like higher order and non-resonant coupling of fast modes and Alvénic processes are only going to increase the importance of reacceleration on the spectrum.

To avoid overprediction of radio luminosity in shocks we limit the turbulent velocity to 50% of the sound speed. This is a conservative approach because our formalism is not capturing the full physics in shocks. Fermi I acceleration predicts additional injection of power-law electrons dependent on the Mach number. On the other hand it is known that clusters like Coma experience *sub-sonic* turbulence in the core of its ICM. So we can neglect this for now.

CR electron injection is treated by a secondary model (Dennison, 1980; Ensslin et al., 2007; Brunetti & Blasi, 2005) which is normalised to 1% of the thermal energy density (Donnert et al., 2010). We use the high energy approximation to the cross-section as given in Brunetti & Blasi (2005). We assume a CR proton spectral index of 2.375 and momentum cutoff at $p_0 = 2m_{\rm p}c$. In figure 7.9 we plot the injection function for a particle with $n_{\rm th} = 10^{-3}\,{\rm cm}^{-3}$.

The runtime of our Fokker Planck code on 32 processors was about 12 hours, which is equivalent to 10^{-4}sec/particle/Gyr/CPU.

We use P-SMAC2 to make projections of the most important MHD quantities (figures 7.10 to 7.14).

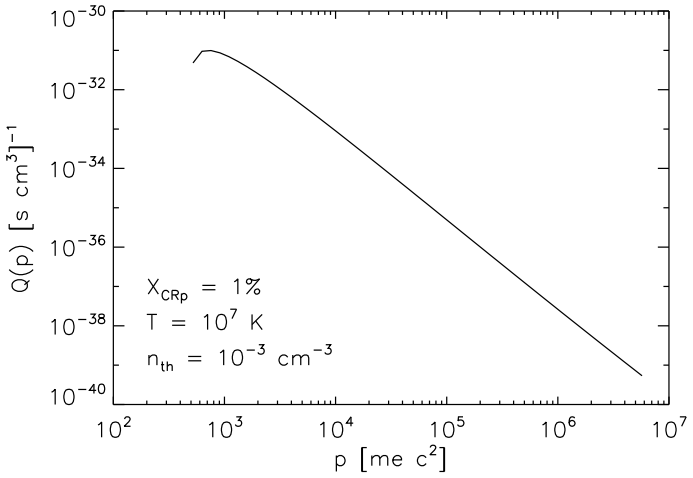

Figure 7.9: Injection function of CR electrons from secondaries (Brunetti & Blasi, 2005) for a gas with thermal number density $n_{th} = 10^{-3}\,cm^{-3}$, $T = 10^7\,K$ and a CR proton fraction of 1 %.

7.6.2 Results

MHD Quantities

In figures 7.10 to 7.14 we show projections of dark matter density, gas density, temperature, velocity divergence, and magnetic field strength, respectively. The panels from left to right are at times: of first contact at $\approx 1\,Gyr$; after first dark matter core passage at $\approx 1.4\,Gyr$; at second core passage after $\approx 1.8\,Gyr$; after fourth core passage at $\approx 2.74\,Gyr$ and at the end of the simulation at $\approx 3.65\,Gyr$. A video of the cluster collision can be found at http://www.mpa-garching.mpg.de/∼jdonnert/joined.avi or upon request by e-mail[2] to the author.

Upon *first approach* the dark matter halo of the small cluster gets distorted by the potential of the large one. A shock forms at the contact surface of the two halos and the gas gets heated, well visible in the temperature and velocity divergence projection. The velocity divergence at the left side of the system shows fluctuations around zero, which is a residual of the setup procedure and does not affect the results presented here.

During the *first core passage* parts of the small dark matter halo get stripped by tidal interactions. In the gas density projection both clusters are not separable anymore, suggesting that the gas core of the small cluster got disrupted. Two shock fronts are travelling along the infall direction of the small cluster. The temperature map shows a circular region on the left side of the projection. Here the shock from the infall is travelling outwards, compressing and therefore heating the gas. On the other side of the object the gas is heated strongly as well by series of complex out-going shocks. There is no significant amplification

[2] jdonnert@mpa-garching.mpg.de

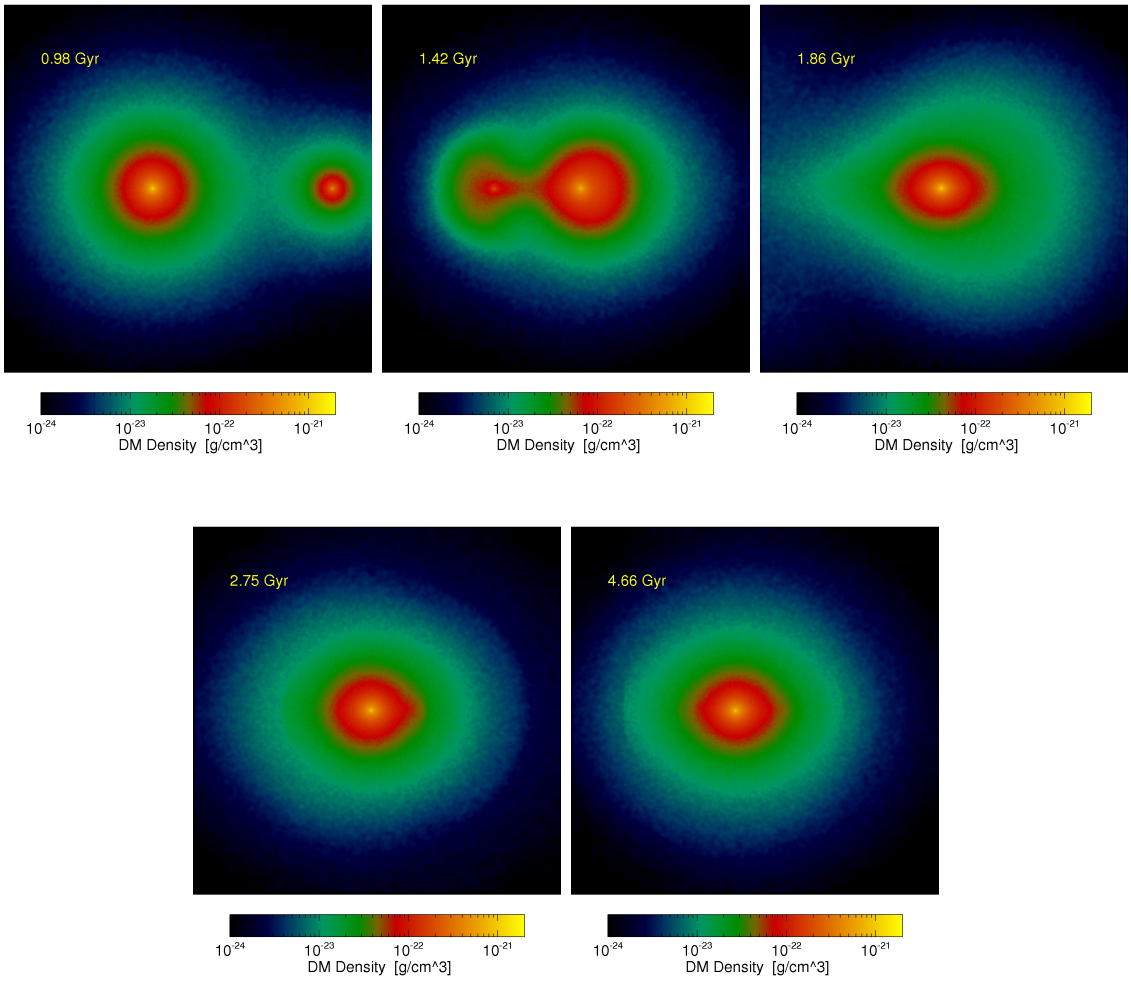

Figure 7.10: Projections of dark matter density of the cluster collision at five different times. Each sub-figure covers 3x3 Mpc.

of the magnetic field strength visible yet apart from adiabatic compression .

At the *second core passage* the remaining dark matter core of the small halo drives only weak shocks inside the central cluster. In contrast the lower mass of the in falling core stirrs the large cluster and induces turbulence(see figure 7.13 panel 3 centre). This is visible in the amplified magnetic field of $\geq 10\,\mu G$ in the centre. At this time we expect the strongest radio halo to form. The gas structure of the cluster is distorted into an triangular shape in this projection. The dark matter halo is elongated along the infall direction.

After the *fourth core passage* dark matter and gas structure of the halo appear already remarkably spherical. The temperature shows rich substructure around around the core where the gas starts to settle in hydrostatic equilibrium again. There are no strong shocks visible anymore in the velocity divergence - the cluster relaxes towards its quite state. The

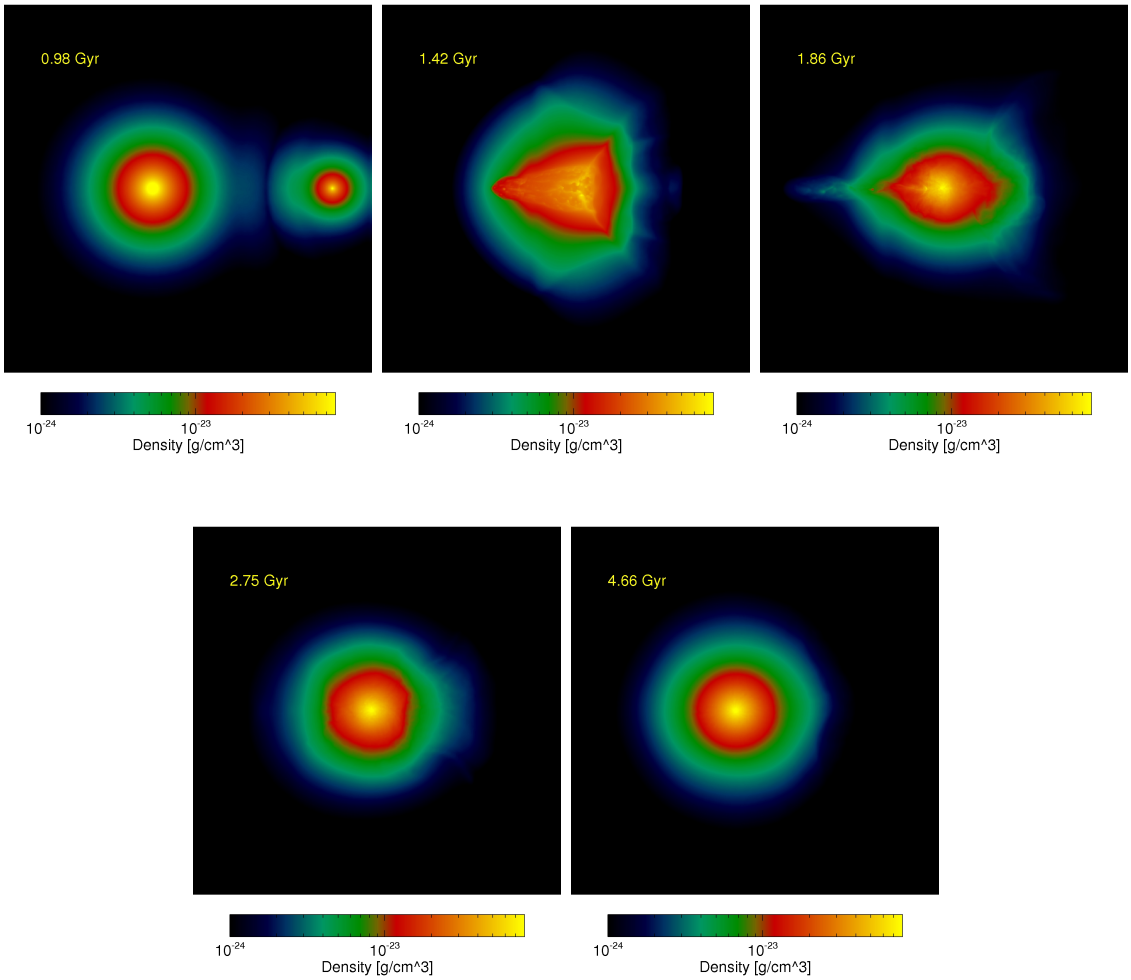

Figure 7.11: Projections of the gas density of the cluster collision at five different times. Each sub-figure covers 3x3 Mpc.

magnetic field has been amplified to its largest values and shows a clearly non-spherical structure. At the *end of the simulation* the cluster is about to relax. The dark matter is still slightly elongated in the direction of the merger. The gas is continuing to settle and the substructure in temperature is evening out. No strong shocks are visible anymore in the velocity divergence. Due to magnetic diffusion the magnetic field is decaying from its large values to the μG range, while maintaining its rich substructure.

Projected Radio Emission

Using our numerical synchrotron solver and projection algorithm P-SMAC2, we build synthetic observations of the radio halo expected from the idealised cluster collision.

In figures 7.15 and 7.16 we show the projected synchrotron emission from a population

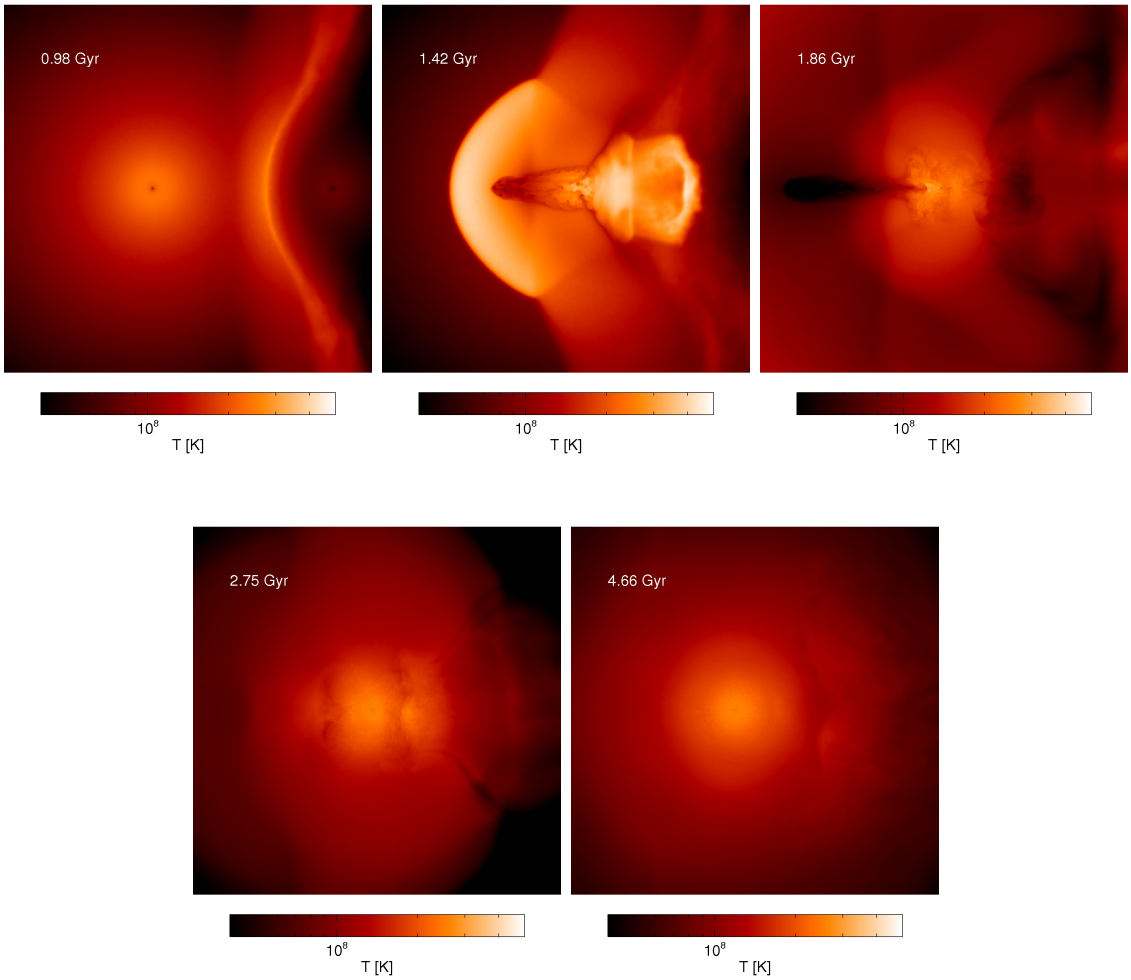

Figure 7.12: Projections of the gas temperature of the cluster collision at five different times. Each sub-figure covers 3x3 Mpc.

of reaccelerated secondary electrons. The panels correspond to the same times as figures 7.10 to 7.14. Again a movie is available at
http://www.mpa-garching.mpg.de/∼jdonnert/synchro.avi or upon request per email.

Before the merger the two sub-clusters show synchrotron emission simply due to the secondary model. It is strongly localised on the densest parts because the steady state spectrum of secondaries scales as density squared. To reproduce the bimodality this has to be below the observational limit of todays instruments.

At the *first core passage* the cluster lights up due to the shock induced by the disruption of both gas cores.

During the *second core passage* the remaining DM core of the small cluster stirrs up the inner part of the system, injecting sub-sonic turbulence in the central 1 Mpc region of

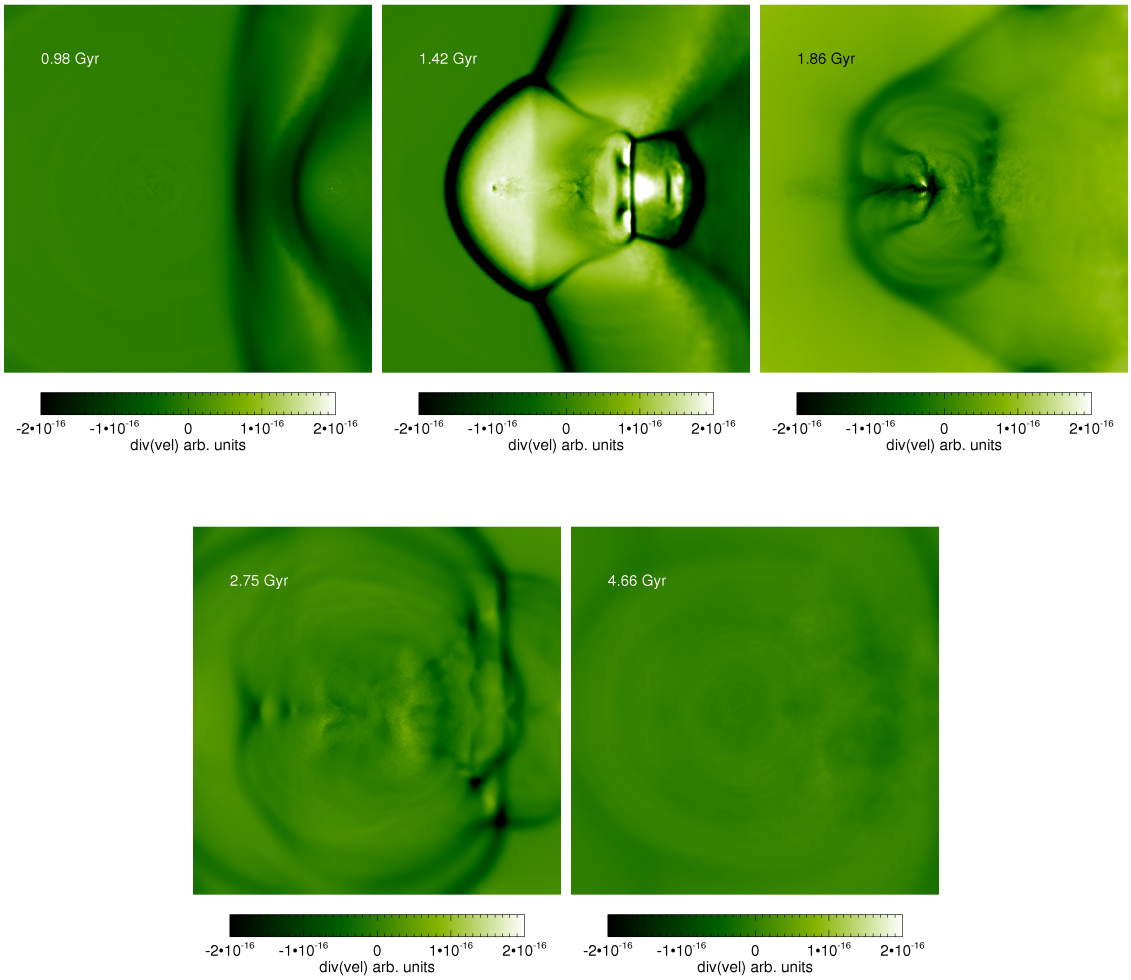

Figure 7.13: Projections of the velocity divergence of the cluster collision at five different times. Each sub-figure covers 3x3 Mpc.

the new cluster. A small shock is visible only in the videos of the collision. This time can be identified with the radio halo in this model.

This behaviour is repeated less strongly at the *fourth core passage* as the small DM core continues to oscillate in the gravitational potential of the large cluster.

At the *end of the simulation* the radio emission declines to the level induced by the hadronic injection. The cluster becomes "invisible".

Lightcurve

For further investigation of the dynamics of the model, figure 7.17 shows a plot of the turbulent energy (black), the reaccelerated synchrotron emission (red), the mean magnetic field strength (green) and the distance of the two dark matter halos (blue) in a region of

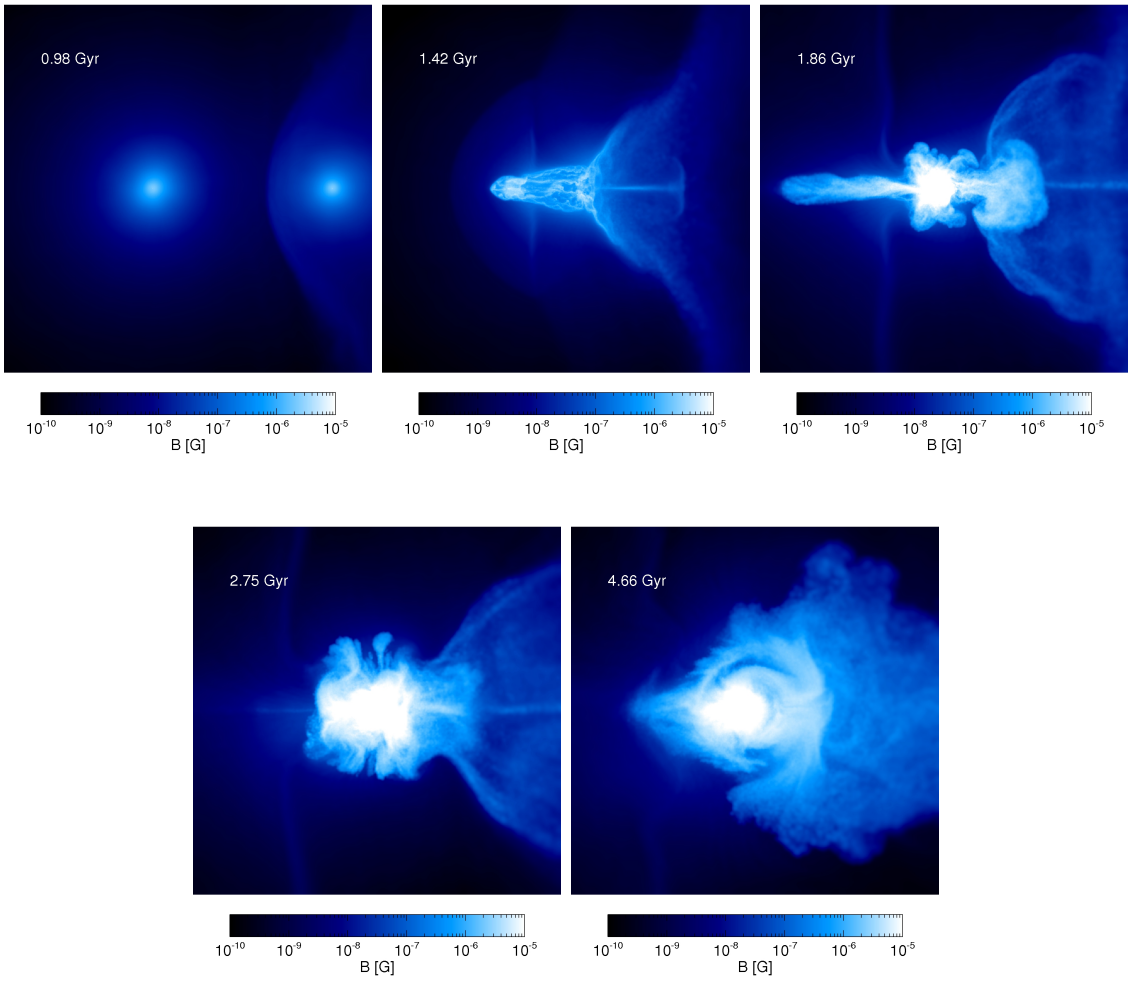

Figure 7.14: Projections of the magnetic field strength of the cluster collision at five different times. Each sub-figure covers 3x3 Mpc.

1 Mpc around the centre of mass of the system. We recommend looking at the movies of the collisions as well.

The *first encounter* is seen at the first minimum of the blue line at $t = 2.3\,\mathrm{Gyr}$, where the two dark matter halos "meet" for the first time. The synchrotron emission peaks to its highest value simply because the impending shock corresponds to large turbulent velocity from divergent components. The actual turbulent component is small, suggested also by the magnetic field. It is amplified only slightly at this time, due to adiabatic compression. Note that the turbulent energy here is calculated with the limiter employed for the reacceleration coefficient.

The *second encounter* at 1.8 Gyr then results in small shocks visible in the movies and in a small spike in the synchrotron emission. Note that the magnetic field is already at

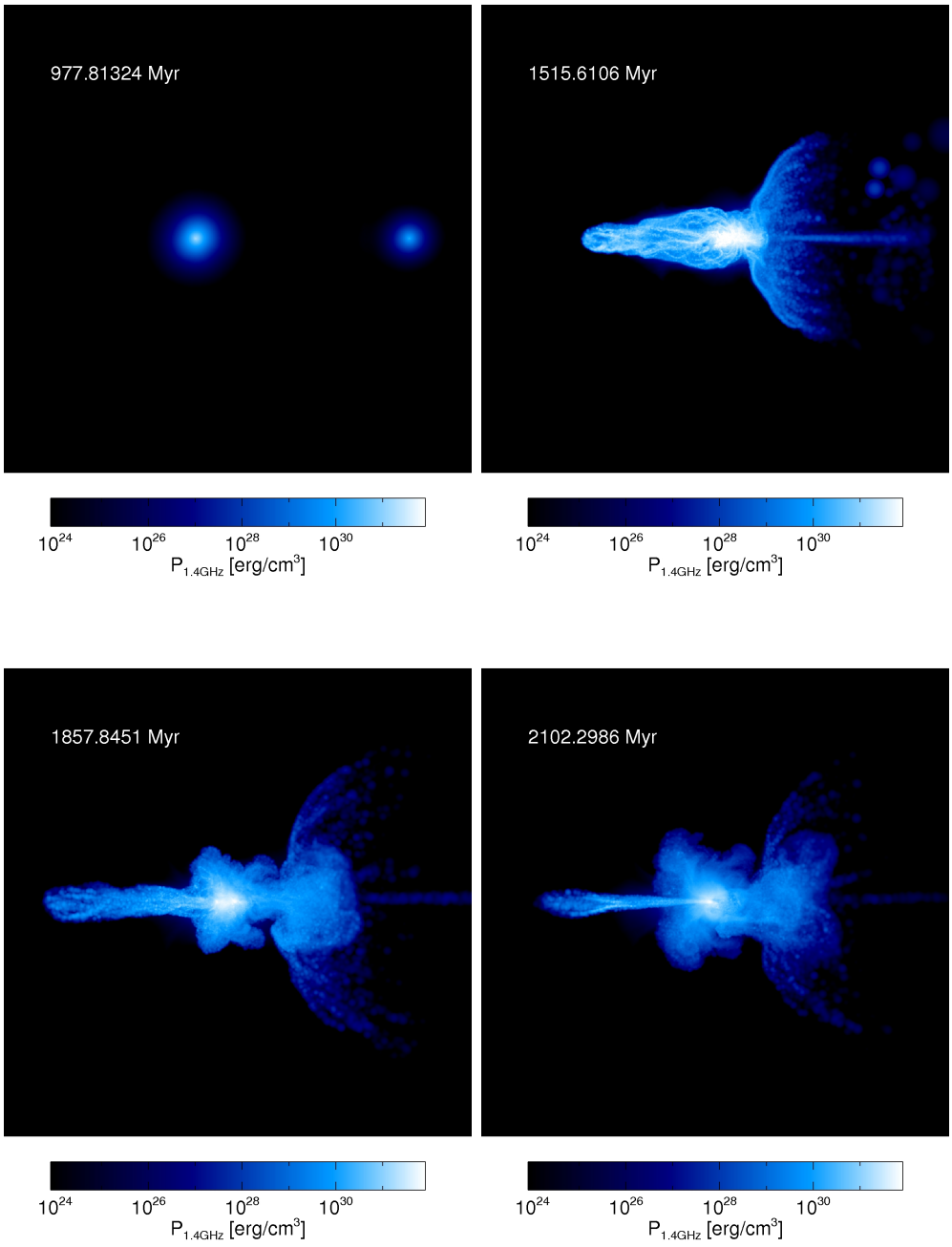

Figure 7.15: Projections of synchrotron luminosity from *reaccelerated* secondary electrons. The upper right panel corresponds to the maximum in synchrotron luminosity. Again each sub-figure covers 3x3 Mpc.

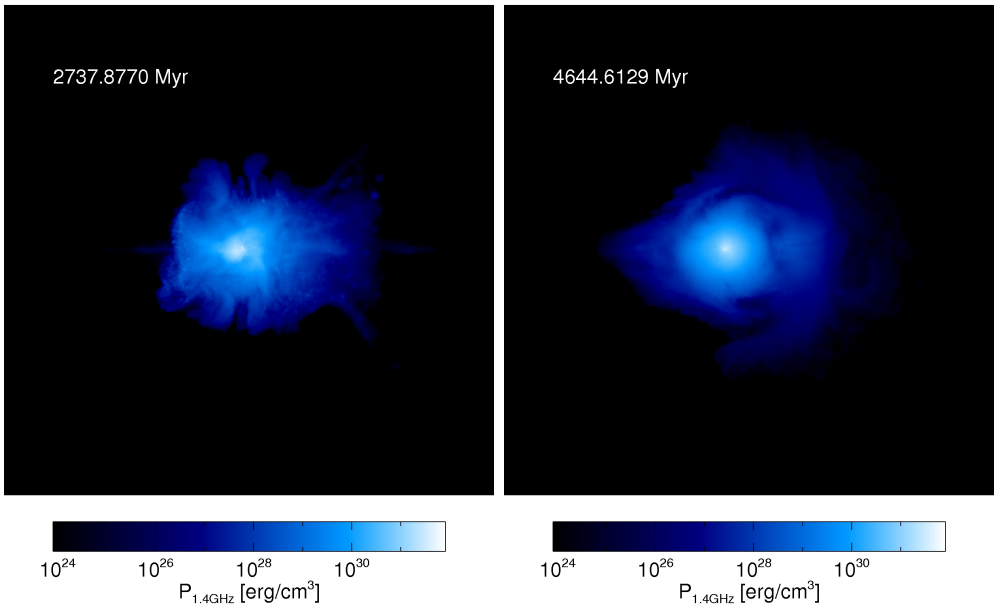

Figure 7.16: Projections of synchrotron luminosity from *reaccelerated* secondary electrons. Again each sub-figure covers 3x3 Mpc.

its maximum value here. Sub-sonic turbulence is therefore strongest between the first and the second DM core passage. The radio halo can therefore be associated with the second hump at 1.5 Gyr after setup.

With increasing time the total synchrotron brightness decays withing a Gyr by approximately a factor of 10. The decay of the turbulent energy is slower as expected from the reacceleration model. The magnetic field strength stays approximately constant within 2 to 3.5 Gyr, as diffusion happens on larger timescales. The DM cores oscillate throughout the whole time, every minimum is followed by a relative maximum in the radio luminosity.

CR Electron Population

To understand what the process of turbulent amplification means in this model, we plot in figure 7.18 the central 600 particle CR electron spectra in gray and overlay a few in black for visibility. We mark the synchrotron bright region for the 90% of the maximum magnetic field in the region in light gray. This is only to guide the eye, as every particle has a different magnetic field, this region is different for every particle in the simulation.

The upper two panels in figure 7.18 show the CR electron spectra before the merger. The self-similar shape from the injection function in figure 7.9 is clearly recognisable. The flatness at low momenta is due to the injection and Coulomb cooling. At intermediate momenta the high energy approximation to the proton-proton cross-section makes the stationary spectrum slightly bent. At high momenta the standard power-law is injected.

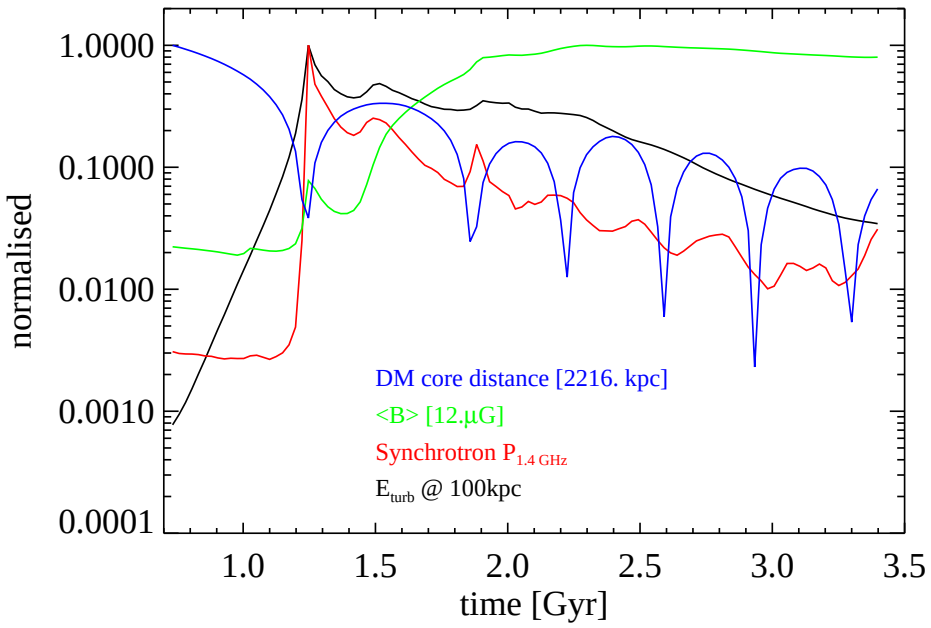

Figure 7.17: Turbulent energy at 100 kpc (black), mean magnetic field (blue), DM core distance (blue) and synchrotron emission (red) over time from a region with radius 1.5 Mpc centred on the CoM of the collision.

The middle two panels show the state of the CR spectra in the radio halo stage of the cluster. The spectra show significant deviation from the power-law injection function at the synchrotron bright momenta. The scatter of different particles is large, as turbulence and cooling is now significantly different between particles. In addition turbulence has amplified magnetic fields, so lower particle momenta are probed by the synchrotron kernel. This is the mechanism of "switching the halo on" in this type of model.

The last two panels correspond to the decay phase. The CR electron spectra cool back into the steady-state shape, similar to the upper-left panel. The scatter in shape between spectra decreases. The "brightness hump" moves from momenta of 10^4 towards 10^3 and becomes less prominent. This results in a decrease in synchrotron brightness given a fixed magnetic field.

Radio Halo Spectrum

We investigate the synchrotron spectrum expected from our model.

In Figure 7.19 we show the radio spectrum of the system at different times. We normalise the spectrum to its value at 430 MHz at 1.72 Gyr after setup. The observed spectrum from the Coma cluster (see Thierbach et al., 2003, and ref. therein) is overplotted in black diamonds.

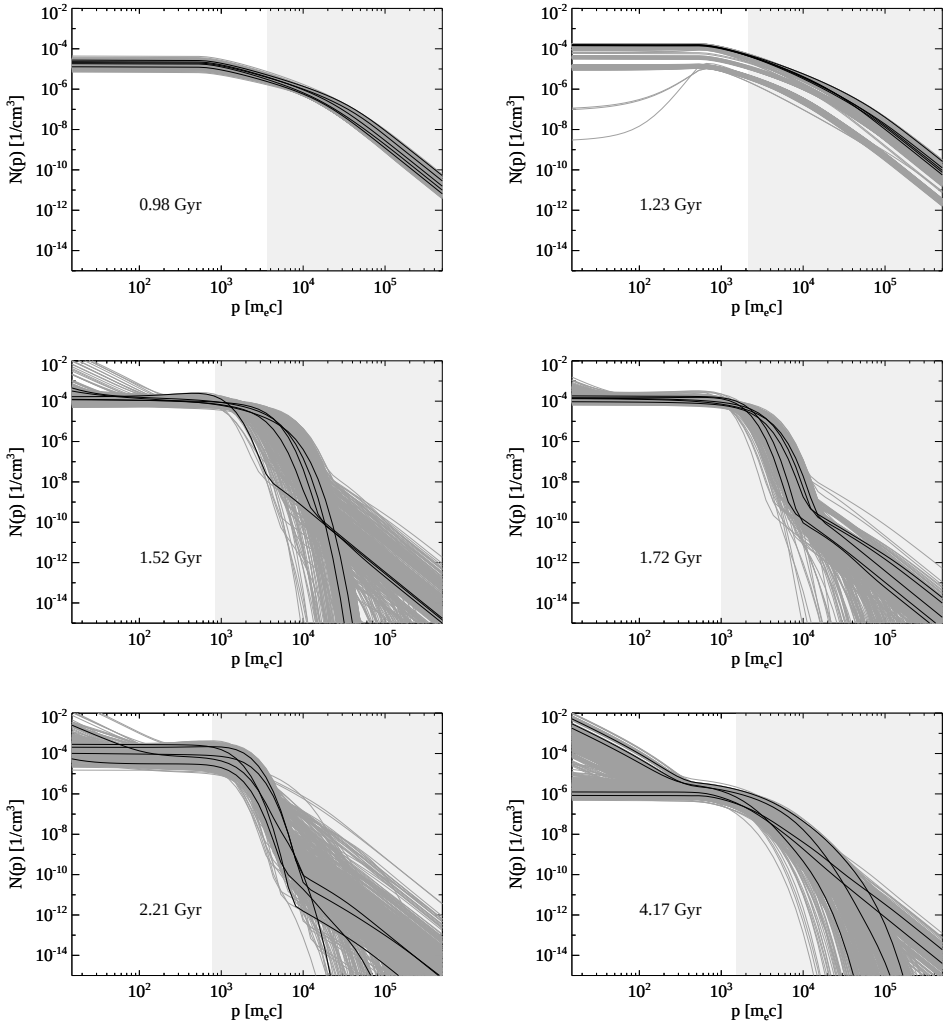

Figure 7.18: CR electron spectra of the brightest 1000 particles in a spherical region around the centre of mass of the merger with radius 1 Mpc in dark gray. We mark a few in black for visibility. The synchrotron bright region from 90% of the maximum magnetic field at 1.4 GHz is marked in light gray.

At early times in the simulation the total luminosity at all frequencies is low, so is the red curve. The spectrum follows an approximate power-law, as expected from hadronic models. During the merger the cluster becomes synchrotron bright and its luminosity increases by a factor of ten at 1.4Ghz. The synchrotron emission now shows stronger deviations from the power-law behaviour and becomes *bent*. The shape of our spectrum is very similar to the one shown in Schlickeiser et al. (1987), typical for a reacceleration model. The simulated spectrum fits the observed one in Coma remarkably well. Note that the spectral break in Coma is a major complication for pure hadronic models (see discussion in Donnert et al., 2010). For the first time a direct simulation of radio halos

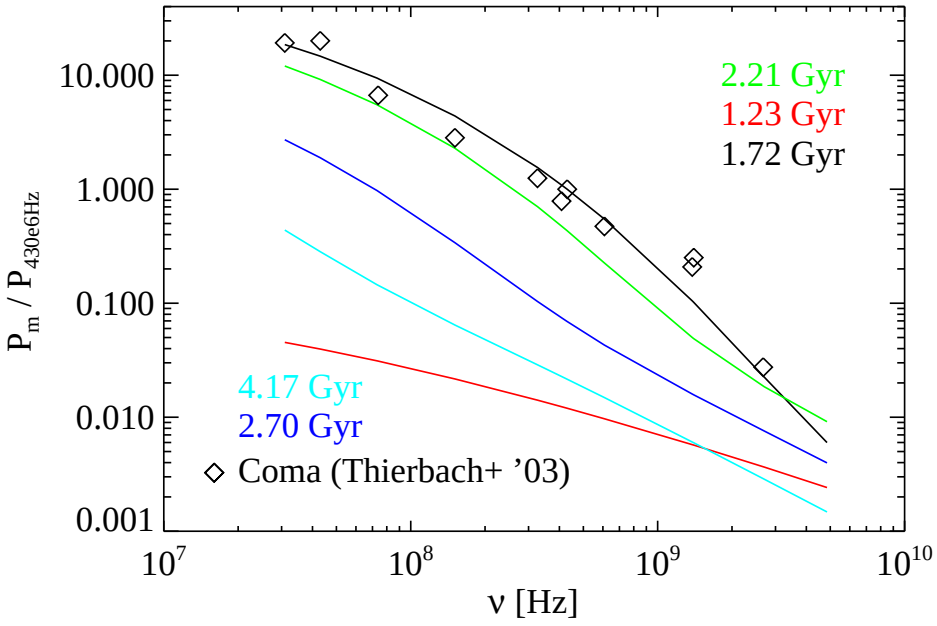

Figure 7.19: Synchrotron spectrum of the cluster merger at different times. In red before the merger. In black at the time shortly after maximum radio luminosity. We include observations of the Coma cluster (see Thierbach et al., 2003, and ref. therein) as black diamonds.

predicts a bend spectrum without further model "tuning".

At later times the cooling of the CR electron population leads to an *aging* of the synchrotron spectrum. It total, normalisation decreases and the break is shifted to lower frequencies (lower ν means lower particle momenta).

Comparison with a Purely Hadronic Model

It is instructive to demonstrate the differences between a reacceleration and a purely hadronic model, given the discussion in the community. We show in figure 7.20 synthetic radio observations from a hadronic model for radio halos. This corresponds to setting $D_{\rm pp} = 0$ in the evolution equation.

The corresponding synchrotron brightness then scales in our case as (Dolag & Ensslin, 2000):

$$j_\nu \propto n_{\rm th}^2 \frac{B_\perp^{\alpha_\nu - 1}}{B^2 + B_{\rm CMB}^2}. \tag{7.31}$$

A comparison by eye of figure 7.20 with figures 7.11 and 7.14 yields that this is indeed the case. In general the emission is centrally more peaked when compared with reacceleration models (see also Donnert et al., 2010).

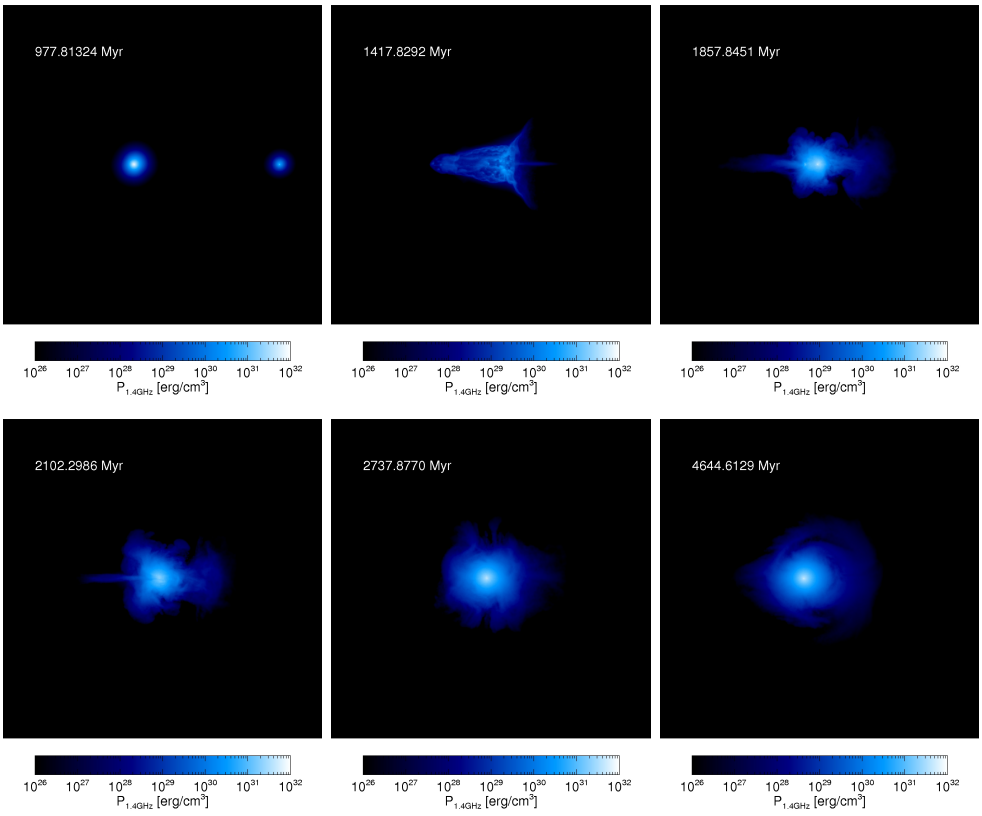

Figure 7.20: Projections of synchrotron luminosity from *pure secondary electrons*. Again each sub-figure covers 3x3 Mpc.

To emphasise the differences in time evolution and dependence on the underlying model we show in figure 7.21 a comparison of the lightcurves. In black we show the X-ray luminosity, in red - the synchrotron emission from the reacceleration model, in pink - the synchrotron emission from the pure hadronic/secondary model and in green the magnetic field evolution as before.

As expected the radio luminosity from the hadronic model follows an evolution that is the superposition of the magnetic field and density (X-ray) evolution. Note that at 1.5 Gyr, when the reacceleration model peaks in brightness, the hadronic model is not at its maximal emission, because the magnetic field is not fully amplified yet. Also the radio emission from the reacceleration model does not follow magnetic field or density evolution, except for the shock events at the first and second core passage (1.2 and 1.8 Gyr).

This illustrates the fundamental differences in the mechanisms and predictions of the two models. A video of the evolution of the two models in the radio regime can be download from
http://www.mpa-garching.mpg.de/∼jdonnert/synchro_joined.avi or on request via email to the first author.

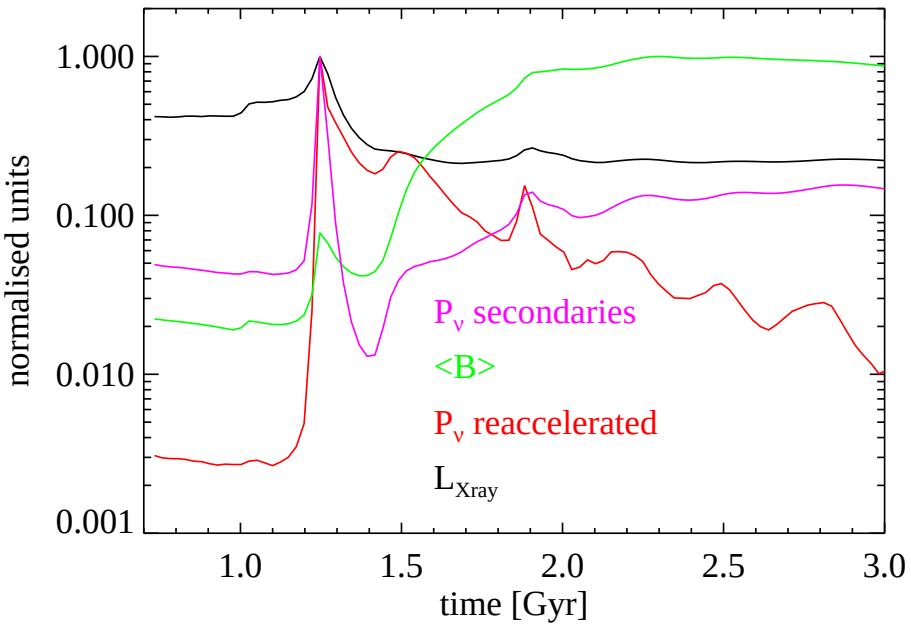

Figure 7.21: Lightcurve comparison between a secondary (pink) and the reacceleration model (red). We plot the magnetic field evolution in green. In black we show the evolution of the *bolometric X-ray luminosity*.

7.7 Conclusions

We have investigated for the first time a reacceleration model coupled to astrophysical MHD simulations.

We estimate turbulence in the SPH code GADGET-3 with RMS velocity dispersion on the kernel scale. Using simulations of ideal sub-sonic and supersonic turbulence, we are able to show that this formalism gives reasonable estimates on the local turbulent energy, when compared with standard grid-FFT-methods. We argue that this is due to the dominance of large scales in the power-spectrum, which are not much affected by the force-smoothing employed in the numerical algorithm.

Using the particle reacceleration mechanism proposed in Brunetti & Lazarian (2007) we introduce a novel implementation of CR electron momentum transport based on Chang & Cooper (1970) to be used in post-processing with MHD-GADGET. The method efficiently follows the evolution of millions of particles over Gyrs of time. We compare our code with a number of analytical solution, like the Hard-Sphere equation and the halo evolution from Cassano & Brunetti (2005), finding excellent agreement. This way we are able to demonstrate accuracy and convergence.

We introduce a new projection code for simulation outputs from particle and grid codes. Aside from a number of thermal and non-thermal emission mechanisms it features

a synchrotron solver for arbitrary particle spectra. This way we are able to extract synthetic observations of radio emission from our simulations.

We apply our new codes to a simulation of an idealised cluster collision. Two clusters are set up with a mass ratio of 1:4 on a zero energy orbit following Springel & Farrar (2007) at a resolution of 256^3 particles. The collision is simulated using the MHD-GADGET code and the evolution of CR electrons spectra is followed over a few Gyrs. We use a hadronic injection model normalised to 1% of the energy density of the thermal gas of the ICM.

- We build projections of density, DM density, temperature, velocity, magnetic field, and synthetic radio observations of the cluster merger. This way are able to show that in this model the DM core of the incoming cluster injects turbulence during the major merger, amplifies magnetic fields and reaccelerates CR electron to synchrotron bright momenta.

- A lightcurve of the time evolution of the system is presented. This way we are able to show that the luminosity of the system drops within 1 Gyr after the merger event by a factor of 10, while the magnetic field stays approximately constant. This way we are able to establish the connection between radio luminosity and turbulence in this model.

- Showing a number of CR electron spectra at different times of the merger event, we understand that the increase in radio luminosity is due to the shift of particles from low synchrotron dark momenta to high synchrotron bright momenta.

- We investigate the radio synchrotron spectrum, predicted from our reacceleration model over time. We find a systematic rise and decline in overall radio luminosity by a factor of 10. Shortly after the maximum brightness, our simulated cluster fits the observed radio synchrotron spectrum of Coma.

- A comparison of our model to a purely hadronic approach is done. From projections of radio synchrotron luminosity of these models we find that a secondary models is generally more peaked in the centre and follows the combined density and magnetic field evolution of the system.

- We use a lightcurve approach to demonstrate that radio halos from reacceleration model evolve very differently from hadronic halos. Specifically reaccelerated halos show the observed transient behaviour, curved spectrum and flat spatial distribution.

We conclude that reacceleration of CR electrons in the ICM during a major merger event of galaxy cluster can be an important process, that is *not to be neglected*. The combined magnetic field amplification and turbulent reacceleration of CR electrons by turbulence makes this process important for the formation of radio halos.

7.8 Acknowledgements

J.D. thanks F.Kitaura for helpful discussions and the organisers of the PiTP summer school 2009 for acceptance and a great experience. Section 7.6 is based on knowledge acquired at the school.

Chapter 8

Conclusions and Outlook

With this work we present a detailed investigation of two models for the diffuse non-thermal emission from galaxy clusters, i.e. radio halos.

In chapter 5 we used a Coma-like cluster from a cosmological MHD simulation and three hadronic models to provide a detailed comparison with observations of the radio halo in Coma.

We demonstrate that our simulated galaxy cluster fits well the observations of mass and magnetic field structure of the real Coma cluster. Our three hadronic models use a constant CRp to thermal gas normalisation as well as a radial scaling motivated from simulations. To cover an extremal case a third model with up-scaled magnetic field is shown as well. We use the high energy approximation to the proton-proton cross-section to obtain the CRe spectra.

Assuming realistic magnetic fields we are able to show:

- None of our three CR proton models are able to fit the spatial distribution of radio surface brightness.

- A fit of the radio surface brightness profile by a purely hadronic model results in an excess of CR protons in the cluster outskirts that contradicts observations.

- The radio emission relative to the X-ray surface brightness observed is too steep at low X-ray brightness. This is in-line with our previous finding.

- The Sunyaev-Zeldovich decrement is not sufficient to explain the break in the radio synchrotron spectrum observed in the Coma cluster. An excellent fit of our simulated cluster to the observed Compton-Y parameter in the Coma cluster confirms the validity of our thermal model for the inner cluster region.

- The expected γ-ray emission from the our simulation is below the lower-limit set from FERMI recently. The observations are therefore not able to constrain the CR proton content of clusters yet.

We extend our investigation of hadronic models to a sample of 16 galaxy clusters from a cosmological MHD simulation. We again use the three hadronic models described before and show full-sky maps of the simulation volume. A comparison with observed rotation measurements in clusters yields a good match in the important outer parts of the cluster. For comparison we use a sample of 15 galaxy clusters observed. We show

- A comparison of radio surface brightness profiles of the simulated and the observed clusters. We find that our simulated clusters are too radially steep to fit the observed profiles.
- A comparison of the thermal X-ray luminosity vers. radio morphology with observed correlations. No CR proton model fits the flattest correlations observed. Only the most extreme model fits the steepest observations.
- Our simulated sample fits the observed cluster mass to halo size correlation. This show the excellent agreement of the simulated thermal model with the observed one.
- Our observed sample does not fit the observed break in self-similarity as implied from virial radius versus halo radius correlation. None of our models is able to correct this.
- The simulated sample does not show the observed bimodality radio halo brightness.
- However the model fits the observed radio brightness to X-ray brightness correlation.
- The γ-ray emission expected from the sample.

There are a number of suggestions how to deal with some of these problems. However it is unclear how hadronic or combined hadronic and primary models explain the spectral break in Coma or the break of self-similarity. We therefore conclude from this part of our work that purely hadronic models are *disfavoured* by observations.

Given this result we decide to investigate reacceleration models. In chapter 7 we for the first time couple a full reacceleration model to simulations of galaxy clusters.

We propose a novel scheme to obtain the local turbulent energy in SPH simulations, based on the kernel velocity of particles. We apply this scheme to idealised simulations of decaying sub- and supersonic turbulence and compare with traditional grid-FFT-based methods. We find a satisfactory match between both methods.

We then present an efficient CR momentum-transport code based on the Chang & Cooper scheme. We compare our code with analytical solutions to the transport equation and find good agreement. Furthermore a comparison with results from a semi-numerical paper by Cassano & Brunetti (2005) yields good convergence of the code even on coarse momentum grids. Furthermore we show a new MPI-parallel implementation of SPH particle projection based on the gathering approach. Our code contains a number of projection algorithms include an efficient numerical synchrotron solver for arbitrary CR electron spectra.

With the reacceleration model from (Brunetti & Lazarian, 2007) we turn to apply our new formalism on a simulation of an idealised galaxy cluster merger. Following the

prescriptions from Springel & Farrar (2007) we set-up a merger with mass ratio of 10 on a zero energy orbit. The magnetic field is modelled to match the best fit from recent observations of the Coma cluster.

We use the MHD-GADGET-3 code to evolve the simulation for 4 Gyrs and apply our formalism in post-processing to the merger. We use an injection function similar to the high energy hadronic injection in the chapters before and scale it to 1% of the thermal energy density. To follow the evolution of the CR electron distribution function we numerically integrate the Fokker-Planck equation of > 8 million particles over four Gyr.

We show:

- Projections of the evolution of all major MHD quantities of the merger.
- A light-curve of the system. It confirms that a reaccelerated halo is indeed a strongly transient phenomenon in that the emission declines by a factor of ten within 1 Gyr.
- A correlation of the synchrotron emission with the distance of the two dark matter cores and not with the magnetic field evolution. This proofs that indeed turbulent reacceleration is responsible for the increase in radio synchrotron luminosity of the system and not magnetic fields.
- A large number of CR electron spectra at different times of the simulation. The effect of reacceleration being very prominent.
- Radio synchrotron spectra of the system at different times. Our simulated radio halo fits very well the observed spectrum in the Coma cluster.
- A direct comparison with a secondary model directly yields a very different behaviour of the two models. The hadronic model evolves with density and magnetic field, but not turbulence and is not transient.
- The hadronic model is more centrally peaked than the reacceleration model.

Now for the first time there is direct evidence from simulations that reacceleration is an important effect in the formation of radio halos and not to be neglected. We want to stress that due to our conservative model of magnetosonic TTD damping the simulations presented here can be seen as a lower limit. Moderately constrained parameters like the amount of turbulence in magnetosonic waves have only minor influence on the result, as was argued before in analytical articles. At the same time SPH as a numerical method to simulate astrophysical fluid dynamics is known to suppress turbulence.

Clearly this work can only be a first step to the investigation of this "class" of models. A proper description has to include the reacceleration and distributions of protons as well. A reformulation of the transport equation in comoving coordinates independent of particles mass can yield an elegant description of the problem. The formalism should be implemented directly into the GADGET code and predictions for the upcoming telescopes should be made. We hope to be able to continue our work in this direction in the next

3-5 years to achieve these goals. It can be hoped, that on the long run this will lead to a better understanding of the complex processes active in the ICM plasma.

Bibliography

Abell G. O., 1957, PhD thesis, CALIFORNIA INSTITUTE OF TECHNOLOGY.

Abramowitz M., Stegun I. A., 1972, Handbook of Mathematical Functions

Ackermann M. e. a., GeV Gamma-ray Flux Upper Limits from Clusters of Galaxies, 2010, ApJ, 717, L71

Aharonian F., Akhperjanian A. G., Anton G., Barres de Almeida U., Bazer-Bachi A. R., Becherini Y., Behera B., Bernlöhr K., Boisson C., Bochow A., et al. Very high energy gamma-ray observations of the galaxy clusters Abell 496 and Abell 85 with HESS, 2009, A&A, 495, 27

Aharonian F. e. a., Constraints on the multi-TeV particle population in the Coma galaxy cluster with HESS observations, 2009a, A&A, 502, 437

Aharonian F. e. a., Very high energy gamma-ray observations of the galaxy clusters Abell 496 and Abell 85 with HESS, 2009b, A&A, 495, 27

Arnaud M., Evrard A. E., The L_X-T relation and intracluster gas fractions of X-ray clusters, 1999, MNRAS, 305, 631

Arnaud M., Pointecouteau E., Pratt G., The structural and scaling properties of nearby galaxy clusters. II. The M-T relation, 2005, A&A, 441, 893

Bacchi M., Feretti L., Giovannini G., Govoni F., Deep images of cluster radio halos, 2003, A&A, 400, 465

Badhwar G. D., Golden R. L., Stephens S. A., Analytic representation of the proton-proton and proton-nucleus cross-sections and its application to the sea-level spectrum and charge ratio of muons, 1977, Phys. Rev. D, 15, 820

Bagchi J., Sirothia S. K., Werner N., Pandge M. B., Kantharia N. G., H I.-C. C., Gopal-Krishna Paul S., Joshi S., Discovery of the first giant double radio relic in a galaxy cluster found in the PLANCK Sunyaev-Zel'dovich cluster survey: PLCK G287.0+32.9, 2011, ArXiv e-prints

Baldwin J. E., Elsmore B., Radio Emission from the Perseus Cluster, 1954, Nature, 173, 818

Baldwin J. E., Smith F. G., Radio emission from the extragalactic nebula M87, 1956, The Observatory, 76, 141

Barnes A., Collisionless Heating of the Solar-Wind Plasma. I. Theory of the Heating of Collisionless Plasma by Hydromagnetic Waves, 1968, ApJ, 154, 751

Battistelli E. S., De Petris M., Lamagna L., Melchiorri F., Palladino E., Savini G., Cooray A., Melchiorri A., Rephaeli Y., Shimon M., Cosmic Microwave Background Temperature at Galaxy Clusters, 2002, ApJ, 580, L101

Beck R., Krause M., Revised equipartition and minimum energy formula for magnetic field strength estimates from radio synchrotron observations, 2005, Astronomische Nachrichten, 326, 414

Berezinskii V. S., Kudriavtsev V. A., On the diffuse gamma radiation at ultra-high energies, E(gamma) greater than about 10 to the 14th eV, 1990, ApJ, 349, 620

Berezinsky V. S., Blasi P., Ptuskin V. S., Clusters of Galaxies as Storage Room for Cosmic Rays, 1997, ApJ, 487, 529

Bertone S., Vogt C., Ensslin T., Magnetic field seeding by galactic winds, 2006, MNRAS, 370, 319

Blandford R. D., 1986, in R. I. Epstein & W. C. Feldman ed., Magnetospheric Phenomena in Astrophysics Vol. 144 of American Institute of Physics Conference Series, Astrophysical particle acceleration. pp 1–23

Blandford R. D., Ostriker J. P., Particle acceleration by astrophysical shocks, 1978, ApJ, 221, L29

Blasi P., The non-thermal radiation-cluster merger connection, 2001, Astroparticle Physics, 15, 223

Blasi P., Shock acceleration of electrons in the presence of synchrotron losses - I. Test-particle theory, 2010, MNRAS, 402, 2807

Blasi P., Amato E., Caprioli D., The maximum momentum of particles accelerated at cosmic ray modified shocks, 2007, MNRAS, 375, 1471

Blasi P., Colafrancesco S., Cosmic rays, radio halos and nonthermal X-ray emission in clusters of galaxies, 1999, Astroparticle Physics, 12, 169

Blasi P., Gabici S., Brunetti G., Gamma rays from clusters of galaxies, 2007, ArXiv Astrophysics e-prints

Blumenthal G. R., Gould R. J., Bremsstrahlung, Synchrotron Radiation, and Compton Scattering of High-Energy Electrons Traversing Dilute Gases, 1970, Reviews of Modern Physics, 42, 237

Boehringer H., Morfill G. E., On the dynamical role of cosmic rays in cooling flows in clusters of galaxies, 1988, ApJ, 330, 609

Böhringer H., Schuecker P., Guzzo L., Collins C. A., Voges W., Cruddace R. G., Ortiz-Gil A., Chincarini G., De Grandi S., Edge A. C., MacGillivray H. T., Neumann D. M., Schindler S., Shaver P., The ROSAT-ESO Flux Limited X-ray (REFLEX) Galaxy cluster survey. V. The cluster catalogue, 2004, A&A, 425, 367

Böhringer H., Voges W., Huchra J. P., McLean B., Giacconi R., Rosati P., Burg R., Mader J., Schuecker P., Simiç D., Komossa S., Reiprich T. H., Retzlaff J., Trümper J., The Northern ROSAT All-Sky (NORAS) Galaxy Cluster Survey. I. X-Ray Properties of Clusters Detected as Extended X-Ray Sources, 2000, ApJS, 129, 435

Bonafede A., Feretti L., Giovannini G., Govoni F., Murgia M., Taylor G. B., Ebeling H., Allen S., Gentile G., Pihlström Y., Revealing the magnetic field in a distant galaxy cluster: discovery of the complex radio emission from MACS J0717.5 +3745, 2009, A&A, 503, 707

Bonafede A., Feretti L., Murgia M., Govoni F., Giovannini G., Dallacasa D., Dolag K., Taylor G. B., The Coma cluster magnetic field from Faraday rotation measures, 2010, A&A, 513, A30+

Bonafede A., Govoni F., Feretti L., Murgia M., Giovannini G., Brüggen M., Fractional polarization as a probe of magnetic fields in the intra-cluster medium, 2011, A&A, 530, A24+

Borgani S., Dolag K., Murante G., Cheng L.-M., Springel V., Diaferio A., Moscardini L., Tormen G., Tornatore L., Tozzi P., Hot and cooled baryons in smoothed particle hydrodynamic simulations of galaxy clusters: physics and numerics, 2006, MNRAS, 367, 1641

Borovsky J. E., Eilek J. A., A study of the stochastic energization of charged particles with and without synchrotron energy loss, 1986, ApJ, 308, 929

Børve S., Omang M., Trulsen J., Regularized Smoothed Particle Hydrodynamics: A New Approach to Simulating Magnetohydrodynamic Shocks, 2001, ApJ, 561, 82

Bozyan E. P., Radio Observations of the Coma Cluster of Galaxies, 1968, ApJ, 152, L155+

Brentjens M. A., de Bruyn A. G., Faraday rotation measure synthesis, 2005, A&A, 441, 1217

Bridle A. H., Spectra Sources of Extended Extragalactic Radio Sources, 1969, Nature, 224, 889

Bridle A. H., Fomalont E. B., Complex radio emission from the X-ray cluster Abell 2256, 1976, A&A, 52, 107

Briel U. G., Henry J. P., Boehringer H., Observation of the Coma cluster of galaxies with ROSAT during the all-sky survey, 1992, A&A, 259, L31

Brown S., Rudnick L., Diffuse radio emission in/around the Coma cluster: beyond simple accretion, 2011, MNRAS, 412, 2

Brüggen M., Ruszkowski M., Simionescu A., Hoeft M., Dalla Vecchia C., Simulations of Magnetic Fields in Filaments, 2005, ApJ, 631, L21

Brunetti G., 2004a, in F. Mantovani & A. Kus ed., The Role of VLBI in Astrophysics, Astrometry and Geodesy Non-thermal emission from extragalactic radio sources: a high resolution broad band approach. pp 29–+

Brunetti G., Particle Acceleration and Non-Thermal Emission from Galaxy Clusters, 2004b, Journal of Korean Astronomical Society, 37, 493

Brunetti G., 2009, in Revista Mexicana de Astronomia y Astrofisica Conference Series Vol. 36 of Revista Mexicana de Astronomia y Astrofisica Conference Series, Non-thermal emission from Galaxy Clusters and future observations with the FERMI gamma-ray telescope and LOFAR. pp 201–208

Brunetti G., Blasi P., Alfvénic reacceleration of relativistic particles in galaxy clusters in the presence of secondary electrons and positrons, 2005, MNRAS, 363, 1173

Brunetti G., Blasi P., Cassano R., Gabici S., Alfvénic reacceleration of relativistic particles in galaxy clusters: MHD waves, leptons and hadrons, 2004, MNRAS, 350, 1174

Brunetti G., Blasi P., Cassano R., Gabici S., 2009, in Bastieri D., Rando R., eds, American Institute of Physics Conference Series Vol. 1112 of American Institute of Physics Conference Series, High energy emission from galaxy clusters and particle acceleration due to MHD turbulence. pp 129–137

Brunetti G., Cassano R., Dolag K., Setti G., On the evolution of giant radio halos and their connection with cluster mergers, 2009, A&A, 507, 661

Brunetti G., Giacintucci S., Cassano R., Lane W., Dallacasa D., Venturi T., Kassim N. E., Setti G., Cotton W. D., Markevitch M., A low-frequency radio halo associated with a cluster of galaxies, 2008, Nature, 455, 944

Brunetti G., Lazarian A., Compressible turbulence in galaxy clusters: physics and stochastic particle re-acceleration, 2007, MNRAS, 378, 245

Brunetti G., Lazarian A., Acceleration of primary and secondary particles in galaxy clusters by compressible MHD turbulence: from radio haloes to gamma-rays, 2011a, MNRAS, 410, 127

Brunetti G., Lazarian A., Particle reacceleration by compressible turbulence in galaxy clusters: effects of a reduced mean free path, 2011b, MNRAS, 412, 817

Brunetti G., Setti G., Feretti L., Giovannini G., Particle reacceleration in the Coma cluster: radio properties and hard X-ray emission, 2001, MNRAS, 320, 365

Brunetti G., Venturi T., Dallacasa D., Cassano R., Dolag K., Giacintucci S., Setti G., Cosmic Rays and Radio Halos in Galaxy Clusters: New Constraints from Radio Observations, 2007, ApJ, 670, L5

Buote D. A., On the Origin of Radio Halos in Galaxy Clusters, 2001, ApJ, 553, L15

Buote D. A., Tsai J. C., Quantifying the Morphologies and Dynamical Evolution of Galaxy Clusters. I. The Method, 1995, ApJ, 452, 522

Buote D. A., Tsai J. C., Quantifying the Morphologies and Dynamical Evolution of Galaxy Clusters. II. Application to a Sample of ROSAT Clusters, 1996, ApJ, 458, 27

Burbidge G. R., Halo of Radio Emission and the Origin of Cosmic Rays, 1956, Physical Review, 101, 906

Burbidge G. R., Possible Sources of Radio Emission in Clusters of Galaxies., 1958, ApJ, 128, 1

Burbidge G. R., Burbidge E. M., The Sources of Radio Emission in NGC 5128 and NGC 1316., 1957, ApJ, 125, 1

Burns J. O., Roettiger K., Pinkney J., Perley R. A., Owen F. N., Voges W., Evidence for an On-going Cluster/Group Merger in Abell 2255, 1995, ApJ, 446, 583

Cane H. V., Erickson W. C., Hanisch R. J., Turner P. J., Observations of rich clusters of galaxies at metre wavelengths, 1981, MNRAS, 196, 409

Carilli C. L., Taylor G. B., Cluster Magnetic Fields, 2002, ARA&A, 40, 319

Cassano R., Large-scale diffuse radio emission from clusters of galaxies and the importance of low frequency radio observations, 2009, ArXiv 0902.2971

Cassano R., Brunetti G., Cluster mergers and non-thermal phenomena: a statistical magneto-turbulent model, 2005, MNRAS, 357, 1313

Cassano R., Brunetti G., Röttgering H. J. A., Brüggen M., Unveiling radio halos in galaxy clusters in the LOFAR era, 2010, A&A, 509, A68+

Cassano R., Brunetti G., Setti G., Statistics of giant radio haloes from electron reacceleration models, 2006, MNRAS, 369, 1577

Cassano R., Brunetti G., Setti G., Govoni F., Dolag K., New scaling relations in cluster radio haloes and the re-acceleration model, 2007, MNRAS, 378, 1565

Cassano R., Brunetti G., Venturi T., Setti G., Dallacasa D., Giacintucci S., Bardelli S., Revised statistics of radio halos and the reacceleration model, 2008, A&A, 480, 687

Cavaliere A., Fusco-Femiano R., The Distribution of Hot Gas in Clusters of Galaxies, 1978, A&A, 70, 677

Cavaliere A. G., Gursky H., Tucker W. H., Extragalactic X-ray Sources and Associations of Galaxies, 1971, Nature, 231, 437

Chang J., Cooper G., A PRactical Difference Scheme for Fokker-Planck Equations, 1970, Journal of Computational Physics, 6, 1

Churazov E., Forman W., Jones C., Sunyaev R., Böhringer H., XMM-Newton observations of the Perseus cluster - II. Evidence for gas motions in the core, 2004, MNRAS, 347, 29

Churazov E., Forman W., Vikhlinin A., Tremaine S., Gerhard O., Jones C., Measuring the non-thermal pressure in early-type galaxy atmospheres: a comparison of X-ray and optical potential profiles in M87 and NGC 1399, 2008, MNRAS, 388, 1062

Clarke T. E., Ensslin T. A., Deep 1.4 GHz Very Large Array Observations of the Radio Halo and Relic in Abell 2256, 2006, AJ, 131, 2900

Clarke T. E., Kronberg P. P., Böhringer H., A New Radio-X-Ray Probe of Galaxy Cluster Magnetic Fields, 2001, ApJ, 547, L111

Colless M., Dunn A. M., Structure and Dynamics of the Coma Cluster, 1996, ApJ, 458, 435

Dallacasa D., Brunetti G., Giacintucci S., Cassano R., Venturi T., Macario G., Kassim N. E., Lane W., Setti G., Deep 1.4 GHz Follow-up of the Steep Spectrum Radio Halo in A521, 2009, ApJ, 699, 1288

De Grandi S., Molendi S., Temperature Profiles of Nearby Clusters of Galaxies, 2002, ApJ, 567, 163

de Grijs R., Star formation time-scales in the nearby, prototype starburst galaxy M82, 2001, ArXiv Astrophysics e-prints

de Vaucouleurs G., de Vaucouleurs A., Corwin Jr. H. G., Buta R. J., Paturel G., Fouque P., 1991, Third Reference Catalogue of Bright Galaxies

Deiss B. M., Reich W., Lesch H., Wielebinski R., The large-scale structure of the diffuse radio halo of the Coma cluster at 1.4GHz., 1997, A&A, 321, 55

Dennison B., On intracluster Faraday rotation. I - Observations, 1979, AJ, 84, 725

Dennison B., Formation of radio halos in clusters of galaxies from cosmic-ray protons, 1980, ApJ, 239, L93

Dermer C. D., Secondary production of neutral pi-mesons and the diffuse galactic gamma radiation, 1986, A&A, 157, 223

Dolag K., Bartelmann M., Lesch H., SPH simulations of magnetic fields in galaxy clusters, 1999, A&A, 348, 351

Dolag K., Bartelmann M., Lesch H., Evolution and structure of magnetic fields in simulated galaxy clusters, 2002, A&A, 387, 383

Dolag K., Ensslin T. A., Radio halos of galaxy clusters from hadronic secondary electron injection in realistic magnetic field configurations, 2000, A&A, 362, 151

Dolag K., Grasso D., Springel V., Tkachev I., Constrained simulations of the magnetic field in the local Universe and the propagation of ultrahigh energy cosmic rays, 2005, Journal of Cosmology and Astro-Particle Physics, 1, 9

Dolag K., Hansen F. K., Roncarelli M., Moscardini L., The imprints of local superclusters on the Sunyaev-Zel'dovich signals and their detectability with Planck, 2005, MNRAS, 363, 29

Dolag K., Jubelgas M., Springel V., Borgani S., Rasia E., Thermal Conduction in Simulated Galaxy Clusters, 2004, ApJ, 606, L97

Dolag K., Meneghetti M., Moscardini L., Rasia E., Bonaldi A., Simulating the physical properties of dark matter and gas inside the cosmic web, 2006, MNRAS, 370, 656

Dolag K., Stasyszyn F., An MHD GADGET for cosmological simulations, 2009, MNRAS, 398, 1678

Dolag K., Vazza F., Brunetti G., Tormen G., Turbulent gas motions in galaxy cluster simulations: the role of smoothed particle hydrodynamics viscosity, 2005, MNRAS, 364, 753

Dolag K., Vogt C., Enßlin T. A., PACERMAN- I. A new algorithm to calculate Faraday rotation maps, 2005, MNRAS, 358, 726

Donnert J., Dolag K., Bonafede A., Cassano R., Brunetti G., Radio haloes from simulations and hadronic models - I. The Coma cluster, 2010, MNRAS, 401, 47

Donnert J., Dolag K., Cassano R., Brunetti G., Radio haloes from simulations and hadronic models - II. The scaling relations of radio haloes, 2010, MNRAS, 407, 1565

Donnert J., Dolag K., Lesch H., Müller E., Cluster magnetic fields from galactic outflows, 2009, MNRAS, 392, 1008

Dubois Y., Teyssier R., Cosmological MHD simulation of a cooling flow cluster, 2008, A&A, 482, L13

Ebeling H., Barrett E., Donovan D., Ma C., Edge A. C., van Speybroeck L., A Complete Sample of 12 Very X-Ray Luminous Galaxy Clusters at $z < 0.5$, 2007, ApJ, 661, L33

Ebeling H., Edge A. C., Bohringer H., Allen S. W., Crawford C. S., Fabian A. C., Voges W., Huchra J. P., The ROSAT Brightest Cluster Sample - I. The compilation of the sample and the cluster log N-log S distribution, 1998, MNRAS, 301, 881

Ebeling H., Voges W., Bohringer H., Edge A. C., Huchra J. P., Briel U. G., Properties of the X-ray-brightest Abell-type clusters of galaxies (XBACs) from ROSAT All-Sky Survey data - I. The sample, 1996, MNRAS, 281, 799

Eilek J. A., Particle reacceleration in radio galaxies, 1979, ApJ, 230, 373

Eilek J. A., Hughes P. A., 1991, Particle acceleration and magnetic field evolution. pp 428–+

Einstein A., Zur Elektrodynamik bewegter Körper, 1905, Annalen der Physik, 322, 891

Ensslin T., Extragalactic Cosmic Rays and Magnetic Fields: Facts and Fiction, 2005, ArXiv Astrophysics e-prints

Enßlin T., Pfrommer C., Miniati F., Subramanian K., Cosmic ray transport in galaxy clusters: implications for radio halos, gamma-ray signatures, and cool core heating, 2011, A&A, 527, A99+

Ensslin T. A., Modification of cluster radio halo appearance by the thermal Sunyaev-Zeldovich effect, 2002, A&A, 396, L17

Ensslin T. A., Biermann P. L., Klein U., Kohle S., Cluster radio relics as a tracer of shock waves of the large-scale structure formation, 1998, A&A, 332, 395

Ensslin T. A., Biermann P. L., Kronberg P. P., Wu X.-P., Cosmic-Ray Protons and Magnetic Fields in Clusters of Galaxies and Their Cosmological Consequences, 1997, ApJ, 477, 560

Enßlin T. A., Lieu R., Biermann P. L., Non-thermal origin of the EUV and HEX excess emission of the Coma cluster - the nature of the energetic electrons, 1999, A&A, 344, 409

Ensslin T. A., Pfrommer C., Springel V., Jubelgas M., Cosmic ray physics in calculations of cosmological structure formation, 2007, A&A, 473, 41

Ensslin T. A., Röttgering H., The radio luminosity function of cluster radio halos, 2002, A&A, 396, 83

Fabian A. C., Arnaud K. A., Nulsen P. E. J., Watson M. G., Stewart G. C., McHardy I., Smith A., Cooke B., Elvis M., Mushotzky R. F., An X-ray, optical and radio study of PKS 0745-191 - A massive cooling flow, 1985, MNRAS, 216, 923

Feretti L., Clusters of galaxies in radio, 2003a, ArXiv Astrophysics e-prints

Feretti L., 2003b, in Bowyer S., Hwang C.-Y., eds, Astronomical Society of the Pacific Conference Series Vol. 301 of Astronomical Society of the Pacific Conference Series, Radio Observations of Clusters of Galaxies. pp 143–+

Feretti L., Dallacasa D., Giovannini G., Tagliani A., The magnetic field in the Coma cluster., 1995, A&A, 302, 680

Feretti L., Dallacasa D., Govoni F., Giovannini G., Taylor G. B., Klein U., The radio galaxies and the magnetic field in Abell 119, 1999, A&A, 344, 472

Feretti L., Fusco-Femiano R., Giovannini G., Govoni F., The giant radio halo in Abell 2163, 2001, A&A, 373, 106

Feretti L., Giovannini G., 1996, in R. D. Ekers, C. Fanti, & L. Padrielli ed., Extragalactic Radio Sources Vol. 175 of IAU Symposium, Diffuse Cluster Radio Sources (Review). pp 333–+

Feretti L., Giovannini G., Bohringer H., The radio and X-ray properties of Abell 2319, 1997, Nature, 2, 501

Feretti L., Schuecker P., Böhringer H., Govoni F., Giovannini G., Diffuse radio emission in a REFLEX cluster, 2005, A&A, 444, 157

Fermi E., On the Origin of the Cosmic Radiation, 1949, Physical Review, 75, 1169

Fermi E., High-energy nuclear events, 1950, Prog. Theor. Phys., 5, 570

Ferrari C., Govoni F., Schindler S., Bykov A. M., Rephaeli Y., Observations of Extended Radio Emission in Clusters, 2008, Space Science Reviews, 134, 93

Fisk L. A., The acceleration of energetic particles in the interplanetary medium by transit time damping, 1976, J. Geophys. Res., 81, 4633

Fokker A., 1914, PhD thesis

Furlanetto S. R., Loeb A., Intergalactic Magnetic Fields from Quasar Outflows, 2001, ApJ, 556, 619

Fusco-Femiano R., Non-thermal Emission in Clusters of Galaxies, 2004, Ap&SS, 294, 37

Fusco-Femiano R., dal Fiume D., Feretti L., Giovannini G., Grandi P., Matt G., Molendi S., Santangelo A., Hard X-Ray Radiation in the Coma Cluster Spectrum, 1999, ApJ, 513, L21

Fusco-Femiano R., Hughes J. P., Nonpolytropic model for the Coma Cluster, 1994, ApJ, 429, 545

Fusco-Femiano R., Orlandini M., Brunetti G., Feretti L., Giovannini G., Grandi P., Setti G., Confirmation of Nonthermal Hard X-Ray Excess in the Coma Cluster from Two Epoch Observations, 2004, ApJ, 602, L73

Gabici S., Blasi P., Nonthermal Radiation from Clusters of Galaxies: The Role of Merger Shocks in Particle Acceleration, 2003, ApJ, 583, 695

Galassi M., 2011, GNU Scientific Library Reference Manual ,3rd Ed.

Giacintucci S., Venturi T., Brunetti G., Bardelli S., Dallacasa D., Ettori S., Finoguenov A., Rao A. P., Zucca E., Spectral properties and origin of the radio halo in A3562, 2005, A&A, 440, 867

Giacintucci S., Venturi T., Brunetti G., Dallacasa D., Mazzotta P., Cassano R., Bardelli S., Zucca E., Testing the radio halo-cluster merger scenario. The case of RXC J2003.5-2323, 2009, A&A, 505, 45

Giacintucci S., Venturi T., Cassano R., Dallacasa D., Brunetti G., A Giant Radio Halo in the Massive and Merging Cluster Abell 1351, 2009, ApJ, 704, L54

Giacintucci S., Venturi T., Macario G., Dallacasa D., Brunetti G., Markevitch M., Cassano R., Bardelli S., Athreya R., Shock acceleration as origin of the radio relic in A 521?, 2008, A&A, 486, 347

Gilfanov M. R., Syunyaev R. A., Churazov E. M., Radial Brightness Profiles of Resonance X-Ray Lines in Galaxy Clusters, 1987, Soviet Astronomy Letters, 13, 3

Ginzburg V. L., Syrovatskii S. I., Cosmic Magnetobremsstrahlung (synchrotron Radiation), 1965, ARA&A, 3, 297

Giovannini G., Bonafede A., Feretti L., Govoni F., Murgia M., Ferrari F., Monti G., Radio halos in nearby (z ¡ 0.4) clusters of galaxies, 2009, A&A, 507, 1257

Giovannini G., Feretti L., Halo and relic sources in clusters of galaxies, 2000, Nature, 5, 335

Giovannini G., Feretti L., Girardi M., Govoni F., Murgia M., Vacca V., Bagchi J., A giant radio halo in the low luminosity X-ray cluster Abell 523, 2011, ArXiv e-prints

Giovannini G., Tordi M., Feretti L., Radio halo and relic candidates from the NRAO VLA Sky Survey, 1999, Nature, 4, 141

Gitti M., Brunetti G., Setti G., 2002, in S. Borgani, M. Mezzetti, & R. Valdarnini ed., Tracing Cosmic Evolution with Galaxy Clusters Vol. 268 of Astronomical Society of the Pacific Conference Series, Reacceleration of Relativistic Electrons in Cooling Flows: the Case of Perseus Cluster. pp 373–+

Gitti M., Ferrari C., Domainko W., Feretti L., Schindler S., Discovery of diffuse radio emission at the center of the most X-ray-luminous cluster RX J1347.5-1145, 2007, A&A, 470, L25

Goossens M., 2003, An Introduction to Plasma Astrophysics and Magnetohydrodynamics. Kluwer Academic Publishers

Gould R. J., Energy loss of fast electrons and positrons in a plasma, 1972, Physica, 60, 145

Govoni F., Ensslin T. A., Feretti L., Giovannini G., A comparison of radio and X-ray morphologies of four clusters of galaxies containing radio halos, 2001, A&A, 369, 441

Govoni F., Feretti L., Giovannini G., Böhringer H., Reiprich T. H., Murgia M., Radio and X-ray diffuse emission in six clusters of galaxies, 2001, A&A, 376, 803

Govoni F., Murgia M., Feretti L., Giovannini G., Dallacasa D., Taylor G. B., A2255: The first detection of filamentary polarized emission in a radio halo, 2005, A&A, 430, L5

Govoni F., Murgia M., Feretti L., Giovannini G., Dolag K., Taylor G. B., The intracluster magnetic field power spectrum in Abell 2255, 2006, A&A, 460, 425

Govoni F., Murgia M., Giovannini G., Vacca V., Bonafede A., The large-scale diffuse radio emission in A781, 2011, A&A, 529, A69+

Grasso D., Rubinstein H. R., Magnetic fields in the early universe, 2001, Phys. Rept., 348, 163

Grindlay J. E., Parsignault D. R., Gursky H., Brinkman A. C., Heise J., Harris D. E., New X-ray and radio observations of the galaxy cluster A2319, 1977, ApJ, 214, L57

Guidetti D., Murgia M., Govoni F., Parma P., Gregorini L., de Ruiter H. R., Cameron R. A., Fanti R., The intracluster magnetic field power spectrum in Abell 2382, 2008, A&A, 483, 699

Hanasz M., Kowalik K., Wóltański D., Pawłaszek R., PIERNIK mhd code - a multi-fluid, non-ideal extension of the relaxing-TVD scheme (III), 2008, ArXiv e-prints

Hanisch R. J., Common properties of clusters of galaxies containing radio halos and implications for models of radio halo formation, 1982, A&A, 116, 137

Harris D. E., Kapahi V. K., Ekers R. D., Westerbork synthesis observations of 8 clusters of galaxies which contain tailed radio galaxies, 1980, A&AS, 39, 215

Heidmann J., Étude comparative optique et radioélectrique de deux amas de galaxies, 1965, Annales d'Astrophysique, 28, 380

Hernquist L., An analytical model for spherical galaxies and bulges, 1990, 356, 359

Hill J. M., Longair M. S., Interacting radio galaxies, 1971, MNRAS, 154, 125

Hockney R. W., Eastwood J. W., 1988, Computer simulation using particles

Hoffman Y., Ribak E., Constrained realizations of Gaussian fields - A simple algorithm, 1991, ApJ, 380, L5

Iapichino L., Maier A., Schmidt W., Niemeyer J. C., 2010, in J.-M. Alimi & A. Fuözfa ed., American Institute of Physics Conference Series Vol. 1241 of American Institute of Physics Conference Series, Turbulence modeling and the physics of the intra-cluster medium. pp 928–934

Iapichino L., Niemeyer J. C., Hydrodynamical adaptive mesh refinement simulations of turbulent flows - II. Cosmological simulations of galaxy clusters, 2008, MNRAS, 388, 1089

Iapichino L., Schmidt W., Niemeyer J. C., Merklein J., Turbulence production and turbulent pressure support in the intergalactic medium, 2011, MNRAS, pp 483–+

Inogamov N. A., Sunyaev R. A., Turbulence in Clusters of Galaxies and X-ray Line Profiles, 2003, Astronomy Letters, 29, 791

Jackson J. D., , 1998, Classical Electrodynamics

Jaffe W. J., Origin and transport of electrons in the halo radio source in the Coma cluster, 1977, ApJ, 212, 1

Jaffe W. J., Rudnick L., Observations at 610 MHz of radio halos in clusters of galaxies, 1979, ApJ, 233, 453

Jaffe W. J., Valentijn E. A., Perola G. C., A Westerbork survey of rich clusters of galaxies. III - Observations of the Coma Cluster at 610 MHz, 1976, A&A, 49, 179

Jennison R. C., Das Gupta M. K., Fine Structure of the Extra-terrestrial Radio Source Cygnus I, 1953, Nature, 172, 996

Jing Y. P., Correcting for the Alias Effect When Measuring the Power Spectrum Using a Fast Fourier Transform, 2005, ApJ, 620, 559

Jokipii J. R., Understanding Cosmic-Ray Acceleration and Transport in the Heliosphere (Invited), 2010, AGU Fall Meeting Abstracts, pp D3+

Jones F. C., Examination of the "Leakage-Lifetime" Approximation in Cosmic-Ray Diffusion, 1970, Phys. Rev. D, 2, 2787

Jubelgas M., Springel V., Enßlin T., Pfrommer C., Cosmic ray feedback in hydrodynamical simulations of galaxy formation, 2008, A&A, 481, 33

Kassim N. E., Clarke T. E., Enßlin T. A., Cohen A. S., Neumann D. M., Low-Frequency VLA Observations of Abell 754: Evidence for a Cluster Radio Halo and Possible Radio Relics, 2001, ApJ, 559, 785

Kempner J. C., Blanton E. L., Clarke T. E., Enßlin T. A., Johnston-Hollitt M., Rudnick L., 2004, in T. Reiprich, J. Kempner, & N. Soker ed., The Riddle of Cooling Flows in Galaxies and Clusters of galaxies Conference Note: A Taxonomy of Extended Radio Sources in Clusters of Galaxies. pp 335–+

Kempner J. C., Sarazin C. L., Radio Halo and Relic Candidates from the Westerbork Northern Sky Survey, 2001, ApJ, 548, 639

Keshet U., Loeb A., Using Radio Halos and Minihalos to Measure the Distributions of Magnetic Fields and Cosmic Rays in Galaxy Clusters, 2010, ApJ, 722, 737

Kim K., Kronberg P. P., Dewdney P. E., Landecker T. L., The halo and magnetic field of the Coma cluster of galaxies, 1990, ApJ, 355, 29

Kim K.-T., Kronberg P. P., Tribble P. C., Detection of excess rotation measure due to intracluster magnetic fields in clusters of galaxies, 1991, ApJ, 379, 80

King I. R., The structure of star clusters. III. Some simple dynamical models, 1966, AJ, 71, 64

Kitsionas S., Federrath C., Klessen R. S., Schmidt W., Price D. J., Dursi L. J., Gritschneder M., Walch S., Piontek R., Kim J., Jappsen A., Ciecielag P., Mac Low M., Algorithmic comparisons of decaying, isothermal, supersonic turbulence, 2009, A&A, 508, 541

Klein U., Wielebinski R., Morsi H. W., Radio continuum observations of M82, 1988, A&A, 190, 41

Koch P., 2009, in Revista Mexicana de Astronomia y Astrofisica Conference Series Vol. 36 of Revista Mexicana de Astronomia y Astrofisica, vol. 27, Magnetic Fields and Turbulences in Clusters of Galaxies. pp 262–+

Kolmogorov A., The Local Structure of Turbulence in Incompressible Viscous Fluid for Very Large Reynolds' Numbers, 1941, Akademiia Nauk SSSR Doklady, 30, 301

Kronberg P. P., Extragalactic magnetic fields, 1994, Reports on Progress in Physics, 57, 325

Kronberg P. P., Kothes R., Salter C. J., Perillat P., Discovery of New Faint Radio Emission on 8 deg to 3 arcmin Scales in the Coma Field, and Some Galactic and Extragalactic Implications, 2007, ApJ, 659, 267

Kronberg P. P., Lesch H., Hopp U., Magnetization of the Intergalactic Medium by Primeval Galaxies, 1999, ApJ, 511, 56

Krymskii G. F., A regular mechanism for the acceleration of charged particles on the front of a shock wave, 1977, Akademiia Nauk SSSR Doklady, 234, 1306

Kuchar P., Enßlin T. A., Magnetic power spectra from Faraday rotation maps. REALMAF and its use on Hydra A, 2011, A&A, 529, A13+

Kulsrud R. M., Cen R., Ostriker J. P., Ryu D., The Protogalactic Origin for Cosmic Magnetic Fields, 1997, ApJ, 480, 481

Kulsrud R. M., Ferrari A., The Relativistic Quasilinear Theory of Particle Acceleration by Hydromagnetic Turbulence, 1971, Ap&SS, 12, 302

Kushnir D., Katz B., Waxman E., Magnetic fields and cosmic rays in clusters of galaxies, 2009, Journal of Cosmology and Astro-Particle Physics, 9, 24

Laing R. A., Bridle A. H., Parma P., Murgia M., Structures of the magnetoionic media around the Fanaroff-Riley Class I radio galaxies 3C31 and Hydra A, 2008, MNRAS, 391, 521

Lane W. M., Clarke T. E., Taylor G. B., Perley R. A., Kassim N. E., Hydra A at Low Radio Frequencies, 2004, AJ, 127, 48

Large M. I., Mathewson D. S., Haslam C. G. T., A High-Resolution Survey of the Coma Cluster of Galaxies at 408 Mc./s., 1959, Nature, 183, 1663

Lawler J. M., Dennison B., On intracluster Faraday rotation. II - Statistical analysis, 1982, ApJ, 252, 81

Lea S. M., Holman G. D., X-ray and radio emission from clusters of galaxies - The heating of intracluster gas by relativistic electrons, 1978, ApJ, 222, 29

Lea S. M., Silk J., Kellogg E., Murray S., Thermal-Bremsstrahlung Interpretation of Cluster X-Ray Sources, 1973, ApJ, 184, L105+

Ledlow M. J., Voges W., Owen F. N., Burns J. O., The X-Ray Properties of Nearby Abell Clusters from the ROSAT All-Sky Survey: The Sample and Correlations with Optical Properties, 2003, AJ, 126, 2740

Li S., Li H., Cen R., CosmoMHD: A Cosmological Magnetohydrodynamics Code, 2008, ApJS, 174, 1

Liang H., Hunstead R. W., Birkinshaw M., Andreani P., A Powerful Radio Halo in the Hottest Known Cluster of Galaxies 1E 0657-56, 2000, ApJ, 544, 686

Lifshitz E. M., Pitaevskii L. P., 1981, Physical kinetics

Longair M. S., 1994, High energy astrophysics. Volume 2. Stars, the Galaxy and the interstellar medium.

Longair M. S., 2010, High Energy Astrophysics

Lutovinov A. A., Vikhlinin A., Churazov E. M., Revnivtsev M. G., Sunyaev R. A., X-Ray Observations of the Coma Cluster in a Broad Energy Band with the INTEGRAL, RXTE, and ROSAT Observatories, 2008, ApJ, 687, 968

Macario G., Markevitch M., Giacintucci S., Brunetti G., Venturi T., Murray S. S., A Shock Front in the Merging Galaxy Cluster A754: X-ray and Radio Observations, 2011, ApJ, 728, 82

Macario G., Venturi T., Brunetti G., Dallacasa D., Giacintucci S., Cassano R., Bardelli S., Athreya R., The very steep spectrum radio halo in Abell 697, 2010a, A&A, 517, A43+

Macario G., Venturi T., Brunetti G., Dallacasa D., Giacintucci S., Cassano R., Bardelli S., Athreya R., The very steep spectrum radio halo in Abell 697, 2010b, ArXiv e-prints

Malkov M. A., O'C Drury L., Nonlinear theory of diffusive acceleration of particles by shock waves, 2001, Reports on Progress in Physics, 64, 429

Mannheim K., Schlickeiser R., Interactions of cosmic ray nuclei, 1994, A&A, 286, 983

Markevitch M., The L X-T Relation and Temperature Function for Nearby Clusters Revisited, 1998, ApJ, 504, 27

Markevitch M., Intergalactic shock fronts, 2010, ArXiv e-prints

Mathis H., Lemson G., Springel V., Kauffmann G., White S. D. M., Eldar A., Dekel A., Simulating the formation of the local galaxy population, 2002, MNRAS, 333, 739

Meekins J. F., Fritz G., Chubb T. A., Friedman H., Physical Sciences: X-rays from the Coma Cluster of Galaxies, 1971, Nature, 231, 107

Melrose D. B., 1980, Plasma astrohysics. Nonthermal processes in diffuse magnetized plasmas - Vol.1: The emission, absorption and transfer of waves in plasmas; Vol.2: Astrophysical applications

Miniati F., 2000, PhD thesis, University of Minnesota, USA

Miniati F., COSMOCR: A numerical code for cosmic ray studies in computational cosmology, 2001, Computer Physics Communications, 141, 17

Miniati F., Numerical modelling of gamma radiation from galaxy clusters, 2003, MNRAS, 342, 1009

Miniati F., Jones T. W., Kang H., Ryu D., Cosmic-Ray Electrons in Groups and Clusters of Galaxies: Primary and Secondary Populations from a Numerical Cosmological Simulation, 2001, ApJ, 562, 233

Miniati F., Martin D. F., Constrained-Transport Magnetohydrodynamics with Adaptive-Mesh-Refinement in CHARM, 2011, ArXiv e-prints

Miniati F., Ryu D., Kang H., Jones T. W., Cosmic-Ray Protons Accelerated at Cosmological Shocks and Their Impact on Groups and Clusters of Galaxies, 2001, ApJ, 559, 59

Miniati F., Ryu D., Kang H., Jones T. W., Cen R., Ostriker J. P., Properties of Cosmic Shock Waves in Large-Scale Structure Formation, 2000, ApJ, 542, 608

Mirnov V. V., Ding W. X., Brower D. L., Van Zeeland M., Carlstrom T., Finite electron temperature effects on interferometric and polarimetric measurements in fusion plasmas, 2007, Physics of Plasmas, 14, 12

Mitton S., The polarization properties of 65 extragalactic sources in the 3Ccatalogue, 1972, MNRAS, 155, 373

Mohr J. J., Mathiesen B., Evrard A. E., Properties of the Intracluster Medium in an Ensemble of Nearby Galaxy Clusters, 1999, ApJ, 517, 627

Mori M., Search for GeV gamma-ray emission from clusters of galaxies studied by TeV telescopes, 2009, ArXiv e-prints

Moskalenko I. V., Strong A. W., Production and Propagation of Cosmic-Ray Positrons and Electrons, 1998, ApJ, 493, 694

Murgia M., Govoni F., Feretti L., Giovannini G., Dallacasa D., Fanti R., Taylor G. B., Dolag K., Magnetic fields and Faraday rotation in clusters of galaxies, 2004, A&A, 424, 429

Murgia M., Govoni F., Markevitch M., Feretti L., Giovannini G., Taylor G. B., Carretti E., Comparative analysis of the diffuse radio emission in the galaxy clusters A1835, A2029, and Ophiuchus, 2009, A&A, 499, 679

Navarro J. F., Frenk C. S., White S. D. M., The Structure of Cold Dark Matter Halos, 1996, ApJ, 462, 563

Noordam J. E., de Bruyn A. G., High dynamic range mapping of strong radio sources, with application to 3C84, 1982, Nature, 299, 597

Oort J. H., Walraven T., Polarization and composition of the Crab nebula, 1956, Bull. Astron. Inst. Netherlands, 12, 285

Pacholczyk A. G., 1970, Radio astrophysics. Nonthermal processes in galactic and extragalactic sources

Pacholczyk A. G., Scott J. S., In situ particle acceleration and physical conditions in radio tail galaxies, 1976, ApJ, 203, 313

Park B. T., Petrosian V., Fokker-Planck Equations of Stochastic Acceleration: Green's Functions and Boundary Conditions, 1995, ApJ, 446, 699

Park B. T., Petrosian V., Fokker-Planck Equations of Stochastic Acceleration: A Study of Numerical Methods, 1996, ApJS, 103, 255

Parker E. N., The Reconnection Rate of Magnetic Fields, 1973, ApJ, 180, 247

Parker E. N., Tidman D. A., Suprathermal Particles, 1958, Physical Review, 111, 1206

Perkins J. S., 2008, in American Institute of Physics Conference Series Vol. 1085 of American Institute of Physics Conference Series, VERITAS Observations of the Coma Cluster of Galaxies. pp 569–572

Perkins J. S., the VERITAS Collaboration TeV Gamma-Ray Observations of the Perseus and Abell 2029 Galaxy Clusters, 2006, ApJ, 644, 148

Petkova M., Springel V., An implementation of radiative transfer in the cosmological simulation code GADGET, 2009, MNRAS, 396, 1383

Petrosian V., On the Nonthermal Emission and Acceleration of Electrons in Coma and Other Clusters of Galaxies, 2001, ApJ, 557, 560

Petrosian V., Bykov A., Rephaeli Y., Nonthermal Radiation Mechanisms, 2008, Space Science Reviews, 134, 191

Pfrommer C., Simulating cosmic rays in clusters of galaxies - III. Non-thermal scaling relations and comparison to observations, 2008, MNRAS, 385, 1242

Pfrommer C., Ensslin T. A., Constraining the population of cosmic ray protons in cooling flow clusters with γ-ray and radio observations: Are radio mini-halos of hadronic origin?, 2004, A&A, 413, 17

Pfrommer C., Ensslin T. A., Springel V., Simulating cosmic rays in clusters of galaxies - II. A unified scheme for radio haloes and relics with predictions of the γ-ray emission, 2008, MNRAS, 385, 1211

Pfrommer C., Ensslin T. A., Springel V., Jubelgas M., Dolag K., Simulating cosmic rays in clusters of galaxies - I. Effects on the Sunyaev-Zel'dovich effect and the X-ray emission, 2007, MNRAS, 378, 385

Pfrommer C., Springel V., Ensslin T. A., Jubelgas M., Detecting shock waves in cosmological smoothed particle hydrodynamics simulations, 2006, MNRAS, 367, 113

Pinzke A., Pfrommer C., Simulating the γ-ray emission from galaxy clusters: a universal cosmic ray spectrum and spatial distribution, 2010, MNRAS, 409, 449

Pizzo R. F., de Bruyn A. G., Bernardi G., Brentjens M. A., Deep multi-frequency rotation measure tomography of the galaxy cluster A2255, 2011, A&A, 525, A104+

Planck M., Ueber einen Satz der statistischen Dynamik und eine Erweiterung in der Quantumtheorie, 1917, Sitzungberichte der Preussischen Akadademie der Wissenschaften, pp 324–341

Poulain P., Nieto J.-L., Davoust E., Isophotal shapes of early-type galaxies. II - The Perseus Cluster, 1992, A&AS, 95, 129

Pratt G. W., Croston J. H., Arnaud M., Boehringer H., Galaxy cluster X-ray luminosity scaling relations from a representative local sample (REXCESS), 2008, ArXiv e-prints

Press W. H., Schechter P., Formation of Galaxies and Clusters of Galaxies by Self-Similar Gravitational Condensation, 1974, ApJ, 187, 425

Press W. H., Teukolsky S. A., Vetterling W. T., Flannery B. P., 1992, Numerical recipes in FORTRAN. The art of scientific computing. Cambridge: University Press, —c1992, 2nd ed.

Price D. J., Federrath C., A comparison between grid and particle methods on the statistics of driven, supersonic, isothermal turbulence, 2010, MNRAS, 406, 1659

Rachen J. P., Ultra-high energy cosmic rays from radio galaxies revisited, 2008, ArXiv e-prints, 808

Rasia E., Ettori S., Moscardini L., Mazzotta P., Borgani S., Dolag K., Tormen G., Cheng L. M., Diaferio A., Systematics in the X-ray cluster mass estimators, 2006, MNRAS, 369, 2013

Reid A. D., Hunstead R. W., Lemonon L., Pierre M. M., Radio study of X-ray clusters of galaxies – II. A1300: a post-merger cluster at z=0.31 containing a halo and a relic, 1999, MNRAS, 302, 571

Reimer A., Reimer O., Schlickeiser R., Iyudin A., The Coma Cluster at γ-ray energies: Multifrequency constraints, 2004, A&A, 424, 773

Reimer O., Pohl M., Sreekumar P., Mattox J. R., EGRET Upper Limits on the High-Energy Gamma-Ray Emission of Galaxy Clusters, 2003, ApJ, 588, 155

Reiprich T. H., Böhringer H., The Mass Function of an X-Ray Flux-limited Sample of Galaxy Clusters, 2002, ApJ, 567, 716

Rephaeli Y., Spatial distribution of Compton-produced X-ray flux from rich and regular clusters of galaxies, 1977, ApJ, 212, 608

Rephaeli Y., Relativistic electrons in the intracluster space of clusters of galaxies - The hard X-ray spectra and heating of the gas, 1979, ApJ, 227, 364

Rephaeli Y., Gruber D., Results from a Second Rossi X-Ray Timing Explorer Observation of the Coma Cluster, 2002, ApJ, 579, 587

Ricker P. M., Sarazin C. L., Off-Axis Cluster Mergers: Effects of a Strongly Peaked Dark Matter Profile, 2001, ApJ, 561, 621

Roettiger K., Burns J., Loken C., When clusters collide - A numerical Hydro/N-body simulation of merging galaxy clusters, 1993, ApJ, 407, L53

Roettiger K., Burns J. O., Stone J. M., A Cluster Merger and the Origin of the Extended Radio Emission in Abell 3667, 1999, ApJ, 518, 603

Roettiger K., Stone J. M., Burns J. O., Magnetic Field Evolution in Merging Clusters of Galaxies, 1999, ApJ, 518, 594

Rosati P., Borgani S., Norman C., The Evolution of X-ray Clusters of Galaxies, 2002, ARA&A, 40, 539

Rottgering H. J. A., Wieringa M. H., Hunstead R. W., Ekers R. D., The extended radio emission in the luminous X-ray cluster A3667, 1997, MNRAS, 290, 577

Ruzmaikin A. A., Sokoloff D. D., The calculation of Faraday rotation measures of cosmic radio sources, 1979, A&A, 78, 1

Rybicki G. B., Lightman A. P., 1986, Radiative Processes in Astrophysics. Radiative Processes in Astrophysics, by George B. Rybicki, Alan P. Lightman, pp. 400. ISBN 0-471-82759-2. Wiley-VCH , June 1986.

Ryle M., Windram M. D., The radio emission from galaxies in the Perseus cluster, 1968, MNRAS, 138, 1

Ryu D., Kang H., Biermann P. L., Cosmic magnetic fields in large scale filaments and sheets, 1998, A&A, 335, 19

Ryu D., Kang H., Cho J., Das S., Turbulence and Magnetic Fields in the Large-Scale Structure of the Universe, 2008, Science, 320, 909

Ryu D., Kang H., Hallman E., Jones T. W., Cosmological Shock Waves and Their Role in the Large-Scale Structure of the Universe, 2003, ApJ, 593, 599

Ryu D., Miniati F., Jones T. W., Frank A., A Divergence-free Upwind Code for Multidimensional Magnetohydrodynamic Flows, 1998, ApJ, 509, 244

Sanders J. S., Fabian A. C., Smith R. K., Constraints on turbulent velocity broadening for a sample of clusters, groups and elliptical galaxies using XMM-Newton, 2011, MNRAS, 410, 1797

Sarazin C. L., 1988, X-ray emission from clusters of galaxies

Sarazin C. L., The Energy Spectrum of Primary Cosmic-Ray Electrons in Clusters of Galaxies and Inverse Compton Emission, 1999a, ApJ, 520, 529

Sarazin C. L., Thermal and Nonthermal Effects of Merger Shocks in Clusters of Galaxies, 1999b, ArXiv Astrophysics e-prints

Scheer D. J., Kraus J. D., A High-Sensivity Survey of the North Galactic Polar Region at 1415 MHz., 1967, AJ, 72, 536

Schlickeiser R., An explanation of abrupt cutoffs in the optical-infrared spectra of non-thermal sources - A new pile-up mechanism for relativistic electron spectra, 1984, A&A, 136, 227

Schlickeiser R., 2002, Cosmic Ray Astrophysics. Cosmic ray astrophysics / Reinhard Schlickeiser, Astronomy and Astrophysics Library; Physics and Astronomy Online Library. Berlin: Springer. ISBN 3-540-66465-3, 2002, XV + 519 pp.

Schlickeiser R., Miller J. A., Quasi-linear Theory of Cosmic-Ray Transport and Acceleration: The Role of Oblique Magnetohydrodynamic Waves and Transit-Time Damping, 1998, ApJ, 492, 352

Schlickeiser R., Sievers A., Thiemann H., The diffuse radio emission from the Coma cluster, 1987, A&A, 182, 21

Schuecker P., Finoguenov A., Miniati F., Böhringer H., Briel U. G., Probing turbulence in the Coma galaxy cluster, 2004, A&A, 426, 387

Seeger C. L., Westerhout G., Conway R. G., Observations of discrete sources, the Coma cluster, the moon, and the Andromeda nebula at a wave length of 75 cm., 1957, ApJ, 126, 585

Sijacki D., Springel V., di Matteo T., Hernquist L., A unified model for AGN feedback in cosmological simulations of structure formation, 2007, MNRAS, 380, 877

Spitkovsky A., Particle Acceleration in Relativistic Collisionless Shocks: Fermi Process at Last?, 2008, ApJ, 682, L5

Spitzer L., 1956, Physics of Fully Ionized Gases

Springel V., The cosmological simulation code GADGET-2, 2005, MNRAS, 364, 1105

Springel V., Farrar G. R., The speed of the 'bullet' in the merging galaxy cluster 1E0657-56, 2007, MNRAS, 380, 911

Springel V., Hernquist L., Cosmological smoothed particle hydrodynamics simulations: the entropy equation, 2002, MNRAS, 333, 649

Stecker F. W., The Cosmic γ-Ray Spectrum from Secondary Particle Production in Cosmic-Ray Interactions, 1970, Ap&SS, 6, 377

Stephens S. A., Badhwar G. D., Production spectrum of gamma rays in interstellar space through neutral pion decay, 1981, Ap&SS, 76, 213

Strom R. G., Radio polarization-Faraday depolarization of extragalactic radio sources, 1972, Nature, 239, 19

Subramanian K., Shukurov A., Haugen N. E. L., Evolving turbulence and magnetic fields in galaxy clusters, 2006, MNRAS, 366, 1437

Sunyaev R. A., Norman M. L., Bryan G. L., On the Detectability of Turbulence and Bulk Flows in X-ray Clusters, 2003, Astronomy Letters, 29, 783

Taylor G. B., Govoni F., Allen S. W., Fabian A. C., Magnetic fields in the 3C 129 cluster, 2001, MNRAS, 326, 2

Taylor G. B., Perley R. A., Magnetic Fields in the Hydra A Cluster, 1993, ApJ, 416, 554

The HESS Collaboration: F. A. Aharonian Constraints on the multi-TeV particle population in the Coma Galaxy Cluster with H.E.S.S. observations, 2009, ArXiv e-prints

The MAGIC Collaboration Aleksić J. e. a., MAGIC Gamma-ray Telescope Observation of the Perseus Cluster of Galaxies: implications for cosmic rays, dark matter and NGC1275, 2009, ArXiv e-prints

Thierbach M., Klein U., Wielebinski R., The diffuse radio emission from the Coma cluster at 2.675 GHz and 4.85 GHz, 2003, A&A, 397, 53

Tornatore L., Borgani S., Matteucci F., Recchi S., Tozzi P., Simulating the metal enrichment of the intracluster medium, 2004, MNRAS, 349, L19

Tribble P. C., Radio emission in a random magnetic field - Radio haloes and the structure of the magnetic field in the Coma cluster, 1991, MNRAS, 253, 147

Tribble P. C., Radio haloes, cluster mergers, and cooling flows, 1993, MNRAS, 263, 31

Völk H. J., Atoyan A. M., Early Starbursts and Magnetic Field Generation in Galaxy Clusters, 2000, ApJ, 541, 88

Vacca V., Murgia M., Govoni F., Feretti L., Giovannini G., Orra E., Bonafede A., The intracluster magnetic field power spectrum in Abell 665, 2010, A&A, 514, A71+

Vallee J. P., MacLeod M. J., Broten N. W., A large-scale magnetic feature in the galaxy cluster A 2319, 1986, A&A, 156, 386

van Weeren R. J., Röttgering H. J. A., Brüggen M., Hoeft M., Particle Acceleration on Megaparsec Scales in a Merging Galaxy Cluster, 2010, Science, 330, 347

Vazza F., Brunetti G., Gheller C., Shock Waves in Eulerian Cosmological Simulations: Main Properties and Acceleration of Cosmic Rays, 2008, ArXiv e-prints, 808

Vazza F., Brunetti G., Gheller C., Brunino R., Massive and refined: a sample of large galaxy clusters simulated at high resolution. I:Thermal gas and shock waves properties, 2010, ArXiv e-prints

Vazza F., Brunetti G., Gheller C., Brunino R., Brüggen M., Massive and refined. II. The statistical properties of turbulent motions in massive galaxy clusters with high spatial resolution, 2011, A&A, 529, A17+

Vazza F., Brunetti G., Kritsuk A., Wagner R., Gheller C., Norman M., Turbulent motions and shocks waves in galaxy clusters simulated with adaptive mesh refinement, 2009, A&A, 504, 33

Vazza F., Gheller C., Brunetti G., The mixing and transport properties of the intra cluster medium: a numerical study using tracers particles, 2010, A&A, 513, A32+

Venturi T., Bardelli S., Dallacasa D., Brunetti G., Giacintucci S., Hunstead R. W., Morganti R., The radio halo in the merging cluster A3562, 2003, A&A, 402, 913

Venturi T., Bardelli S., Morganti R., Hunstead R. W., Radio properties of the Shapley Concentration - I. The Abell cluster A3556, 1997, MNRAS, 285, 898

Venturi T., Giacintucci S., Brunetti G., Cassano R., Bardelli S., Dallacasa D., Setti G., GMRT radio halo survey in galaxy clusters at z = 0.2-0.4. I. The REFLEX sub-sample, 2007, A&A, 463, 937

Venturi T., Giacintucci S., Cassano R., Brunetti G., Dallacasa D., Macario G., Setti G., Bardelli S., Athreya R., 2009, in D. J. Saikia, D. A. Green, Y. Gupta, & T. Venturi ed., The Low-Frequency Radio Universe Vol. 407 of Astronomical Society of the Pacific Conference Series, The GMRT Radio Halo Survey and Low Frequency Follow–up. pp 232–+

Venturi T., Giacintucci S., Dallacasa D., Cassano R., Brunetti G., Bardelli S., Setti G., GMRT radio halo survey in galaxy clusters at z = 0.2-0.4. II. The eBCS clusters and analysis of the complete sample, 2008, A&A, 484, 327

Venturi T., INAF di Radioastronomia I., Observational properties of diffuse radio sources in Galaxy Clusters. Current knowledge and open questions, 2011, ArXiv e-prints

Viner M. R., Erickson W. C., 26.3-MHz radio source survey. II - Radio source positions and fluxes, 1975, AJ, 80, 931

Vogt C., Dolag K., Enßlin T. A., PACERMAN- II. Application and statistical characterization of improved RM maps, 2005, MNRAS, 358, 732

Vogt C., Ensslin T. A., Measuring the cluster magnetic field power spectra from Faraday rotation maps of Abell 400, Abell 2634 and Hydra A, 2003, A&A, 412, 373

Vogt C., Ensslin T. A., A Bayesian view on Faraday rotation maps Seeing the magnetic power spectra in galaxy clusters, 2005, A&A, 434, 67

Völk H. J., Aharonian F. A., Breitschwerdt D., The Nonthermal Energy Content and Gamma-Ray Emission of Starburst Galaxies and Clusters of Galaxies, 1996, Space Science Reviews, 75, 279

Völk H. J., Atoyan A. M., Clusters of galaxies: magnetic fields and nonthermal emission, 1999, Astroparticle Physics, 11, 73

Wentzel D. G., Cosmic-ray propagation in the Galaxy - Collective effects, 1974, ARA&A, 12, 71

Werner N., Zhuravleva I., Churazov E., Simionescu A., Allen S. W., Forman W., Jones C., Kaastra J. S., Constraints on turbulent pressure in the X-ray haloes of giant elliptical galaxies from resonant scattering, 2009, MNRAS, 398, 23

Wielebinski R., Waldthausen H., Kronberg P. P., Haslam C. G. T., Radio counterpart of the X-ray source 3U0901-09, 1977, Nature, 266, 239

Wik D. R., Sarazin C. L., Finoguenov A., Baumgartner W. H., Mushotzky R. F., Okajima T., Tueller J., Clarke T. E., The Lack of Diffuse, Non-thermal Hard X-ray Emission in the Coma Cluster: The Swift Burst Alert Telescope's Eye View, 2011, ApJ, 727, 119

Wik D. R., Sarazin C. L., Finoguenov A., Matsushita K., Nakazawa K., Clarke T. E., A Suzaku Search for Nonthermal Emission at Hard X-Ray Energies in the Coma Cluster, 2009, ApJ, 696, 1700

Wikipedia, 2011, Faraday effect — Wikipedia, The Free Encyclopedia

Willson M. A. G., Radio observations of the cluster of galaxies in Coma Berenices - the 5C4 survey., 1970, MNRAS, 151, 1

Wu X., Xue Y., Fang L., The L_X-T and L_X-σ Relationships for Galaxy Clusters Revisited, 1999, ApJ, 524, 22

Zhuravleva I. V., Churazov E. M., Sazonov S. Y., Sunyaev R. A., Dolag K., Resonant scattering in galaxy clusters for anisotropic gas motions on various spatial scales, 2011, Astronomy Letters, 37, 141

Zhuravleva I. V., Churazov E. M., Sazonov S. Y., Sunyaev R. A., Forman W., Dolag K., Polarization of X-ray lines from galaxy clusters and elliptical galaxies - a way to measure the tangential component of gas velocity, 2010, MNRAS, 403, 129

Acknowledgements / Danksagung

The author thanks his friends and family for the continuous support during the formation of this thesis. Klaus and Gianfranco for great tutoring. Margarita for support and proofreading the thesis. Harald for his support in bureaucratic matters; Rossella, Franco and Annalisa for helpful discussions, fun at conferences and an overdose of Italianess. The IMPRS community for international help, and his flat-mates for enduring the construction noise. Ole and Inga for making far feel close.
I thank my parents for love and support. Oma, Opa, Mamama and Papapa for a perfect combination of guidance and spoiling.

Der Autor dankt seinen Freunden und seiner Familie für den andauernde Unterstützung während des Abfassens dieser Arbeit; Klaus und Gianfranco für die grossartige Betreuung; Margarita für ihre Unterstützung und das Korrekturlesen; Harald für vorbildliche Unterstützung bei den Formalien; Rossella, Franco und Annalisa für hilfreiche Diskussionen, Spass auf Konferenzen und einer Überdosis italienisch; Der IMPRS Gemeinschaft für internationale Hilfe; seinen Mitbewohnern für das Ertragen des Baustellenlärms.
Ich danke meinen Eltern für die Liebe und Unterstützung. Oma, Opa, Mamama und Papapa für die perfekte Kombination aus Führung und Verwöhnen.